Labyrinth Weir Hydraulics:

Validation of CFD Modelling

by

Guy Kinloch Robertson

Thesis presented in partial fulfilment of the requirements for the degree Master of Science in Engineering at Stellenbosch University

Supervisor: Prof. G.R. Basson

Faculty of Engineering

April 2014

Declaration

By submitting this thesis, I declare that the entirety of the work contained therein is my own, original work, that I am the sole author thereof (save to the extent explicitly otherwise stated), that reproduction and publication thereof by Stellenbosch University will not infringe any third party rights and that I have not previously in its entirety or in part submitted it for obtaining any qualification.

Signed ……………………. Date …………………….

Abstract

The use of computational fluid dynamics (CFD) as a design tool is becoming increasingly popular in the water resources field. This thesis aims to extend the knowledge of CFD and determine the usefulness of current CFD programs as a modelling tool. This thesis also seeks to determine the accuracy of CFD modelling when compared to physical modelling, the more established form of model testing.

It is important that research is conducted on the validation of CFD because with an increase in computer power, processing speed and continual development in the programs used to generate the models, CFD could become an essential tool for the hydraulic engineer. A current key difficulty faced by CFD programs is the mapping of the free surface level of a body of fluid in a two-phase (water and air) flow condition. This is further complicated by the existence of three-dimensional flow over a labyrinth weir and a fluctuating nappe, which at times requires a free surface level to be mapped both above and below the nappe.

This thesis begins by detailing the design methods and actual design of a typical labyrinth weir. It then describes the construction of a 1:20 scale physical model, testing procedures, goals, and the results of the physical model tests. Following the physical model study, the thesis discusses the development of a three-dimensional CFD model, designed in a way that matched the physical model. Simulation results obtained from the CFD model are then compared to those from the physical model study and the accuracy and suitability of CFD modelling as a design tool are evaluated. This evaluation considers the surcharge upstream of the weir and transient pressures on the weir. The thesis concludes with recommendations for further research in this field.

The results achieved show that the CFD model was able to accurately map the movement of particles within the domain, to fully develop a flow profile, and to accurately predict the water surface level. The pressure readings obtained during CFD modelling were in the same order as those obtained during physical modelling. However, the CFD modelling pressure readings did not often accurately correspond with the physical modelling data, with the average error being 92%.

These results indicate that there is still further development required in CFD before it can be relied upon as a design tool independent of other experimental methods. The difficulty and the length of time taken to generate the results also indicate that, at this stage and in this particular scenario, the engineer would be better served through the use of a physical model.

Opsomming

Die gebruik van gerekenariseerde vloeidinamika (CFD) as ’n ontwerpinstrument het toenemend gewild begin raak op die gebied van waterhulpbronne. Die doel van hierdie verslag is om kennis van CFD uit te brei en die nut van huidige CFD-programme as ’n modelleringsinstrument te bepaal. Daar word voorts ook gepoog om die akkuraatheid van CFD-modellering te bepaal in vergelyking met fisiese modellering – die meer gevestigde vorm van modeltoetsing.

Dit is noodsaaklik dat navorsing gedoen word oor die bekragtiging van CFD, want met ’n toename in rekenaarkrag, verwerkingsnelheid en deurlopende ontwikkeling in die programme wat gebruik word om die modelle te genereer, sal CFD ’n noodsaaklike instrument vir die hidroulika-ingenieur word. ’n Belangrike probleem wat CFD-programme tans inhou, is die kartering van die vry oppervlak van ’n liggaam vloeistof in ’n tweefasse vloeitoestand (water en lug). Dit word verder bemoeilik deur die bestaan van driedimensionele vloei oor ’n labirint-stuwal en ’n skommelende “nappe”, wat by tye vereis dat ’n vry oppervlak sowel bo as onder die “nappe” gekarteer met word.

Die verslag begin met ’n uiteensetting van die ontwerpmetodes en fisiese ontwerp van ’n tipiese labirint-stuwal. Die bou van ’n 1:20-skaal- fisiese model, toetsprosedures, doelwitte en die resultate van die toetse op die fisiese model word dan beskryf. Ná die studie van die fisiese model, word die ontwikkeling van ’n driedimensionele CFD-model bespreek, wat ontwerp is om by die fisiese model te pas. Die simulasie-resultate van die CFD-model word dan vergelyk met dié van die studie van die fisiese model en die akkuraatheid en geskiktheid van CFD-modellering as ’n ontwerpinstrument word geëvalueer. In hierdie evaluering word die opdamming stroomop van die stuwal en druk op die stuwal ondersoek. Die verslag word afgesluit met aanbevelings vir verdere navorsing op hierdie gebied.

Die resultate toon dat die CFD-model die beweging van partikels in die domein akkuraat kon karteer ten einde ’n volledige vloeiprofiel te ontwikkel en die watervlak akkuraat te voorspel. Die drukke wat tydens CFD-modellering verkry is, stem egter nie ooreen met die lesings wat tydens fisiese modellering verkry is nie. Die gemiddelde fout is 92%.

Hierdie resultate toon dat verdere ontwikkeling in CFD nodig is voordat daarop staat gemaak kan word as ’n ontwerpinstrument wat onafhanklik van ander eksperimentele metodes gebruik kan word. Die moeilikheidsgraad en die lang tydsduur betrokke by die generering van resultate is ook ’n aanduiding dat die gebruik van ’n fisiese model die ingenieur op hierdie stadium en in hierdie spesifieke scenario beter tot diens sal wees.

Acknowledgements

Firstly, many thanks must go to my supervisor Prof. Gerrit Basson for his advice, thoroughness, and for never failing to push me to produce high quality work.

I would like to thank to Mr Christiaan Visser for his continual support, enthusiasm and willingness to discuss the intricacies of this thesis. As well as the Stellenbosch Water Laboratory staff members for their assistance with the physical modelling component.

I am extremely grateful to the professionals at Qfinsoft (Pty) Ltd for their assistance and time, in particular Mr Stephan Schmitt, for his help with the use of ANSYS Fluent.

The compilation of this thesis and my full-time attendance at Stellenbosch University would not have been possible if it were not for the generosity of SANCOLD who have funded my studies, for which I am sincerely grateful.

Lastly, I would like to express thanks to my family and fiancé, for their constant support and encouragement – especially to my father and brother, whose knowledge and advice have been invaluable to me during the process of compiling this thesis.

Contents

List of Figures

List of Tables

Glossary

Computational fluid dynamics (CFD) – CFD is the use of numerical methods and algorithms for the solving and analysing of problems associated with fluid flows.

Convection – Transport due to fluid flow.

Diffusion – Transport due to variation of ϕ from point to point.

Effective length of disturbance (L_{de}) – The equivalent length of a weir over which $C_d = 0$.

Full supply level – The normal maximum operating water level of a dam or reservoir.

Freeboard – The area between the water surface level and the crest of a dam or reservoir wall.

Interference length – The length of the area of the downstream portion of a labyrinth weir where nappes from adjacent cycles collide.

Nappe – The profile of a body of water flowing over a weir or similar hydraulic structure.

Transient – Changing with time.

List of Symbols and Acronyms

CFD - Computational fluid dynamics

FSL - Full supply level

GB - Gigabyte

GHz - Gigahertz

IDF - Inflow design flood

PDEs - Partial differential equations

RAM - Random access memory

RANS - Reynolds-average Navier-Stokes

a - One-half of the weir apex

B - Weir side length

h_m - Measured head upstream of weir

H_o - Design head for ogee weir

H_t - Total upstream head

l - Developed length of one cycle ($l = 4a + 2b$)

L - Total developed length of weir

n - Number of cycles

P - Weir height

Q_L - Discharge over labyrinth weir (sometimes Q_{LAB})

Q_N - Discharge over linear weir (sometimes Q_{LIN})

Q_L/Q_N - Discharge magnification

t - Crest thickness

w - Width of one weir cycle

w/P - Vertical aspect ratio

W - Total width of weir

α - Sidewall angle

C - Coefficient of discharge

L_{de} - Effective length of disturbance

L_{de}/B - Disturbance length ratio (Interference ratio)

Φ - A general variable in CFD, such as velocity

$u, v \; and \; w$ - Velocities in the x, y and z directions respectively

$A_x, A_y \; and \; A_z$ - Fractional areas, across each cell face in the noted directions, open to flow;

P' - Pressure

ρ - Density

g_i - Gravitational force in the noted direction

f_i - Represents the Reynolds stresses.

Chapter 1: Introduction

1.1. Introduction

This thesis examines computational fluid dynamics (CFD); in particular, it compares results produced through physical modelling and mathematical modelling using CFD, of a labyrinth weir.

CFD is rapidly developing as a means to predict the behaviour of real-life structures. As computer power has increasingly become less of an issue and various programs have become more capable of accurately developing means to map the patterns represented by the interaction of water with sediment, structures and topography, the use of CFD has become more widespread. As an alternative to physical modelling, CFD will in time become cheaper, faster and perhaps as accurate, as a result of improving technology.

The high level objective of this thesis (described in detail in the next section) is to determine the current level of accuracy of CFD. Additionally, it is to conclude whether or not this level is sufficient for sole reliance on the results produced from CFD to safely submit designs and recommendations on a project.

The focus of this thesis is limited to the validation of CFD modelling through the design and testing of one labyrinth weir. For further conclusions to be drawn a more extensive study involving different models and methods of testing would be required; however, that is outside the scope of this thesis.

The first part of this thesis contains an extensive review of literature informing the relevant sections of the thesis. This is followed by a detailed design of a ‘typical’ labyrinth weir, a review of the physical model study, and an evaluation of the mathematical model study using CFD. The thesis then examines the validation of CFD modelling with reference to the results obtained in the two model studies. Finally, conclusions are drawn and recommendations are made for further research.

1.2. Objectives of Study

The objectives of this thesis were to determine:

1. The pressure readings on the downstream face of a labyrinth weir using both physical and CFD modelling;
2. When, where, and to what extent negative pressures occur and which flow conditions cause them to arise;
3. Water levels for each of the discharges tested using theoretical calculations, analytical modelling and physical modelling;
4. The usefulness of CFD modelling as a method of determining the behaviour of two-phase flows (water and air);
5. The accuracy of the results determined through the use of CFD modelling with regards to this specific scenario; and
6. Specific areas where further research is required surrounding labyrinth weirs and CFD modelling.

To achieve these, a physical model of a labyrinth weir with pressure sensors to monitor specific locations on the downstream face of the weir was constructed and tested.

Following the testing of the physical model a CFD model of an identical labyrinth weir with two phase flow conditions was generated in order to meet the objectives of when, where and to what extent negative pressures occur on the downstream face under various flow conditions.

The CFD model results, in comparison with the physical modelling results, were used to determine the accuracy of the CFD modelling procedure in this case.

1.3. Methodology

The preliminary research for the thesis began with a literature review of journals, books and articles to better understand labyrinth weirs, physical modelling and CFD. Obtaining a better understanding of CFD required attending a course on how to use the selected program, the study of the theory behind the programs and the use of manuals, user-guides and personal communication with the support staff in order to obtain results. The literature review also included a brief analysis of a number of reference projects, these projects all contained similarities to this thesis and were useful during the processes described below.

Following the literature review, the objectives of the study were outlined. The first step towards being able to study the behaviour of a labyrinth weir was to design one. A prototype was designed by using the laboratory set up to generate limitations of size and flow volume. This was then scaled down to a model with a scale of 1:20. Further descriptions on the limits of the model in the laboratory and the design procedure behind the labyrinth are discussed in detail in Chapter 3.

The construction of the model was completed using drawings of the scaled design created in AutoCAD. The model was built using a range of materials and was waterproofed to ensure it endured the entire testing period. The positioning of the model at the end of a 2 m high, 1.5 m wide and 5 m long flume created adequate space for storage and allowed uniform flow to develop fully when testing both low and high-flow conditions. Inserting pressure sensors into the model was also an important part of the model's set-up as the holes in the downstream part of the wall needed be connected by tubes leading to the pressure sensors.

The physical model testing was performed for a range of flows for time periods of 5 minutes per test: from a low flow of 60 *l*/s to a high of 600 *l*/s. The measurements were focussed on the surcharge 1.5 m upstream of the weir and the transient pressures along the downstream face of the weir. The latter were measured using piezometer pressure sensors.

Physical model depth of flow results were documented and compared directly with the results predicted by theoretical equations. The pressures measured were also converted into an appropriate form and calibrated according to calibration tests performed on the day of testing to ensure similar conditions.

Using ANSYS Fluent, a CFD model was created to the same dimensions as the physical model and with surface monitor points located in the same positions as in the physical model. In addition to the flow depth and the pressures recorded at specific points, as in the physical model, the CFD model allowed for further information to be extracted from the model. This included flow patterns, velocities, densities and flow rates as well as the general changes in pressure across the entire system, not just at specific points where monitors have been inserted, as with the physical model.

The CFD model was initially run with steady state flow conditions, giving an average pressure across time and a depth of flow. The model was then used to run transient flow simulations, the results from which were subsequently compared directly with the flow depths and piezometer pressure readings that came from the physical model.

The results from the CFD model were compared with the physical model results in an attempt to determine the accuracy and usefulness of the computer modelling process in this scenario. The limitations of CFD modelling are also discussed in reference to the compared results. Chapter 6 of the thesis focusses on the validation process of CFD modelling which deals with the results comparison and discusses the accuracy of the model.

Once the results have been discussed and conclusions drawn, potential areas of further research are identified and recommended. These areas are inclusive of specific research that could be used to extend this body of work as well as additional necessary research concerning labyrinth weirs, CFD modelling and CFD validation.

Chapter 2: Literature Review

2.1. Introduction

This chapter focusses on the various aspects of the labyrinth weir. This includes the development of the weir, various design methods and approaches, and the advantages and disadvantages associated with the use of a labyrinth.

This chapter also deals with the hydraulic performance of the weir, including topics such as crest shape, crest performance, shape in plan form, sub-atmospheric (negative) pressures and the nappe, interference, aeration and downstream flow conditions.

CFD modelling is explained, with discussions on the development and validation through comparison of results between physical and numerical models.

The design and methodology used when designing and testing a labyrinth is examined before a description of a number of existing projects with relevant similarities to this thesis, conclude the chapter.

2.2. Spillways and Weirs

2.2.1. Spillways

A spillway is a type of control structure, usually placed perpendicular to the flow direction in a dam. It forms an integral part of any dam design: it ensures the safety of the dam wall, regulates flow downstream of the wall, and protects a dam from overtopping and possible failure during wet periods or flooding. Spillways are designed to allow excess water to pass from the upstream side of the dam downstream; they release the surplus or flood water that exceeds the dam's full supply level (FSL) and protect the downstream face of the dam from erosion caused by flowing waters.

The water being discharged over a spillway can flow at a high velocity due to the energy head in the dam; this can cause damage and erosion to the banks and river downstream. To avoid this, energy dissipaters and/or stilling basins can be included in the design.

There are two main categories of spillways: service spillways and auxiliary spillways. Where service spillways are designed to pass common or frequently occurring floods and auxiliary spillways are designed to operate once the size of the flood exceeds those passable by a service spillway.

1. Service Spillways: Service spillways may operate alone or be accompanied by an auxiliary spillway. Service spillways may be gated – allowing for greater control of the flow going downstream and can effectively reduce the flood peaks when early warnings are available.

Ungated spillways are typically favoured as they are more reliable; however, gated spillways are sometimes favoured in projects depending on what is downstream of the dam. When operating a gated service spillway system an auxiliary spillway should be included as a safety precaution in case of mechanical or electrical failure of the gate system (SANCOLD, 1991).

2. Auxiliary Spillways**:** Auxiliary spillways are built to accompany service spillways or in conjunction with flood outlets (in which case service spillways are not required). When built to accompany a service spillway, an auxiliary spillway is particularly useful if the service spillway fails, as mentioned above, and should be designed to cope with the safety evaluation discharge (SED) (SANCOLD, 1991).

The topography, geology, and hydrology, dam type and expected reliability of maintenance and operation all can play a role – to varying degrees – in selecting the type of spillway required. The types of spillways are generally described according to their features, the following being common (Sharma & Sharma, 1992):

- Free overfall or straight drop spillway;
- Ogee or overflow spillway;
- Chute spillway;
- Side channel spillway;
- Bywash spillway;
- Piano key weir; and
- Labyrinth spillway.

2.2.2. Weirs

A weir is an artificial barrier, in a watercourse, which is used to regulate flow rate and water depths, and to measure discharge. For some flow conditions, the construction of a weir structure increases the water surface level upstream. The capacity of a given weir or spillway refers to the capable discharge of a weir for a given head of flow over its crest. The chief functions of any spillway or weir include (Ghare, et al., 2008):

- Water level management;
- Flow measurement;
- Creating a pool from which to pump or divert water;
- Environmental enhancement; and
- Channel stabilization.

2.2.3. Description of a Labyrinth Spillway

A labyrinth spillway or weir is a linear weir that has been folded in plan-view, as can be seen in Figure 2.1. This is done to provide increased effective crest length (L_e) over a given spillway width. Labyrinth weirs can be an economical solution for passing large floods as they provide increased unit discharge when compared to conventional weirs for given head (Darvas, 1971). The labyrinth is explored in more detail in section 2.3 below.

Figure 2.1 Raised labyrinth spillway, Dog River Dam, Georgia (U.S. Society on Dams, 2011)

2.3. Background and Development of the Labyrinth

Due to the interesting hydraulics of labyrinth weirs, they have been researched for many years. Gentilini (1940) formed triangular weirs by placing a number of oblique weirs together. Three side wall angles were tested (α=30°, 45° and 60°) for a sharp-crested weir and the presented results were a function of the h/w ratio. Kozák and Sváb (1961) tested flat-topped crested trapezoidal labyrinths with chamfered edges and found that when comparing a labyrinth to a linear weir under similar head conditions, the labyrinth performed with a higher discharge capacity (Crookston, 2010).

The development of the modern labyrinth spillway design began with Taylor (1968) and later Hay and Taylor (1970). In 1985, the Bureau of Reclamation established a design method for engineers to use in the publication *Design and Construction of Labyrinth Spillways* (Lux III & Hinchcliff, 1985). This method was based on the estimation of discharge for spillways with sharp and quarter-round crests using design curves and an equation. Tullis et al. (1995) extended the knowledge base of labyrinth performance and design, developing the 'Tullis method' for trapezoidal labyrinth spillways with a quarter-round crest shape (Paxson, et al., 2011).

Over approximately the last 25 years there has been a significant increase in the number of labyrinth spillways used, particularly in the USA (Khode & Tembhurkar, 2010). This has been attributed to the development of the Lux and Tullis design methods and the change in flood design requirements which has resulted in the increase of required spillway capacities in order to meet the new criteria (Paxson & Savage, 2006). It has been said that Falvey's publication (*Hydraulic Design of Labyrinth Spillways*, 2003) also brought about significant expansion in the use of the labyrinth by furthering the knowledge base of labyrinth weirs through the combination of key publications and additional research (Paxson, et al., 2011).

Assessments completed by ICOLD (International Commission on Large Dams) found that nearly a third of dam failures were due to the spillway capacity being insufficient. ICOLD hence adjusted the design capacity requirements and recommended the upgrading of many spillways. In an attempt to keep these projects economical by simplifying construction, the design engineers attempted to reduce the total dimensions of the re-adapted spillways without affecting the levels of safety. According to Ouamane and Lempérière (2006), the design best able to satisfy these requirements is the labyrinth spillway.

The use of a labyrinth is now a standard approach available to engineers designing weirs or spillways. Due to the inherent advantages of labyrinths regarding flow magnification and structural stability, they should continue to be used to greater extent for future projects (Ghare, et al., 2008).

2.4. Characteristics of Labyrinth Weirs

2.4.1. General

The defining characteristic of the labyrinth weir is its ability to supply increased discharge when compared to conventional weirs for a given head (Paxson, et al., 2011). For any existing weir, the discharge capacity can be increased by either lengthening the weir crest, or increasing the discharge coefficient or operating head. Labyrinths are well suited to sites where increasing the weir width and maximum reservoir water surface elevation would be difficult, yet larger discharge capacities are needed (Khode & Tembhurkar, 2010). As they are able to do all of this effectively due to the increase in capacity and the decrease in flood attenuation under low flow conditions they are particularly well suited to the rehabilitation of existing spillway structures (Houston, 1982). There are infinitely many geometric configurations of labyrinth weirs, as discussed later in this chapter; however, shown in Figure 2.2 are the three general cycle shapes: triangular, rectangular and trapezoidal. It has been found through tests based on the discharge across a unit length that rectangular labyrinths are the least efficient of these shapes (Crookston, 2010).

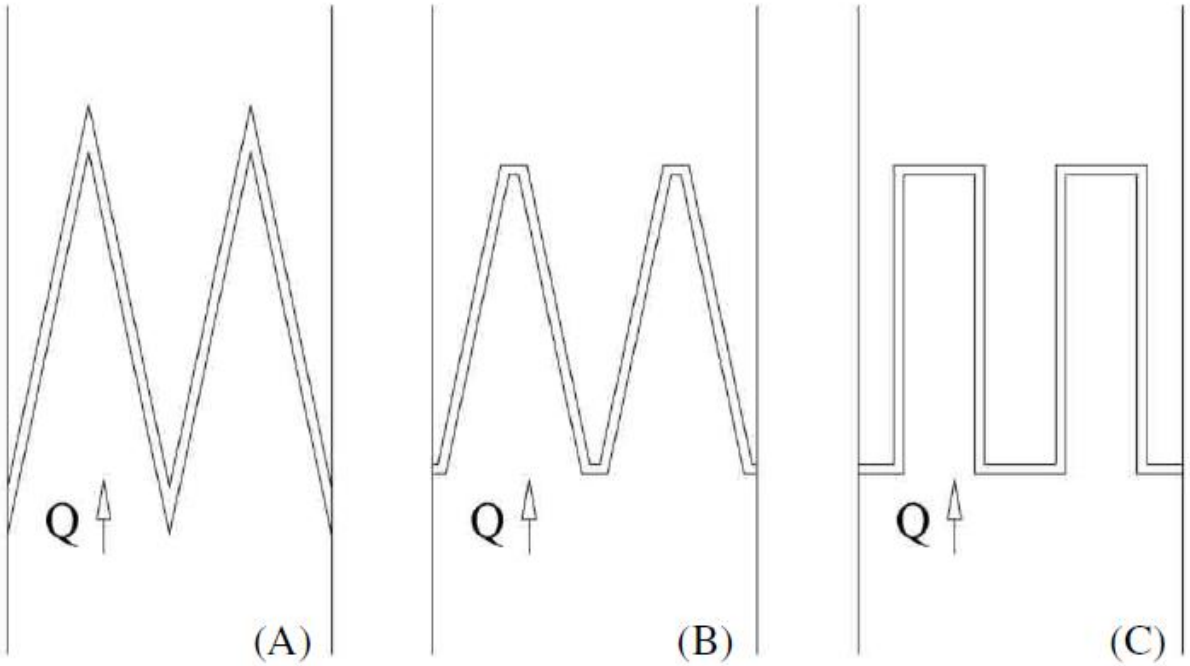

Figure 2.2 Cycle shapes for labyrinth weirs, in plan view: (A) Triangular, (B) Trapezoidal, (C) Rectangular (Crookston, 2010)

The use of labyrinth weirs has become an established option for design engineers, however, because of the hydraulic complexity of these spillways resulting from the range of available geometries, headwater, tail water, approach conditions and other performance factors, there is room for further research to be conducted and uncertainties still exist (Paxson, et al., 2011). The discharge a labyrinth is capable of passing is a function of the total head, effective crest length and crest coefficient. The crest coefficient depends on the total head, weir height, thickness, crest shape, apex configuration and side angle (6-35°) (Tullis, et al., 1995).

During the construction and design of a labyrinth, it is obvious that one would want the most “hydraulically” efficient design obtainable; unfortunately, this is not always possible due to increased construction costs or an inability to construct a hydraulically-optimised weir into site topographic, geological and facility constraints. As a result of this, the overall effectiveness of the project is the determining factor for the design of a weir (Paxson, et al., 2011). Ultimately, the engineer should seek a layout that is economical and exhibits good hydraulic functioning (Ghare, et al., 2008).

There are a number of options available to the engineer when designing a labyrinth weir. Based on a specific crest geometry there are many layouts that provide the required design flow at the design head. (Tullis, et al., 1995). For relatively small dams (i.e. less than 7.6 m) it can be economical to construct a full height labyrinth where the base slab is at the level of the embankment foundation. This construction eliminates the need for a chute to convey flow to the downstream toe (Paxson, et al., 2011). The labyrinth can also be inverted as tested during the modelling phase of the Hyrum Dam, although Falvey (2003) noted that the weir was more efficient when in the regular position. The typical placement for a labyrinth weir is on a flat floor as that was the condition used to develop the design curves (Savage, et al., 2004).

Although readily used, the design theory for labyrinths is not complete. The use of CFD allows the flow field to be mapped and this mapping, along with additional physical model studies, will continue to provide further information to strengthen the current theory and design guidelines of labyrinth weirs (Savage, et al., 2004).

2.4.2. Design Approaches and Methods

Hay and Taylor (1970)

Hay and Taylor developed a design procedure in 1970 based on hydraulic model tests and expressed the hydraulic performance as $Q_{LAB}\ /Q_{LIN}$ vs. h/P, where Q_{LAB} is the discharge over a labyrinth, Q_{LIN} is the discharge over a linear weir, h is the depth of flow over the weir crest and P is the weir height. They wanted to show the advantages of using a labyrinth over a linear weir and thus developed an expression for the effectiveness (E) of the weir (Crookston, 2010):

$$E(\%) = \frac{Q_{LAB}/Q_{LIN}}{L/w} \times 100$$

Where:

L is the developed crest length; and

w is the width of one labyrinth weir cycle.

Hay and Taylor concluded that discharge was not directly related to w/P and did not include the velocity component in the upstream head measurement (Crookston, 2010). Additionally the expression for the discharge coefficient used was not dimensionally homogenous (Ghare, et al., 2008).

Lux Method (1985)

The Lux and Hinchliff (1985) discharge coefficient (C_{d-Lux}) was used to determine the discharge over one labyrinth cycle (Q_{Cycle}) and included an apex shape constant (k) and the vertical aspect ratio (w/P):

$$C_{d-Lux} = \frac{Q_{cycle}}{\frac{w/P}{w/P\ +k}\, w\,\sqrt{g}H_t^{3/2}}$$

This is accompanied by the limiting design factor of $(w/P) \geq 2.0$, which has the potential to complicate the method. This dimensionless equation applies to both triangular and trapezoidal weirs (Crookston, 2010).

Tullis Method (1995)

The Tullis method uses the equation that was developed for linear weirs:

$$Q = \frac{2}{3} C_d \, L \sqrt{2\,g} \, H_t^{1.5}$$

Where:

C_d is the dimensionless crest coefficient;

L is the effective length of the weir;

g is gravitational acceleration; and

H_t is the total upstream head.

For linear weirs, L is the weir's measured length; however, for a labyrinth spillway L is found through the equation:

$$L = 2\,N\,(A + L_2)$$

Additionally, the total length of the crest is found through the equation:

$$Total\ Crest\ Length = N\,(2L_1 + A + D)$$

Where:

N is the number of cycles (4 cycles shown in Figure 2.3);

A is the inside apex width;

L_1 is the actual length of side leg;

L_2 is the effective length of side leg; and

D is the outside apex width.

These parameters are shown in Figure 2.3 below.

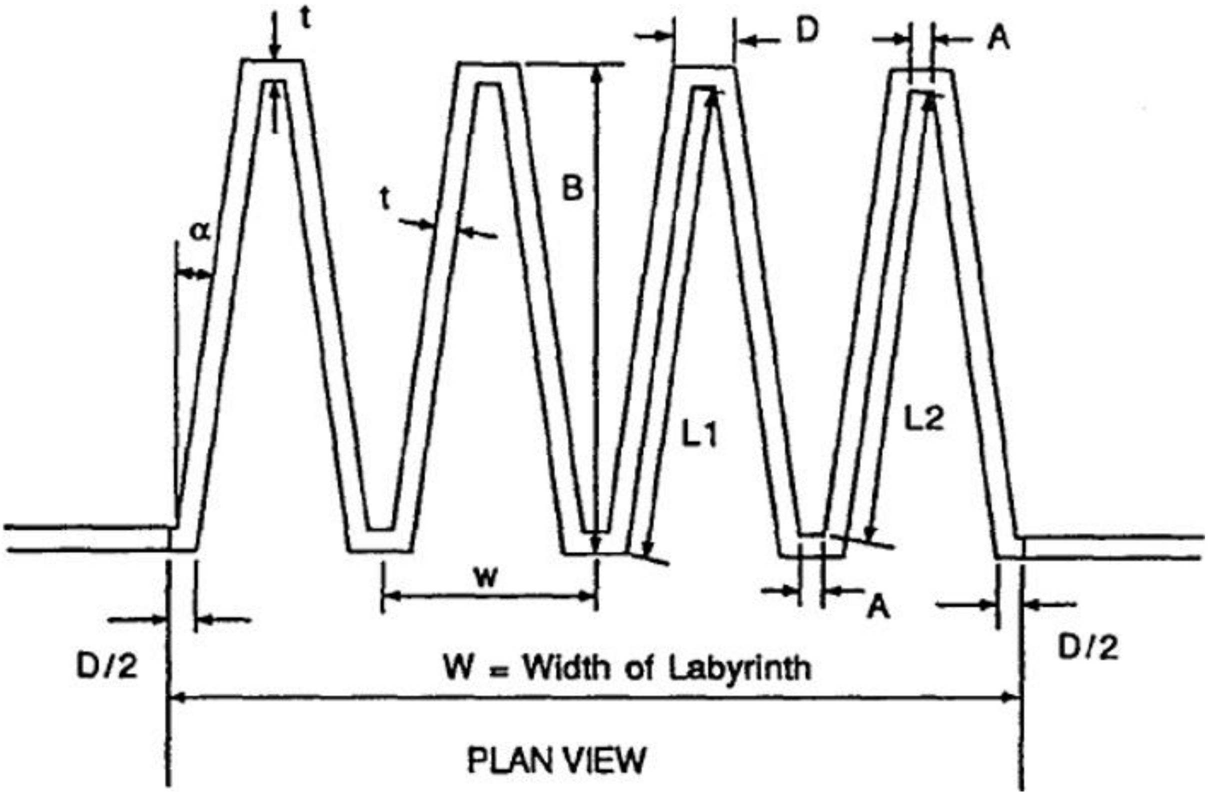

Figure 2.3 Plan view of a labyrinth weir with important dimensions shown (Tullis, et al., 1995)

The curves of Tullis, et al. (1995) were developed for a labyrinth with a quarter-round crest and a trapezoidal shape. The most significant parameter of these curves is the angle of the crest, not the flow magnification which Hay and Taylor (1970) used to define the hydraulic performance of a labyrinth weir with, as described in section 2.5.2. Each of the curves, presented in Figure 2.4, show a deviation from the behaviour of a linear weir which occurs when interference becomes a significant factor. The Tullis, et al. (1995) curves are useful for initial computations for both triangular and trapezoidal-shaped labyrinths (Falvey, 2003). An equation for each of the varying angles of α has been published by Tullis, et al. (1995) to assist with the design method. When plotted, these produce the curves in Figure 2.4 and account for angles (α) between 6° and 35° for a quarter-round crest shape.

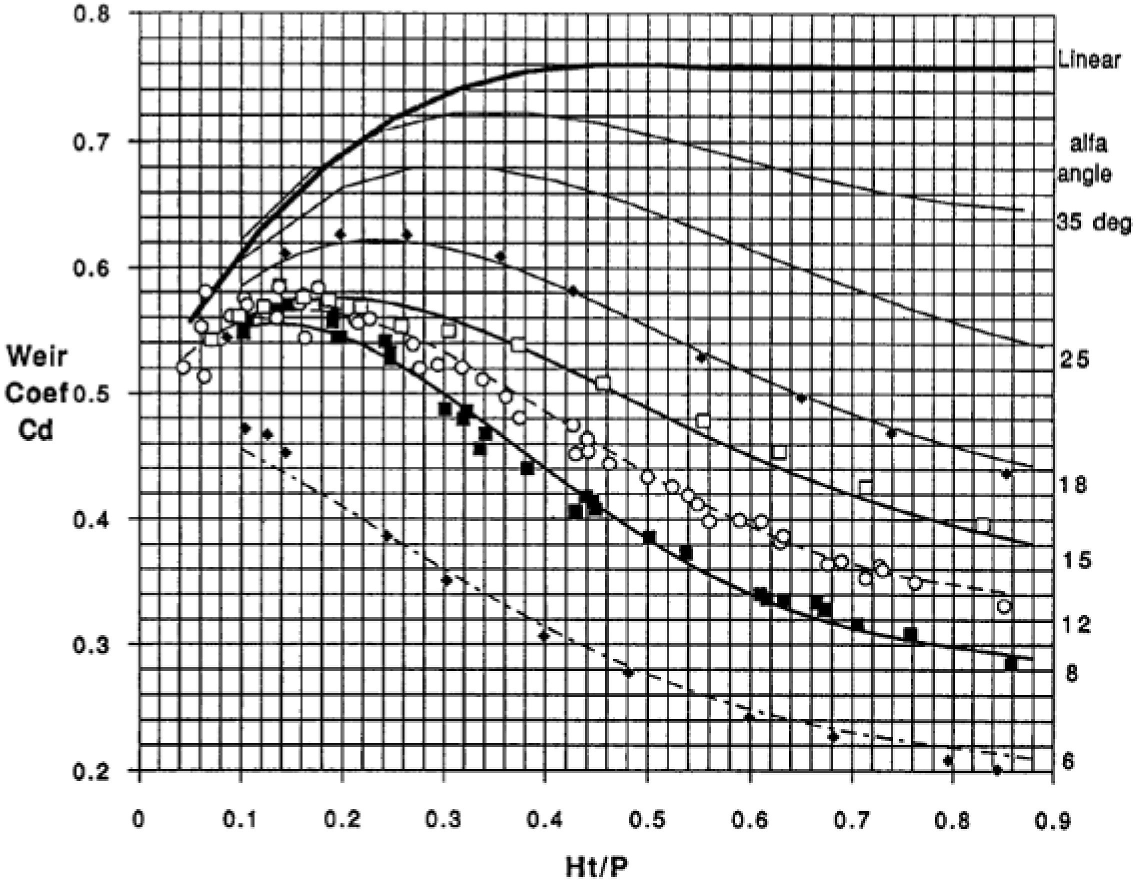

Figure 2.4 Crest coefficient values against the ratio between total head and crest height, for varying values of α, for labyrinth spillways (Tullis, et al., 1995)

When designing the layout of a labyrinth the C_d value should lie as close to the peak values of the curve as possible. This is suggested by the shape of the curves, which contain a peak followed by a long downward slope (Ghare, et al., 2008).

2.4.3. Comparisons between Preferred Design Approaches

Both the Lux and Tullis methods were developed empirically, based on studies conducted within a flume. This means that neither considered possible approach conditions leading up to the weir such as entrance losses (Paxson, et al., 2011). Incorporating non-standard approach conditions into a design increases the complexity of the hydraulic behaviour, meaning that it is most probable that the labyrinth performance cannot be accurately modelled using the Lux or Tullis design methods under these conditions (Paxson & Savage, 2006).

The discharge coefficient for the Lux method is obtained from design curves whilst the Tullis method discharge coefficient (C_d) is computed using polynomial equations based on various sidewall angles relating C_d to (H_t/P) (Paxson, et al., 2011).

The two methods produce similar results, with the Lux method generally determining discharge values at about ten per cent less than the Tullis method (Paxson & Savage, 2006). This is as a result of the Lux method under-predicting C_d (Khode & Tembhurkar, 2010). It was later discovered, in further studies by Tullis (2008) and Crookston (2010), that the Tullis method overestimates the discharge coefficient for the 8° sidewall angle labyrinth (Paxson, et al., 2011).

Lux (1985) notes that the vertical aspect ratio (w/P) should be greater than 2. Tullis, et al. (1995), however, says that the ratio should lie between 3 and 4, as used in the Hyrum dam. Whilst Falvey (2003), says that the studies of Hay and Taylor (1970) show that the aspect ratio does not have a significant effect on the hydraulic performance of the spillway provided it is larger than 2. Lux and Tullis have both shown that, hydraulically, there is improvement as P increases and w/P thus decreases. Both methods suggest a maximum H_t/P of 0.7, although the Tullis equation is applicable provided $H_t/P < 0.9$, despite Paxson et al. (2011) noting that it underestimates discharges for H_t/P ratios less than 0.3.

A more recent study by Crookston and Tullis (2013), provides an amended version of the Tullis 1995 design method with new C_d values for $H_t/P \leq 0.4$ as well as new C_d curves for $\alpha = 25°$ and $\alpha = 35°$ for a quarter-round crest. The study also includes a new C_d curve for $\alpha = 8°$ which is based on data obtained from Willmore (2004), also for quarter-round crests.

2.4.4. Advantages

Due to the developed crest length being greatly increased for a given spillway width, labyrinth weirs are particularly well suited for the rehabilitation of existing spillway structures (Ouamane & Lempérière, 2006). The configuaration of the labyrinth ensures the design fits the site topography and the existing spillways structure (Houston, 1982). Labyrinths can be used to increase the capacity of an outlet for a given spillway crest elevation (Tullis, et al., 1995) as well improving flow aeration, headwater control and energy dissipation (Crookston, 2010).

A free overflow labyrinth spillway provides additional reservoir storage capacity as an alternative to the traditional gated structure which requires manual or mechanical operation (Houston, 1982). It is also more reliable than a gated weir (Ouamane & Lempérière, 2006).

The labyrinth allows for passing of an increased inflow design flood (IDF) as a result of the increase in effective length when compared to rectilinear spillways (Houston, 1982), with the total effective length of the labyrinth being approximately three to five times the actual spillway width (Tullis, et al., 1995). It also has a high level of capacity of evacuation under a relatively weak load; up to two times that of a standard weir of the same width (Tullis, et al., 1995). In addition the labyrinth has a lower cost of realisation and maintenance (Ouamane & Lempérière, 2006). A labyrinth with a small side wall angle has significantly higher capacity at low reservoir levels than one with a large angle. With this increased capacity more of the flood is passed through the reservoir, reducing the maximum reservoir elevations, and potentially allowing the spillway length to be reduced, saving construction costs (Tullis, et al., 1995).

The increased sill length of a labyrinth effectively reduces the upstream head for a particular discharge. This characteristic becomes particularly useful where the width of a channel is restricted and a weir is required to pass a range of discharges with a limited variation in upstream levels. At low heads, the discharge over labyrinth weirs is greater than that over an equivalent normal weir (i.e., a straight weir across the same channel width) in the ratio of the weir sill lengths.

The geometry of labyrinth weirs provides increased sill length and often results in the overfall jets colliding with each other, which may lead to increased aeration. A series of laboratory experiments run on rectangular labyrinth weirs showed that, although detailed geometry of the weir was not important, the labyrinth weirs aerated significantly better than an equivalent straight weir, particularly at low drop heights (Wormleaton & Chau, 2000). These collisions, however, do decrease the capacity of the spillways at higher heads.

With the increase in the collisions of the overfall jets the labyrinth, for a given upstream head, provides more energy dissipation than a traditional drop structure (Vermeyen, 1991). This characteristic could be useful on a canal system and the labyrinth could simultaneously maintain a more consistent flow depth in the canal than could be achieved with a conventional drop structure (Ghare, et al., 2008). The aeration performance of the labyrinth is also significantly better than other spillways. Particularly in situations where allowable drop height or head loss across the spillway is limited, which is common in natural streams and in treatment plant design (Wormleaton & Chau, 2000).

2.4.5. Disadvantages

Due to the increase in hydraulic efficiency that the labyrinth offers, there can be resulting downstream impacts. This normally occurs under moderate flood conditions, which occur more frequently, as there is reduced flood attenuation with the increased efficiency under lower heads (Paxson and Binder, 2009). A possible solution to this problem is to have staged or notched spillways (Vermeyen, 1991).

As the head over a labyrinth increases above a certain point, depending on the geometry of the spillway, the effective head begins to decrease as shown experimentally by Taylor (1968) and Hay and Taylor (1970). This phenomenon is due to the effect of the downstream overfall jets colliding which each other and eventually leads to a ‘choking’ of the spillway to the point that it effectively becomes a straight broad-crested weir (Wormleaton & Chau, 2000).

Labyrinth spillways are now widely used but they are hydraulically complex with the range of available geometries, headwater, tailwater, approach conditions and other performance factors making it difficult to design the most hydraulically efficient structure possible. This goal is also not always achievable due to increased construction costs or site topographic and geological constraints. To overcome these challenges, project effectiveness should become the most important factor on which the designer should focus (Paxson, et al., 2011).

Although the labyrinth is one of the more efficient ways of passing floods, moderate geometric changes can significantly affect discharge characteristics (Savage, et al., 2004). At low discharges, subatmospheric pressures develop under the nappe near the top of the crest. This should be considered during the design of a labyrinth and splitter piers on each cycle may alleviate these pressures (Houston, 1982).

2.5. Hydraulic Performance and Parameters

2.5.1. Influences

Labyrinth weirs offer significant flow magnification for a set spillway width; however, there are many factors that influence the capacity – and therefore the hydraulic design – of a labyrinth spillway. These include the head to crest height ratio, the angle of side walls, the vertical aspect ratio, the apex width and approach, and downstream conditions (Ghare, et al., 2008). For example, a spillway with a small α has significantly higher capacity at lower reservoir levels than a spillway with a large α (Tullis, et al., 1995).

2.5.2. Crest Shape

The hydraulic performance of the weir depends on the parameters mentioned above as well as the crest shape (Paxson & Savage, 2006). There are four basic options when considering the design of the crest shape for a labyrinth: sharp crest, flat top, quarter-round, half-round. These are shown in Figure 2.5.

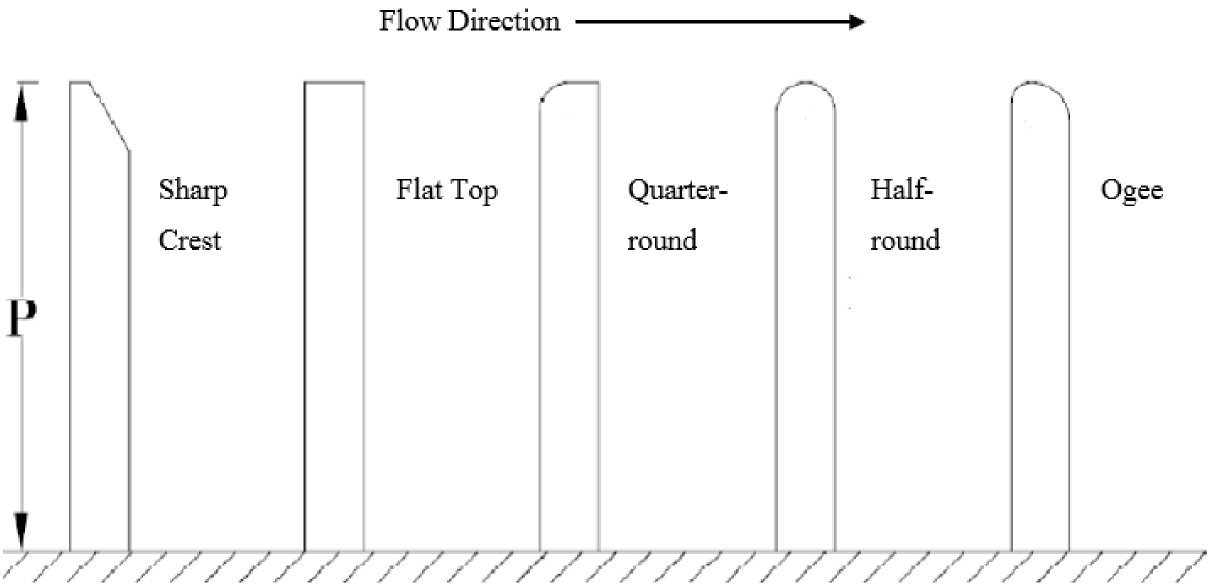

Figure 2.5 Crest shape options available for labyrinth weirs (Crookston, 2010)

The sharp crest and flat crest generally have crest coefficients that are measurably less than those of rounded crest weirs – resulting in lower discharges – and are thus not preferred. Amanian (1987) notes that the most efficient shape is the quarter-round crest; this shape is also recommended by Khode and Tembhurkar (2010). The quarter-round crest may have a lower C_d at low heads than the half-round crest, but at high heads it has a larger C_d. In addition, the quarter-round crest has the advantage of being easier to construct than the half-round crest (Tullis, et al., 1995).

A crest with a rounded edge on the downstream side – such as the half-round crest - allows the flow to ‘cling’ to the wall on the downstream face of a weir which results in a slight increase in efficiency and discharge capacity under low flow conditions. However, once the nappe has detached from the downstream face, the advantages gained from the crest are lost when comparing to a quarter-round crest. A further crest shape, the ogee-type crest, is essentially a modified half-round crest with a slightly different shape: the ogee-type crest has an upstream radius of $r = t/3$ and a downstream radius of $r = 2t/3$, where t is the thickness of the crest (Crookston & Tullis, 2013).

2.5.3. Crest Performance

As mentioned above, the capacity of a labyrinth is a function of the crest coefficient of the spillway. The crest coefficient depends on the total head, weir height, weir thickness, crest shape, apex configuration and side angle (maximum range 6°-35°) (Tullis, et al., 1995). As the total head increases, the crest coefficient continues to decrease until such a point that spillway capacity equals that of a linear weir (Ghare, et al., 2008).

Figure 2.4, included in section 2.4.2, maps the various crest coefficient values for different values of α.

2.5.4. Nappe Behaviour

On a labyrinth, the nappe forces can be significant at higher discharges and can have an effect on the stability of a weir, especially in the case of partially submerged or drowned weir (Savage, et al., 2009). The way the nappe behaves, along with the air cavity which exists behind the nappe, can also impact the discharge efficiency of the weir (Crookston, 2010).

2.5.5. Aeration

Nappe aeration has an influence on the crest coefficient, and therefore the capacity, of a labyrinth. The primary purpose for including vents on linear weirs is to reduce vibrations caused by pressure variations under the nappe. When the nappe is not aerated the weir passes a higher flow than that predicted by the C_d values shown in Figure 2.4. When aerated, the pressure in the cavity beneath the nappe is close to atmospheric pressure and the C_d has a minimum value. A labyrinth weir tends to operate with a slight negative pressure for the range of H_t/P between approximately 0.1 and 0.2 (Tullis, et al., 1995).

The additional aeration produced through the collision of the nappe of the labyrinth is considered an advantage due to the positive environmental impact it has on the oxygen levels in the water. Flow over a labyrinth is considered to be fully aerated if the H_t/P ratios are between 0.1 and 0.2. At these ratios the weir acts in a similar manner to a linear weir (Paxson & Savage, 2006).

Crookston (2010) says that it is possible for the nappe of a labyrinth weir to pass through four stages as H_t increases, although there are a number of other factors which influence the aeration condition of the nappe such as crest shape, crest height, submergence of the crest and the total upstream water depth (H_t):

1. A *clinging nappe* leads to sub-atmospheric pressures developing on the crest.
2. The development of subatmospheric pressures can also be caused by an *aerated nappe* that does not have any air vents.
3. A *partially aerated nappe* results when an aerated nappe becomes unstable, as the air cavity which exists behind the nappe changes in size and space over time. The air cavity in question can oscillate between the weir’s apexes which can lead to instability due to the resulting forces and fluctuating pressures. The unstable nappe is often accompanied by a flushing noise resulting from the escaping and forming of air behind the nappe.
4. A *drowned nappe*, or submerged nappe has no air cavity and the nappe is thick.

2.5.6. Streamlines

For inclined weirs like the labyrinth, the streamlines under the nappe are almost perpendicular to the crest, whereas at the free surface the streamlines are pointing downstream. The labyrinth weir flow is further complicated by the interference of jets near the upstream apex. At high discharge levels, the jets from adjacent crests strike each other and in the process create a nappe that is not aerated. This results in a decrease of the weir's discharge coefficient. The amount of impact increases as the labyrinth angle decreases and the head over the crest increases. As a result of this, the underside of the nappe is aerated for low heads only and the advantage of the labyrinth, over a linear weir, diminishes for increasing head over the crest (Ghare, et al., 2008).

2.5.7. Interference

For a given upstream head, a labyrinth weir provides more energy dissipation than a traditional drop structure as a result of nappe interference (Paxson, et al., 2011). This interference occurs as a result of converging nappes colliding on the downstream portion of a labyrinth. As opposed to triangular weirs, the trapezoidal nature of the labyrinth helps to reduce the impacts of this nappe interference as the inside apex width separates the downstream flows.

Interference length, which is the length of the area where the nappes from adjacent cycles collide, is reduced by decreasing the number of cycles, thus increasing the side wall length. This improves the labyrinth hydraulically but is not better economically as the labyrinth would require a larger base area. With regards to the effects of interference, there is a large disparity in predicted discharge between current theory and physical modelling results. Additionally, current theory loses accuracy when applied to particularly tall weirs (Savage, et al., 2004).

The Tullis method does not deal with nappe interference directly, although Paxson, et al. (2011) suggest that it should be dealt with in the design approach. Falvey (2003) recommends maintaining an interference length ratio (L_{de}/B) – where L_{de} is the effective length of disturbance – of less than 0.3 to ensure that the Tullis method is applicable. More recent studies have shown, however, that the Tullis method is still applicable for ratios higher than 0.3 and that the criteria suggested by Falvey (2003) may be overly restrictive (Paxson, et al., 2011).

2.5.8. Shape (in Plan View)

During the design phase the selection of various geometric parameters and the location and orientation of the weir all have an impact on the discharge capacity. Flow conditions downstream could also affect the discharge, as well as the design of a stilling basin (Paxson, et al., 2011). The inside apex width determines whether the labyrinth is triangular or trapezoidal. It should be as small as possible as it reduces the net crest length and decreases discharge capacity of the weir. Although it should be small, the inclusion of the inside apex width in the labyrinth design is important as it negates some of the effects of nappe interference as discussed earlier (Ghare, et al., 2008).

The sidewall angle affects both the capacity and the layout of the labyrinth: a smaller angle produces a higher capacity with lower reservoir elevations and this happens because with a smaller angle the effective length is increased. A larger angle can help to reduce changes to the up and downstream channels. The sidewall angle can be varied to maintain the length of the apron (B) which essentially remains constant. The optimum angle is between 7° and 16°; as the angle increases the length of the weir decreases for a set width. The number of cycles in a given weir (N) does not influence the crest coefficient but does have an effect on the cost of construction: with a low N value, the length of the apron increases, as the angle remains constant, resulting in a larger base required and hence, an increase in expenses. Figure 2.6 shows all the relevant dimensions and allows for a better understanding of the labyrinth shape as seen from above (Tullis, et al., 1995).

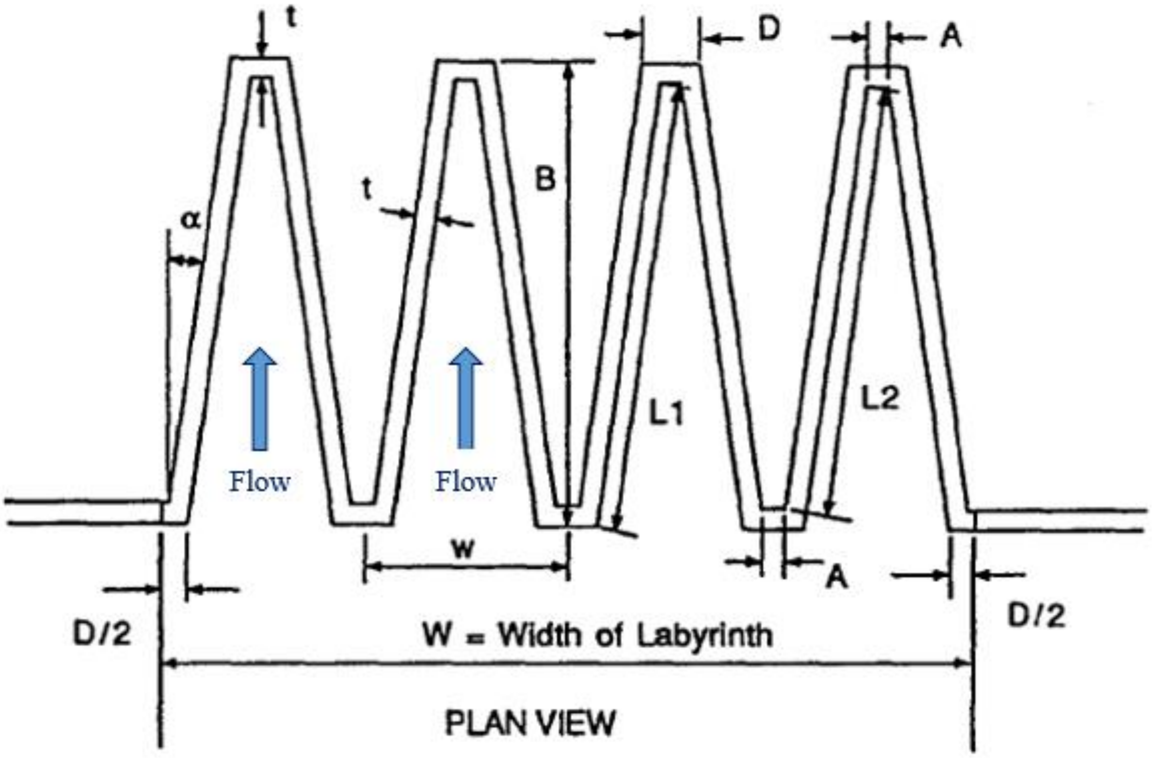

Figure 2.6 Plan view of a labyrinth weir with important dimensions shown. (Tullis, et al., 1995)

It is possible to consider a labyrinth layout in either a regular position or an inverted one. An inverted labyrinth weir, as shown in Figure 2.7, is essentially a labyrinth where the crest of the weir extends into the upstream channel as opposed to extending downstream. Houston (1983) notes in the Hyrum discussion that weirs in the normal position are slightly more efficient than those in the inverted position. Falvey (2003) found that the weir used for the Hyrum Dam design in the normal position had a discharge 9% greater than when in the inverted position. The loss in efficiency can potentially be attributed to two things: firstly, the friction along the sidewalls within the weirs footprint; and secondly, there are now more upstream axes and this means there is an increase in the resulting nappe interference (Paxson, et al., 2011).

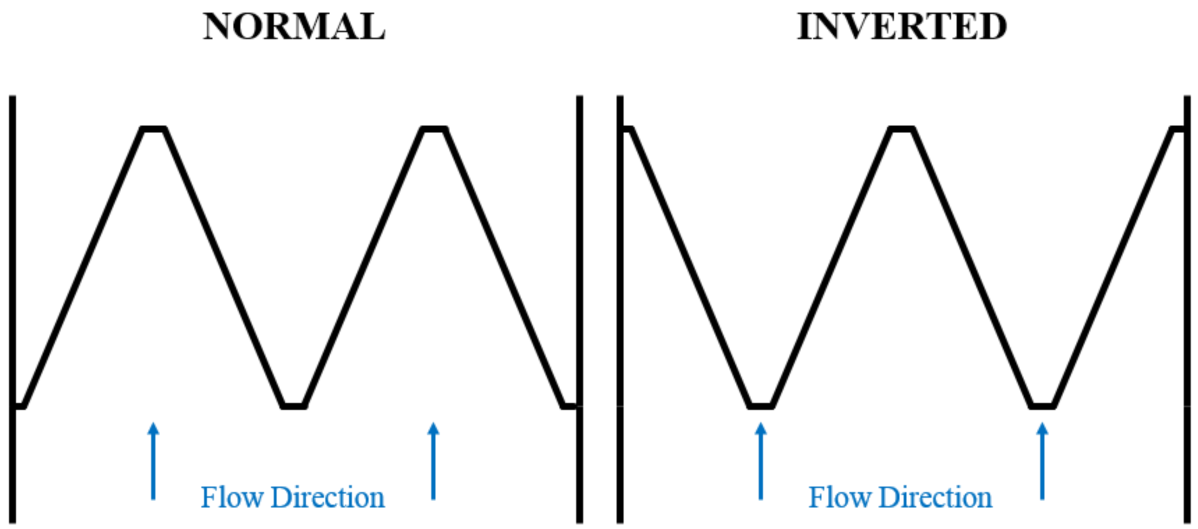

Figure 2.7 Plan view of labyrinth weir in normal and inverted positions

2.5.9. Aspect Ratio

The vertical aspect ratio, which is the ratio of width to height of the crest, is another factor that influences the hydraulic efficiency of the labyrinth (Ghare, et al., 2008). Falvey (2003) notes that the studies of Hay and Taylor showed the aspect ratio does not significantly affect the weir if it is greater than two (Khode & Tembhurkar, 2010).

Both the Lux and Tullis methods indicate that the hydraulic performance increases with increasing weir height and a corresponding decrease in the aspect ratio for a given plan geometry, especially for higher heads. This occurs despite the design methods not being appropriate for aspect ratios lower than two. There is therefore potential for engineers to design for a slightly lower weir height than would be implemented: this should result in a conservative design as the approach will be expected to underestimate discharge. As Paxson and Savage (2006) note, further tests to define the hydraulic behaviour at these lower ratios should be conducted.

2.5.10. Downstream Flow Conditions

Ghare, et al. (2008) suggest that the downstream flow from the labyrinth should be supercritical to avoid submergence effects. Lopes et al. (2006, 2008) indicate that if there are no tail water affects, flow downstream of a labyrinth weir with a sidewall of 30° (L/W ≈ 2.0) is supercritical for H/P values of 0.6 and less. For all other labyrinth geometries tested and for higher H/P values, the flow downstream of the labyrinth is subcritical with Froude numbers ranging from 0.6 to 0.9. Using the methods developed by Lopes (2006), the energy head immediately downstream of a labyrinth can be estimated. This value is useful for estimating flow depth and also assists with the design of stilling basins. Lopes (2006) also indicates that the residual energy downstream may be more closely related to the unit discharge than to the upstream head for a range of sidewall angles (Paxson, et al., 2011).

2.6. CFD Modelling

2.6.1. Introduction to CFD

Computational fluid dynamics (CFD) is the analysis, through the use of numerical methods and computer based simulations, of systems which involve heat transfer, fluid flow and other associated problems such as chemical reactions (Institute for Water and Environmental Engineering, 2012).

CFD is a tool which has been developed since the 1960s and the aerospace industry has put it to good use during design and manufacturing processes. CFD is increasingly becoming an irreplaceable component of design, especially in the industrial sector. In water resource applications, CFD is currently used in conjunction with other methods such as physical modelling or other experimental methods. It therefore forms a part of the solution to the analysis of a problem or scenario, rather than being the producer of a final result. The main reason behind this is the number of assumptions which govern the numerical methods used in order to obtain results in CFD (Versteeg & Malalasekera, 1995).

2.6.2. Development

Advances in the area of CFD have provided engineers with another tool in addition to physical modelling and other experimental methods with which to evaluate weirs and many other hydraulic structures. As computer performance improves, we may reach a stage where a CFD model will be able to analyse a hydraulic structure at a lower cost than a physical model. Additionally, CFD accurately maps the flow field and allows for easy extraction of data – such as forces, velocities and pressures – across the computational domain where collecting this data from physical modelling can be costly and time consuming (Paxson & Savage, 2006).

A large disadvantage of CFD modelling is that the accuracy is largely unproven, especially for open channel flow problems. A difficulty being tracking the free surface movement over a weir, especially with rapidly varied flow such as the flow changing from subcritical to supercritical, which is the case with flow over the crest of a labyrinth weir. Flow over a weir can further complicate this when the nappe springs away from the weir, creating a jet with an air surface interface on the top and bottom of the nappe, both of which need to be tracked (Paxson & Savage, 2006). When the weir position is at an acute angle to the flow, the flow becomes three dimensional (3D) which complicates the modelling process (Ghare, et al., 2008). This is unlike straight weirs where all streamlines are perpendicular to the crest and are two dimensional (2D).

2.6.3. Comparison between CFD and Physical Modelling

Savage, et al. (2004), Paxson and Savage (2006), and Paxson, et al. (2008) have discussed comparisons between physical and numerical model results for labyrinth spillways and demonstrated that CFD can be used to accurately model the discharge of labyrinth spillways (Paxson, et al., 2011). CFD is, however, a relatively new technology when compared to other experimental methods used in water engineering and there is still room for much testing to be done in order to verify the accuracy and range of the CFD (Savage, et al., 2009).

Although numerical tools still have limitations (including turbulence representation, aeration, grid resolution, run times, and numerical instabilities), there are areas where numerical modelling may be more accurate than a physical model. Numerical models can provide more detail about velocity and pressure distributions than can a physical model and may be more economical in some cases (Savage, et al., 2009).

According to Falvey (2003), taking into consideration the large differences between the conditions on site and the idealised conditions used to determine design curves and equations, modelling of site conditions is often a necessary procedure. Numerical modelling has the potential to offer the option of assessing various different proposed spillway designs at a cost lower than physical modelling of each design. The CFD model also allows the examination of the entire flow field for information such as velocities and pressures, whereas with a physical model these processes take a lot of time. However, CFD modelling is relatively new and still needs to be operationally proven (Savage, et al., 2004).

Labyrinth weirs are essentially straight weirs folded into an accordion shape in plan form and although this change in shape increases the efficiency, it also complicates the flow patterns. Due to the angular shape, flow interference from the jets of adjacent crests can occur at the upstream apex (Savage, et al., 2004). Thus, even though design procedures are quite accurate, it is still recommended that the capacity and performance be verified by means of a model study. The model is capable of realising effects such as aeration effects at low heads, unusual flow conditions in approach, and discharge channels (Tullis, et al., 1995).

2.6.4. Advantages of CFD

There are a number of clear advantages to the use of CFD modelling, including:

- CFD has the ability to map the computed flow field. Due to the flow domain being discretized, the computed velocities, pressures, location of free surface and other values are known at each cell (Savage, et al., 2004).
- CFD allows experiments with potentially dangerous and/or expensive outcomes to be tested without repercussions such as accident scenarios or safety studies.
- As computers become more powerful and less expensive, larger and more detailed simulations can be run using CFD models.

- Using CFD there is potential for the reduction in the amount of time required for testing and the cost of attempting to test numerous alternate designs.
- Successful models can provide an almost unlimited detail level in the results produced.

2.7. Reference Projects

This section presents a review of available data on a number of projects involving labyrinth weirs, physical modelling and CFD modelling, in chronological order. The background of these projects is explored along with the design and/or modelling details and the key lessons learnt.

2.7.1. Ute Dam Labyrinth Spillway (Houston, 1982)

Background

Studies were completed to develop a spillway to increase the storage and discharge capacity of Ute Dam (New Mexico) whilst still being able to pass the design flood. Two methods of obtaining this were suggested: installing spillway gates and developing a more economical alternative. A labyrinth spillway was selected as the more economical alternative due to the labyrinth's ability to incease the effective length provided for the given channel width.

Physical Model and Testing

The initial tests for the physical modelling were all completed within a flume. Hay and Taylor design curves were used for the design of the models, using Froude law relationships to accurately model the prototype. The final design ratios were calculated to be:

$w/P = 2$;

$Q_L/Q_N = 2.44$; and

$h_m/P = 0.63$.

Where:

w is the width of one cycle;

P is the spillway crest height;

h_m is the measured upstream head;

Q_N is the discharge over an equivalent linear weir; and

Q_L is the maximum discharge.

The crest shape used – sharp-crest with a 45° angle on the upstream side – was the same as that used by Hay and Taylor to determine their design curves and this was done in order to verify these curves. The initial tests were conducted in a flume and the weirs were made of aluminium and sealed to the side walls and floor of the flume. Stiffeners, symetrical about the centreline of the channels, were added in the upstream portion to provide structural stability. These stiffeners did not affect the discharge capacity and were necessary as the hydrodynamic forces tend to pull the walls away from the abutments at the point of attachment.

The next set of tests were completed on a 1:80 scale model of Ute Dam, including additional details such as embankments and approach conditions. On this model the spillways were made of mahogany and water measurements were done with venturi meters.

Piezometers were installed, in both sets of tests, to determine the pressure profiles for use in the design of foundation support for the base and walls of the labyrinth. They were placed along the centre line and parallel to the sidewalls.

In order to aerate the nappe and to prevent oscillation, as was the case in Avon Dam (Australia), splitter piers were included in both sets of tests. Several locations were tested and the best was found to be near the downstream apex of the weir at a location approximately $9.9/b$ from the downstream apex along the crest. Figure 2.8, indicates the suggested location of the splitter piers.

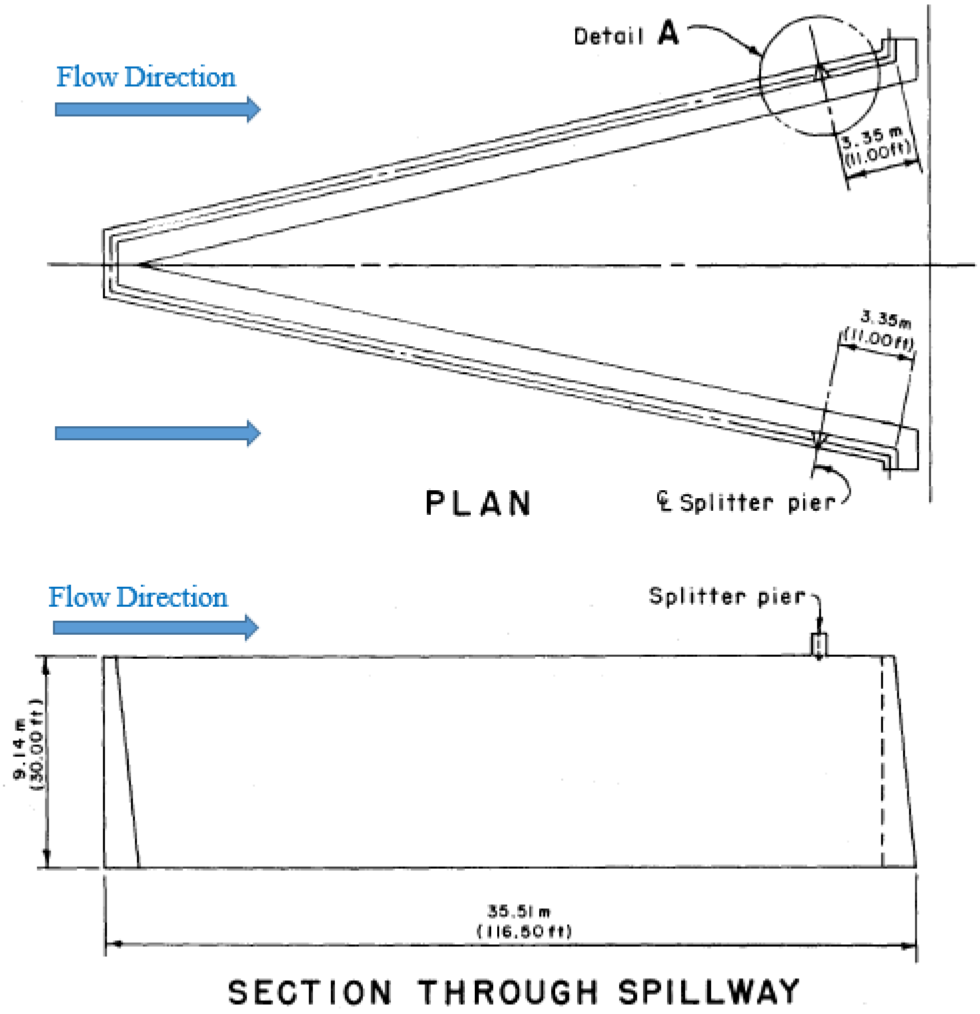

Figure 2.8 Plan view and view of a section through the labyrinth weir indicating the proposed positioning of the splitter piers (Houston, 1982)

Lessons Learnt

The curves produced by Hay and Taylor (1970) were not adaptable to a reservoir scenario without including the velocity head in addition to the measured head value. Houston and Lux used the total head for their calculations instead of the piezometric head as the latter does not allow for differences in the approach velocity and can introduce significant errors in the predictions (Tullis, et al., 1995).

Having an aspect ratio of two produced a small reduction in discharge magnification due to nappe interference and loss of efficiency at higher flows.

2.7.2. Hyrum Dam Labyrinth Spillway (Houston, 1983)

Background

The design flood requirements for Hyrum Dam, located in Utah, were revised in 1981 and the existing hydraulic structure did not meet the updated requirements. Raising the spillway using a labyrinth was the most economical solution to pass the new flood requirements. The new spillway height provided reservoir storage as an alternative to a gated structure.

The spillway configuration was based on the procedure developed by Hay and Taylor (1970) and modified design curves generated by the United States Bureau of Reclamation (USBR) Hydraulics Laboratory. A 1:30 scale model was built and varying approach conditions and spillway orientations were investigated. Water surface profiles were measured over the spillway and in the chute downstream. Splitter piers were installed to provide aeration under low flow conditions.

Physical Model and Testing

The model built was a 1:30 scale of a two-cycle labyrinth and included the reservoir topography on either side which was modeled using concrete. The chute and walls of the spillway were modeled in plywood with the labyrinth being constructed out of mahogany. All water measurements were done using venturi meters.

The effects of approach conditions on the discharge are not considered in the Lux or Tullis design processes as both methods were developed using data from flume studies. The Hyrum final design is a labyrinth projecting into the reservoir with a curved channel entrance. Incorporating non-standard approach conditions into the design increases the complexity of the hydraulic behaviour, making it probable that the labyrinth performance cannot be accurately modelled using the Lux or Tullis design methods (Paxson & Savage, 2006).

Spillway operation under low flow conditions resulted in a problem with nappe oscillation, this occurred when the nappe intermittently became aerated at the apex and sprang free from the downstream crest, the nappe then reattached to the downstream crest as the air was exhausted. Installation of splitter piers on the spillway crest provided aeration to prevent this. Under low flow conditions the nappe clung to the downstream face of the spillway.

At higher discharges the nappe became submerged; therefore, the piers were designed for the lower flows where oscilation occurs. Overtopping of the piers at higher discharges did not result in any hydraulic problems. Placement of the piers in several locations near the downstream apexes were tested, with the recommended position being 1.8 m upstream of the downstream apex on each side length.

Lessons Learnt

A weir orientation of two apexes downstream was slightly more hydraulically efficient than the inverted labyrinth with two apexes upstream. However, good entrance conditions had a greater effect on spillway efficiency than spillway orientation did.

Splitter piers on the spillway crest were used to prevent nappe oscillation during low discharge operation and to provide aeration; these did not significantly affect the performance under high flow conditions but decreased the crest length of the spillway by 3.3%.

2.7.3. Ritschard Dam (Vermeyen, 1991)

Background

To assist with the design of the Ritschard Dam hydraulic structures, the USBR used hydraulic model studies to investigate a labyrinth spillway as the emergency spillway and an uncontrolled Ogee service spillway. Preliminary flume studies were conducted on the labyrinth spillway and the ogee crest to determine discharge coefficients and surface pressure distributions (ogee only).

Physical Model and Testing

A total of four models were used during the testing procedure: two were specifically for the ogee crest; one specifically for the labyrinth; and one was a model of the entire Ritschard Dam. The following paragraphs focus on the models inclusive of the labyrinth weir; the labyrinth model and the model of the entire dam.

The labyrinth model was a 1:20 scale model of two trapezoidal cycles of the weir including bridge piers. For the sectional labyrinth model, stage discharge relationship was established for varying reservoir elevations. Water surface levels or depth of flow above the weir crest were measured using a point gauge located 3 m upstream of the labyrinth. Head measurements were corrected to account for velocity head ($v^2/2g$). Reduced sidewall angles and the bridge piers both increased nappe interference which reduced discharge capacity.

The Ritschard Dam model was a 1:45 scale 3D model of the entire dam and was used to examine the overall performance of the hydraulic structures, as well as to look at the performance of the dams' natural downstream channel. For this model, a gravel-filled head box was installed to simulate the reservoir topography, smooth the water surface and evenly distribute the inflow from the supply pipe. The labyrinth had a quarter-round crest and included nine cycles; on each downstream apex there was a 0.76 m diameter bridge pier (at the prototype scale, 0.038 m at a scale of 1:20). Model inflow rates were determined using the laboratory venturi meters and the reservoir and tail water elevations were measured using point gauges mounted in stilling wells. The average surface pressures were found using piezometer taps connected to water column manometers, whilst flow velocities were measured using an electromagnetic current meter.

The design of the labyrinth weir was based on the hydraulic model study results for Hyrum Dam, Utah, with similar geometric parameters.

Lessons Learnt

A number of important lessons were learnt during the Ritschard Dam project. The design for this dam was based on the Hyrum Dam labyrinth with a few deviations which resulted in the physical weir passing about 2% less flow than the theoretical design capacity.

During the modelling phase it was also discovered, as expected, that reducing the side wall angle of the labyrinth increases the amount of nappe interference, as does the inclusion of bridge piers. This increase in nappe interference reduces discharge capacity.

Paxson and Binder (2009) note that the increase in hydraulic efficiency results in reduced flood retention, especially under moderate floods and lower head levels. The labyrinth can thus have negative downstream impacts. The Ritschard Dam project found a solution for this in the form of staged and notched spillways (Figure 2.9).

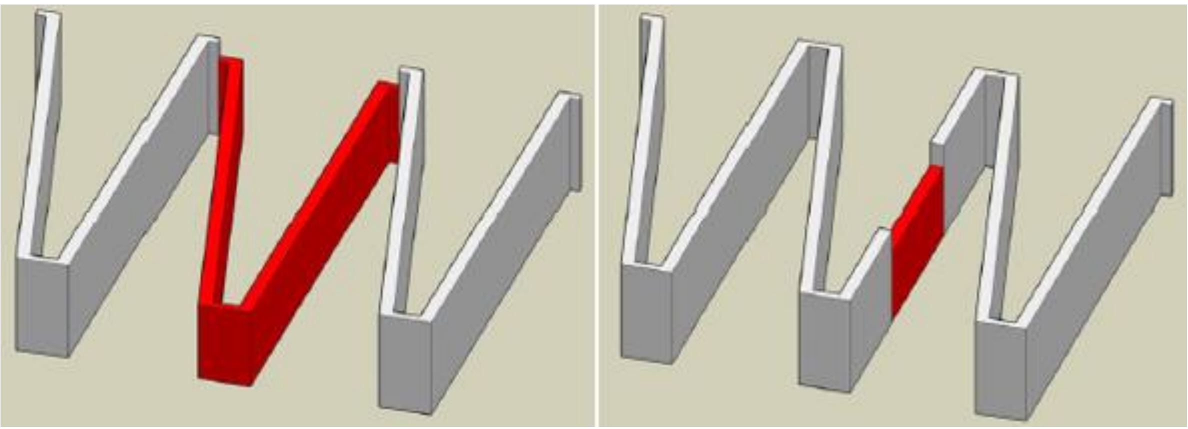

Figure 2.9 Labyrinth weirs in plan view showing staged and notched crests, respectively (U.S. Society on Dams, 2011)

2.7.4. Dog River Dam (Savage, et al., 2004)

Background

Constructed in the 1990s, the Dog River Dam was built for water storage and supply. The outlet works for this dam include a drop inlet riser; a box conduit which exits through the base of the dam; and a 73 m wide, 4.6 m high, 8-cycle labyrinth crested-chute spillway.

Engineers were tasked with increasing the dam’s storage levels by approximately 3 m. It was decided that this could be achieved through increasing the crest height of the existing labyrinth spillway. This provided an economic solution, however, it meant the weir would be outside of the hydraulic design ratios, with the vertical aspect ratio now being very small, a physical model study was recommended.

Design

The typical placement for a labyrinth weir is on a flat floor; this was the condition used to develop the design curves. The Dog River Dam placed the labyrinth on the crest of an embankment. The adjusted design for the increase in dam storage left most of the design ratios the same as they were previously. The plan view layout of the dam did not change, leaving $\alpha = 11.33°$ and $l/w = 4$. For the new weir the discharge coefficient was found to be higher and the change in crest height also impacted the vertical aspect ratio. The original ratio was the accepted minimum ratio of $w/P = 2$, which changed to $w/P = 1.2$ – significantly lower than the recommended value of 2. The labyrinth designed had a quarter-round crest on the upstream side.

Physical Model and Testing

Due to the perpendicular flow approach conditions and allowing for better model scaling, the study focussed on 2 cycles as opposed to the full 8 as in the prototype design. This reduction allowed the model to be built to a scale of 1:15.

Two different setups were tested: one on a model of the existing embankment and one on a flat flume floor. This allowed for the effects of the embankment to be tested.

Computer Model

The computer modelling component of the project focussed only on the configuration with the labyrinth positioned on a flat surface. Computation of the embankment set up would have significantly increased the flow domain, which in turn would have increased the required computation time.

When solving the flow over weirs, one of the bigger numerical issues faced is the accurate mapping of the free surface. This surface is transient in nature, meaning that it changes with time, and its location needs to be solved as part of the solution. Complicating this further is the fact that the flow over a labyrinth weir passes through critical depth; this creates a free surface both on top of the nappe as well as underneath.

The grid cells defining the dam wall needed to be small enough to accurately capture the geometry of the weir, without being so small that the computational power is insufficient to run the model in a timely manner. Boundary conditions for the model included a pressure boundary for the upstream condition, which allows for a hydrostatic upstream depth to be defined. The downstream end of the model had an "outflow" condition. The depths used for the upstream boundary conditions were those measured during physical model testing.

Lessons Learnt

From the physical modelling, it was found that the results of the two configurations did not differ drastically. By changing the height of the weir, the w/P ratio was reduced drastically. This ratio is used as an indicator of nappe interference as with a reduction in w for a constant crest height there is an increase in the interference observed. However, with an established setup, increasing the crest height should not impact on the weir angles and thus should have very little impact on the nappe interference. The results produced for the physical model discharge show discrepancies between the theoretical calculations and the results to be quite different, with up to approximately 25% relative error. This may be an indication that the existing theory is not accurate for relatively “tall” weirs.

Computation of the weir on the embankment would significantly increase the flow domain, increasing the required time to complete the computations. The grid cells defining the dam wall need to be small enough to accurately capture the geometry of the weir. The writers do note that the results obtained through the CFD study were realistic, regarding the discharge over the weir tested.

Chapter 3: Labyrinth Weir Design

3.1. Design Procedure

A prototype labyrinth was designed for this thesis using the iterative Tullis method as documented in *Design of Labyrinth Spillways* (Tullis, et al., 1995). The following section deals with the design factors as well as the scaling of the prototype design into laboratory size determined by the laboratory limitations described in section 3.2.

The head-discharge relationship of labyrinth weirs is expressed by the general weir equation:

$$Q = \frac{2}{3} C_d L \sqrt{2g} H_t^{1.5}$$

3.2. Laboratory Limitations

The laboratory equipment assigned for this project allowed for a maximum flow of 600 *l*/s or 0.6 m^3/s to flow through the model. A 5 m long flume with plastered brick walls 2 m high and 1.5 m apart was used for installation of the weir. The weir had sufficient space to be approximately 1 m in length parallel to the flow. After this point, a channel guiding the water into the laboratory drainage system allows for the downstream flowing water to be controlled and removed.

Due to the repetitive nature of the shape of labyrinth weirs it was possible to use symmetry during the model testing. The line of symmetry was chosen to be the centre line through the weir. This allowed for the model to be designed to a width of 3 m instead of 1.5 m, giving the potential for a larger model scale and importantly a larger crest height, allowing a greater potential for negative pressures to exist.

As the design width was increased to 3m, so too the design flow rate was increased from 0.6 m^3/s to 1.2 m^3/s (at a scale of 1:20).

3.3. Scaling

Using a model to obtain data on the performance of a structure requires scaling. This scaling can be geometric – a set ratio between the dimensions of the original structure and the model – or it can be kinematic – requiring scaling of velocities and potentially acceleration (Crookston, 2010). The Froude Law relationships were used to convert the designed labyrinth (prototype) into the model used for testing and are included in Table 3.1. During the design of the labyrinth weir the target was to be able to construct a model as large as possible, various scales were trialled with the final scale being set to 1:20 to limit possible scale effects.

Table 3.1 Froude law relationships for similitude (Houston, 1983)

Froude Law Relationships			
Parameter		**Ratio**	**Scale (1:20)**
Lengths	L_r	L_r^1	20^1
Velocity	V_r	L_r^1/2	20^1/2
Area	A_r	L_r^2	20^2
Volume	V_r	L_r^3	20^3
Discharge	Q_r	V_r A_r	20^5/2

3.4. Headwater Ratio (H_T/P)

Although the recommended ratio of $P = 1.4H_t$ (Tullis, et al., 1995) was aimed for, the design restrictions meant that the final ratio used was 1.111. This falls within the restrictions $0.1 \leq H_t/P \leq 0.9$ which Tullis, et al. (1995) suggests obtains sufficient accuracy of calculation for C_d values when α is between 6° and 18°. The ratio obtained was the same as the Ritschard Dam (Vermeyen, 1991) and the Hyrum Dam (Houston, 1983).

Labyrinth weirs are generally designed for $H_t/P \leq 0.9$ at maximum flow (Crookston, 2010). This is also the upper requirement for which the Tullis (1995) discharge curves are valid. The labyrinth becomes increasingly inefficient with increasing head and the advantage of the labyrinth design diminishes (Tullis, et al., 1995).

3.5. The Vertical Aspect Ratio

Expressed as w/P, the vertical aspect ratio influences the hydraulic efficiency of the labyrinth (Ghare, et al., 2008). Using the Tullis method, the suggested range of the ratio is between 3 and 4. Falvey (2003) suggests that any ratio greater than 2 is acceptable; and Ghare, et al. (2008) suggest that the range should fall between 2 and 4. Taylor (1968) also suggests that the ratio should be larger than 2 in order to minimise the nappe interference. Wanting to ensure that the laboratory model had two cycles (that the design before using symmetry had four cycles) meant the constraints reduced this ratio until it equalled 2.

3.6. Crest Height to Thickness Ratio

The recommended value of P/t is 6 where t is the wall thickness (Tullis, et al., 1995). For the design of the weir, however, a value of $P/t = 5$ was obtained due to the width restrictions. As discussed below, the quarter-round crest shape was selected and the suggested radius for the curved section $R = t/2$ was used.

3.7. Crest Shape

Figure 2.5 indicates the various options for the shape of the labyrinth crest. For the purpose of this design, the quarter-round crest shape was chosen, with a vertical drop on the downstream side of the wall.

In *Hydraulic Design of Labyrinth Weirs*, Falvey (2003) suggests that the shape of the crest does not influence the performance of the weir in a significant manner but that the half-round and quarter-round crest shapes are most commonly found in prototype design. Khode & Tembhurkar (2010) state that for both the Lux and Tullis methods the quarter-round crest is recommended.

3.8. Sidewall Angle

Tullis, et al. (1995) states that the side wall angle (α) has a large effect on the layout, capacity, performance and the economics of the labyrinth weir. As the angle increases, the overall crest length of the weir decreases as does the length of the apron parallel to the flow. This shows that the lowest cost of the weir design may not be found by minimizing the width as this would require an increase in α to maintain the required capacity (Tullis, et al., 1995).

Various options of α were tried in the design, including 8°, 9°, 10°, 12° and 15°. The range for α was limited to between 6° and 18° as Tullis, et al. (1995) found that the standard deviation for is range of α was less than ±3% when comparing measured data and calculated data when using the regression equations developed for C_d.

On conclusion of the design of the hydraulic model, an angle of 15° was selected as this angle allowed for the maximising of the P/t ratio to 5, following Tullis, et al.'s (1995) recommendation to approximately equal 6.

3.9. Determination of the Crest Coefficient

The C_d calculation is dependent on the selection of α (sidewall angle). Tullis, et al. (1995) provides regression equations for the determination of C_d based solely on the total head to crest height ratio (H_t/P) and the value of α for varying values ranging from 6° to 35°, as well as an equation for 90° which is valid for the condition $H_t/P < 0.7$.

The equations displayed below have been taken from *Design of Labyrinth Spillways* (Tullis, et al., 1995):

- $For\ \alpha = 6°;\ \ C_d = 0.49 - 0.24(H_t/P) - 1.20(H_t/P)^2 + 2.17(H_t/P)^3 - 1.03(H_t/P)^4$
- $For\ \alpha = 8°;\ \ C_d = 0.49 + 1.08(H_t/P) - 5.27(H_t/P)^2 + 6.79(H_t/P)^3 - 2.83(H_t/P)^4$
- $For\ \alpha = 12°;\ \ C_d = 0.4 + 1.06(H_t/P) - 4.43(H_t/P)^2 + 5.18(H_t/P)^3 - 1.97(H_t/P)^4$
- $For\ \alpha = 15°;\ \ C_d = 0.49 + 1.00(H_t/P) - 3.57(H_t/P)^2 + 3.82(H_t/P)^3 - 1.38(H_t/P)^4$
- $For\ \alpha = 18°;\ \ C_d = 0.49 + 1.32(H_t/P) - 4.13(H_t/P)^2 + 4.24(H_t/P)^3 - 1.50(H_t/P)^4$
- $For\ \alpha = 25°;\ \ C_d = 0.49 + 1.51(H_t/P) - 3.83(H_t/P)^2 + 3.40(H_t/P)^3 - 1.05(H_t/P)^4$
- $For\ \alpha = 35°;\ \ C_d = 0.49 + 1.69(H_t/P) - 4.05(H_t/P)^2 + 3.62(H_t/P)^3 - 1.10(H_t/P)^4$
- $For\ \alpha = 90°\ and\ H_t/P < 0.7;\ \ C_d = 0.49 + 1.46(H_t/P) - 2.56(H_t/P)^2 + 1.44(H_t/P)^3$

Based on an H_t/P ratio of 1.111 and having selected α to equal 15°, the C_d value was found to be 0.378. It is worth mentioning that various combinations of these factors were considered during the design process; however, these values are indicative of the final design only.

3.10. Number of Cycles

The number of cycles (N) also influences the economy and layout of the labyrinth weir (Tullis, et al., 1995). It does not, however, influence the value of the crest coefficient (C_d), as Waldron discovered in 1994. Considering the fact that the side walls of the model could potentially influence the accuracy of the results when using the assumed symmetry model, it was important for the areas of the model where pressure measurements were to be taken would not be close to the side walls. Thus it was decided that the model should have at least 2 cycles so that all pressure measurements could be taken away from the walls. This meant that the designed prototype should have at least 4 cycles, due to the symmetry.

3.11. Apron Length

The apron length (B), is affected by N and the selection of α. A decrease in both of these factors leads to an increase in B, resulting in an increase of the volume of concrete required and a resulting increase in costs. On the other hand, decreasing B increases the total width (W) required for the weir. By monitoring the vertical aspect ratio the width and length are kept within acceptable ranges allowing for a hydraulically efficient and cost-effective design (Tullis, et al., 1995).

3.12. Spreadsheet for Labyrinth Weir Design

Tullis, et al. (1995) recommend a spreadsheet for the purposes of designing a labyrinth weir. The two tables included below (Table 3.2 and Table 3.3) are based on those developed by Tullis, et al. (1995). The first of these indicates the scale chosen, constants used and the results of using Froude similitude to determine certain important parameters. The second table is a replica of the one used by Tullis, et al. (1995) in *Design of Labyrinth Spillways*, only with the appropriate numbers included. Table 3.3 also includes the parameters discussed above and was used to determine the final design of the prototype weir.

Table 3.2 Assumptions made and laboratory limitations for the design of a prototype labyrinth weir

Assumptions Made Using Froude Similitude and Lab Limitations			
Parameter	Symbol	Value	Units
Gravitational Acceleration	g	9.81	m/s^2
Model Scale		1 : 20	
Model Max Discharge	Q_M	1200	*l*/s
Model Max Width (Using Symmetry)	W_M	3	m
Prototype Max Discharge	Q_P	2147	m^3/s
Prototype Max Width	W_P	60	m
Prototype Max Head	H_{tP}	6.75	m
Prototype Required Effective Length of Crest	L_{eP}	110	m
Model Required Effective Length of Crest	L_{eM}	5.5	m

Table 3.3 The spreadsheet used for the design of the prototype labyrinth

Design of Labyrinth Weir				
Parameter	Symbol	Value	Units	Equation/source
Input Data				
Maximum Flow	Q_{MAX}	2146.6	m^3/s	Input - From Froude Similitude
Maximum Reservoir Elevation		40	m	Input
Approach Channel Elevation	GL	0	m	Input
Crest Elevation	CL	33.25	m	Input
Total Head	H_t	6.75	m	Ht = Q_{MAX} Level - CL - Loss
Assumed Data				
Estimated Inlet Losses at Qmax	Loss	0	m	Estimated
Number of Cycles	N	4		Adjust so w/P >2
Crest Height to Total Head Ratio	$P{:}H_t$	1.111		P:Ht ≈1.4
Crest Height	P	7.5	m	
Angle of Side Legs	α	15	°	Normally 8-16
Angle of Side Legs	α	0.2618	radians	
Output Data				
Crest Height to Thickness Ratio	P:t	5		P/t ≈ 6
Thickness of Wall	t	1.5	m	
Thickness to Apex Ratio	A:t	1.67		2> A:t >1
Inside Width at Apex	A	2.50	m	
Outside Width of Apex	D	4.80	m	$D = A + 2t\tan(45 - \alpha/2)$
Total Head/crest Height	H_t/P	0.90		$0.9 > H_t/P > 0.1$
Crest Coefficient	C_d	0.38		$C_d = 0.49+1.00(H_t/P)-3.57(H_t/P)^2+3.82(H_t/P)^3-1.38(H_t/P)^4$
Effective Crest Length	L	109.76	m	$L = 1.5Q_{MAX}/((C_d\, H_t^{1.5})(2g)^{0.5})$
Length of Apron Parallel to Flow	B	15.86	m	$B = (L/2N) + t\tan(45 - \alpha/2))\cos(\alpha) + t$
Actual Length of Side Leg	L_1	14.87	m	$L_1 = (B - t)/\cos(\alpha)$
Effective Length of Side Leg	L_2	13.72	m	$L_2 = L_1 - t\tan(45 - \alpha/2)$
Total Length of Walls	L_3	148.18	m	$L_3 = N(2L_1 + D + A)$
Max Possible Distance Between Required Distance Between Cycles	w_{REQ}	15.00	m	
Distance Between Cycles	w	15.00	m	$w = 2L_1\sin(\alpha) + A + D$
Width of Labyrinth (Normal to Flow)	W	60.00	m	$W = N w$
Cd for Linear Weir	C_d (Lin)	0.76		
Length of Linear Weir for Same Flow	LLW	54.54	m	$LLW = 1.5Q_{MAX}/((C_d\, H_t^{1.5})(2g)^{0.5})$
Distance Between Cycles/Crest Height	w/P	2.00		w/P >2

Using these tables and Froude similitude once more, the dimensions of the prototype were then adapted to generate the dimensions needed for the design of the laboratory model of the labyrinth. As mentioned above, only 2 cycles of the model were actually constructed to ensure the model was as large as possible and within the confines of the laboratory space available. Figure 3.1 and Figure 3.2 indicate a plan view and cross sections, respectively, of the designed labyrinth weir. These diagrams indicate the details of the model constructed at a scale of 1:20. All dimensions have been given in millimetres. Further details on the design of the model can be found in Appendix A in the form of design drawings.

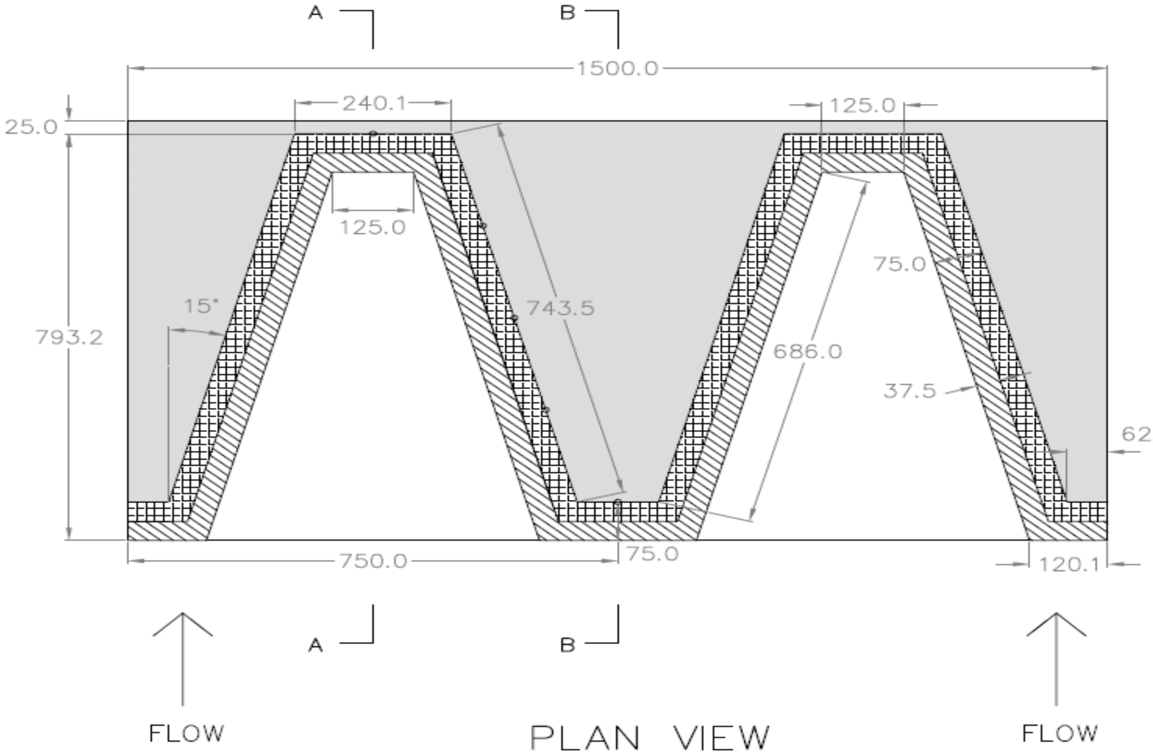

Figure 3.1 Plan view of labyrinth weir crest with dimensions at a scale of 1:20

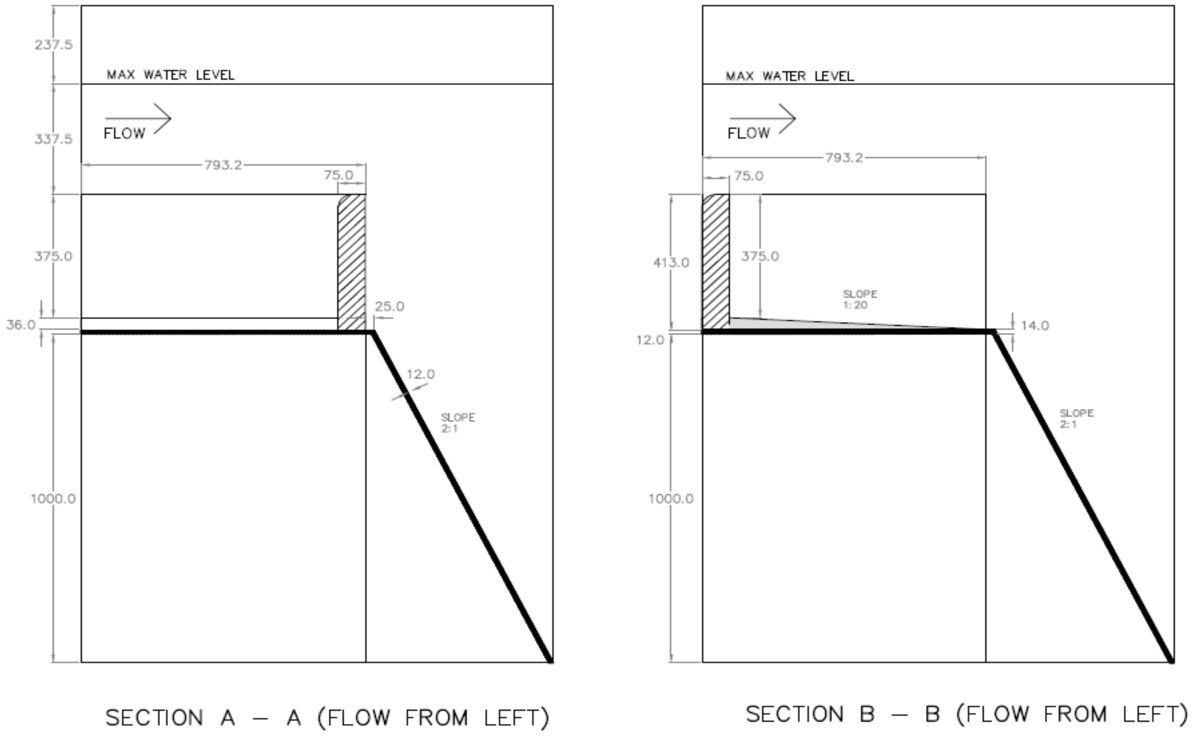

Figure 3.2 Section views through the labyrinth weir crest with dimensions at a scale of 1:20

Chapter 4: Physical Modelling

4.1. Reasons for Physical Modelling

The construction and testing of a physical model used for the study of the performance of a weir allows the design of the weir to be refined and for potential areas of weakness to be avoided before a final design is submitted. It is also important for verification of the hydraulic performance of the weir under site-specific conditions which could impact on the operation and performance of the weir. Furthermore, the model allows for the testing of elements under real conditions and can lead to savings through the reduction of estimated construction costs (Crookston, 2010).

A physical model is also useful when current theory and formulae are unable to determine design dimensions with sufficient accuracy. A side channel spillway is an example of this, where formulae exist and are useful but have limitations. A scale model is, therefore, necessary to refine the design.

4.2. Test Facilities

All physical model testing for this study was completed in the Stellenbosch University's Hydraulics Laboratory, located in Stellenbosch, South Africa. The laboratory had previously installed a flume 1.5 m wide, 2 m high and approximately 5 m in length where the model was to be built. At this part of the laboratory, the maximum discharge available with consistent pressure was 600 *l*/s and all outflow would lead back to the flume to be re-used. 12 pressure sensors, discussed later in this section, were available for use as was the piezometer pressure reader they connected to.

4.3. Model Establishment

The aim was to build the physical model as large as possible and to effectively utilise the space available, but before any design steps were taken, the limitations of the laboratory needed be considered. The size of the flume and maximum water supply mentioned above were key design factors giving width and height limitations and a design flood for the labyrinth design.

Following Waldron's (1994) conclusion that the crest coefficient is independent of the number of cycles in a labyrinth weir, symmetry was used along the middle plane of the model to allow for the construction of a larger model. The model was designed to a width of 3m as this is twice that of the 1.5m wide reservoir available in the laboratory. This meant that the model constructed consisted of two cycles of the labyrinth weir as opposed to the prototype's four cycles.

During the prototype design a scale needed be set, as discussed earlier, various scales and the size and set-up of the physical model were all taken into consideration during this phase. With the final scale being set to 1:20. Figure 4.1, below, shows the model setup in the laboratory in both plan and sectional views and includes the important dimensions.

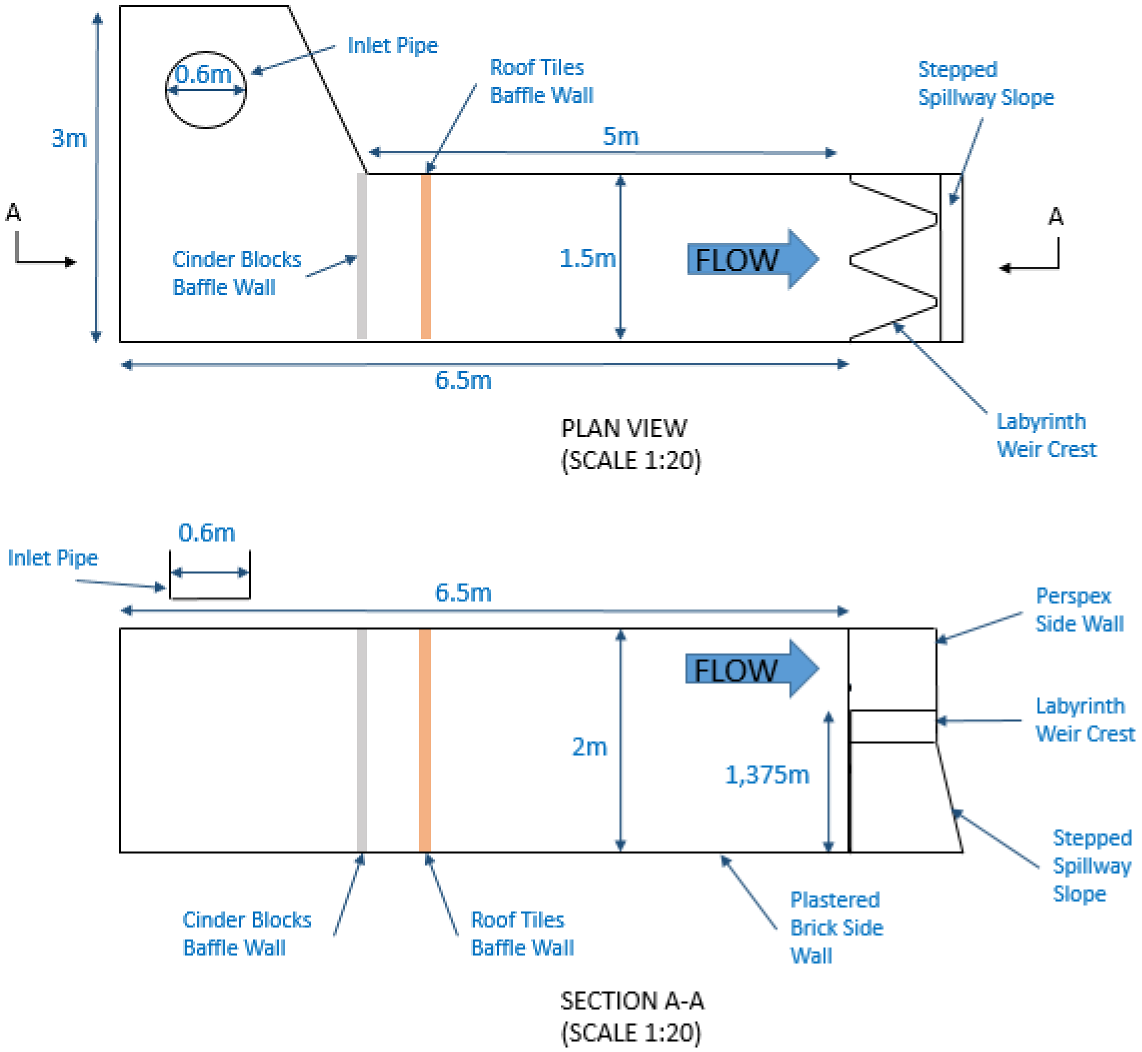

Figure 4.1 Schematic of laboratory model setup showing a plan and a section view

4.4. Model Construction

The flume was constructed out of plastered brick walls, with an area for the water supply line to pump into the reservoir at the point furthest from the weir. Moving from this point toward the weir, the water was then met with two baffle structures constructed of cinder blocks and roof tiles, these were used to stabilise the flow and establish uniform flow conditions in the approach to the weir.

The base of the weir model was built using a marine ply wood, as were the walls. The crest had a quarter-round shape. This provided some difficulty during the construction phase and ultimately a pipe, of the required outside diameter, was cut into quarters and sealed to the wood adjoining it on the crest and walls below.

The walls were hollow inside to create space for pressures sensors and the accompanying tubes to be attached. Supports were included at strategic locations to ensure that the model would be able to withstand the higher flows for a sustained period of time.

The entire model was then covered in waterproof paint to ensure its durability and to improve the overall appearance, as can be seen in Figure 4.2 below.

Figure 4.2 View of model constructed, from above and upstream of the crest

For the outflow, a portion of a previously used stepped spillway was used. Aside from ensuring the weir was never submerged, this had no impact on the readings taken and allowed for a better visual guide as to the behaviour of the water once it had passed the weir.

The side walls of the reservoir only continued until such a point as the water reached the crest of the spillway. Thus, to control the direction of the water flow once it had passed over the crest the side walls were extended using Perspex sheeting to ensure that all aspects were still visible (Figure 4.3).

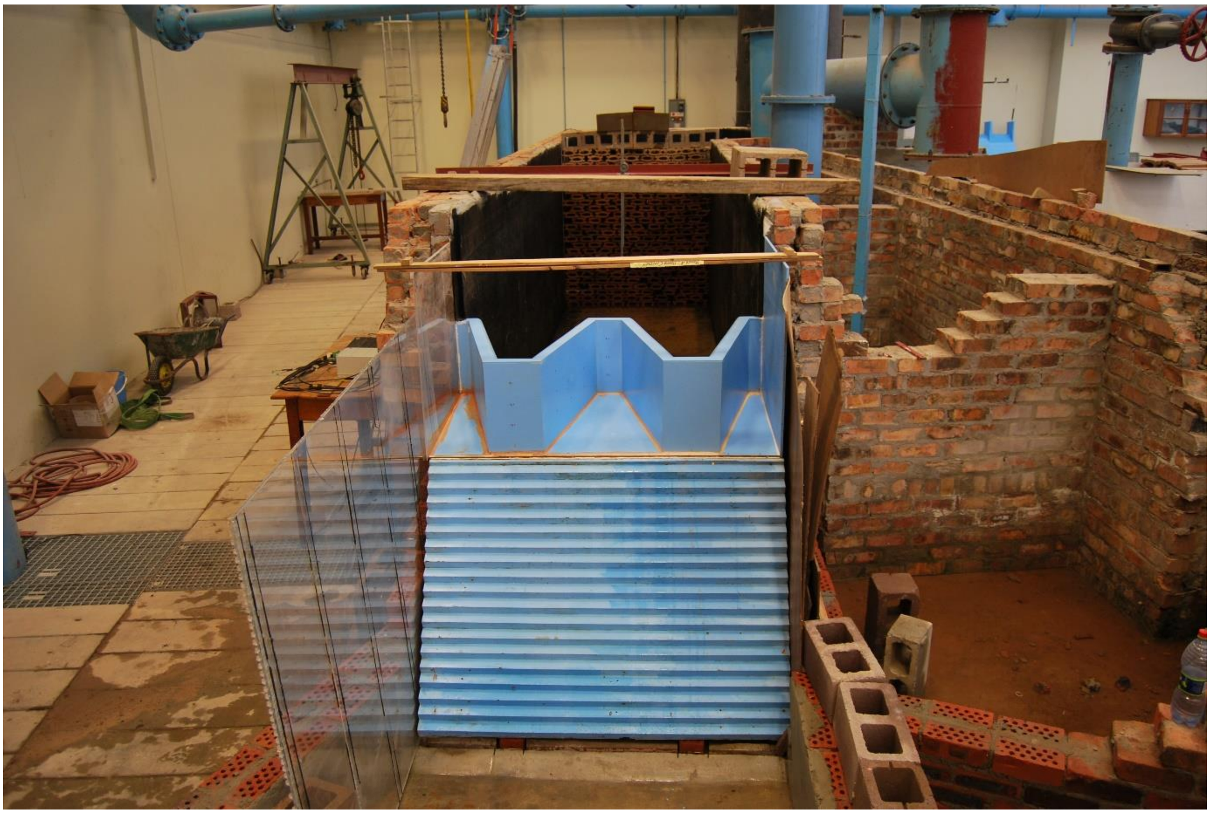

Figure 4.3 View of model constructed and flume from downstream of the model

The aim was to produce an accurate template from which to complete all necessary measurements and to be able to repeat the entire process if it proved necessary. The set-up was definitely repeatable and proved accurate enough to meet the requirements for this study.

4.5. Pressure Sensors

Fifteen holes, with a diameter of 3 mm, were drilled into the downstream face of the labyrinth on one of the two middle faces to avoid any chance that the water friction against the walls could have an impact on the results of the pressure meters. Hard plastic tubes were inserted into these holes from the inside of the model. Soft plastic tubes were attached to these hard tubes; these then ran down through the model and out underneath the model behind the outflowing water. The soft plastic tubes were connected at the other end by a T-piece which had an open stretch of further soft plastic tube – used for priming – and a sensor connected to a cable which in turn ran to the piezometer pressure reader. This was then connected to a computer.

Figure 4.4, below, indicates the positions of the sensors on the weir. These were numbered and are referenced in the physical modelling results. Figure 4.5 indicates the positions of the pressure sensors according to the drawings used during construction of the physical model.

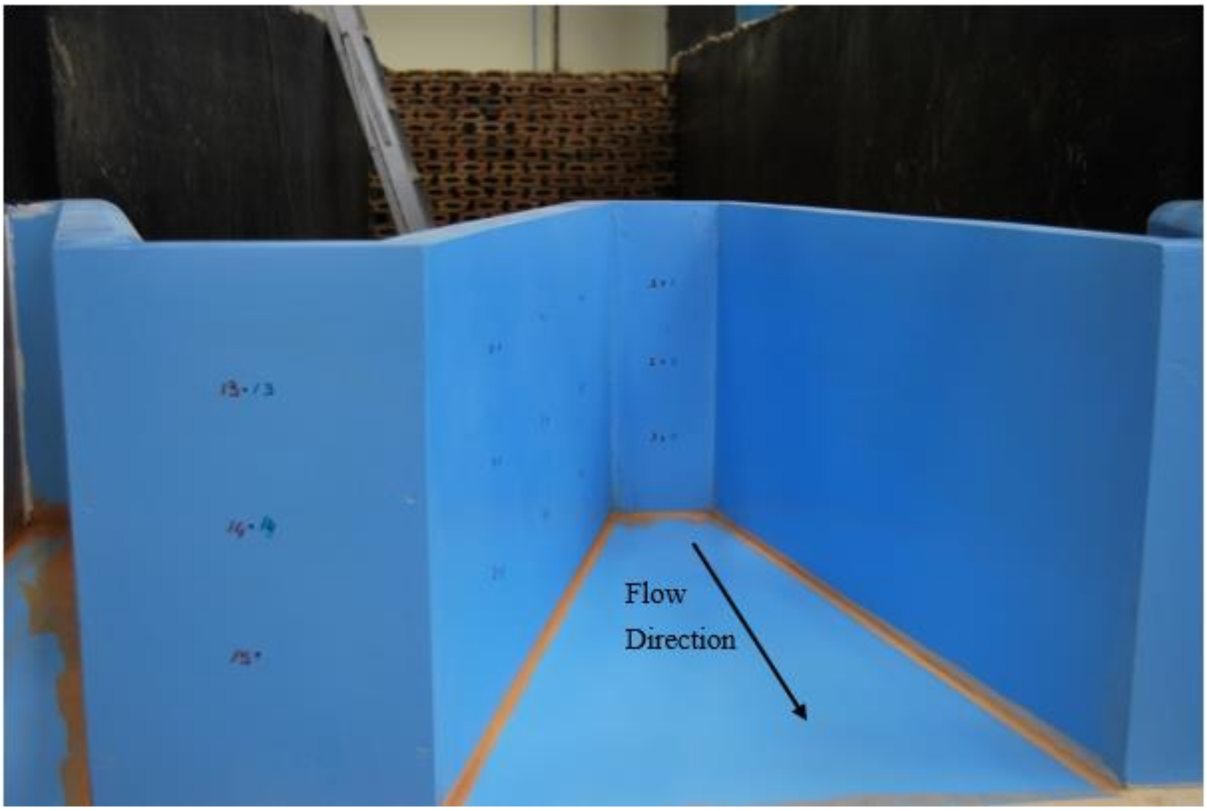

Figure 4.4 Laboratory model showing pressure sensors and labels

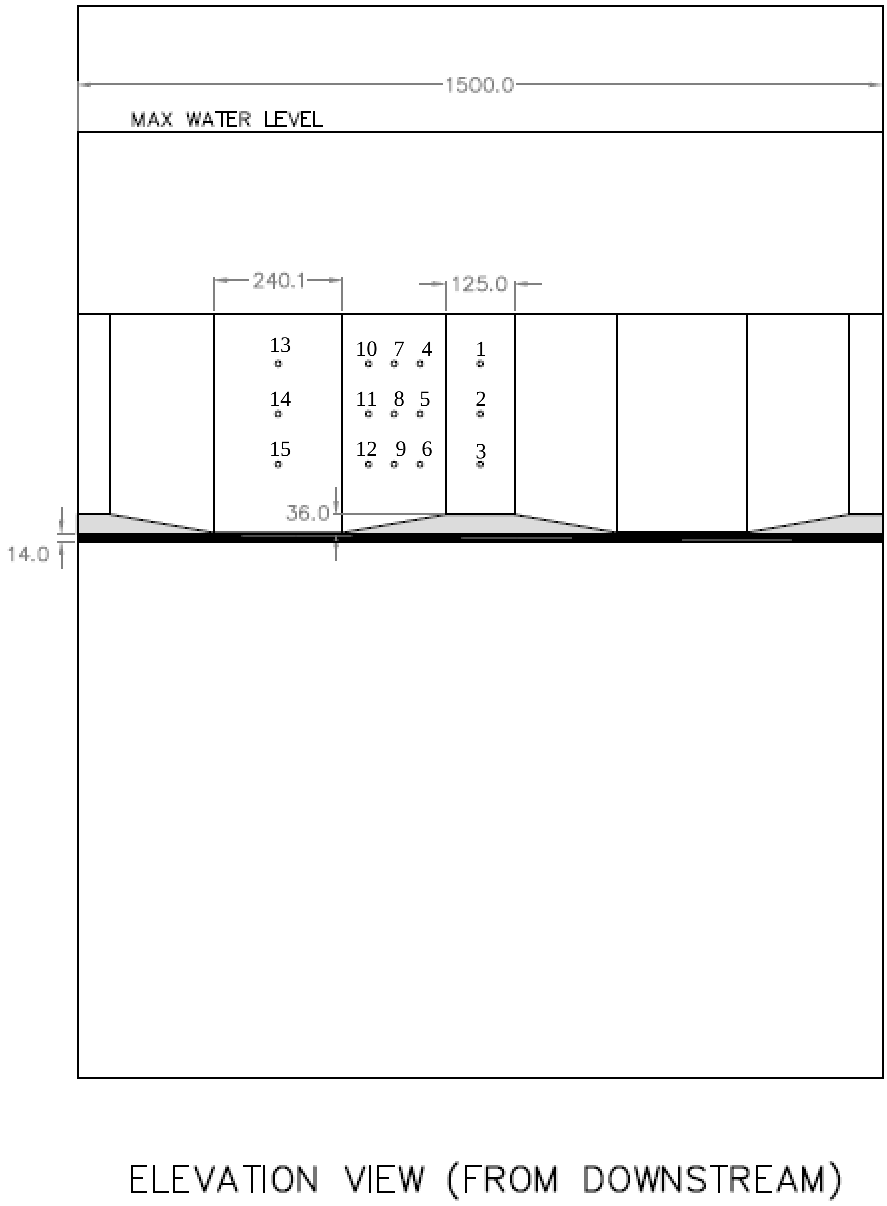

Figure 4.5 Diagram showing the labyrinth model design from downstream, with labels for pressure sensors

4.6. Testing Procedure

The main variable in the test conducted was the discharge channelled over the weir. For each test, readings were taken for the depth of flow over the weir at a point 1.5 m upstream of the crest and the transient pressures at fifteen points on the downstream face of the weir.

Initial pressure tests were completed with water in the channel filled to the crest level of the labyrinth, with no flow (Q = 0 in m^3/s or *l*/s) over the weir. The measurements taken at this point provided a base measurement which could be used to determine the change in pressure and depth of flow as a result of the increase in flow.

Tests where completed in the laboratory for Q = 0, 60, 100, 150, 200, 250, 300, 350, 400, 450, 500, 550 and 600 *l*/s; the results for these tests have been included in section 4.7. These flow rates were the intended or target flows for each test. With the valve controlling the flow through the pipes being a relatively coarse method of obtaining a specific flow, the actual flow rates for each test often varied from the intended flows by 1 or 2 *l*/s. In section 4.7, an achieved flow rate is stated for each test.

For each value of Q, the flow was stabilised and then tested for 5 minutes to align with Crookston's (2010) assertion that 5-7 minutes was the approximate time required for an accurate reading of Q and H_t. This also allowed for an accurate average to be taken and when plotted, the graphs made it easy to discover if the flow rate had changed during the test.

For each of the tests, the depth of flow and transient pressures have been measured and an average pressure calculated for each of the sensors. The depth of flow was measured using a point gauge which is accurate to 0.001 m. The initial reading of the piezometer pressure reader is a value in amperes. This is converted to voltage using Ohm's law which states that voltage or potential difference (in volts) is equal to current (in amperes) multiplied by the resistance (in ohms), or:

$$V = I \times R$$

The piezometer pressure reader was calibrated using a range of different pressure heads as indicated in Figure 4.6 below. This calibration produced a way of converting the readings into a pressure reading and the resulting equation of:

$$y \ = 0.1348x - 1.576$$

Where:

y is the pressure head in meters; and

x is the current measured in amperes.

This is represented graphically below by Figure 4.6:

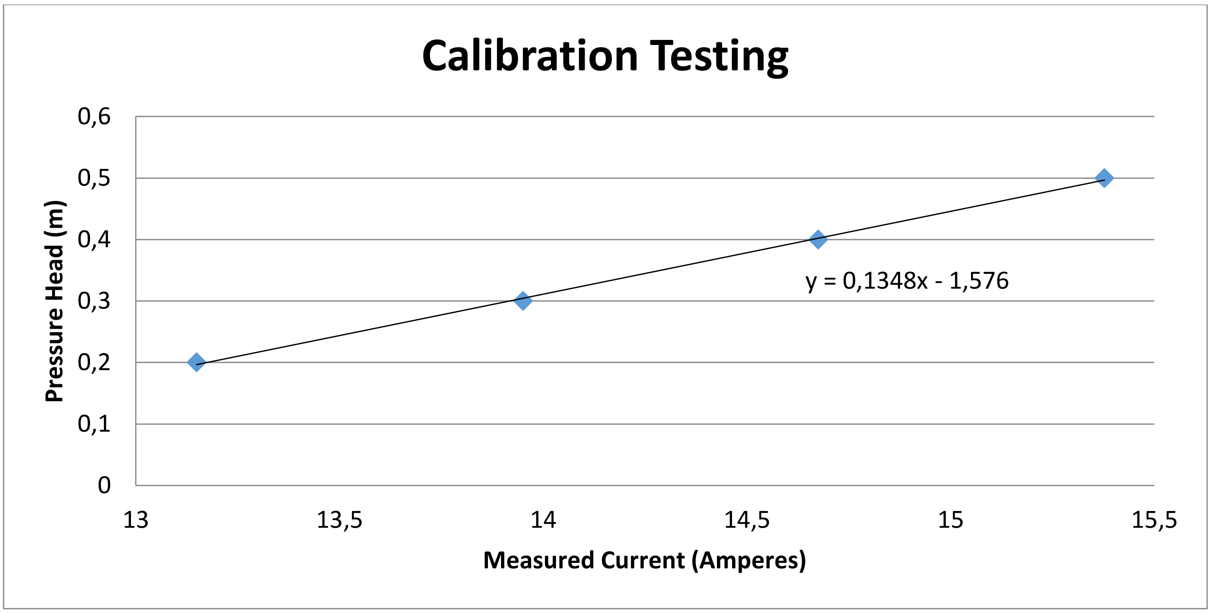

Figure 4.6 Calibration testing results

4.7. Physical Test Results

4.7.1. Tests Conducted

The changing variable for the physical modelling tests was the discharge. This was set using the electromagnetic flow meter linked to the water supply line leading to the model setup. With a maximum of 600 *l*/s available for the tests, 12 tests were conducted in increments of approximately 50 *l*/s to give a sufficient range of flows. As mentioned, the exact discharges were difficult to achieve with the coarse gate valve, additionally with the pumping system there will always be some minor flow variations. The achieved flow rates are included in Table 4.1, below, and were determined by the average flow over the course of an experiment.

4.7.2. Pressure Results

A sample of the data recorded from the physical model test of 200 *l*/s has been included as Figure 4.7 and Figure 4.8, this flow correlates to a prototype flow rate of 712 m^3/s which is a unit discharge of 11.9 $m^3/s\cdot m$ – where the width of the weir is used to determine the unit discharge, not the crest length. This data shows the five minute testing period and the transient nature of the pressure readings.

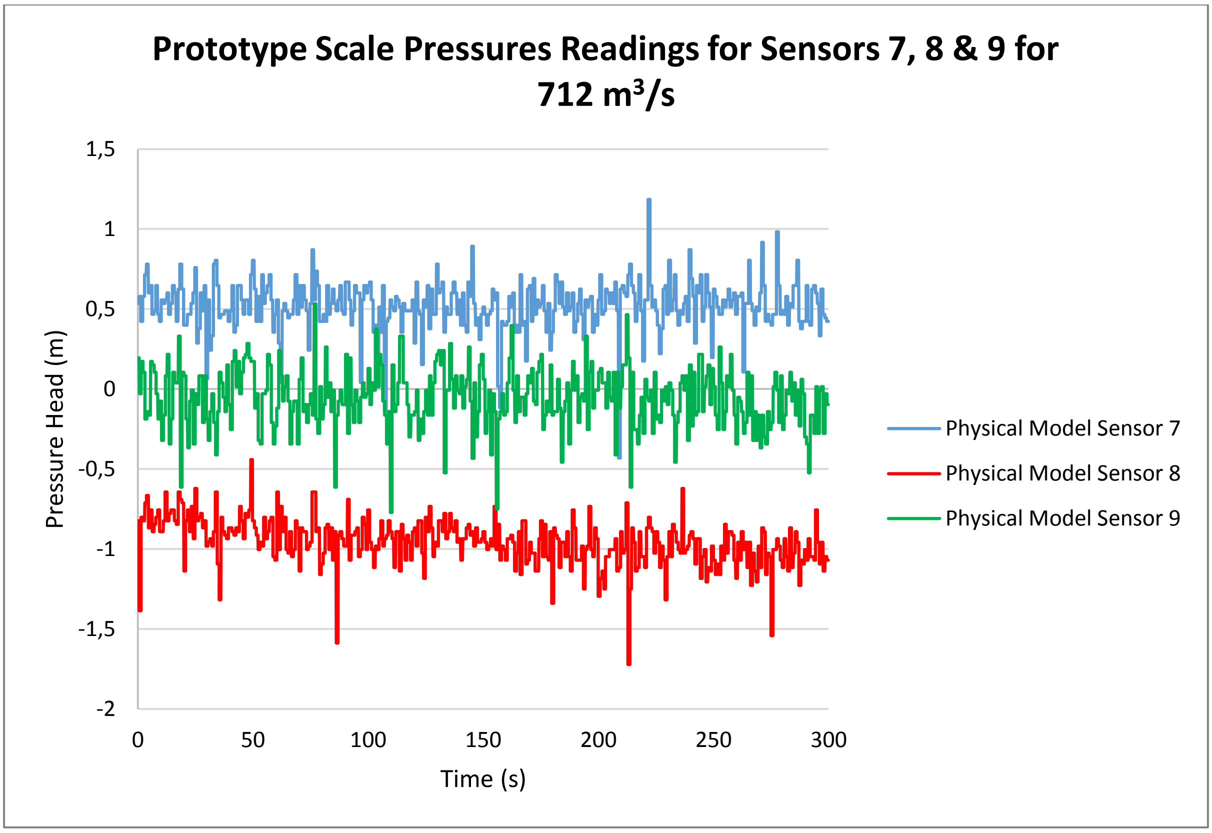

Figure 4.7 Physical modelling results for sensors 7, 8 and 9 for a prototype flow rate of 712 m^3/s (199 l/s at a scale of 1:20)

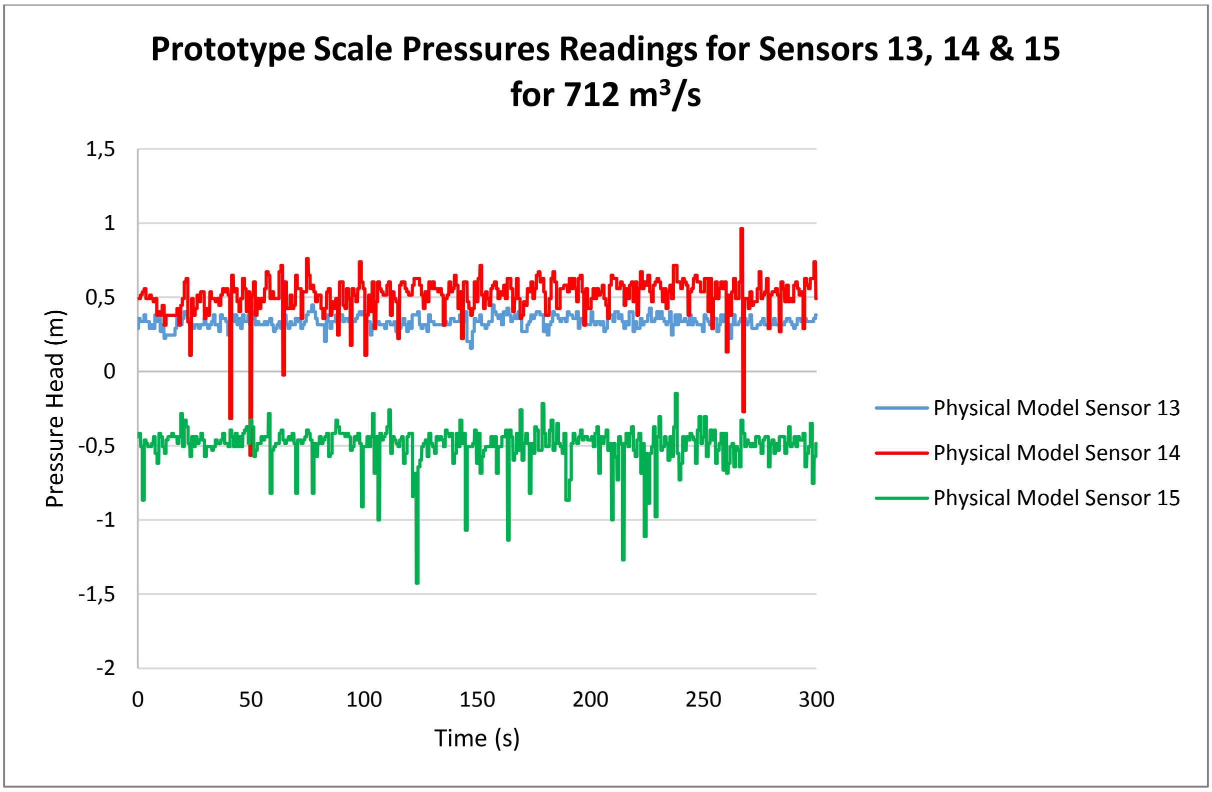

Figure 4.8 Physical modelling results for sensors 13, 14 and 15 for a prototype flow rate of 712 m^3/s (199 l/s at a scale of 1:20)

Figure 4.7 shows the results obtained through physical modelling for a prototype flow rate of 712 m^3/s, for sensors 7, 8 and 9. The image indicates the existence of negative pressures on the downstream face of the weir as well as showing that for a given flow rate the pressures differ along the face of the crest. Figure 4.8 also indicates the differences in pressure across the face of the crest, for the same discharge as Figure 4.7, and the existence of negative pressures.

A summary table (Table 4.1) and graphs (Figure 4.9, Figure 4.10 and Figure 4.11) of the tests conducted have been included below and on the following page. These indicate the targeted flow rate, achieved flow rate, the upstream water level and the average pressure heads measured at each sensor. The sensors were positioned as indicated in Figure 4.4 and Figure 4.5.

Table 4.1 Results summary table for physical model testing

Prototype Flow Rate (m^3/s)	**Model Flow Rate (l/s)**	**Physical Modelling: Average Piezometer Pressure at Prototype Scale (By Sensor in m Pressure Head)**														
		1	**2**	**3**	**4**	**5**	**6**	**7**	**8**	**9**	**10**	**11**	**12**	**13**	**14**	**15**
0	0	0	0	0	0	0	0	0	0	0	0	0	0	0	0	0
215	60	-0.04	-0.12	0.02	-0.06	0.12	0.3	-0.1	0	0.3	-0.28	-0.06	0.34	-0.08	-0.12	0
361	101	0.16	-0.08	0	-0.24	0.06	0.26	-0.34	0.26	0.24	-0.54	-0.06	0.6	-0.08	-0.46	0.1
544	152	0.44	-0.04	0.04	-0.34	-0.02	0.12	-0.48	0.48	0.08	-0.36	0.24	0.42	-0.14	-0.36	0.14
712	199	0.78	-0.36	0.32	-0.52	-0.24	0.08	-0.5	0.8	0	-0.34	-0.14	0.4	-0.34	-0.52	0.5
898	251	0.9	-0.36	1.1	-0.82	-0.44	0.34	-0.72	2.56	0.38	-0.72	-0.26	0.46	-0.54	-0.44	0.48
1063	297	0.86	-0.08	1.78	-1.14	-0.46	0.7	-1.06	2.42	3.6	-0.98	-0.38	0.84	-0.68	-0.24	0.46
1249	349	0.92	0.42	2.22	-1.42	-0.24	0.92	-1.22	2.3	5.74	-1.06	0.02	2.96	-0.74	0.84	0.38
1424	398	1.04	0.6	2.06	-1.4	-0.14	0.82	-1.34	2.28	6.2	-0.7	-0.18	5.42	-0.8	0.88	0.4
1606	449	1.26	0.02	1.1	-1.04	-0.38	0.28	-0.72	2.64	4.64	0.56	0.4	5.54	-0.2	0.98	0.16
1789	500	1.3	0.14	1.22	-0.96	-0.4	0.3	-0.64	2.7	4.72	0.5	0.38	5.54	-0.2	0.9	0.16
1968	550	1.26	0.24	1.36	-1	-0.3	0.52	-0.58	2.84	4.8	0.42	0.38	5.46	-0.22	0.96	0.16
2136	597	1.24	0.68	1.9	-1.04	-0.22	0.9	-0.56	2.92	5.38	0.4	0.42	5.7	-0.18	0.98	0.24

As previously mentioned, Table 4.1 includes the average pressure results obtained from physical modelling for all pressure sensors and for all flow rates tested. The numbers indicate the existence of negative pressures on the downstream face, with the most negative average pressure being -1.42 m at the prototype scale, which was measured at sensor 4 for a 1 249 m^3/s discharge at the prototype scale. The highest average pressure, 6.2 m pressure head at the prototype scale, was measured at sensor 9 for a discharge of 1 424 m^3/s at the prototype scale. Figure 4.9, Figure 4.10 and Figure 4.11 graphically indicate the same results contained in Table 4.1.

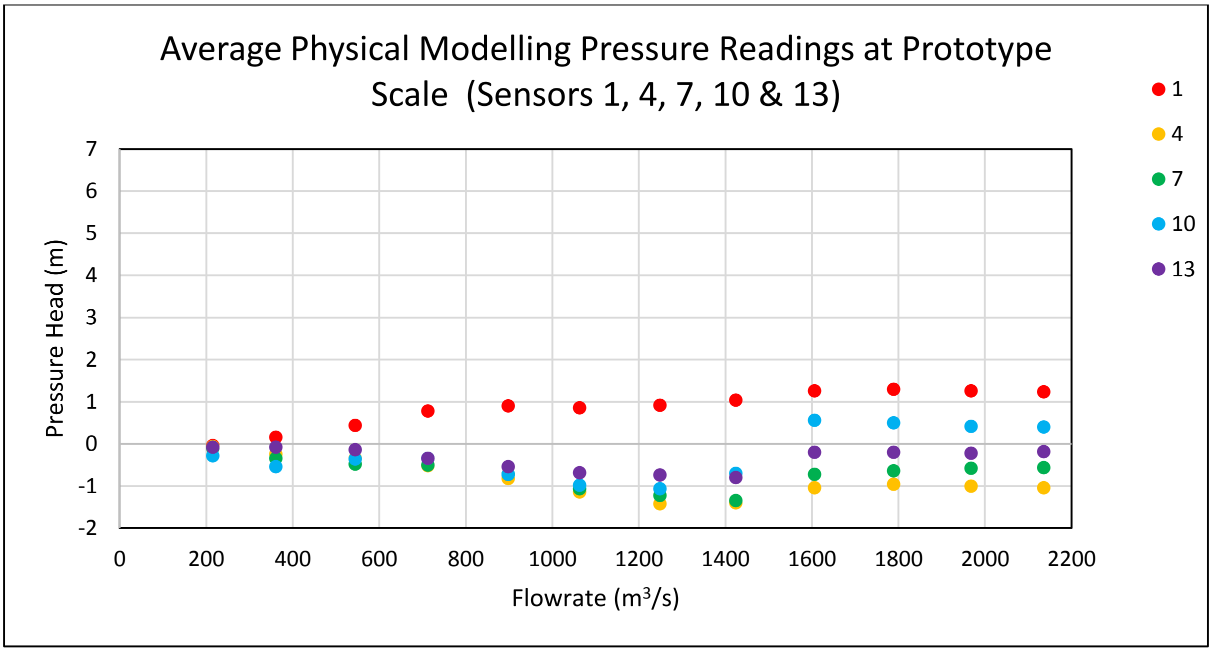

Figure 4.9 Summary graph showing physical modelling results for the average pressure readings obtained during testing at the prototype scale, for sensors 1, 4, 7, 10 and 13

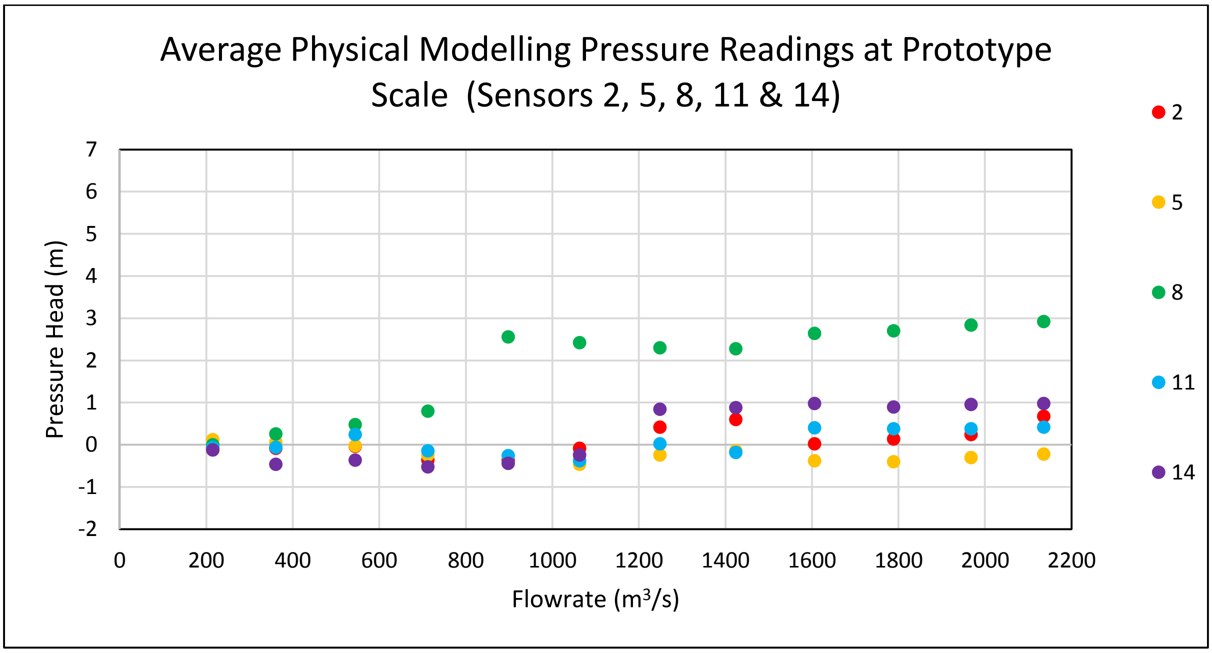

Figure 4.10 Summary graph showing physical modelling results for the average pressure readings obtained during testing at the prototype scale, for sensors 2, 5, 8, 11 and 14

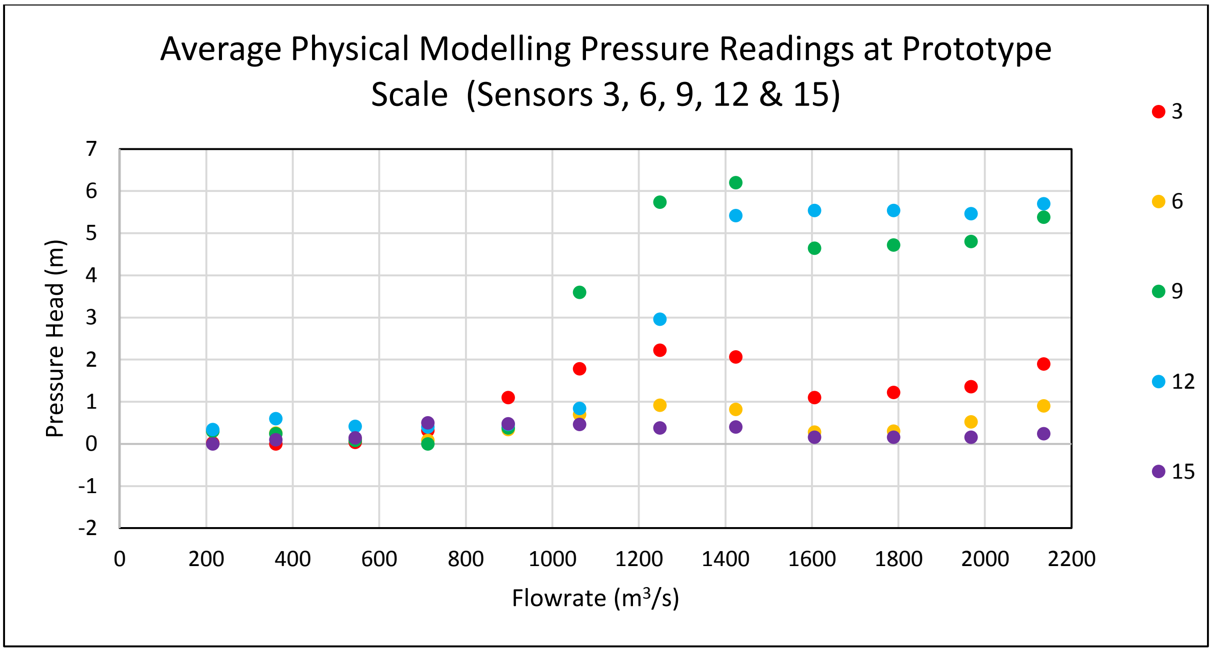

Figure 4.11 Summary graph showing physical modelling results for the average pressure readings obtained during testing at the prototype scale, for sensors 3, 6, 9, 12 and 15

Figure 4.9 shows that the majority of the average pressures recorded, for the upper row of sensors, were negative. Figure 4.10 indicates that the middle row of sensors produced mixed positive and negative results. Whilst the bottom row of sensors, as shown in Figure 4.11, produced entirely positive results.

The USBR publication, *Design of Small Dams* (1987), design recommendations for ogee weirs suggest that the SEF should be passed at a head (H_e) equal to 1.33 times the design head (H_o), in order to slightly improve the hydraulic performance of an ogee. This head level, however, creates sub-atmospheric pressure conditions at the crest equal to approximately half of H_o. These negative pressures need be considered during stability analysis of the ogee.

This indicates that typically a sub-atmospheric pressure equal to half the design head is an acceptable level for the design of a weir. The most negative pressure on the labyrinth weir, as determined through physical modelling, was found to be -1.42 m pressure head at the prototype scale. Half of H_o equals 3.375 m (at the prototype scale) and this indicates that the recorded subatmospheric pressures were well within the maximum design limits as set by the USBR.

The average negative pressures recorded may be well above the design limits, however, the pressure readings did fluctuate and on a number of occasions the instantaneous pressures did exceed the sub-atmospheric pressure limits meaning that cavitation could still occur.

4.7.3. Water Depths (Surcharge)

The upstream water levels were measured at a point 1.5 m upstream of the start of the labyrinth crest. The positioning of the measuring station is important; if it is too close to the weir, then the drawdown effect resulting from flow entering the weir or the surge in the water level due to it passing over the crest impacts on the measurement; if the measurement is taken too far upstream, then the bottom slope of the river/channel becomes an influencing feature. The British Standards (BS3680) recommend that the measuring point be positioned between $4H$ and $5H$ upstream of the crest (Chadwick, et al., 2004).

The 1.5 m distance used for this study, which is equal to $4H$, was based on the design head of $H_t = 375\,mm$. This was deemed acceptable as the head levels during tests would all be less than the design head. There was also no issue with the measuring point being too far upstream as all tests were conducted on a channel with an unchanging head level. The results of the water level are included below, in Table 4.2, against theoretical calculations based on the same flows in both tabular and graphical form.

Table 4.2 Table showing measured and analytical water depths for labyrinth spillway (Scale 1:20)

Target Discharge (l/s)	**Achieved Discharge (l/s)**	**Measured Water Depth Above Crest (mm)**	**Theoretical Water Depth Above Crest (mm)** (Tullis, et al., 1995)
0	0	0	0
50	60	50	46
100	101	69	65
150	152	90	85
200	199	110	102
250	251	126	119
300	297	145	133
350	349	162	148
400	398	179	162
450	449	199	175
500	500	217	188
550	550	233	201
600	597	247	212

("-" denotes a division by 0 error)

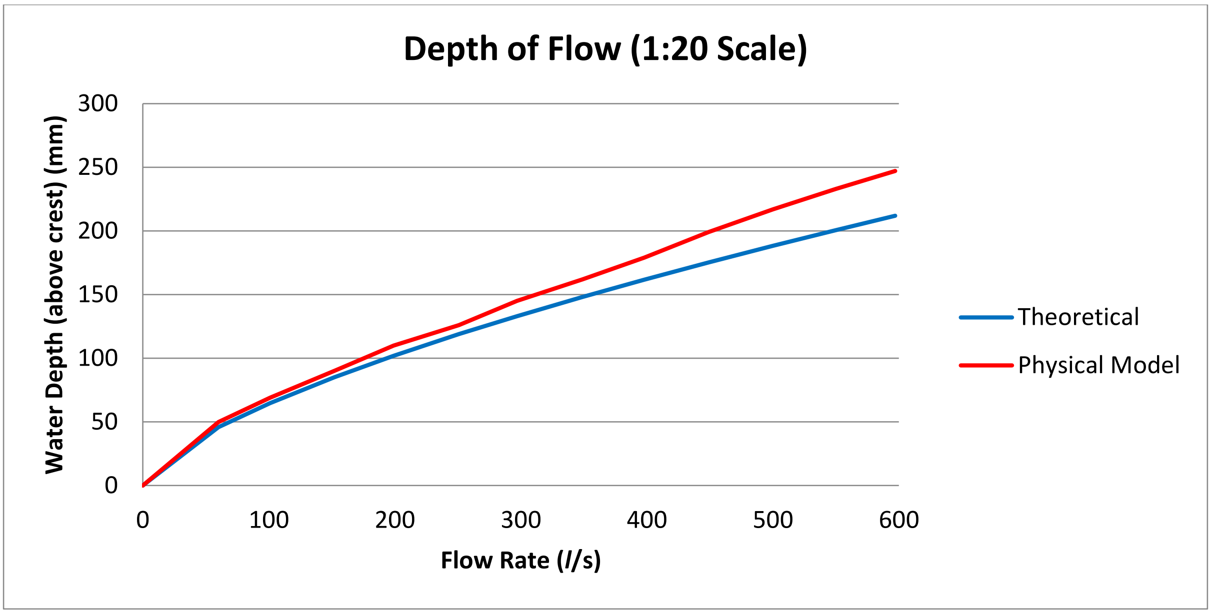

Figure 4.12 Theoretical and measured depth of flow over labyrinth weir (Scale 1:20)

As can be seen above in Figure 4.12, the physical model produced results indicating a higher water level 1.5 m upstream of the crest when compared to theoretical calculations. These values indicated above are for the 1:20 scale model and, thus, should be scaled in order to understand what the surcharge difference would be at the prototype scale. The difference between the values produced through physical modelling and theoretical calculations increased as the flow increased and had a maximum value, at maximum flow of 597 *l*/s at a scale of 1:20, of 35 mm. This is 0.7 m at the prototype scale with a discharge of 2 136 m^3/s as displayed by Figure 4.13. This increase in error could be attributed to increased turbulence and decreased uniformity of the flow as for discharge's less than 1 200 m^3/s at the prototype scale the surcharge measurements are similar, with a maximum difference of 0.28 m at the prototype scale.

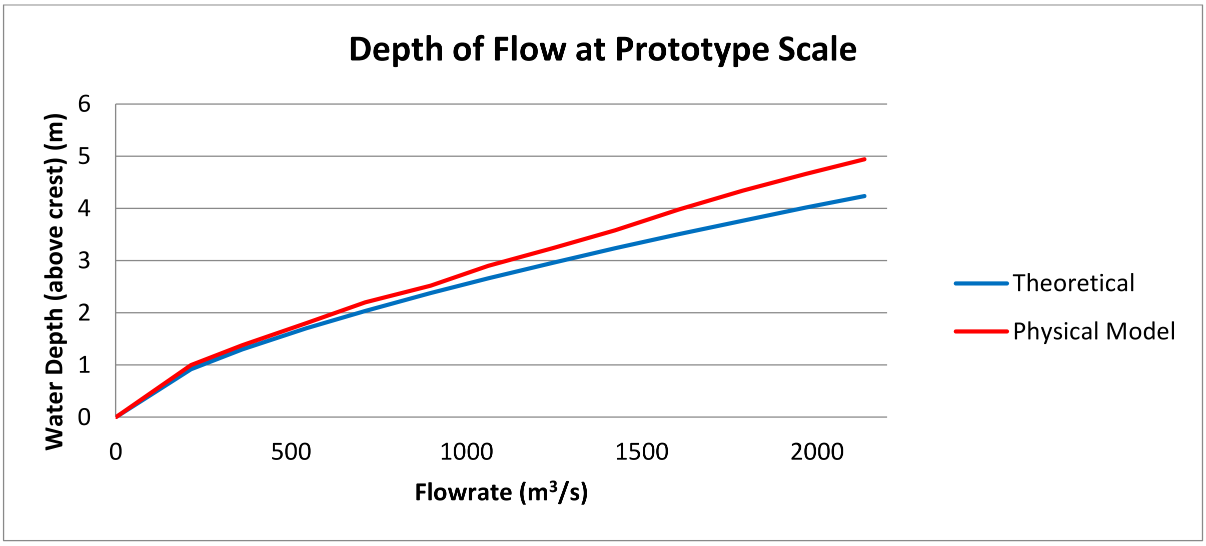

Figure 4.13 Theoretical and measured depth of flow over labyrinth weir at the prototype scale

The reasons for the discrepancies will be dealt with in greater detail in Chapter 6, which focuses on the validation of CFD modelling and will also include the results obtained from CFD modelling procedure. However, it should be noted that some differences between the results arising from the physical model could be due to the quality of the model construction, approaching flow conditions (turbulence and uniformity being the main factors for consideration), model size, accuracy of measuring techniques and equipment or instrumentation and the ability of the water supply system to maintain a steady flow condition (Crookston, 2010).

It should also be noted that the physical model would, in this case, be the more accurate method of predicting the surcharge of a prototype. The theoretical calculations cannot consider all environmental factors and the behaviour of the water has had to be simplified in order to create equations that are of use to engineers. Additionally, empirical relationships are based on a limited number of experiments and setup conditions.

4.7.4. Aeration and Flow Patterns

Various aeration and flow patterns where displayed by the physical model when the different flow rates were tested. Figure 4.14 – Figure 4.19 show photographs taken during physical modelling testing for low flow, medium flow and high flow conditions.

In Figure 4.14 and Figure 4.15, which are for low flow conditions, the water pulls away from the crest on the downstream side, creating a fully aerated condition. The figures also show the 3D nature of the flow over the weir and that the interference between the nappes between cycles is minimal under low flow conditions. These figures also indicate the impact the inside apex width has on the flow; with a smaller inside apex with the nappes would have collided more, which in turn would have reduced the advantages gained by using a labyrinth weir over a linear weir.

Figure 4.14 Physical model of labyrinth weir with a discharge of 60 l/s at a scale of 1:20, viewed from above (215 m^3*/s discharge at the prototype scale, at a unit discharge of 3.6 m*^{3}*/s·m)*

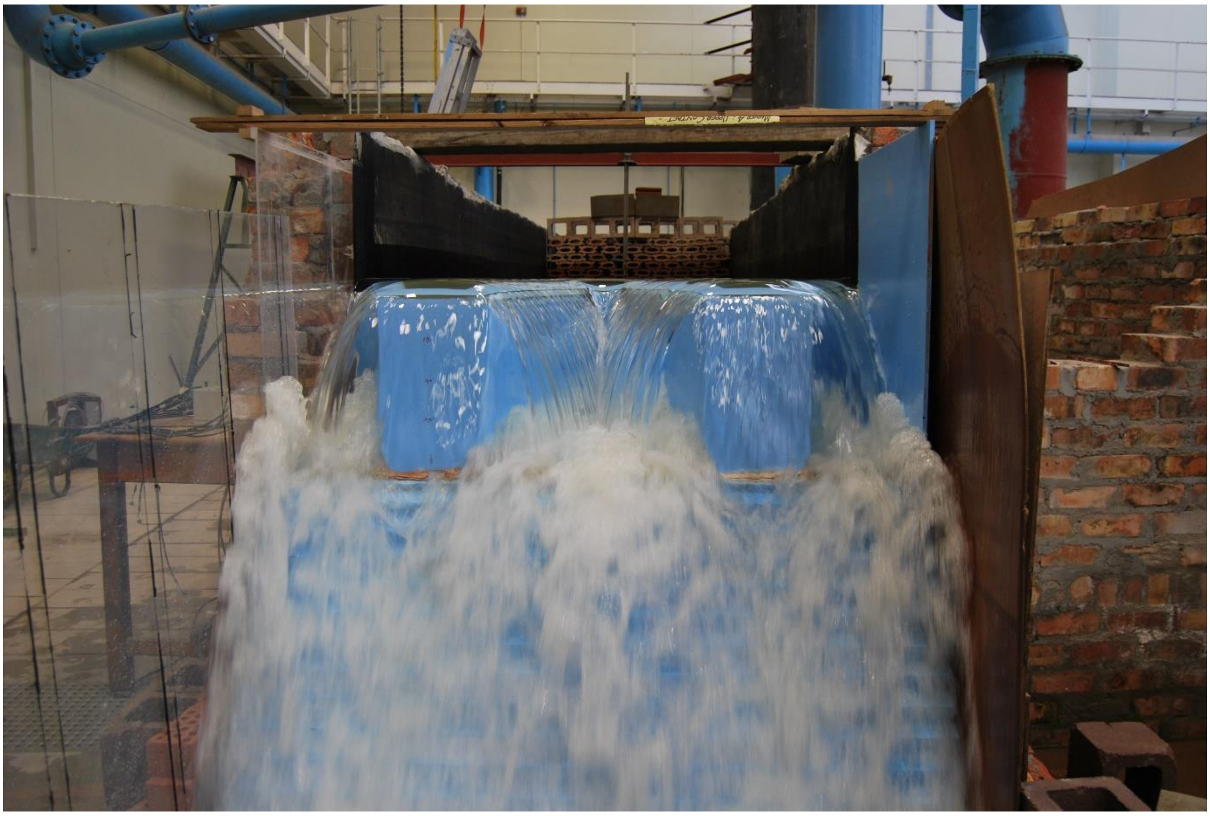

Figure 4.15 Physical model of labyrinth weir with a discharge of 60 l/s at a scale of 1:20, viewed from downstream (215 m^3*/s discharge at the prototype scale, at a unit discharge of 3.6 m*^{3}*/s·m)*

Figure 4.16 and Figure 4.17, below, show the physical model under medium discharge conditions of 297 *l*/s at a scale of 1:20, which is 1 063 m^3/s at the prototype scale (with a unit discharge of 17.7 m^3/s·m). The 3D nature of the flow is, again, visible in Figure 4.16. These figures also show an increase in the amount of nappe interference, when compared to the previous figures (Figure 4.14 and Figure 4.15). The aeration of the weir varies along the downstream part of the crest, with the downstream apex being aerated close to the crest, but submerged from about a quarter of the way down the face. The side legs of the weir are at some places completed submerged and at others a nappe forms over the crest, this appears to occur closer to the apexes.

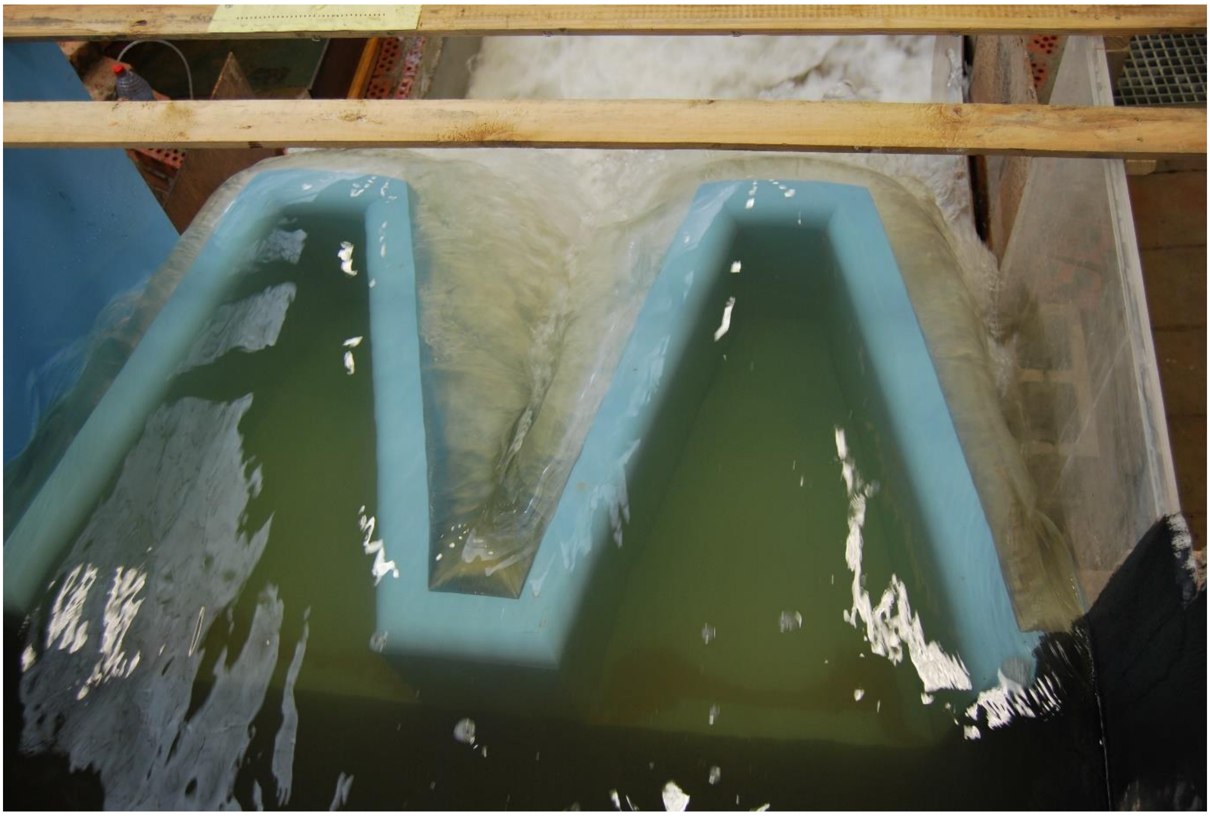

Figure 4.16 Physical model of labyrinth weir with a discharge of 297 l/s at a scale of 1:20, viewed from above (1 063 m^3/s discharge at the prototype scale, at a unit discharge of 17.7 m^3/s·m)

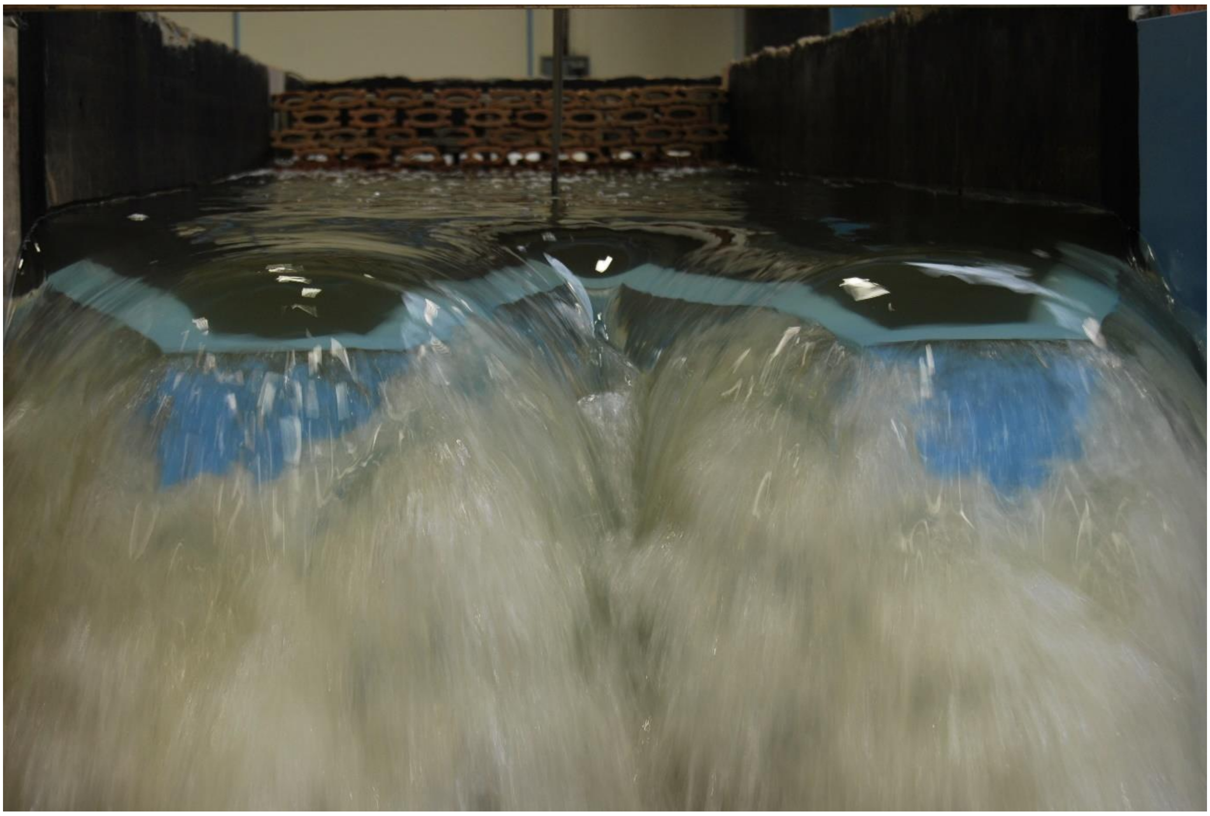

Figure 4.17 Physical model of labyrinth weir with a discharge of 297 l/s at a scale of 1:20, viewed from downstream (1 063 m^3/s discharge at the prototype scale, at a unit discharge of 17.7 m^3/s·m)

Figure 4.18 and Figure 4.19 show the weir under the highest flow tested in the laboratory, 597 *l*/s at a scale of 1:20 (2 136 m^3/s, with a unit discharge of 35.6 m^3/s·m, at the prototype scale). Figure 4.19 shows that the downstream apex is still aerated at the top of the crest, whilst the rest of the crest appears to be submerged due to the turbulence of the colliding nappes. The flow direction of the water over the crest is still 3D, although under high flow conditions it is more linear than under lower flows as the colliding nappes reduce the advantages of the labyrinth weir shape.

Figure 4.18 Physical model of labyrinth weir with a discharge of 597 l/s at a scale of 1:20, viewed from above (2 136 m^3/s discharge at the prototype scale, at a unit discharge of 35.6 m^3/s·m)

Figure 4.19 Physical model of labyrinth weir with a discharge of 597 l/s at a scale of 1:20, viewed from downstream (2 136 m^3/s discharge at the prototype scale, at a unit discharge of 35.6 m^3/s·m)

4.7.5. Further Results

There are many ways of presenting the information attained during the physical modelling phase of the study. Appendix B contains a number of graphs which further express the information acquired, whilst Appendix C contains photographs taken during the testing. Additionally, Chapter 6 deals with the validation of CFD modelling and compares the results obtained during the physical modelling stage to those obtained during the mathematical modelling process, as does Appendix E.

Chapter 5: Numerical Modelling

5.1. Introduction

This chapter initially describes the procedure required to generate a CFD model and the details that surround each step. The various tests conducted and the approaches used are then discussed. Lastly, the chapter presents the results obtained through CFD modelling for water depths and pressures, as well as showing a comparison between results produced by the steady state and transient tests.

5.2. Numerical Procedure

CFD is governed by a number of overriding equations which each cell should satisfy. In order to solve these governing equations of fluid flow, the program provides solutions for the commonly used Reynolds-average Navier-Stokes (RANS) equations with some slight modifications. These have been included to assist with the tracking of the free water surface and to determine the way in which the water behaves around obstacles such as weirs. The modified RANS equations for continuity and momentum are presented below (Savage, et al., 2004):

- $Continuity: \ \frac{\partial}{\partial x}(uA_x) + \frac{\partial}{\partial y}(vA_y) + \frac{\partial}{\partial z}(wA_z) = 0$
- $Momentum: \ \frac{\partial U_i}{\partial t} + \frac{1}{V_f}\left(U_j A_j \frac{\partial U_i}{\partial x_j}\right) = -\frac{1}{\rho}\frac{\partial P\prime}{\partial x_i} + g_i + f_i$

Where:

$u, v \ and \ w$ are velocities in the x, y and z directions respectively;

$A_x, A_y \ and \ A_z$ are fractional areas, across each cell face in the noted directions, open to flow;

P' is the pressure;

ρ is the density;

g_i is gravitational force in the noted direction; and

f_i represents the Reynolds stresses.

There are a number of commercially available CFD packages that could be used to simulate the flow over a weir. Some of these include PHOENICS, FLOW-3D, STAR-CD and ANSYS Fluent (Versteeg & Malalasekera, 1995). All of these packages mentioned are focussed on solving the finite volume method, which is discussed in section 5.2.2.

In order to map the 3D flow field that exists over a labyrinth weir, the ANSYS Fluent CFD package was utilised. This model package was selected as it is a general purpose CFD programme with the required abilities to map a flow field and licences were made available through Stellenbosch University. There are three chief stages to the Fluent setup, each with their own processes and requirements which need to be met. These are discussed in the following sections before presenting the findings and are as follows:

i. Pre-processing;
ii. Solver; and
iii. Post processing.

5.2.1. Pre-processing

The two steps involved in pre-processing are: creating an accurate geometry of the study objects and surrounding area, and generating a mesh of this area. These steps are taken through the ANSYS program setup using the ANSYS CAD interface for the geometry setup and the meshing interface for the mesh. They are completed in order to provide the solver with a control volume and cells over/within which to solve the RANS equations.

Geometry

The geometry for the CFD model is a model of the prototype, as was the physical model. It was built to the same size specifications as the physical model in order to attempt to have a closer correlation to it. The close correlation was desirable as the focus of the thesis was on validation of the CFD process, this is performed through comparisons between the CFD model and the physical model. The geometry is built in such a way as to create a control volume within which the fluids involved would be able to move and interact. The conservation of momentum, mass and energy are required to be satisfied over the region (Institute for Water and Environmental Engineering, 2012). Boundary conditions, material types and other details of the constructed geometry are included during the processing or “Solver” phase.

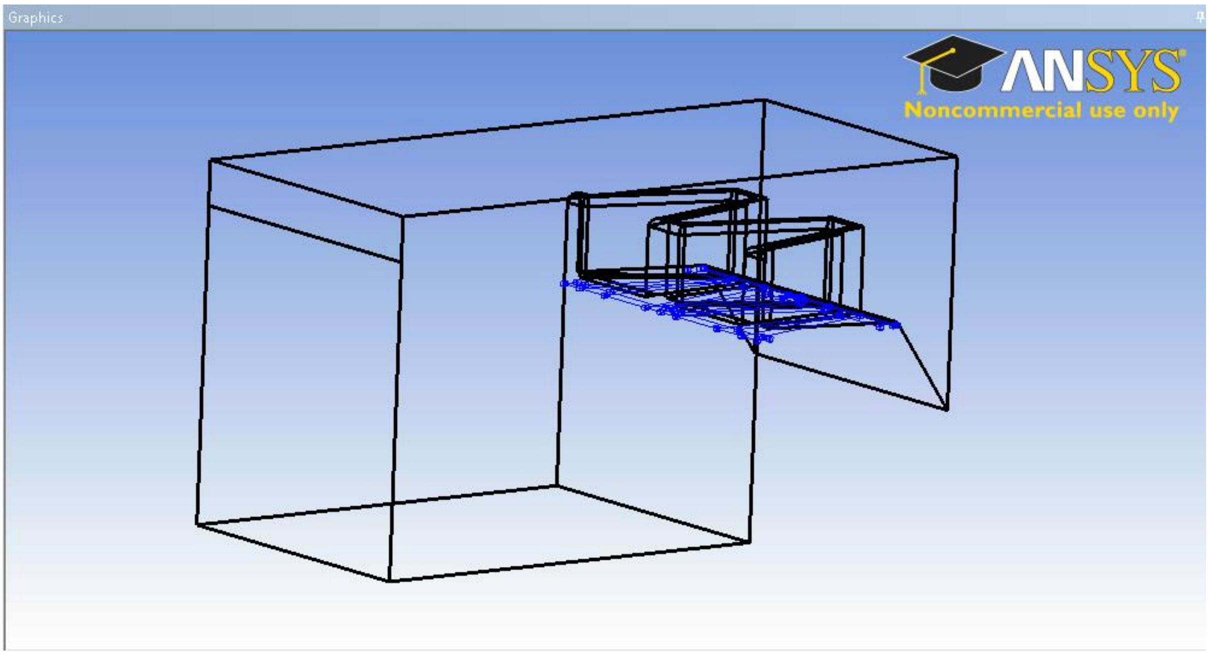

Figure 5.1 Geometry constructed for mathematical modelling

As seen in Figure 5.1, the geometry is inclusive of an upstream section to allow for a fully developed channel of water to be established.

Meshing

The meshing process involves the breaking down of the control volume into smaller cells/elements or grids. The CFD program develops algebraic equations using discretisation methods, to find solutions for the governing equations and principles of fluid mechanics, some of which have been discussed above (Institute for Water and Environmental Engineering, 2012).

The meshing process represents a trade-off between accuracy and cost, with cost coming in the form of computer time and hardware. With solutions for the fluid behaviour in terms of pressure, velocity and density to name a few, being solved at each of the cells inside the domain, the accuracy of the model increases with an increase in the number of cells generated. However, with the increase in nodes and elements, the cost is also increased as the solver time and potential complications continue to increase with the complexity of the grid (Institute for Water and Environmental Engineering, 2012).

The mesh can be made up of either tetrahedrons, quadrilaterals or a combination of both. For this scenario using a cutcell mesh, which is made up of quadrilaterals proved to be the best option. The model was unable to complete successful simulations with the tetrahedron mesh as the solution continually diverged. The cutcell mesh, in contrast to this, was stable and required a lower number of elements. A combination of the two meshing options could have proved successful, however, it was not possible to generate a combination mesh without the number of nodes increasing significantly and this would have drastically increased the simulation run time. Thus, a cutcell mesh was used as seen in Figure 5.2.

In an attempt to keep the number of cells in the mesh as low as possible, the mesh was made in such a way that the areas of least importance had the coarsest mesh, with the intricate areas, water surface areas and areas where the values calculated by the nodes were considered integral to the results, having a far finer mesh, as seen in Figure 5.2.

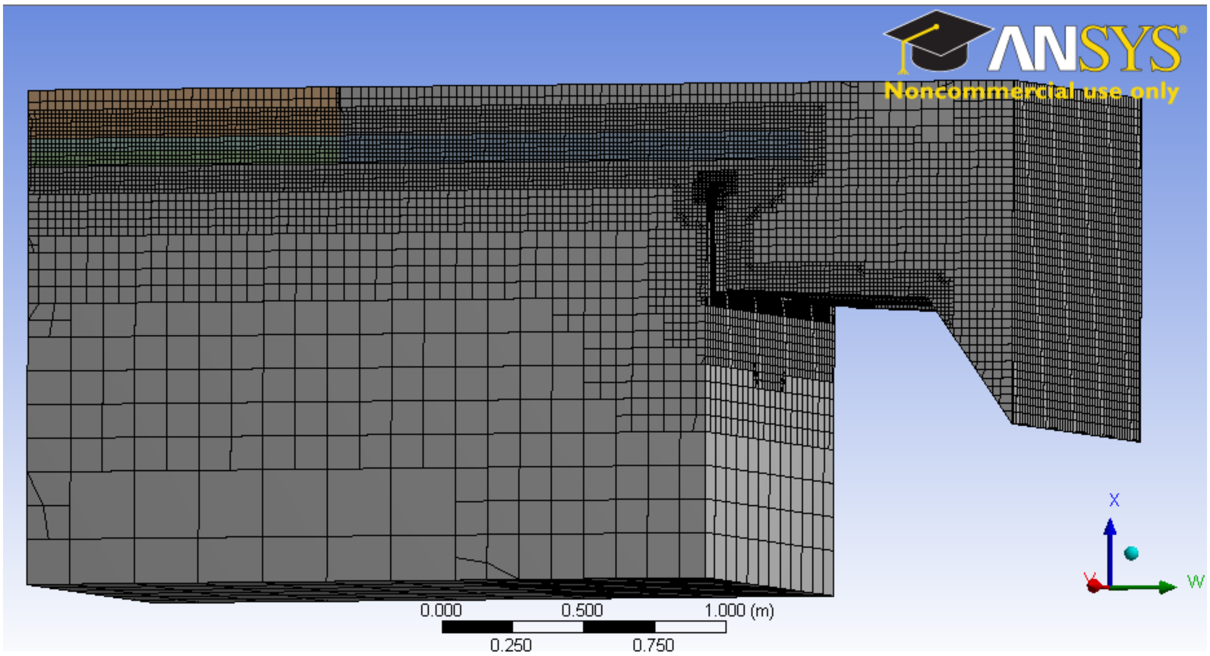

Figure 5.2 View of the generated mesh, showing a finer mesh along the water surface level

5.2.2. Solver

The solver in four of the five main commercial CFD codes is primarily focussed on solving the finite volume method. This is done across all the cells or control volumes of the specified domain in three steps (Versteeg & Malalasekera, 1995):

1. Integrating the fluid flow equations over each of the finite cells;
2. Converting the integral equations that result, through discretization into an algebraic equation system; and
3. Solving the algebraic equations by means of an iterative method.

Other techniques, such as the spectral method and the finite element method, do exist for the solution of CFD problems. However, the integration of a control volume sets the finite volume method apart. This expresses the conservation within a finite cell of relevant properties such as velocity or mass flow. Expressing one of these properties as ϕ, the conservation of this property can be expressed in words as (Versteeg & Malalasekera, 1995):

- $\left\{\begin{matrix}\text{Rate of change}\\ \text{of } \phi \text{ in the}\\ \text{control volume}\end{matrix}\right\} = \left\{\begin{matrix}\text{Net rate of}\\ \text{increase of } \phi \text{ due}\\ \text{to convection into}\\ \text{the control volume}\end{matrix}\right\} + \left\{\begin{matrix}\text{Net rate of}\\ \text{increase of } \phi \text{ due}\\ \text{to diffusion into}\\ \text{the control volume}\end{matrix}\right\} + \left\{\begin{matrix}\text{Net rate of}\\ \text{creation of } \phi\\ \text{inside the}\\ \text{control volume}\end{matrix}\right\}$

The CFD codes used contain discretization techniques, these are suitable for the management of the important transport phenomena, convection – which is transport due to fluid flow – and diffusion – which is transport due to variations of a property (ϕ) from point to point. These codes can also manage source terms – which are associated with the creation or destruction of ϕ. The physical phenomena on which this is based is very complex and solutions are non-linear, thus an iterative solution is required. In the following sections it is indicated that the SIMPLE algorithm was used. This is because the SIMPLE algorithm ensures a correct linkage between velocity and pressure.

Model Setup

Once the geometry of the model is created in the FLUENT CAD system and the mesh is generated in the Meshing program, the mesh is imported into the solver program. Within the program, a number of settings are made to set up the details of the model, before the solver runs, as discussed below.

The Volume of Fluid (VOF) model was selected, and within this setup the “implicit scheme” chosen. Additionally “implicit body forces” were enabled. All values within this model were left as default values.

For turbulence modelling, the k-ϵ model was selected, with two eulerian phases: water as the primary phase and air as the secondary phase. With the k-ϵ model, values for k and ϵ are inserted for all the open boundaries, as described below in “Boundary Conditions”.

For the two phases (water and air), the default values of density, viscosity and density, based on a reference temperature of 25°, were taken as this is sufficiently close to the temperature of water during the physical modelling (22°).

Boundary Conditions

Upon completion of the model type and solver setup, the various boundary conditions were set for all the outer boundaries of the model. During the geometry creation and meshing phase, these areas are named and each of these named sections will receive an independent boundary condition. These sections are named and explained below:

- Walls – The surrounding walls of the model were set to have no-slip conditions and to be unmovable all times. This allows the model to determine an accurate unit discharge for the weir, as the walls have little or no impact on flow patterns.
- Inlet – The inlet conditions for the model are possibly the most important. There are a limited number of options for the inlet to select from, considering that the inlet in this case was required to supply water to the model. A "velocity-inlet" boundary condition was used, with the velocity being the main variable factor between the various tests conducted. For each of the flow rates required to match the flow rates of the physical modelling tests, a velocity was calculated which was dependent on the inlet area. With a change in velocity, new values of k and ϵ were required with each test. The initial pressures were left at atmospheric pressure (101325 Pa), which was set as the operating pressure. The volume fraction of air in the inlet was set to 0 for all tests.
- Roof – Various boundary condition options for the roof of the model were trialled. In the 2D model, used during the trial modelling stages, the solution converged with the roof condition set to "outlet-vent", however, this did not work in the 3D model. To obtain a solution in 3D, the roof was set as a "wall" and matched the conditions, as mentioned above, for the other "wall" sections.
- Air Inlet – It was important to allow air to enter the model domain in order to avoid a vacuum forming within the boundaries. Thus, the area between the inlet and the roof was named "inlet for air" and used to ensure this scenario did not occur. As with the "roof", many options were trialled and the "pressure-inlet" condition was finally selected. This allows for the domain to remain at atmospheric pressure, as is the case with the physical model. The gauge pressure is set to 0, as is the case with the velocity inlet, the turbulence parameters are set to match those of the velocity inlet. This allows for the air to be stable above the water surface and for any turbulence that is generated within the model to be able to dissipate.
- Outlet – The outlet of the model allows the water and air inside the domain to flow out, as well as allowing for air to flow back into the model to ensure it stays at atmospheric pressure. The outlet condition selected was "outflow". The gauge pressure is set to 0, as with the other boundaries, to allow for atmospheric pressure to be retained.

Run Initialization

For each test of the model it is necessary to 'prime' the model. This is done in three steps:

1. The model conditions are initialized with the pressure set to atmospheric and the entire interior of the model filled with air. The interior is then "patched" with water set to the level expected by the flow rate for which the model shall be tested.

2. This model is then run under steady state conditions until the solution has converged. Convergence is based on residuals reaching a value significantly close enough to zero to be considered negligible. The most important of the residuals is the mass balance.
3. Upon convergence, the model is changed from being a “steady-state” model to “transient”. The time for the model is set to 300 seconds, to match the time of the physical model tests, and the number of iterations per time step is also set. The model is then run to produce results. The recording and documenting of this is discussed in “Post Processing”.

5.2.3. Post Processing

Upon completion of the processing, the information gathered from the simulation run is sent to the post processor. This collects the information from the code and presents the data in many practical and interesting ways. With the large extent of data recorded during simulations there are endless ways of showing the data. Some of the tools available for visualisation manipulation are:

- Geometry and mesh displays
- Plotting of vectors
- Contour plots of pressures/densities/phases/velocities/turbulence
- Pathlines
- Tabulated results
- 3D surface plots and 2D plotting of results

A number of these methods have been used to analyse and verify the results and the more significant of these have been included below in the ‘Results’ section. Further results have been included in Chapter 6 as a form of comparison or verification of CFD and summary results for all flow rates tested during CFD modelling are included in Appendix D.

5.3. Tests Conducted

For each of the 12 flow rates tested with the physical model – ranging from 60 *l*/s to 600 *l*/s at a scale of 1:20, or 107 m^3/s to 2 136 m^3/s at the prototype scale – two tests were run using CFD. These were in different states, steady and transient state. Further tests were conducted to determine the appropriateness of using a coarser mesh during transient simulations to decrease computation time. A brief description of the tests are discussed in this section as well as comparisons made between the outcomes of the steady and transient state solutions. All results concerning the pressures on the downstream face are discussed in the next section (5.4 Discussion of Results).

5.3.1. Steady State Tests

For the tests run in steady state the model was setup, in addition to previously mentioned parameters, to run as an implicit model at a consistent flow rate for a large number of iterations. The convergence of the model was based upon the consistency and nearness to zero of the mass balance between the flux into and the flux leaving the model. As this neared zero, with a tolerance of 1% of the inlet flux being allowed, the model results were recorded using monitors on the downstream face of the weir, set to matching locations as those used during the physical modelling. Results were recorded for 2 000 iterations at the end of which a mass flux report was conducted to check the mass balance and ensure convergence was achieved, pressure readings at the 15 monitors were recorded, averaged and converted to the prototype scale. Additionally, the water depth was measured and expressed as the depth above the crest level (at the prototype scale of 1:1). These results are discussed in section 5.4 and are compared to the theoretical results.

5.3.2. Transient Tests

Model Set-up

A number of changes in the model set-up were made for the transient runs, these were required because the transient simulations ran against time and were far less stable than the steady state simulations. At the pressure outlet boundary an open channel setting was included, this allowed the water level at the outlet to be set to assist with stabilising the simulations. The ‘Pressure Specification Method’ was selected as ‘Free Surface Level’ and the ‘Density Interpolation Method’ was selected as the ‘Neighbouring Cell Volume Fraction’ option. The ‘Bottom Level’ was set to match that of the base level of the outlet (-0.414 m) and the ‘Free Surface Level’ was selected independently for each of the varying inlet velocities. The ‘Free Surface Level’ was determined through the running of transient tests for the specified inlet velocity whilst allowing the program to determine the level of the free water surface independently.

Tests were initially conducted using the ‘Pressure Specification Method’ as ‘From Neighbouring Cell’. This allows the program to determine the level of flow free of constraint, as used to determine the level of the free surface before testing. The ‘Pressure Specification’ method is, however, far slower to run than the ‘Free Surface Level’ method, running at approximately 100 time steps per hour where the ‘Free Surface Level’ method runs at approximately five times this speed. Additionally, the ‘From Neighbouring Cell’ method is far less stable, but in terms of flow behaviour at the outlet, the ‘From Neighbouring Cell’ pressure specification method more accurately simulates the behaviour as it is not constricted in any way. As all pressure measurements taken were on the downstream face of the spillway and therefore not influenced by the behaviour of the flow at the outlet (provided the mass flux report remained close to zero and the weir was not submerged) the faster method could be used without influencing the results.

Courant Number

As the name suggests, the transient model was run against time and so a time step was set. With the desire to achieve accuracy a small time step was desirable, however, the smaller the time step the longer the model will take to complete a run of a specified length of time. It was possible to make the time step extremely small (1e-6 seconds), however, it was essential to find the largest possible time step increment for which the model would run in a stable manner. This was dependent on the Courant number (C_r), which is determined through the following equation:

$$C_r = \frac{\bar{\nabla} \triangle t}{\triangle I}$$

Where:

$\bar{\nabla}$ is the average linear velocity at that location;

$\triangle t$ is the maximum time step size; and

$\triangle I$ is the dimension of the grid cell at each location.

The default value for the Courant number is two (ANSYS Inc., 2009), in order to ensure the stability of the model a variable time step setting was used with the starting time step equalling 0.0001. The variable time step size allowed the model to determine what time step was most fitting for the situation, increasing and decreasing as the model required it to, with the aim of achieving the set Courant number.

The Courant number was initially left as two, but it was found that the model was far more stable and likely to complete a successful run with a smaller value. Thus, the number was set to 0.5 for the start of the run and slowly raised during the run (with a maximum of 1.6 being used during testing), whilst ensuring the model remained stable. With $C_r = 1$ the time step size would be approximately 0.0018 s.

Transient Test Length

The goal when developing the CFD model was to run tests for the same time period as done during the physical model study – five minutes. However, with the complexities of CFD modelling to complete just one test of this length would take a month. The two computers used for the required simulations contained 8 and 16 gigabytes (GB) of random access memory (RAM) with quad core dual processors, with a processing speed of 2.9 gigahertz (GHz). However, a restricting factor was the number of licences available, as each licence allowed up to four processors to be run. Thus, with more licences a higher number of processors could have been used per computer and the simulation speed could have been increased.

Fortunately, initial simulation results showed that tests of this length would not be necessary as the pressures produced by the model, once running in a stable manner, did not appear to have an upward or downward trend. This behaviour has been indicated by Figure 5.3 and Figure 5.4 which show simulated transient state results obtained for all the pressure sensors for a flow rate of 1 063 m^3/s plotted against time. For this discharge the readings did not fluctuate much, however, for some of the other discharges the fluctuations in the simulated results (shown in section 4.7) are clear. What was significant was that there were no upward or downward trends in the simulations, taking this and simulation run time concerns into account, all transient simulations conducted were done to a length of ten seconds.

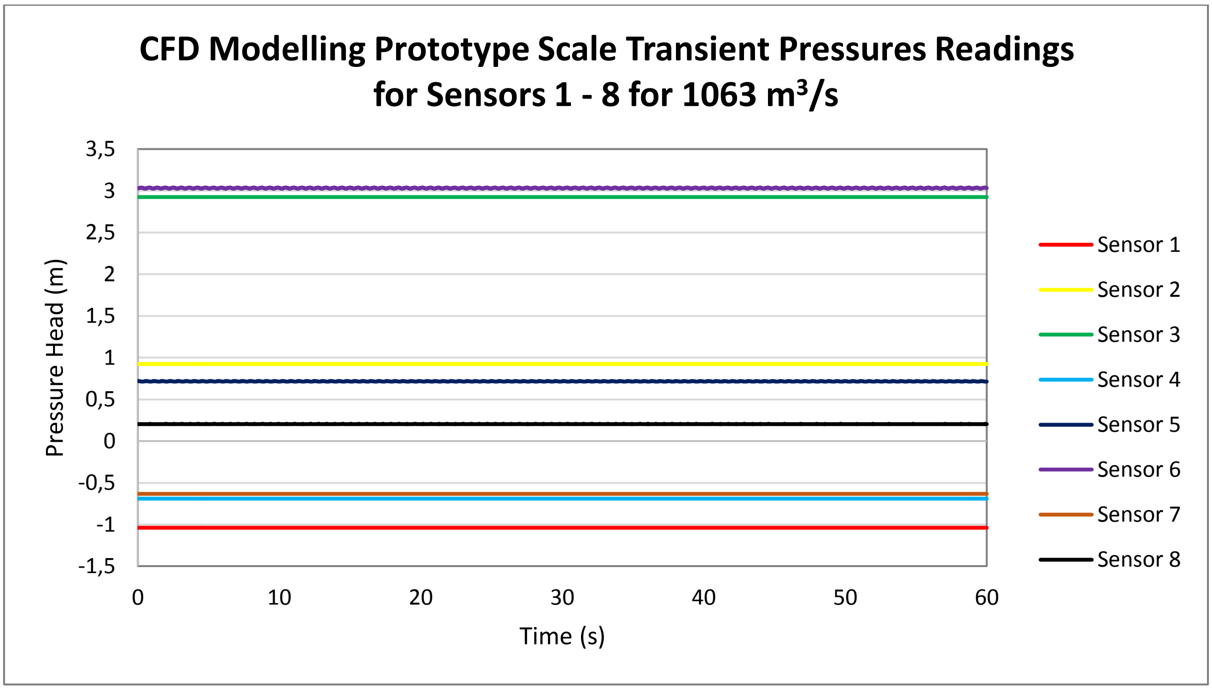

Figure 5.3 CFD modelling transient simulation results for sensors 1-8 for a flow rate of 1 063 m^3/s at the prototype scale

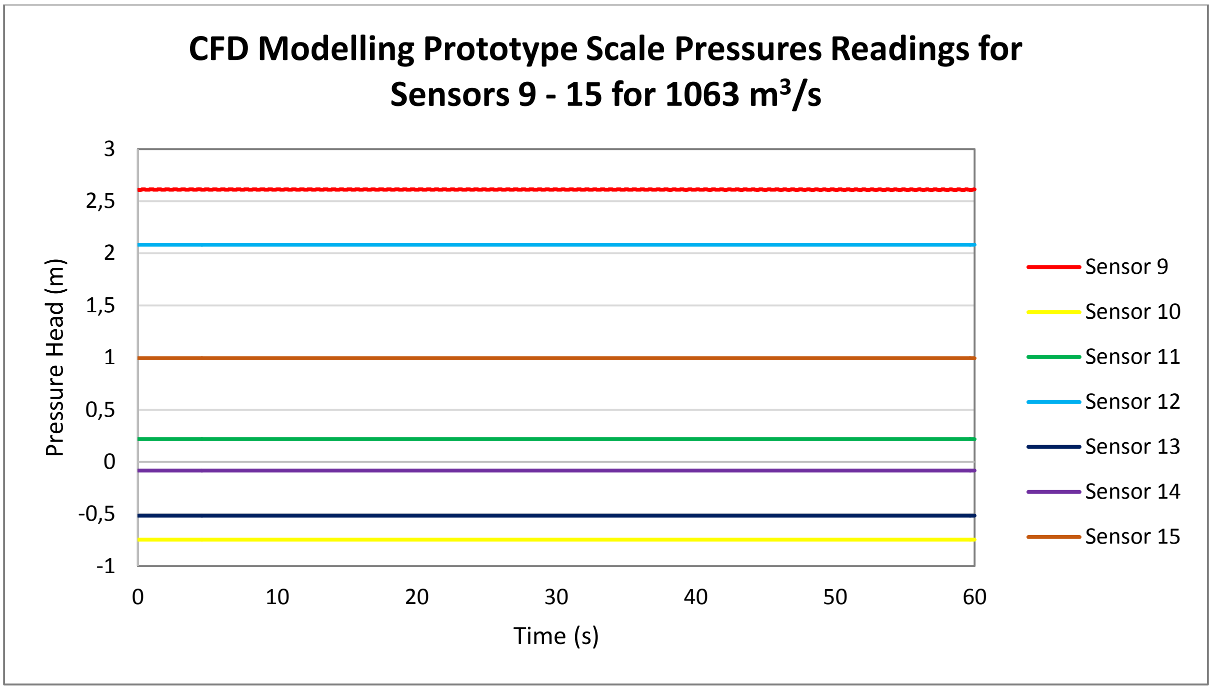

Figure 5.4 CFD modelling transient simulation results for sensors 9-15 for a flow rate of 1 063 m^3/s at the prototype scale

The results shown in Figure 5.3 and Figure 5.4 are for the purpose of determining the length of simulations required for the conducting of transient state CFD runs. It is interesting to note, however, that the sensors have recorded pressures that are both positive and negative as well as being within the outer limits of the physical modelling pressure results. The maximum and minimum pressures recorded for a flow rate of 1 063 m^3/s for the transient state simulations were 3.03 m and -1.04 m pressure head.

5.3.3. Meshes Used During Testing

The steady state tests ran with the model averaging 1 000 iterations per hour for a mesh with 923 990 nodes (Figure 5.5 and Figure 5.6). This speed was unfortunately not duplicated by the unsteady or transient model which took 20 days to complete a run of 12 seconds. This meant that a coarser mesh with 334 477 nodes (Figure 5.7 and Figure 5.8) was required to be used in order to achieve results within a reasonable time period. The minimum cell size specified for the 923 990 node mesh was 0.006 m, whilst this value was 0.02 m for the 334 477 node mesh. The minimum size of the smallest cell size in the mesh would be significantly smaller than this around the curves and corners of the mesh, however, across flat surfaces the mesh would adhere to this set limitation. Thus, one can expect a difference in results produced by the two meshes to differ by the same percentage as the cell sizes do – as it is known that a coarser mesh will be slightly less accurate than a fine mesh.

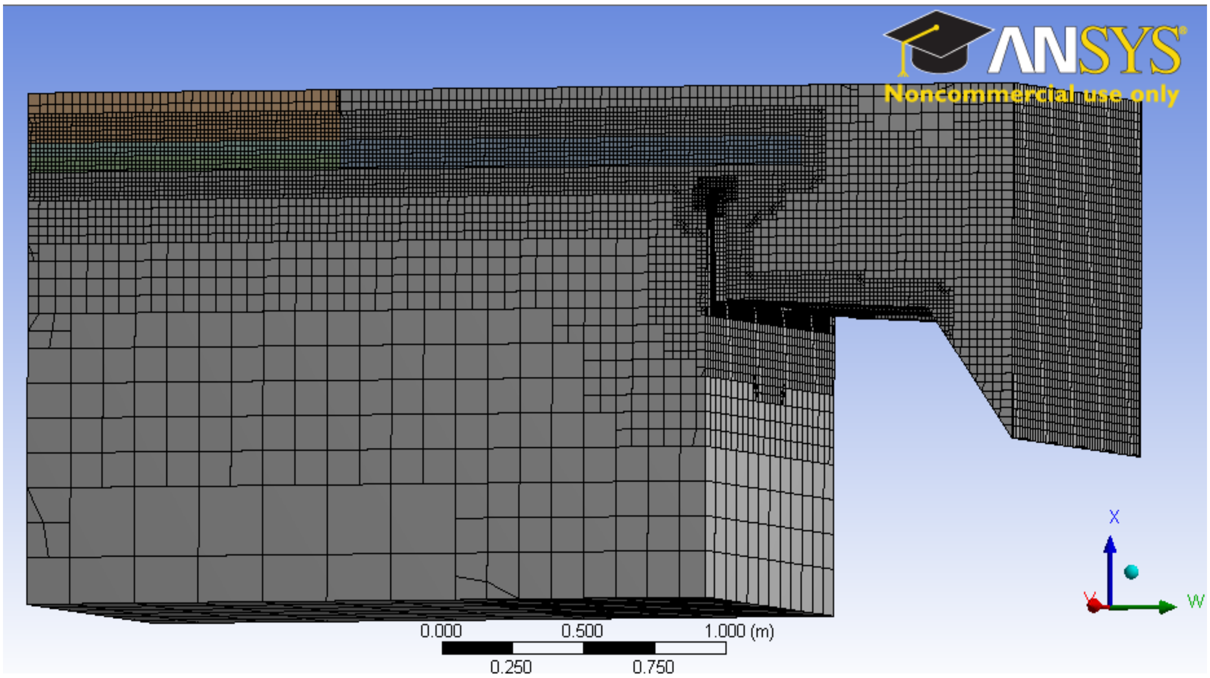

Figure 5.5 Cutcell mesh with 923 990 nodes used for steady state tests

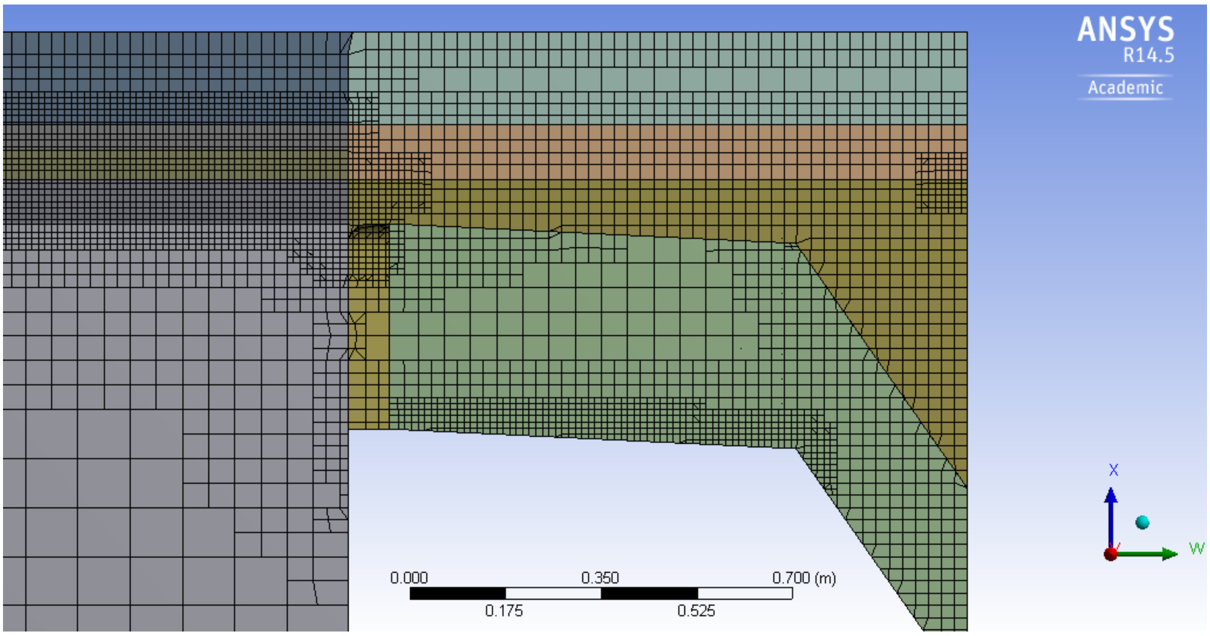

Figure 5.6 Crest of cutcell mesh with 923 990 nodes used for steady state tests

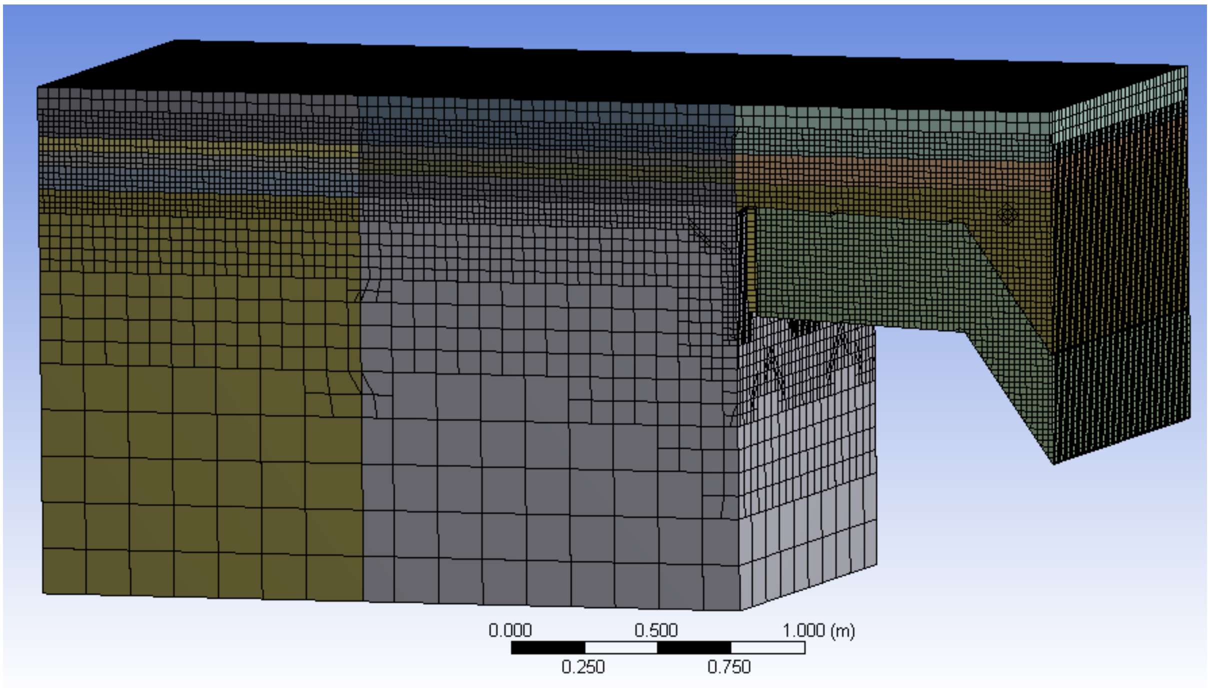

Figure 5.7 Coarse cutcell mesh with 334 477 nodes used for transient state tests

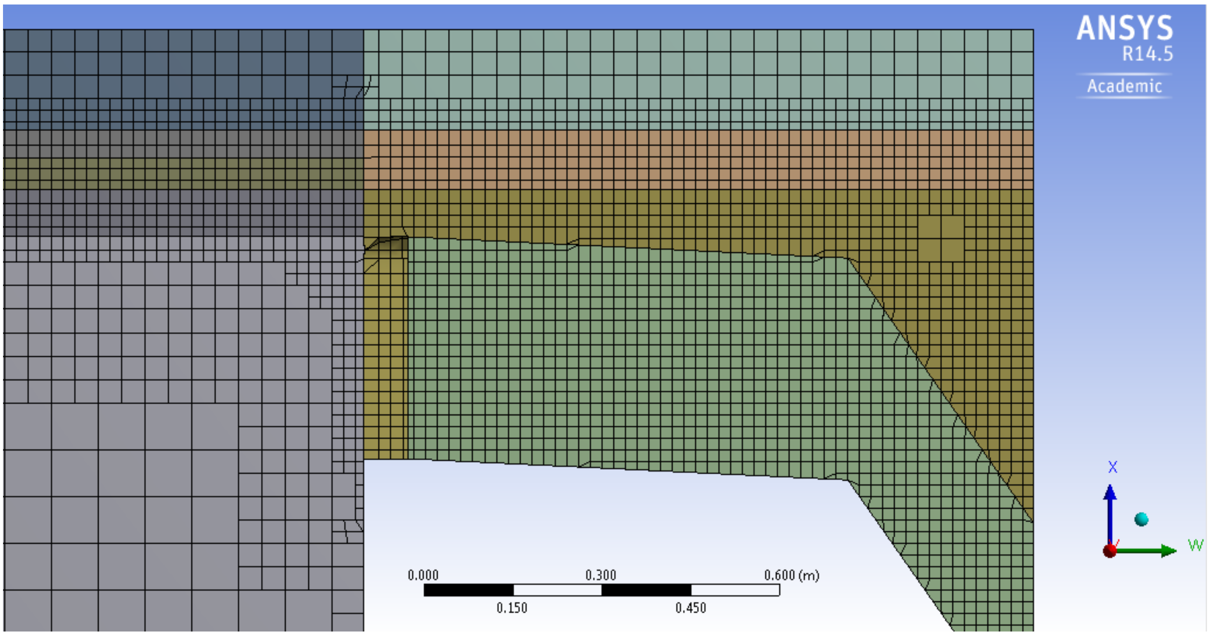

Figure 5.8 Crest of coarse cutcell mesh with 334 477 nodes used for transient state tests

Before they could be used for simulations the meshes had to meet quality requirements for orthogonal quality, where the minimum orthogonal quality had to be greater than 0.05 and skewness, where maximum skewness could not exceed 0.98. For both meshes these limits were adhered to. Additionally, it was important that the results produced by the coarse mesh correlated to those of the fine mesh for the transient simulations. Results obtained for both meshes and for two different flow rates (one low and one high) are presented in Figure 5.9, Figure 5.10, Figure 5.11 and Figure 5.12. The scales of these figures have been kept different to allow the reader to clearly see the detail on each graph.

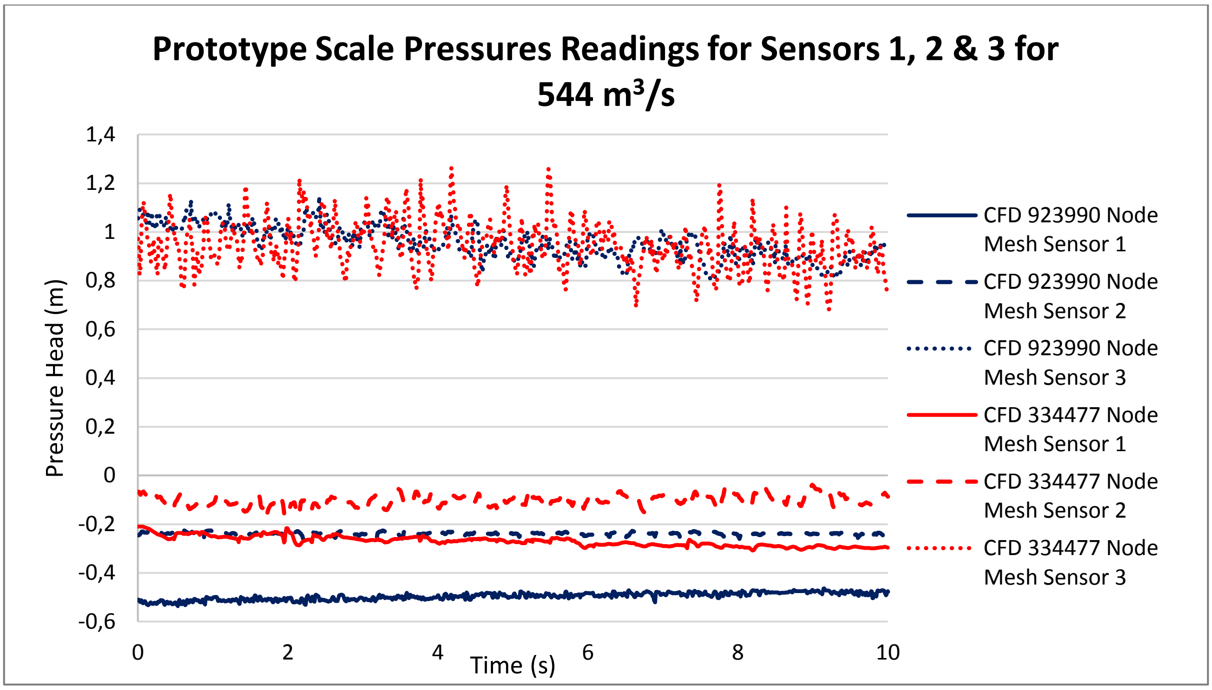

Figure 5.9 Transient test results for both 334 477 and 923 990 node meshes for sensors 1, 2 and 3 for a prototype flow rate of 544 m^3*/s*

What is important in these images is the similarity of the simulated results across the two meshes used. Figure 5.9 shows a good correlation between the meshes with the largest difference, equalling 0.31 m pressure head at the prototype scale (0.016 m pressure head at a scale of 1:20) being found at sensor 1. This difference is very similar to the difference between cell sizes of the two meshes.

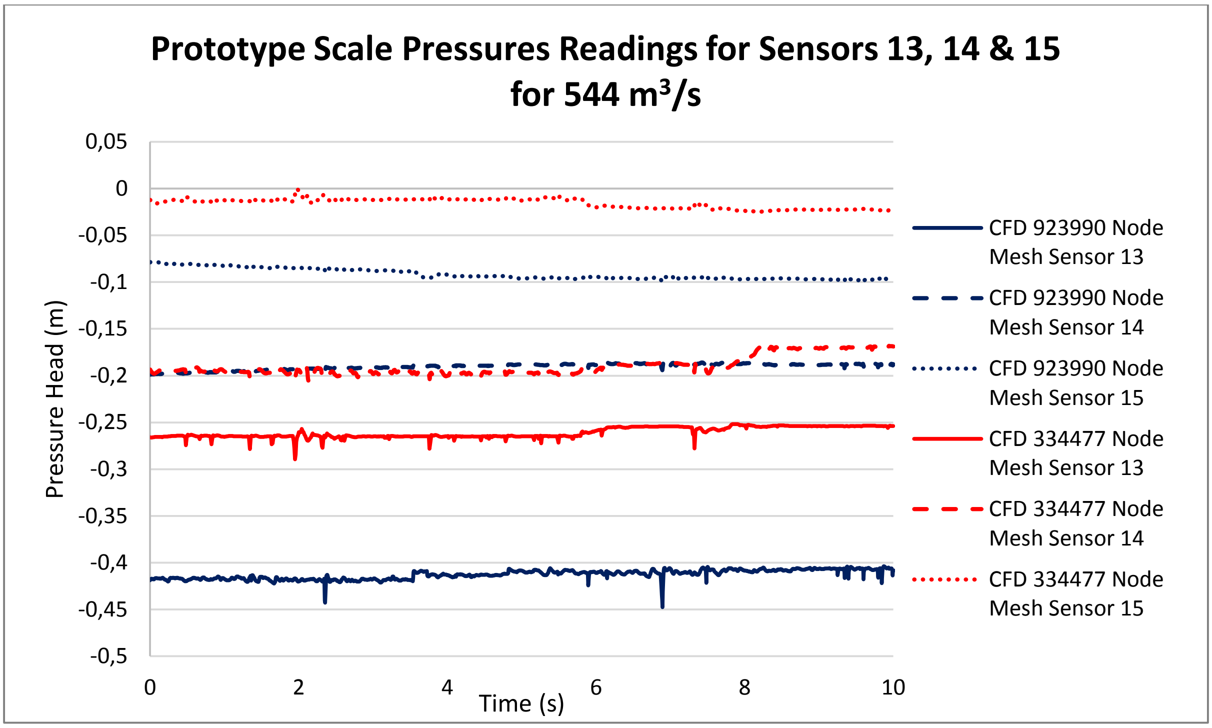

Figure 5.10 Transient test results for both 334 477 and 923 990 node meshes for sensors 13, 14 and 15 for a prototype flow rate of 544 m^3/s

Figure 5.10 indicates that for sensors 13, 14 and 15 the biggest difference found between the two meshes was 0.19 m at the prototype scale, on sensor 13. This again shows a minor difference between the two meshes.

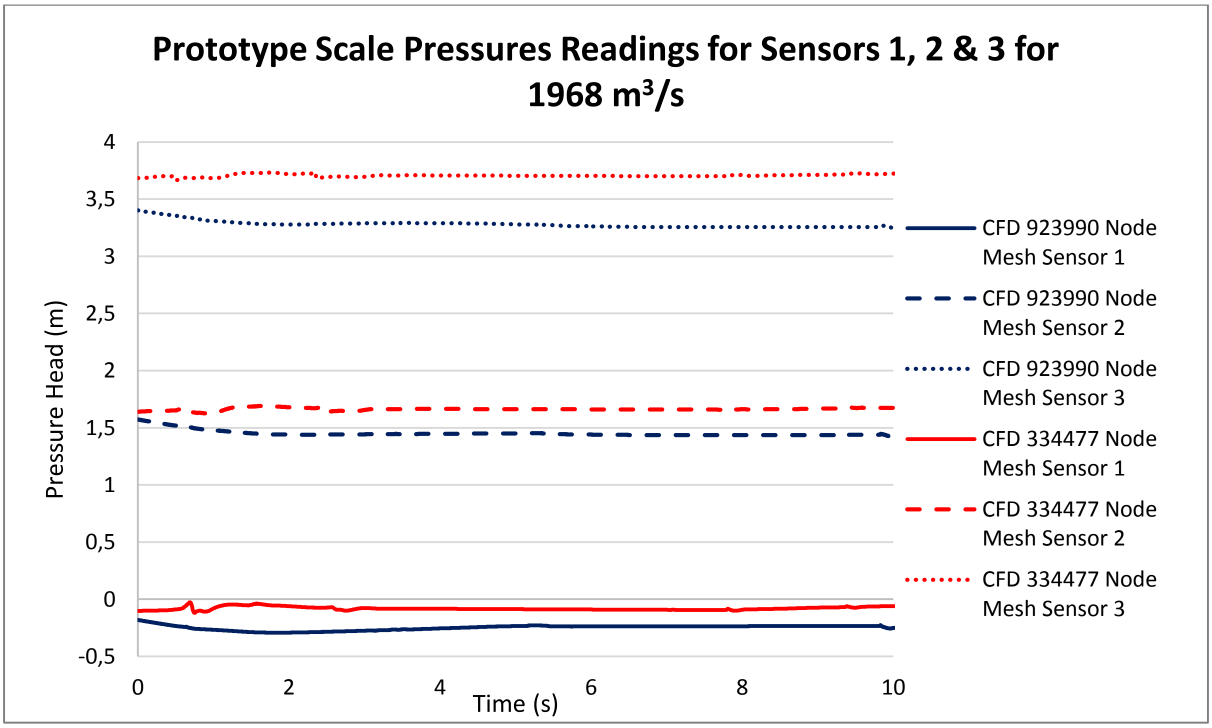

Figure 5.11 Transient test results for both 334 477 and 923 990 node meshes for sensors 1, 2 and 3 for a prototype flow rate of 1 968 m^3/s

For the larger flow rate of 1 968 m^3/s at the prototype scale, shown in Figure 5.11, the largest difference between the two meshes was 0.47 m pressure head found at sensor 3. At a scale of 1:20 this pressure head equals 0.023 m, which is only slightly more than the change in cell size between the two meshes.

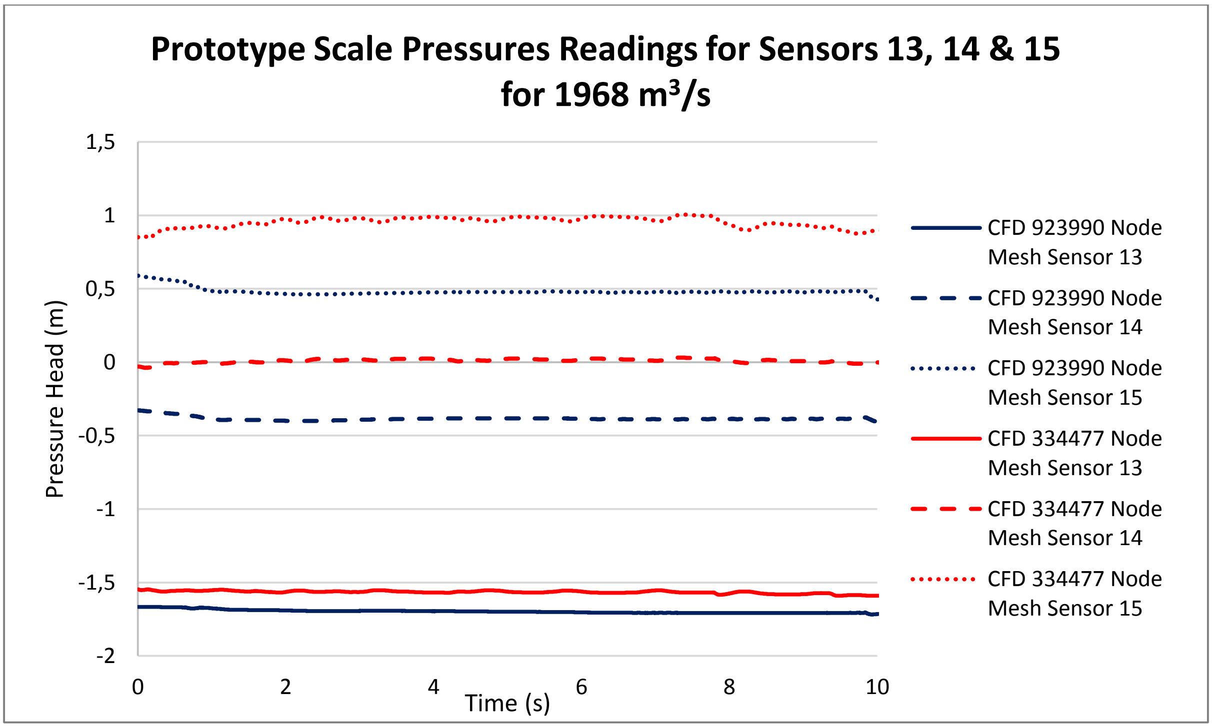

Figure 5.12 Transient test results for both 334 477 and 923 990 node meshes for sensors 13, 14 and 15 for a prototype flow rate of 1 968 m^3/s

Figure 5.12 shows that at sensor 15 there is a maximum difference of 0.53 m pressure head between the two meshes, which is 0.263 m pressure head at a scale of 1:20. This is, again, slightly more than the difference in cell size between the meshes, but is still a small difference.

Taking the differences in the minimum cell sizes between the two meshes into consideration the results produced by the coarse mesh were sufficiently close to those produced by the fine mesh for the coarse mesh to be used in all of the transient simulations conducted.

5.3.4. Steady State vs. Transient Solutions

To compare the results from the steady state to the transient solutions, graphs were plotted with the average steady state value plotted against the recorded transient state values. Additionally, both sets of pressure results were also averaged and these values are displayed in the following section.

The transient model uses the “Geo-reconstruct” method as the interpolation method for cells which are partially filled with the two phases (water and air). This method uses a piecewise-linear approach to reconstruct the interface that exists between the two phases, assuming a linear slope for the interface.

This shape is then used for the calculations of the movement of fluid through the cells (ANSYS Inc., 2009). The steady state model uses the "Least Squares Cell Based" method.

5.4. Discussion of Results

5.4.1. Flow Development

The development of flow is an important part of CFD modelling as it ensures the user that the flow matched the conditions that would have been experienced in the laboratory. Figure 5.13 and Figure 5.14, included below, indicate cross sections through the simulated behaviour of the flow.

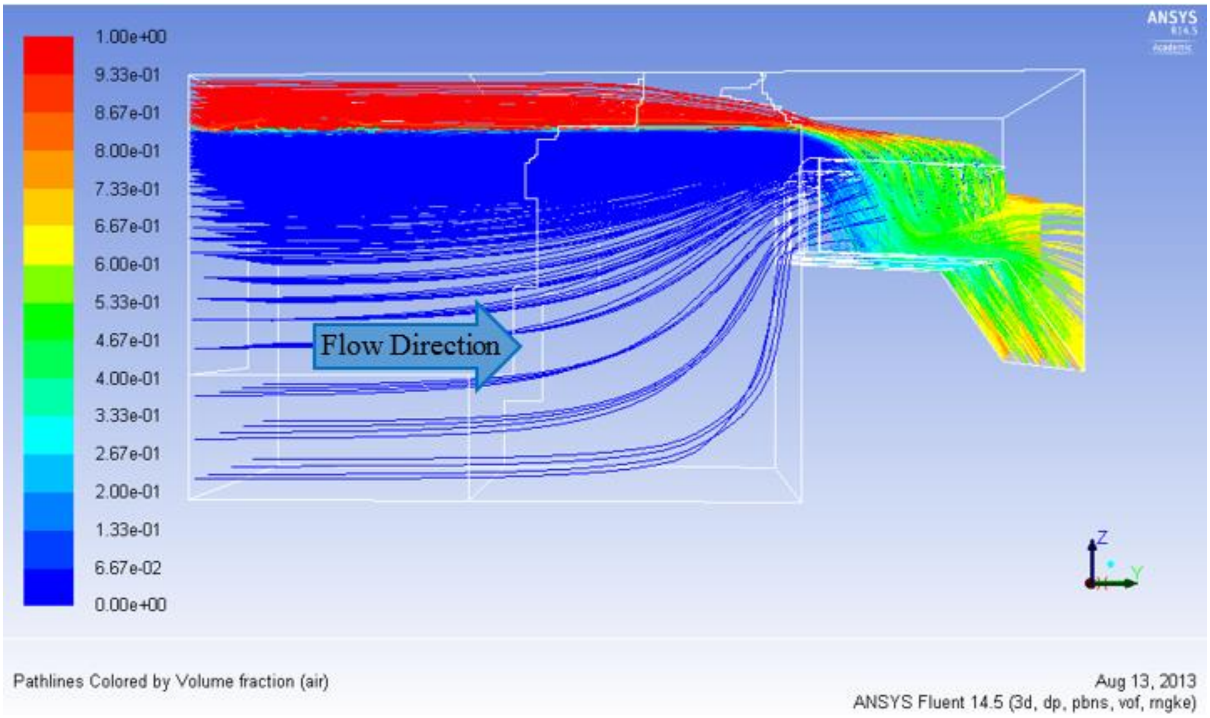

Figure 5.13 Simulated CFD pathlines of particles for 1 063 m^3/s coloured by volume fraction of air

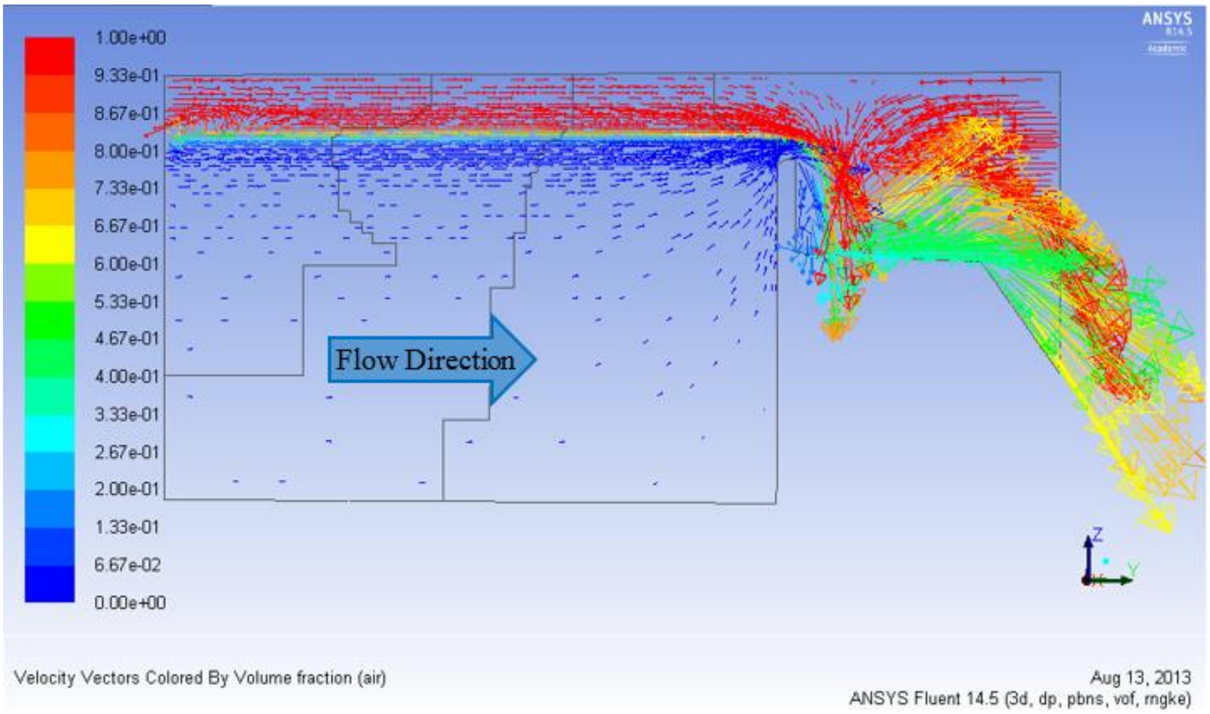

Figure 5.14 Simulated CFD vector arrows for 544 m^3/s showing flow and air velocities, coloured by volume fraction of air

The pathlines traced in Figure 5.13 show that particles of flow move from the inlet to the outlet without changing course along the way, forming vortices or behaving in any unexpected manner. The velocity arrows in Figure 5.14, show that the flow speed nearer the water surface exceeds that of the water near the base of the model. This is an important factor as the flow enters the inlet at a speed that is consistent in the z-direction, thus, the pattern needs to change this in order to simulate the flow as it would behave in a channel or in the physical model.

The flow patterns over the weir are also significant, as are the aeration conditions. Figure 5.15 and Figure 5.16 indicate the flow behaviour and aeration for both the physical model and the CFD model for high flow conditions.

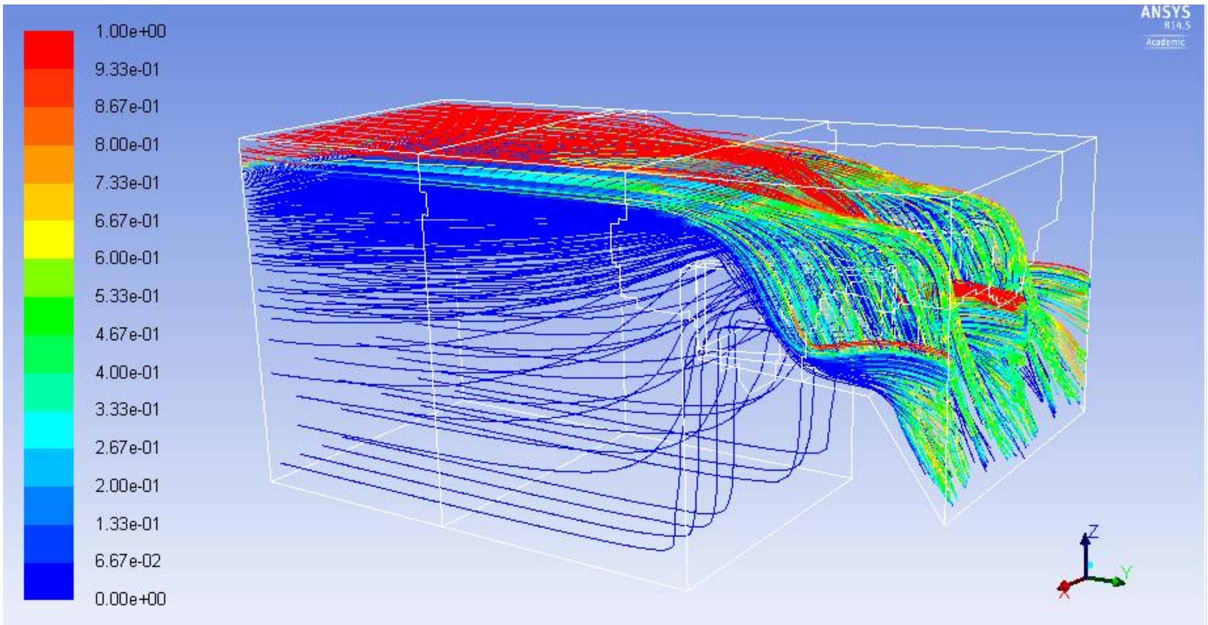

Figure 5.15 Simulated CFD flow pathlines for 1 606 m^3/s coloured by the volume fraction of air

Figure 5.16 Physical model aeration and flow behaviour under high discharge conditions 1 606 m^3/s (450 l/s at a scale of 1:20)

Based on visual assessment the water profile, flow patterns and aeration over the weir and immediately downstream of the weir were similar in the physical model (Figure 5.16) and the simulated results produced through CFD (Figure 5.15). It is noted, however, that the model does not appear to display separation of the nappe from the downstream face of the weir (Figure 5.21, Figure 5.22 and Figure 5.23). This might, however, be attributed to the larger cell sizes that were used to reduce computer time, as mentioned in section 5.3.3.

It was also important to consider that the behaviour of the water flow patterns and aeration would vary with discharge. Figure 5.17 and Figure 5.18 show the aeration and flow patterns of the weir for low flow conditions.

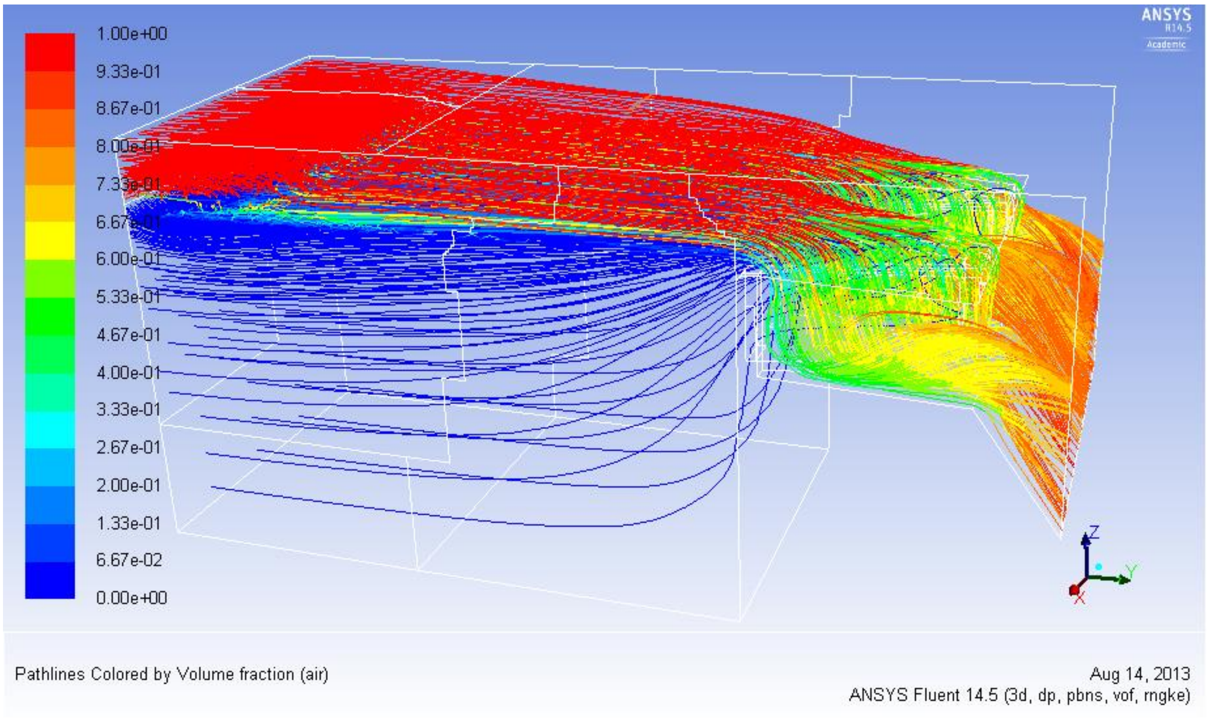

Figure 5.17 Simulated CFD flow pathlines for 544 m^3*/s coloured by the volume fraction of air*

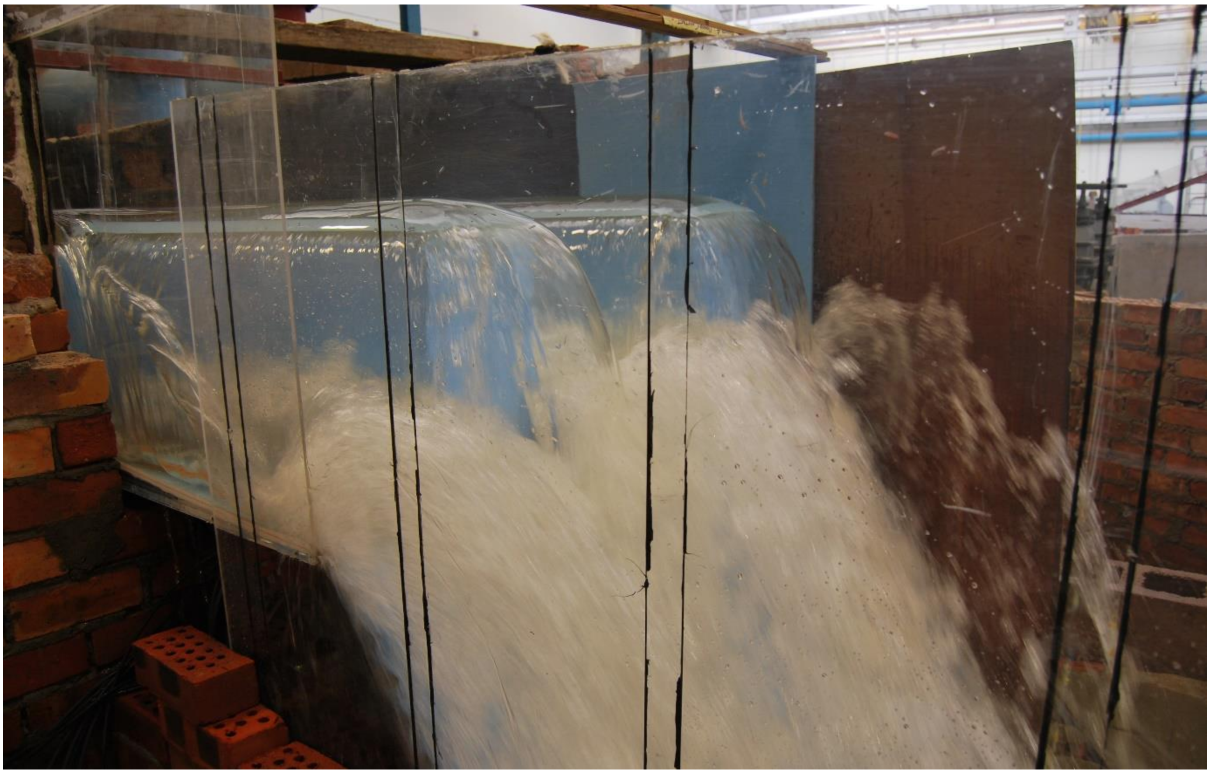

Figure 5.18 Physical model aeration and flow behaviour under low discharge conditions of 544 m^3*/s (153 l/s at a scale of 1:20)*

Figure 5.17 and Figure 5.18 show that the simulated and actual flow behaviour of the labyrinth weir are similar for low flow conditions. What is immediately apparent is the way in which the water behaves downstream of the labyrinth crest, this is consistent across both images.

In order to view the behaviour of the flow as it enters the weir and the manner in which it moves over the crest, Figure 5.19 and Figure 5.20 have been included for a medium discharge value. These images are taken from above the weir.

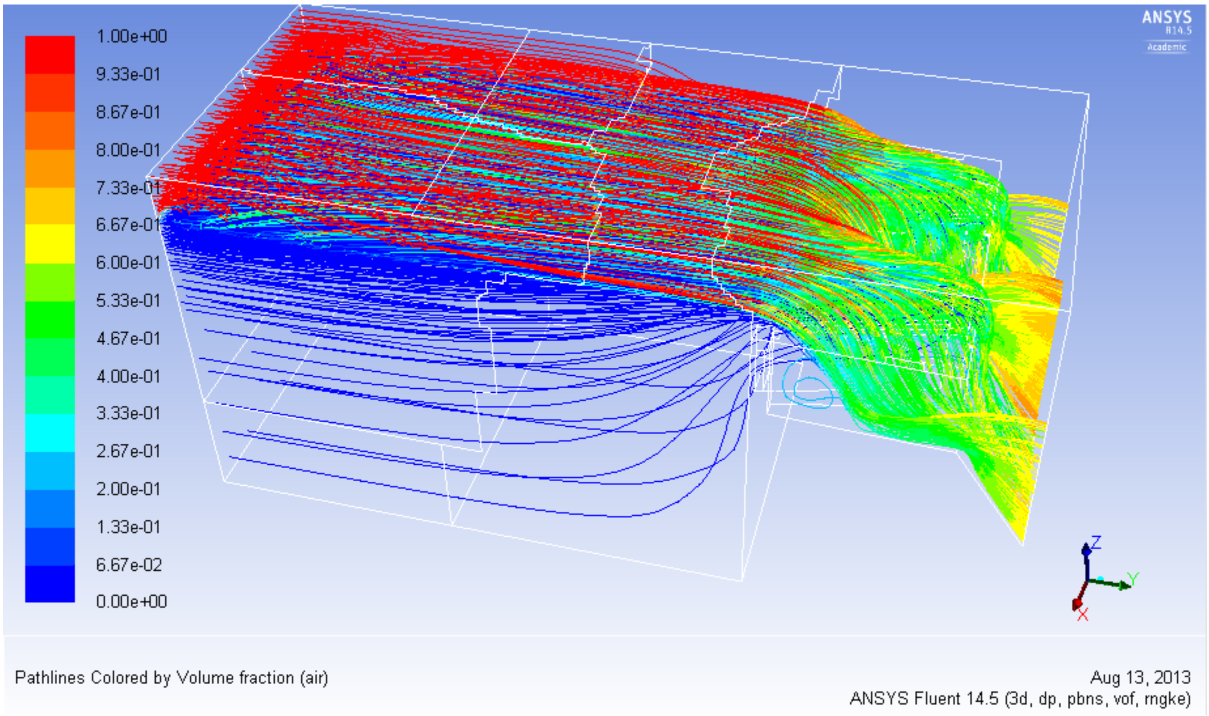

Figure 5.19 Simulated CFD flow pathlines for 1 063 m^3*/s, viewed from above and coloured by the volume fraction of air*

Figure 5.20 Physical model aeration and flow behaviour under medium discharge conditions of 1 063 m^3/s (297 l/s at a scale of 1:20)

The 3D nature of the flow patterns of a labyrinth weir are made clear when looking at the weir from above. The simulated flow patterns, shown in Figure 5.19, clearly indicate the flow directions over the weir. These accurately represent the patterns seen during physical testing, as shown in Figure 5.20.

These images (Figure 5.19 and Figure 5.20) as well as the previous images (Figure 5.15, Figure 5.16, Figure 5.17 and Figure 5.18) indicate that the flow behaviour and aeration are consistent for both the physical model and the CFD model.

5.4.2. Water Depths (Surcharge)

A key result during the running of CFD simulations was the flow level upstream of the crest. This was important as it gave credibility to the set-up used for the model and showed that the flow was behaving in a way that corresponded with the physical model and depths determined through analytical calculations. The CFD model is able to produce visuals of the phases present on cross section planes. Figure 5.21, Figure 5.22 and Figure 5.23 show cross sections through different parts of the model, under various flow conditions indicating the different water levels. The images are coloured by the volume fraction of air, with red being 100% air and blue being 0% – indicating water. Included in Figure 5.24 are the water depths determined through CFD modelling plotted against those determined through physical modelling.

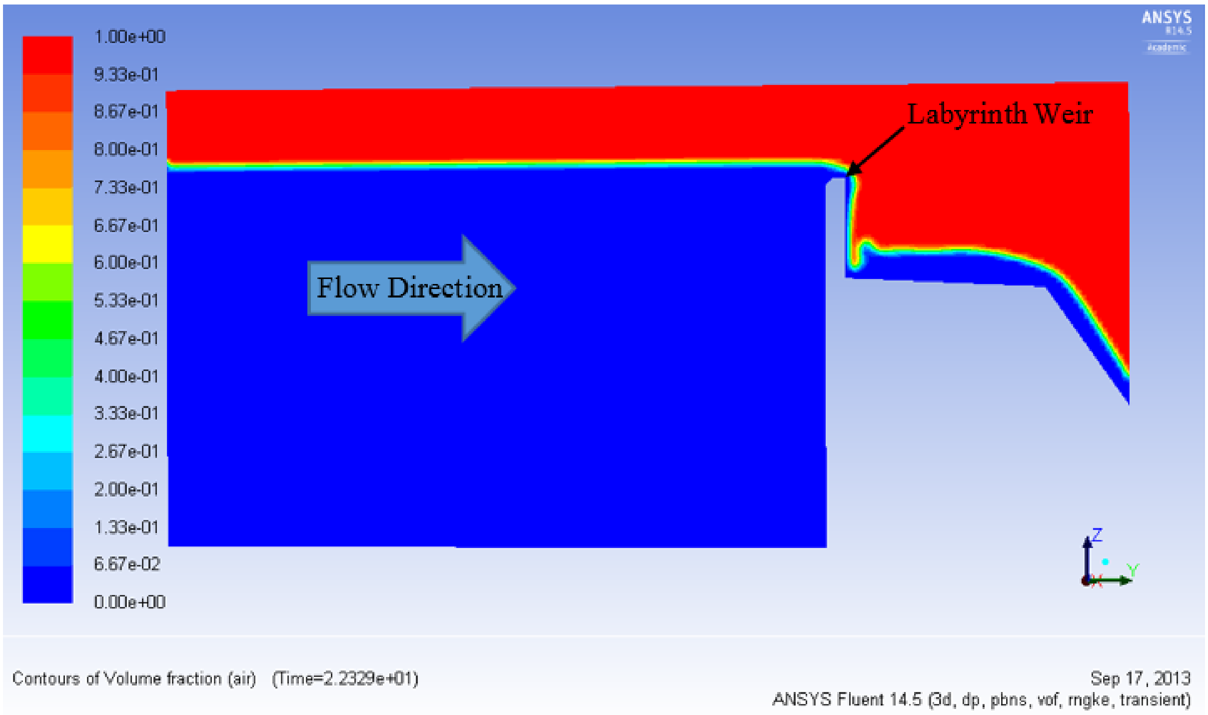

Figure 5.21 Contours of phases through model centreline for 361 m^3/s, coloured by volume fraction of air

Figure 5.21 shows the phases of the CFD model during a low flow simulation. The blue area represents water, the red area represents air and everything in between represents the transition area. On advice from ANSYS support staff the water depths were measured at 0.5 volume fraction of air. Figure 5.21 also indicates the position of the weir when the cross section is taken through the centreline. Figure 5.22 shows the position of the weir when the cross section is taken one third of the way across the model, as a result of this positioning it is possible to see the effects of the water flowing over the crest, upstream of this point, on the water level.

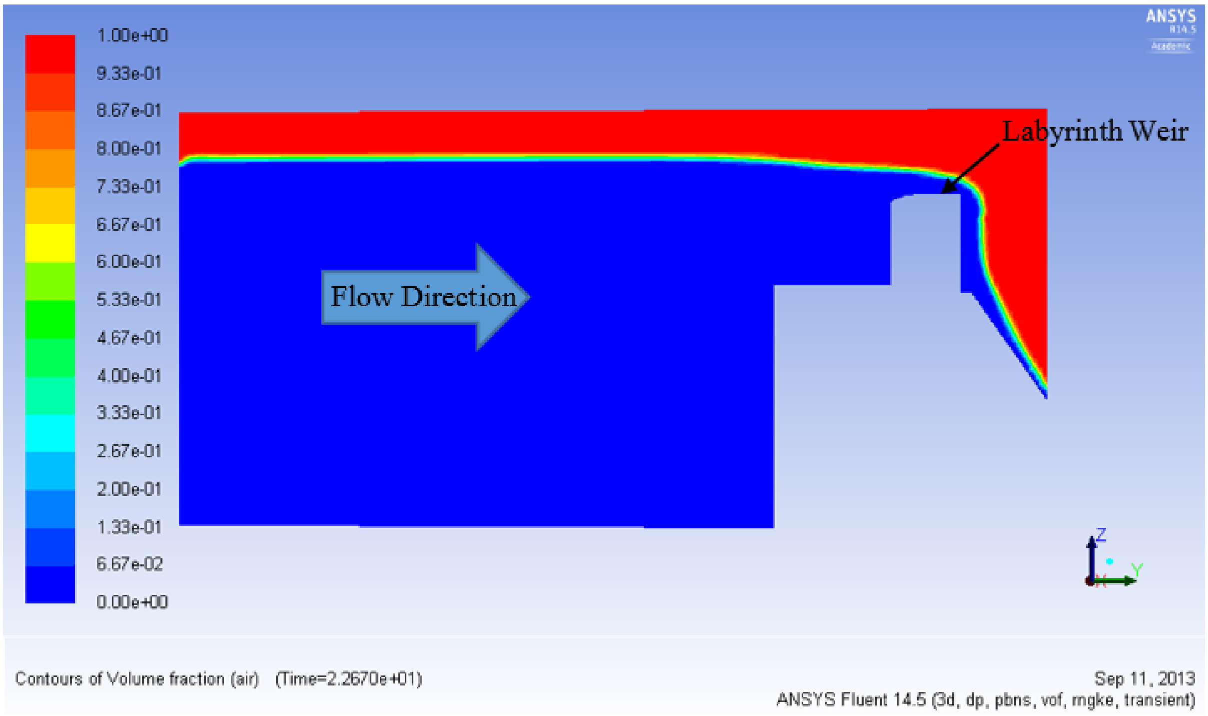

Figure 5.22 Contours of phases on cross section one third of the way through the model for 1 249 m^3/s, coloured by volume fraction of air

Figure 5.22 shows the cross section for a medium flow rate and it is evident that the water level is higher than it is in Figure 5.21 and lower than Figure 5.23, which shows a cross section for high flows.

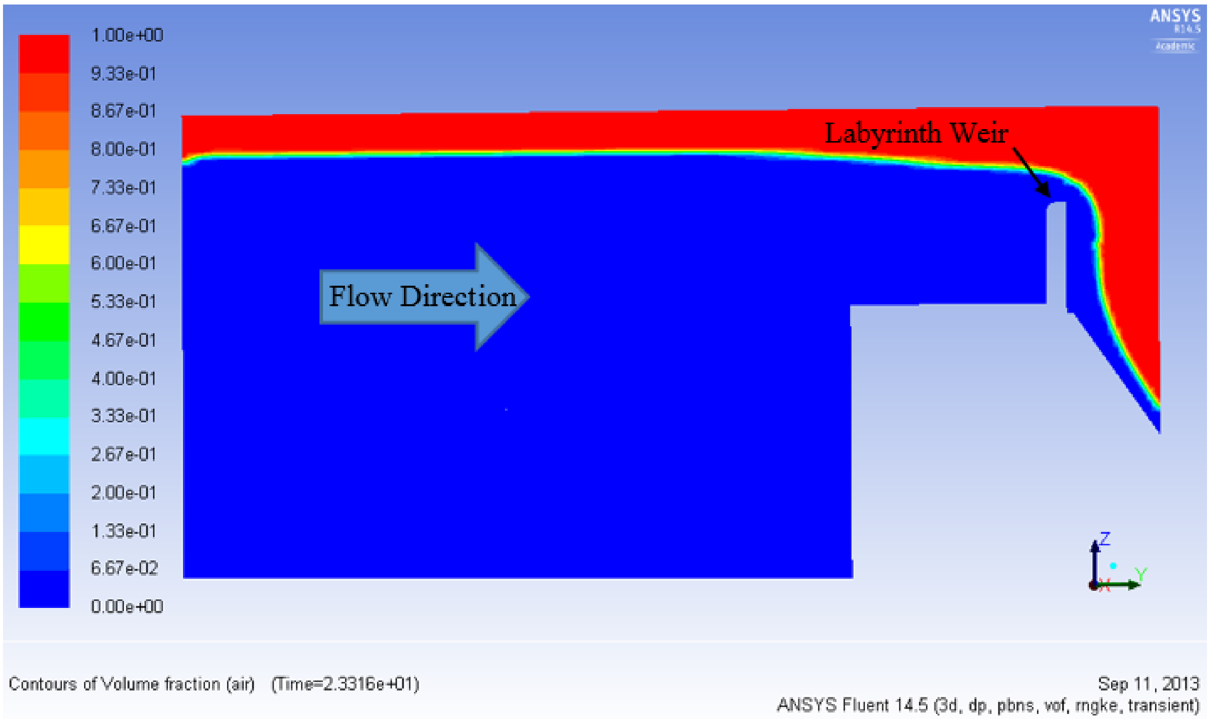

Figure 5.23 Contours of phases on cross section one quarter of the way through the model for 1 606 m^3/s, coloured by volume fraction of air

Figure 5.23 is a cross section one quarter of the way through the CFD model and shows a high discharge level. In this image the section is through the downstream apex of the crest and the drawdown effect of the water flowing over the crest before reaching the downstream apex is clearly evident as the level drops.

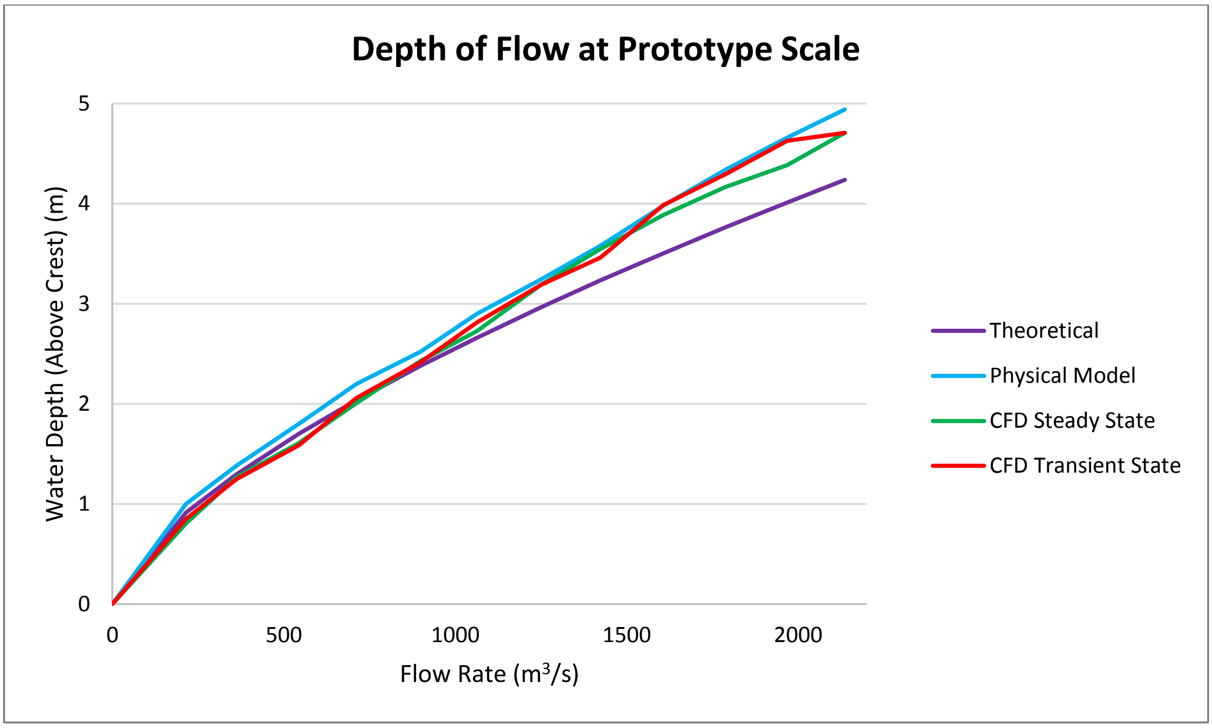

Figure 5.24 Physical modelling, CFD and theoretical water depths above the crest, measured 1.5 m upstream of the weir

The results presented above in Figure 5.24 show that the water depths as predicted by the CFD model simulations were similar to those determined through physical modelling.

For the lower flow rates, until approximately 1 200 m^3/s, the water depths as predicted through physical modelling are the highest, although the various methods are all similar. There is some divergence of the results as the flow increases above 1 200 m^3/s, with the theoretical and physical modelling results being the most different.

Whilst there was some slight difference between the physical modelling results and the CFD results before the flow increases above 1 000 m^3/s, after this point the results were very similar until the peak discharge was tested. The maximum distance between the transient state and physical modelling data sets is 0.233 m, which is 12 mm at a scale of 1:20 (which was measured with an accuracy of 1 mm), at a flow rate of 2 136 m^3/s. The steady state data and the physical modelling results were also closely matched with the maximum distance between the two found to be 0.273 m at a flow rate of 1 968 m^3/s at the prototype scale, 14 mm at a scale of 1:20. The steady and transient state simulations produced very similar surcharge results with the largest difference between water depths above the crest equalling

0.240 m at a flow rate of 1 968 m^3/s at the prototype scale. This difference is equal to 12 mm at a scale of 1:20 and is less than the difference between the cell sizes of the meshes.

5.4.3. Pressure Results

Presented in the following tables (Table 5.1 and Table 5.2) are the simulated pressure results for each of the 15 monitors included in the CFD model, for both steady state and transient (respectively) simulations. Table 5.3 shows the ratio of transient state to steady state average pressure results.

The steady state pressure results were determined through the average pressures recorded at each of the 15 monitors over a stable period of 2 000 iterations, while the average transient pressure results were determined through an averaging of the simulated pressures recorded over the run time of ten seconds.

Table 5.1 CFD modelling simulated steady state pressure results

Flow Rate (m^3/s)	**CFD Modelling: Steady State Pressure Readings at Prototype Scale (By Sensor in m Pressure Head)**														
	1	**2**	**3**	**4**	**5**	**6**	**7**	**8**	**9**	**10**	**11**	**12**	**13**	**14**	**15**
0	0	0	0	0	0	0	0	0	0	0	0	0	0	0	0
215	0.02	0.28	0.87	0.07	0.05	0.29	0.08	0.10	0.37	0.07	0.08	0.22	-0.01	-0.02	-0.02
361	-0.08	0.42	1.64	0.11	0.18	0.29	0.27	0.18	-0.25	0.27	0.68	-0.21	0.00	-0.01	0.00
544	-0.51	0.73	2.39	0.09	0.16	0.98	-0.05	0.09	0.82	-0.20	0.16	0.93	-0.05	0.07	0.12
712	-0.61	0.99	2.83	-0.03	1.15	2.89	-0.28	0.80	2.55	-0.54	0.70	2.11	-0.33	0.24	0.38
898	-0.43	0.92	2.80	-0.21	1.16	2.47	-0.80	1.09	2.60	-0.96	0.76	2.17	-0.71	0.31	0.62
1063	0.15	1.38	2.95	-0.48	1.13	2.58	-1.19	1.67	3.29	-1.56	1.25	2.88	-0.95	0.26	0.84
1249	0.52	1.66	3.15	-0.55	1.05	2.54	-1.11	1.85	3.64	-1.71	1.40	3.00	-1.12	0.25	0.95
1424	0.70	1.75	3.32	-0.80	0.85	2.39	-1.99	1.97	3.92	-2.39	1.46	3.51	-1.48	0.05	0.43
1606	0.78	1.87	3.48	-0.93	0.74	2.30	-2.45	1.92	4.04	-2.74	1.47	3.80	-1.62	-0.16	0.12
1789	0.96	2.01	3.71	-0.90	0.77	2.09	-2.85	1.80	3.76	-3.11	1.49	4.10	-1.70	-0.36	-0.14
1968	0.04	1.44	3.18	-0.89	0.76	2.14	-2.48	0.64	3.37	-2.87	0.74	3.82	-1.66	-0.52	-0.29
2136	1.06	2.23	3.98	-0.94	0.62	2.09	-3.38	1.53	3.53	-3.62	1.45	4.52	-1.81	-0.69	-0.42

Table 5.1 lists all of average steady state pressure results for all flow rates simulated. The results show that negative pressures existed at sensors 1, 4, 7, 9, 10, 12, 13, 14 and 15 for some of the discharges simulated. The highest average pressure recorded was found to be 4.52 m pressure head at a flow rate of 2 136 m^3/s at the prototype scale at sensor 12. The lowest pressure recorded was -3.62 m pressure head, also at a flow rate of 2 136 m^3/s at sensor 10.

Table 5.2 CFD modelling simulated transient pressure results

Flow Rate (m^3/s)	**CFD Modelling: Transient State Pressure Readings at Prototype Scale (By Sensor in m Pressure Head)**														
	1	**2**	**3**	**4**	**5**	**6**	**7**	**8**	**9**	**10**	**11**	**12**	**13**	**14**	**15**
0	0	0	0	0	0	0	0	0	0	0	0	0	0	0	0
215	-0.06	-0.07	0.09	0.06	-0.05	0.06	-0.08	-0.05	0.04	-0.08	-0.04	0.00	-0.03	-0.01	-0.01
361	-0.13	-0.09	0.34	-0.17	-0.10	0.36	-0.08	-0.11	0.23	-0.14	-0.11	0.05	-0.23	-0.03	-0.01
544	-0.27	-0.10	0.95	-0.18	-0.09	0.61	-0.01	-0.07	0.46	-0.08	-0.06	0.13	-0.26	-0.19	-0.02
712	-1.40	0.52	2.33	-0.19	-0.13	0.54	-0.07	-0.04	1.01	-0.10	-0.08	0.62	-0.31	-0.15	-0.05
898	-1.59	0.63	2.85	-0.27	-0.17	1.25	-0.35	-0.07	0.58	-0.40	0.00	0.94	-0.29	-0.25	0.36
1063	-1.04	0.92	2.93	-0.69	0.72	3.03	-0.63	0.20	2.61	-0.75	0.22	2.08	-0.52	-0.08	0.99
1249	-0.67	1.23	3.22	-0.93	1.00	2.99	-1.02	1.08	3.62	-1.10	0.90	3.14	-0.96	0.25	1.43
1424	-0.49	1.37	3.38	-1.13	1.00	2.92	-1.31	1.44	3.46	-1.30	1.08	3.10	-1.32	0.53	1.66
1606	-0.38	1.44	3.46	-1.27	0.95	2.87	-1.53	1.32	3.40	-1.48	0.91	2.79	-1.43	0.43	1.44
1789	-0.24	1.55	3.59	-1.38	0.93	2.86	-1.72	1.07	3.39	-1.60	0.62	2.66	-1.49	0.19	1.18
1968	-0.08	1.66	3.71	-1.43	0.87	2.80	-1.92	0.98	3.36	-1.73	0.48	2.81	-1.56	0.01	0.95
2136	0.00	1.73	3.78	-1.45	0.86	2.80	-2.10	0.91	3.29	-1.89	0.34	2.93	-1.66	-0.15	0.74

Table 5.2 lists all of average transient state pressure results for all flow rates simulated. The results show that negative pressures existed at sensors 1, 2, 4, 5, 7, 8, 10, 11, 12, 14 and 15 for some of the discharges simulated. The highest average pressure recorded was found to be 3.78 m pressure head at a flow rate of 2 136 m^3/s at the prototype scale at sensor 3. The lowest pressure recorded was -2.10 m pressure head, also at a flow rate of 2 136 m^3/s at sensor 7. To compare the transient and steady average simulated pressures Table 5.3 includes the ratio of transient to steady state pressure readings obtained.

Table 5.3 Ratio of CFD modelling simulated transient pressures to steady state pressure results

Flow Rate (m^3/s)	**CFD Modelling: Ratio of Transient Over Steady State Average Pressure Readings at Prototype Scale (By Sensor in m Pressure Head)**														
	1	**2**	**3**	**4**	**5**	**6**	**7**	**8**	**9**	**10**	**11**	**12**	**13**	**14**	**15**
0	0	0	0	0	0	0	0	0	0	0	0	0	0	0	0
215	-3.0	-0.3	0.1	0.9	-1.0	0.2	-1.0	-0.5	0.1	-1.1	-0.5	0.0	3.0	0.5	0.5
361	1.6	-0.2	0.2	-1.5	-0.6	1.2	-0.3	-0.6	-0.9	-0.5	-0.2	-0.2	-	3.0	-
544	0.5	-0.1	0.4	-2.0	-0.6	0.6	0.2	-0.8	0.6	0.4	-0.4	0.1	5.2	-2.7	-0.2
712	2.3	0.5	0.8	6.3	-0.1	0.2	0.3	-0.1	0.4	0.2	-0.1	0.3	0.9	-0.6	-0.1
898	3.7	0.7	1.0	1.3	-0.1	0.5	0.4	-0.1	0.2	0.4	0.0	0.4	0.4	-0.8	0.6
1063	-6.9	0.7	1.0	1.4	0.6	1.2	0.5	0.1	0.8	0.5	0.2	0.7	0.5	-0.3	1.2
1249	-1.3	0.7	1.0	1.7	1.0	1.2	0.9	0.6	1.0	0.6	0.6	1.0	0.9	1.0	1.5
1424	-0.7	0.8	1.0	1.4	1.2	1.2	0.7	0.7	0.9	0.5	0.7	0.9	0.9	10.6	3.9
1606	-0.5	0.8	1.0	1.4	1.3	1.2	0.6	0.7	0.8	0.5	0.6	0.7	0.9	-2.7	12.0
1789	-0.3	0.8	1.0	1.5	1.2	1.4	0.6	0.6	0.9	0.5	0.4	0.6	0.9	-0.5	-8.4
1968	-2.0	1.2	1.2	1.6	1.1	1.3	0.8	1.5	1.0	0.6	0.6	0.7	0.9	0.0	-3.3
2136	0.0	0.8	0.9	1.5	1.4	1.3	0.6	0.6	0.9	0.5	0.2	0.6	0.9	0.2	-1.8

(“-“ denotes a division by 0 error)

In Table 5.3, above, the ratios of transient state to steady state simulated average pressure results are, for some of the senses, found to equal or be close to the desired value of one. However, many values (73%) differ from 1 by more than 0.2 indicating a lack of correlation between the steady state and transient methods in most of the sensors. It should be noted, however, that the numerical value of these numbers are small. Relatively minor differences in absolute values can, therefore, result in unacceptable ratio values.

Figure 5.25, Figure 5.26 and Figure 5.27 indicate the difference between steady and transient state simulation results in graphical form and present a picture that differs from that of Table 5.3. Specific results from chosen sensors have been presented as these give a good indication of the range of all of the results recorded, whilst the full results have been included in Appendix D.

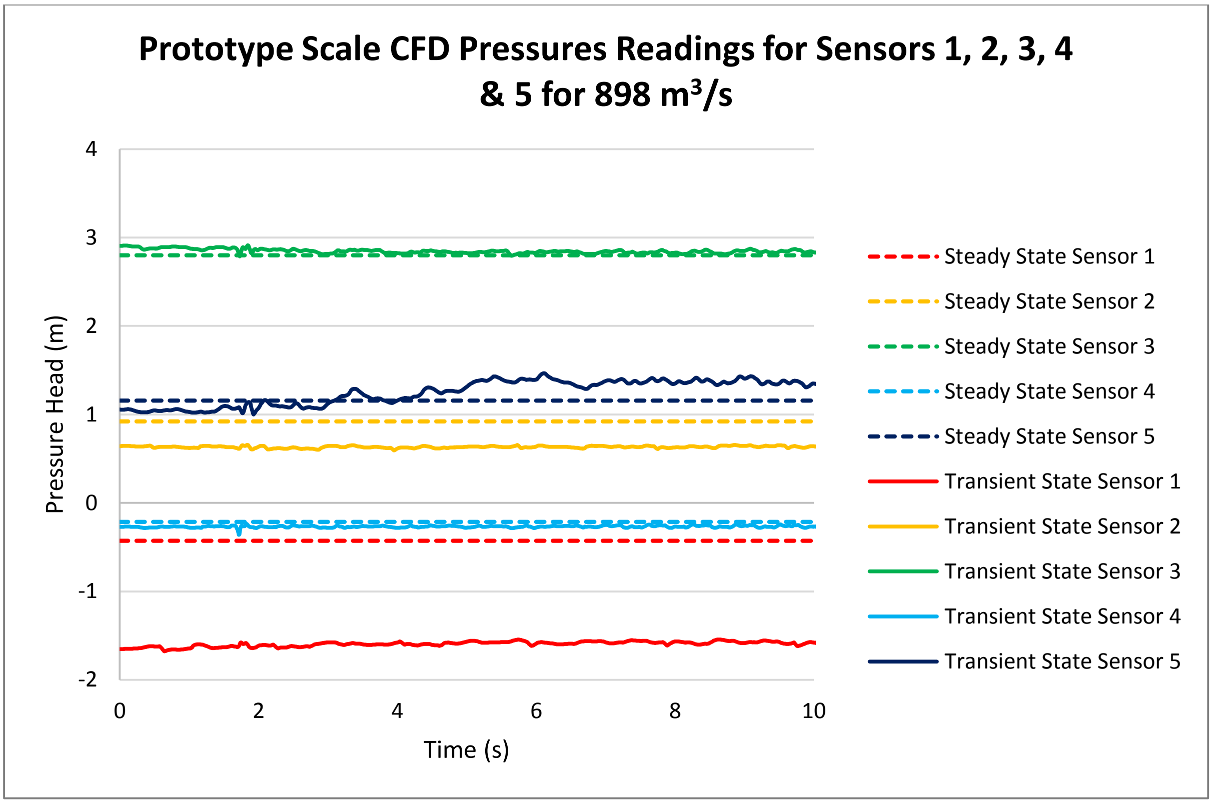

Figure 5.25 Comparison between simulated transient and steady state models pressure simulators for sensors 1,2,3,4 & 5 for a flow rate of 898 m^3/s

The above image, Figure 5.25, shows that for a flow rate of 898 m^3/s at the prototype scale the steady state and transient state readings mostly corresponded well. Sensors 1, 2, 3 and 4 were all very similar between the two states, whilst sensor 5 had a larger difference of approximately 1.23 m at the prototype scale.

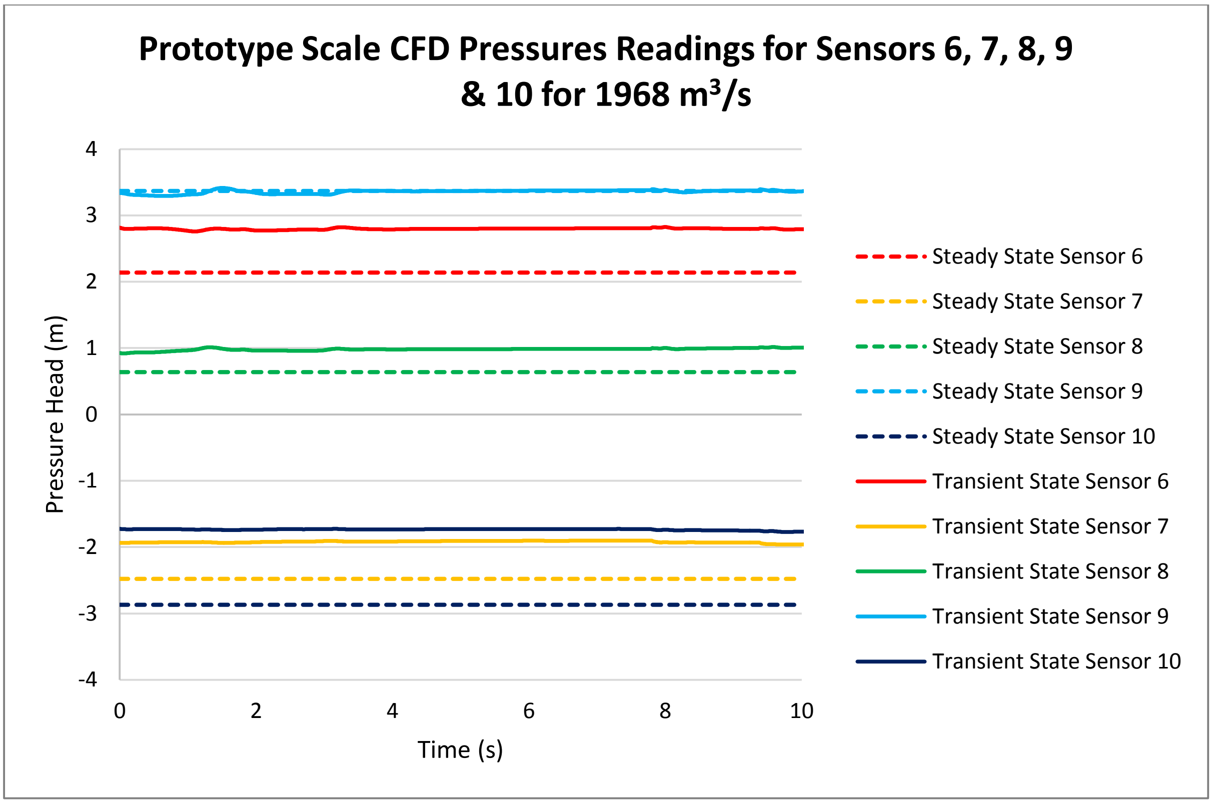

Figure 5.26 Comparison between simulated transient and steady state models pressure simulators for sensors 6,7,8,9 & 10 for a flow rate of 1 968 m^3/s

Figure 5.26 indicates that the two states simulated produced similar results, with the largest difference seen between the states, at sensor 10, equalling 1.14 m pressure head at the prototype scale. This is a difference of 0.057 m at a scale of 1:20, some differences can be expected as the steady state simulations are run with the fine mesh and the transient simulations with the coarse mesh.

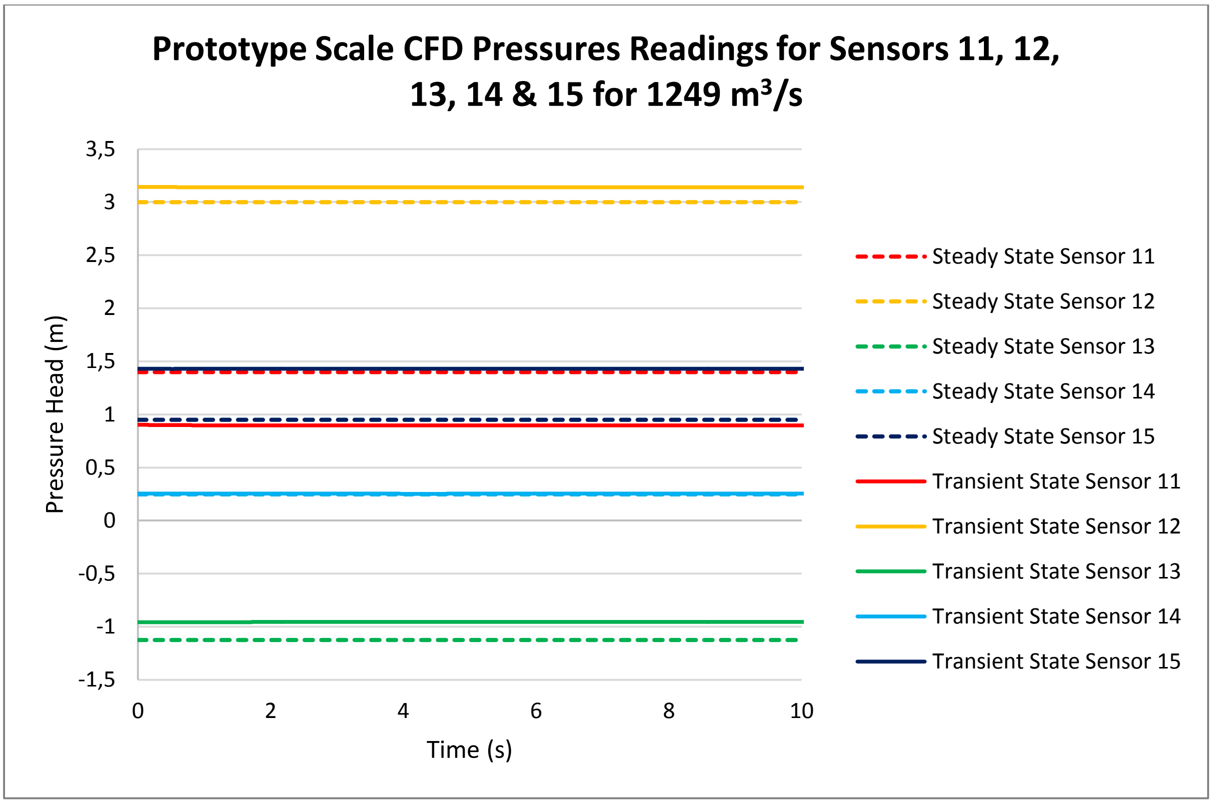

Figure 5.27 Comparison between simulated transient and steady state models pressure simulators for sensors 11,12,13,14 & 15 for a flow rate of 1 249 m^3/s

Figure 5.27 shows that the two states produced similar results, with sensor 14 producing an identical result for both simulation states. The largest difference in the results shown above was found to be 0.53 m pressure head, at the prototype scale, at sensor 11.

The transient simulations produced pressure readings which oscillated slightly with time, whilst the steady state readings used for the above graphs (Figure 5.25, Figure 5.26 and Figure 5.27) are the average results taken across 2 000 iterations of a converged solution with a mass imbalance across the boundaries of the model equal to less than 1% of the total flux entering the model. These include a select number of sensors which best represent the various patterns found in the results for two different flow rates. Comparisons for all the steady and transient results obtained can be seen in Appendix D.

The transient and steady state simulations produced similar pressure values to each other and on a number of occasions were almost identical. There were times when the results did differ, with the biggest difference being 2.35 m at the prototype scale, approximately 0.12 m at a scale of 1:20. The average difference across all of the simulations was 0.16 m at the prototype scale, which is 0.008 m at a scale of 1:20. This is not large difference considering the difference between the minimum cell size between steady state and transient state simulations exceeds this value.

Chapter 6: CFD Validation

6.1. Introduction

This chapter addresses the validation of CFD modelling and does so through the comparison of results obtained for corresponding flow rates from physical modelling tests run and CFD modelling tests. The chapter initially focusses on the errors and uncertainty associated with the different modelling methods used, where error is defined in the AIAA Guidelines (1998) as:

"A potential deficiency in any phase or activity of the modeling process that is due to the lack of knowledge." (AIAA G-077-1998)

And uncertainty as:

"A recognizable deficiency in any phase or activity of modeling and simulation that is not due to a lack of knowledge." (AIAA G-077-1998)

The chapter then shows the results obtained from both types of modelling side by side in order to compare them. The chapter ends with a brief comment on the usefulness and accuracy of the use of CFD modelling in this scenario.

6.2. Physical Modelling Errors and Uncertainty

6.2.1. Systematic Errors

Scale effects

The effects of using a scaled model to determine values for use at a prototype scale can have an influence on the accuracy of the results produced. This effect results from the water surface tension and is described by the Webber number (W). This is a dimensionless parameter, defined below, which is indicative of the ratio that exists between the forces of inertia and surface tension (Falvey, 2003).

$$W = \frac{V}{\sqrt{{}^{\sigma}/_{\rho h}}} = \frac{{}^{2}/_{3}\sqrt{2g}hC_d}{\sqrt{{}^{\sigma}/_{\rho}}}$$

Where:

V is the velocity;

σ is the interfacial surface tension;

ρ is the density of water;

h is the head on the weir; and

C_d is the coefficient of discharge.

Operational Method

The testing of the physical model was done through setting a flow rate over the model and allowing it to stabilise (this typically took between two and three minutes) before recording the desired measurements and then moving on to the next flow. Theoretically, however, with a constant inflow the flow depth will never stabilise as the reservoir level will continue to rise in ever decreasing increments, an equation to represent this phenomenon can be determined by equating the difference between the outflow and inflow discharges of the flume or reservoir. This can be expressed, in dimensionless terms, as follows (Falvey, 2003):

$$d\left(\frac{t\,Q_o}{A_r h_o}\right) = \frac{1}{1-\left(\frac{h}{h_o}\right)^{3/2}} d\left(\frac{h}{h_o}\right)$$

Where:

Q_o is the inflow discharge;

A_r is the reservoir area;

h is the head at any time;

h_o is head over the weir crest at steady state; and

t is time.

6.2.2. Instrumentation Errors

Pressure Readers

The pressure readers used to record the pressures during the physical modelling were WIKA Model S-10 pressure transmitters for general applications. The transmitters have an accuracy of 0.25% of the span of pressures appropriate for that model, in this case 1m (WIKA, 2013). Thus, the accuracy of the transmitters was ±2.5 mm pressure head which is ±50 mm at the prototype scale. For comments on calibration of the pressure readers see section 4.6.

Flow rate measurement

The flow rate entering the model was measured using an electromagnetic flow meter (Flowmetrix product model: SAFMAG 600B2NRSSR0061 with SABS ISO-9001:2008 quality approval). This model has a documented accuracy of 0.5% of the flow rate it is measuring (Flowmetrix, 2012). The lowest and highest flow rates measured during testing were 60 and 600 *l*/s respectively, meaning the accuracy of the meter ranges from ±0.3 *l*/s to ±3 *l*/s. At the prototype scale the accuracy of the flow meter ranges between ±0.027 m^3/s and ±0.27 m^3/s respectively.

Flow Depth

The accuracy of the water depth readings take on the model were ±0.001 m (at a scale of 1:20), this corresponded to an accuracy of ±0.02 m at the prototype scale.

6.2.3. Physical Modelling Uncertainty

Flow Rate

With the vast amounts of water flowing through the model for the duration of testing there is a possibility that a small amount of leakage, or other forms of losses, occurred during the tests. This is considered negligible at less than 1%.

Side Walls

The side walls of the physical model were constructed out of plastered brick and cement and then smoothed with a bitumen water proof paint, the roughness of the side walls may, however, still have impacted the direction of streamlines, or on the behaviour of the fluid. Care was taken to avoid any impact of this, as tests were conducted only on the middle portion of the model. However, this roughness may well have been the reason for the increased depth of flow, when results were compared to theoretical calculations.

6.3. CFD Modelling Errors and Uncertainty

A successful CFD model produces a vast amount of information to the modeller all of which, should it be proved to be accurate, would give invaluable details on the expected behaviour of a designed scenario. The effects of obstructions, alternate designs and flood events can all be traced with the correct set-up and the effects of scaling can be ignored if models are built to match the dimensions of the prototype. The limiting factors to all of this being the accuracy of the model and the confidence of engineers to rely entirely on CFD generated data for the design verification. Another major limiting factor is that CFD modelling is extremely complex and minor changes in the parameters, which can easily go unseen, could result in major errors in the results.

6.3.1. Numerical Errors

As discussed in the Literature Review, CFD models use non-linear partial differential equations (PDEs) to describe the behaviour of flow within the control volume, where these PDEs are solved at each of the nodes located within the domain. The use of these equations can result in three different types of error: discretisation and solution errors, rounding errors and iterative convergence error.

Discretisation and Solution Errors

These errors are caused from the use of numerical algebraic expressions to represent the PDEs, which in turn express the boundary conditions and the physical and auxiliary models (Perez, 2008). It is possible to reduce the discretised error to a point where it is negligible through reducing the size of the time step and increasing the number of cells in the mesh. This, however, requires an ever increasing amount of time and computer hardware capability. The extent to which the errors associated with discretisation and solution are thus determined by the resources available to the user and the ability of the user to effectively negate them.

Rounding Errors

Computer rounding errors arise due to the representation of floating point numbers to a finite number of significant points. These errors are not considered as significant as computers are able to store numbers with 16, 32 or 64 bits (NPARC Alliance, 2008).

Iterative Convergence Error

The existence of this error results from the need for a model, running an iterative process, to be solving towards an end point. The iterative method means that after each step the model is slightly more accurate than it was previously, assuming that the model is converging towards a final solution. Thus, considering the effects of time and resources on a project the ‘solution’ is assumed to be obtained once a model has converged to within a desired range of the actual solution. This indicates that the difference between the solution obtained at the end of convergence and the actual solution is the error associated with iterative convergence.

6.3.2. Human Error

This type of error originates from faults made while operating and the incorrect operation of the tools available. Human error also extends to the incorrect analysis of information provided through CFD modelling. This is, for the most part, avoidable through gaining understanding of the parameters/intricacies involved with the work and software. These errors can exist in the Geometry, Mesh, Processing and Post-Processing stages of the project.

6.3.3. Code Errors

Computer programming errors or *Code Errors* are mistakes made during the programming or writing of the code. These errors are difficult to trace as they are built into the software. They can, however, be identified through extensive and detailed validation and verification of the code and its subprograms (NPARC Alliance, 2008).

6.3.4. Physical Approximation Uncertainty

The existence of this form of uncertainty arises from the difference between actual fluid behaviour and CFD from the assumptions made to represent physical and chemical processes in the forming of the model. These errors are linked to the governing equations and methods used to solve for and model the fluids properties (NPARC Alliance, 2008). These errors can exist due to the lack of a better way to represent a property or behaviour, or as a result of simplifying the behaviour of a fluid to reduce computation time, for example; incompressible flow (Institute for Water and Environmental Engineering, 2012).

6.3.5. Model Setup Uncertainty

Uncertainty with regards to the model input data can arise from three sources; the geometry, the boundary conditions and the fluid properties. The uncertainty arises from approximations and limited amounts of information leading to inaccuracies in the modelled values.

Geometry

The geometry is built to contain the entire area of study and designed in a way to match the characteristics of the prototype. However, through the use of CAD programs and the meshing process, it should be noted that the domain will not be built and meshed to exactly the same specifications as laid out in the design. The same is true with the manufacturing of a physical model or the prototype itself where the levels of accuracies obtained will differ vastly between different construction techniques and materials used.

Boundary Conditions

It is difficult to acquire a very high degree of accuracy at the input boundary conditions when specifying values for velocities, pressures, phase interactions and temperatures, to name a few. This leads to uncertainty as the behaviour of a fluid is dependent on all of these factors. A number of boundary conditions can be measured before the modelling begins and can be included in an accurate manner, however, there will always be conditions that are set based on assumptions or generalised values and are approximately true. The Fluent set-up is further limited by the determining of a boundary type at all of the inlet and outlet boundaries. The type of boundary is selected from a short list, where the best fit option is selected. In two-phase conditions the boundaries need to consider the inlet and outlet of both water and air, all of which complicates the set-up of the model and can lead to uncertainty in its behaviour.

Fluid Properties

The properties of the fluid which govern the way it behaves, such as density and viscosity, are all dependent on the temperature and pressure values which surround the fluid. Thus, in order to simplify calculations, constant values are often assumed to be the case when creating the environment within which the fluid will flow. It is unlikely that the conditions will be consistent in reality and thus, these assumptions may lead to a degree of uncertainty in the results obtained.

6.4. Comparison between Physical and CFD Modelling Results

6.4.1. Depth of Flow (Surcharge)

The depth of flow results, as shown in Figure 5.24, include the surcharge readings obtained through CFD modelling, physical modelling as well as theoretical calculations plotted together.

It should be noted that the physical modelling results are the most reliable data source as the physical model considers all influencing factors. Figure 5.24 physical modelling and the transient state CFD modelling results are consistently similar indicating that the CFD model is able to accurately simulate the surcharge of the flow.

The maximum distance between the steady state and theoretical data sets was found to be 0.469 m at a flow rate of 2 136 m^3/s at the prototype scale, which is 23 mm at a scale of 1:20 (measured with an accuracy of 1 mm). The largest difference between the steady state simulation results and the physical model was found, at a discharge of 1 968 m^3/s, to be 0.273 m at the prototype scale, 14 mm at a scale of 1:20. The maximum head between the transient state and theoretical data is 0.617 m at a flow rate of 1 968 m^3/s at the prototype scale, 31 mm at a scale of 1:20.

At a peak discharge of 2 136 m^3/s, the difference between the physical modelling surcharge result and the theoretical and transient state CFD results were 0.70 m and 0.23 m respectively, at the prototype scale. These values indicate the biggest difference between the methods mentioned, indicating that the CFD simulations produced results that were similar to the physical modelling results with the largest difference equalling only 12 mm at a scale of 1:20. Depth measurements are extremely important to design engineers, especially in the design of freeboard calculations, which are critical for safety requirements when designing dams.

6.4.2. Pressure Readings

All average pressure readings obtained through physical and CFD modelling have been shown previously in this thesis (Table 4.1, Table 5.1 and Table 5.2) and in this section the average readings for the steady state simulations and the actual readings for the transient state simulations and physical modelling have been compared to determine the accuracy of CFD modelling in this scenario. Figure 6.1, Figure 6.2, Figure 6.3, Figure 6.4 and Figure 6.5, below, indicate some of the results obtained for prototype flow rates of 712, 898, 544 and 1 789 m^3/s in graphical form for clarity. These particular results were selected to highlight the typical range of results. Appendix E contains further graphics, for comparison, of all flow rates tested for all sensors.

Comparisons between the steady and transient state simulation pressure results have been made earlier in section 5.4, but the following images compare these results to the physical modelling pressure results. Figure 6.1, below, shows that for sensors 1 and 2 at a flow rate of 712 m^3/s, the pressure readings are quite similar between CFD and physical modelling. However, the transient state simulated pressures for sensor 3 differ by between 2.19 m and 3.95 m, of pressure head at the prototype scale, from the physical modelling results.

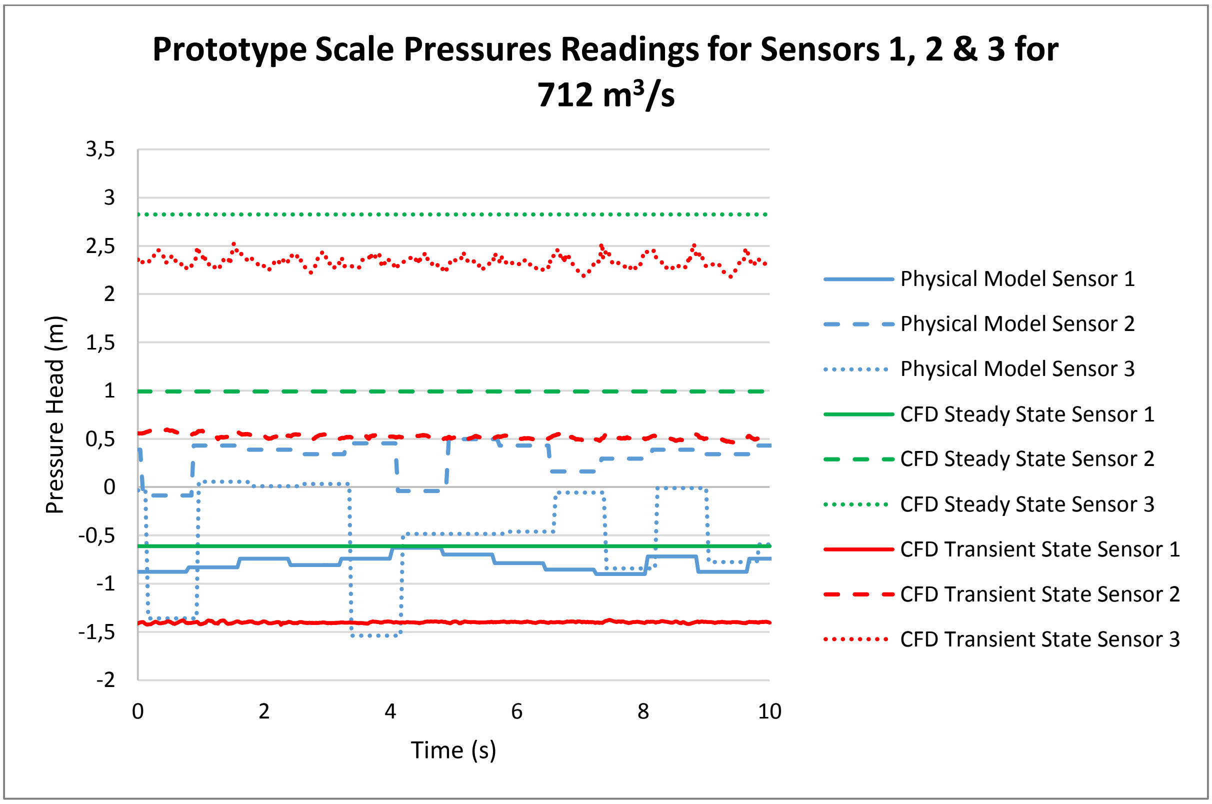

Figure 6.1 Physical modelling, CFD steady state and CFD transient state pressure readings for 712 m^3/s for sensors 1, 2 & 3

Unlike Figure 6.1 above, Figure 6.2 shows large differences between the simulated pressure readings and those taken from the physical model. The smallest and largest of these being 1.72 m and 7.41 m pressure head at the prototype scale for sensors 4 and 5 respectively.

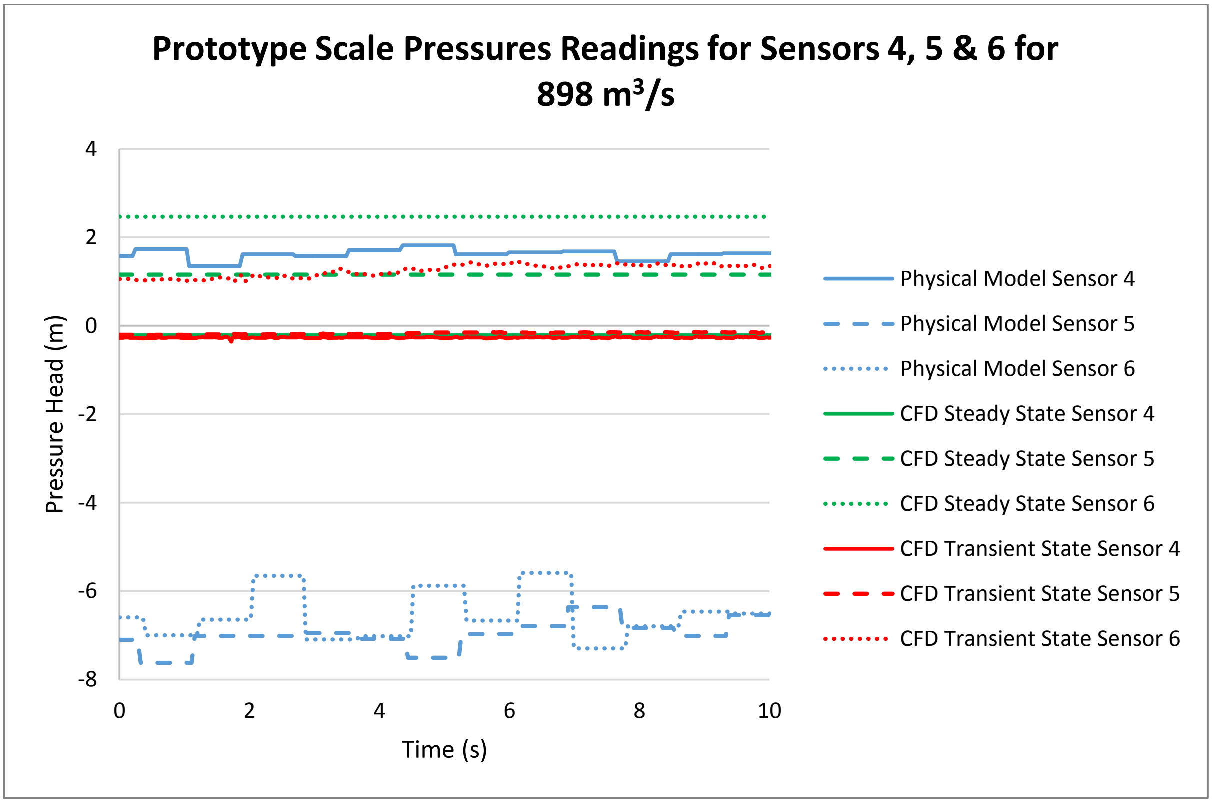

Figure 6.2 Physical modelling, CFD steady state and CFD transient state pressure readings for 898 m^3/s for sensors 4, 5 & 6

Figure 6.3 shows again that the similarities between CFD and physical modelling were quite varied for each flow rate. In this image the simulated results and those obtained from the physical model were very similar for sensor 8. Sensor 9 had a maximum difference of approximately 0.75 m between the transient state and the physical model, whilst the difference between sensor 7's simulated transient state results and those from the physical model fell between 0.42 m and 0.45 m pressure head at the prototype scale.

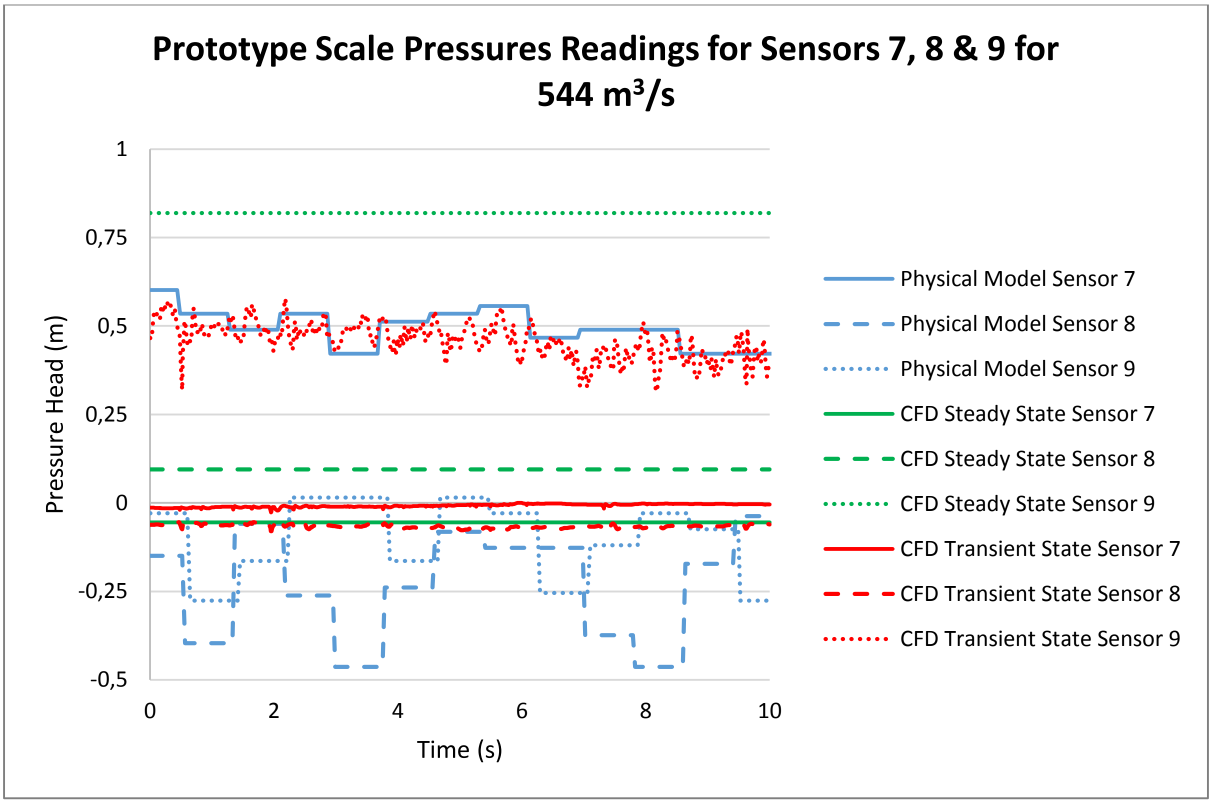

Figure 6.3 Physical modelling, CFD steady state and CFD transient state pressure readings for 544 m^3/s for sensors 7, 8 & 9

Figure 6.4 shows a large variation in the similarity of the results achieved. Sensor 10 was found to have no difference between the transient simulation results and the physical modelling results at some points, but there were large fluctuations in the pressure readings for the physical model for this sensor. Sensor 11 also showed similar results between the CFD and physical models. Sensor 12, however, recorded considerably different values between the CFD and physical models.

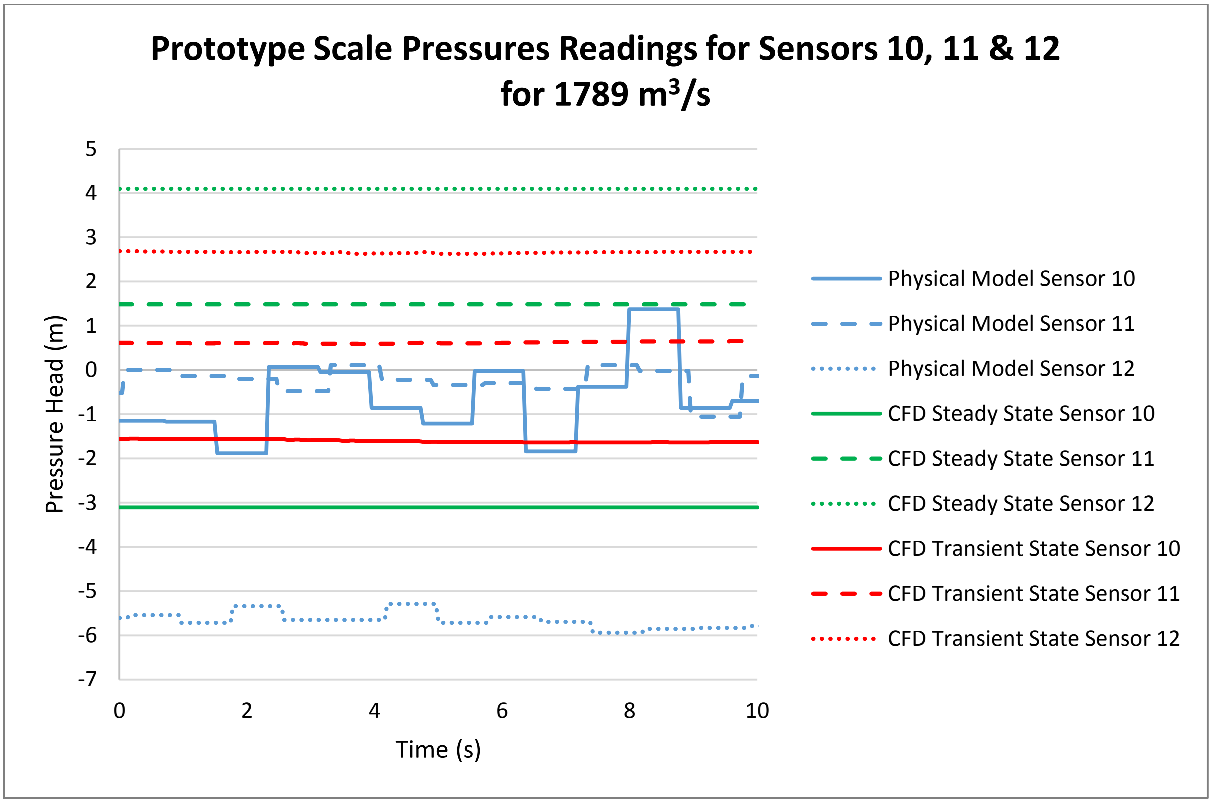

Figure 6.4 Physical modelling, CFD steady state and CFD transient state pressure readings for 1 789 m^3/s for sensors 10, 11 & 12

Figure 6.5 shows data obtained during simulation and testing of a higher flow rate than the previous images. The results, however, are much the same with little consistency of the pressure readings across the CFD and physical modelling methods being found. Sensor 13 and 14 show a difference of approximately 1 m between the transient simulated pressures and those recorded during physical model testing. Sensor 15 has a larger difference between the transient state readings and those of the physical model, with the difference ranging from 1.43 m to 2.11 m pressure head at the prototype scale.

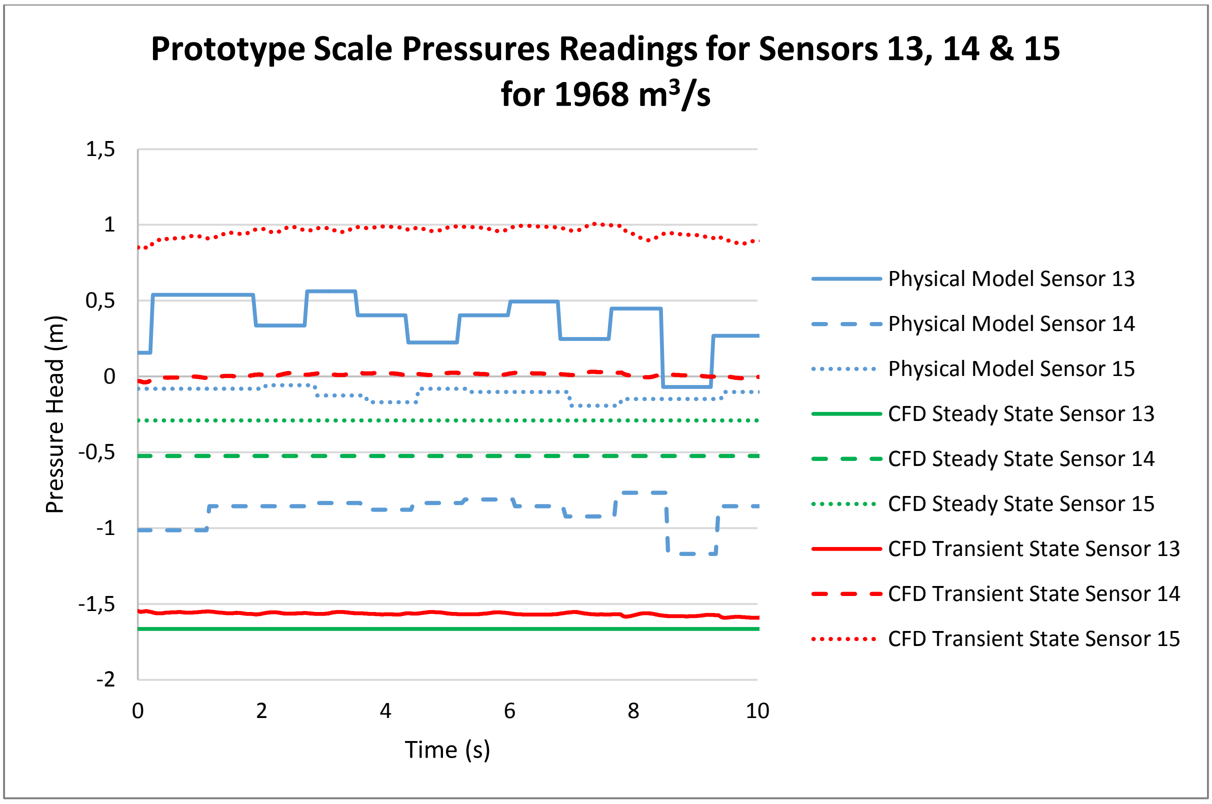

Figure 6.5 Physical modelling, CFD steady state and CFD transient state pressure readings for 1 968 m^3/s for sensors 13, 14 & 15

In Figure 6.1, Figure 6.2, Figure 6.3, Figure 6.4 and Figure 6.5 the physical model results show rapid pressure oscillations in the form of steps. Similar fluctuations in the pressure readings can also be seen in the transient state CFD results, although to a lesser extent. The amount of fluctuation that occurs on a sensor is also influenced by the flow rate of that particular test. Whilst the steady state results included above are, as before, the average pressures over 2 000 iterations of a converged solution. Table 6.1 shows the ratio between the transient state average pressures and the physical modelling average pressures in order to determine the accuracy of the CFD modelling.

Table 6.1 Ratio of average transient state simulated pressures to physical modelling average pressure readings

Flow Rate (m^3/s)	**Ratio of Transient State Over Physical Modelling Average Pressure Readings at the Prototype Scale (By Sensor in m Pressure Head)**														
	1	**2**	**3**	**4**	**5**	**6**	**7**	**8**	**9**	**10**	**11**	**12**	**13**	**14**	**15**
0	0	0	0	0	0	0	0	0	0	0	0	0	0	0	0
215	1.5	0.6	4.5	-1.0	-0.4	0.2	0.8	-	0.1	0.3	0.7	0.0	0.4	0.1	-
361	-0.8	1.1	-	0.7	-1.7	1.4	0.2	-0.4	1.0	0.3	1.8	0.1	2.9	0.1	-0.1
544	-0.6	2.5	23.8	0.5	4.5	5.1	0.0	-0.1	5.8	0.2	-0.3	0.3	1.9	0.5	-0.1
712	-1.8	-1.4	7.3	0.4	0.5	6.8	0.1	-0.1	-	0.3	0.6	1.6	0.9	0.3	-0.1
898	-1.8	-1.8	2.6	0.3	0.4	3.7	0.5	0.0	1.5	0.6	0.0	2.0	0.5	0.6	0.8
1063	-1.2	-11.5	1.6	0.6	-1.6	4.3	0.6	0.1	0.7	0.8	-0.6	2.5	0.8	0.3	2.2
1249	-0.7	2.9	1.5	0.7	-4.2	3.3	0.8	0.5	0.6	1.0	45.0	1.1	1.3	0.3	3.8
1424	-0.5	2.3	1.6	0.8	-7.1	3.6	1.0	0.6	0.6	1.9	-6.0	0.6	1.7	0.6	4.2
1606	-0.3	72.0	3.1	1.2	-2.5	10.3	2.1	0.5	0.7	-2.6	2.3	0.5	7.2	0.4	9.0
1789	-0.2	11.1	2.9	1.4	-2.3	9.5	2.7	0.4	0.7	-3.2	1.6	0.5	7.5	0.2	7.4
1968	-0.1	6.9	2.7	1.4	-2.9	5.4	3.3	0.3	0.7	-4.1	1.3	0.5	7.1	0.0	5.9
2136	0.0	2.5	2.0	1.4	-3.9	3.1	3.8	0.3	0.6	-4.7	0.8	0.5	9.2	-0.2	3.1

(“-“ denotes a division by 0 error)

Table 6.1, Figure 6.1, Figure 6.2, Figure 6.3, Figure 6.4 and Figure 6.5 indicate that through the use of CFD, pressures can be simulated that are in the same range as those measured using the physical model. The ratios obtained in Table 6.1 do, however, cover a wide range of values and although there are only a limited amount of accurate correlations between the physical and CFD model results, the results obtained are similar in magnitude. This is the case for both the transient and steady state conditions. This is significant because the results presented are at the scale of the prototype. There is also some correlation, although limited, with the signage (negative or positive) of the pressure at each sensor and this indicates that the model is able to determine, to some extent, the existence of negative pressures. Negative pressures are an important design factor as they can influence the structural stability of a labyrinth weir.

6.4.3. Usefulness of CFD Modelling

As mentioned throughout this thesis, the potential that CFD has as a tool for engineers is great. The program used to conduct the simulations is incredibly powerful and has shown a good correlation, in some instances, to what is seen in the field and in laboratory tests.

Some results, however, have not been accurate and the causes for these variations are often difficult to identify. The challenge the engineer faces when using CFD software is that the programs are only really suited to expert users and this is a title not easily acquired. Thus, for someone new to CFD it requires a large amount of time (over 400 hours) and effort to reach a capability level at which there would be sufficient confidence in the results obtained to justify basing a design of a weir or other structure upon. Additionally, to achieve a sufficient simulation speed a large amount of computer capacity is required and even then the time taken for simulations remains a significant factor.

6.4.4. Summary

Establishment of the CFD model, to a point ready for testing, involved ensuring the water flow profile matched that of water flowing in a channel. This was achieved through the manipulation of model set-up and boundary conditions.

The water depth measurements, which were measured at a point 1.5 m upstream of the crest, were to some extent consistent across the three different calculation methods, with the results from the CFD model generally falling between those from analytical methods and those from the physical model.

The pressure readings were less consistent and whilst there was some correlation between the steady state and transient state CFD calculations, this was not completely consistent. Thus, in this scenario and with the set-up as it has been tested, the CFD model was unable to accurately record the pressures on the downstream face of the spillway. However, the results were in the same order as those produced by the physical modelling, with the average error of the transient state CFD simulated average pressure head at the prototype scale being 92%. The largest difference between the averaged results was found to be 2.88 m at the prototype scale (0.144 m at a scale of 1:20).

In this scenario the physical model would be the preferred method of testing for pressures on the downstream face of the spillway, as it is a more proven method and therefore more reliable. Additionally the amount of time taken for the physical modelling was significantly less than that taken for CFD modelling, as well as being more accurate when reading the transient pressures on the downstream face of the spillway.

Considering the results presented above it appears that for the modelling of two-phase 3D flow there is still some room for improved accuracy from the CFD programs. However, there is definitely a large role for CFD to play in the water resources environment going forward.

Chapter 7: Conclusions and Recommendations

7.1. Conclusions

A four cycle labyrinth spillway was designed using the Tullis method (1995) with a crest height of 7.5 m, a total crest length of 148 m, an effective crest length of 110 m, a total width of 60 m and a maximum discharge capacity of 2 147 m^3/s (prototype values).

A two-cycle physical model of the designed labyrinth spillway was constructed, using symmetry to allow for a larger model to be built. The model was built to a scale of 1:20 giving it a crest height of 0.375 m, a total width of 1.5 m and a maximum discharge capacity of 0.6 m^3/s, which was equal to the laboratory pump capacity.

The physical model was tested for flow rates of 0, 60, 101, 152, 199, 251, 297, 349, 398, 449, 500, 550 and 597 *l*/s at the 1:20 scale which are equivalent to prototype flow rates of 0, 215, 361, 544, 712, 898, 1 063, 1 249, 1 424, 1 606, 1 789, 1 968 and 2 136 m^3/s. The maximum unit discharge was 35.6 m^3/s·m. During tests, each of which ran for five minutes, measurements of the water depth above the crest at a point 1.5 m (equal to $4H$) upstream of the weir, were taken. These corresponded reasonably well with theoretically determined water depths for $Q < 1\ 200\ m^3/s$, but theoretical calculations underestimated the surcharge by 14.2% at $Q = 2\ 136\ m^3/s$. Pressure readings were taken on the downstream crest of the physical model using 15 piezometer pressure readers, these were recorded and converted into values in pressure head (m) at the prototype scale, with the most negative average pressure found to be -1.42 m pressure head. This was within the design limitations set by the USBR (1987), however, the pressure reading did fluctuate and a number of recorded instantaneous pressures dropped below the sub-atmospheric pressure limit, implying that cavitation could still occur.

Upon completion of the physical modelling, the CFD modelling program ANSYS Fluent was setup by using the attached CAD application, a geometry was established. This geometry was drawn to the same scale as the physical model and sought to correspond with the model as closely as possible. Using the meshing program within ANSYS Fluent, two meshes were then generated, the geometry domain was broken into 923 990 nodes for the finer mesh and 334 477 nodes for the coarser mesh.

The model was set-up and boundary conditions selected for all the boundaries of the domain. Inlet and outlet conditions were determined and prior to each test the model was primed in order to establish a fully developed flow profile specific to the inlet flux for that simulation. Simulations were carried out for the same flow rates as those tested by the physical model, for both steady and transient states.

Results from the physical model, steady state CFD model and transient state CFD model were then plotted together and compared. The findings suggested that although the CFD models were able to develop a flow profile and simulate surcharge similar to the physical model test results, they were – in this scenario – unable to accurately determine the pressures on the downstream face of the spillway. The pressure results were, however, in the same order as those obtained through physical modelling, with the average error found to be 92%.

Regarding the comparison of physical and CFD modelling it has been found that physical modelling, being the more proven of the two methods, is more reliable as well as being easier to manage and interpret. The generating of a CFD model able to develop a two-phase (water and air) flow profile with 3D flow patterns and a fluctuating nappe that exists on the downstream side of a labyrinth spillway is both a time consuming and intensive operation. Additionally, unless the parameters and code that have been included in the set-up of the program are fully understood is it difficult to determine the accuracy of the results produced by the CFD simulations in their current form.

Thus, the thesis has shown that CFD modelling should not yet be used as the sole provider of information for engineers, although it has proven to be an extremely useful supplementary tool when used in conjunction with physical modelling.

7.2. Recommendations

With regard to the above conclusions the following recommendations should be taken into consideration:

7.2.1. Computer Hardware and Run-time

The improvement in speed of computers hold the key to the development and further use of CFD modelling. During the set-up and running of the CFD model the largest obstruction to obtaining results was the amount of time it took for simulations to be performed and for results to be obtained. Typically, a one minute simulation, in this scenario, would require approximately two months of run time (when using one licence) on a mesh of one million nodes, or take two days to run a ten second simulation on a coarse mesh of 400 000 nodes. Per licence, the computers are able to run four parallel processors, thus, with more licences, the run time would be decreased by approximately 25% per licence.

7.2.2. Mesh Development

The meshing of the domain significantly affects the running of the model and takes as up to as much as 50% of the entire time taken to obtain a result using CFD. The model used in this thesis did not run successfully at all with a tetrahedron mesh and so a cutcell mesh was used. Further research into this project could be done using a mixed mesh. The mixed mesh could be established by ‘sweeping’ the areas of the domain where the flow becomes 3D and including tetrahedron shaped cells in this area, with the rest of the domain being left as quadrilaterals – as is the case when the cutcell mesh is used.

This approach was not taken for this thesis because in order to establish a connection between the quadrilaterals and tetrahedrons that allowed for the mesh quality to meet the limitations for skewness and/or orthogonal quality, the mesh required too many elements and nodes. Due to the length of run time required for a ten second simulation using a coarse cutcell mesh, this was not achievable.

7.2.3. Testing Procedure

Upon completion of the design, construction and establishment of the physical model, testing the 12 different flow rates took only three days, although data still needed to be sorted and analysed. The speed at which one is able to conduct a physical model test, where the fluid is the only dynamic element, means that it is easy to test many different flow rates. In hindsight, fewer flow rates should have been tested as the time required for testing using CFD is significantly increased for every new test which needed be conducted. This is due to limited licenses available for the use of the software and limitations in hardware capability. It would therefore have been better to have run half the amount of tests, for double the amount of time. This would indicate further fluctuations in the pressures, should they have existed, and allowed for a longer period of comparison with the physical model tests results. The fewer flow rates would also allow for physical model test to be run multiple times to ensure the accuracy of the readings.

7.3. Further Research and Development Required

7.3.1. Labyrinth Weirs

The study completed by Paxson and Savage (2006) shows that for aspect ratios lower than 2 ($w/P < 2$) the hydraulic performance of the labyrinth weir increases, however, the design methods and curves of Lux (1985) and Tullis (1995) are not considered appropriate for aspect ratios lower than 2. Therefore it is recommended that further testing should be conducted in order to define the hydraulic behaviour for designs where the vertical aspect ratio is less than two (Khode & Tembhurkar, 2010).

The disturbance length ratio (L_{de}/B) is a concept introduced by Falvey (2003), where B is the weir side length (Paxson, et al., 2011). The effective length of disturbance, L_{de}, is the equivalent length of the weir over which the discharge coefficient would be zero, meaning that the flow over the remaining length of the weir would discharge with a coefficient equal to that of a straight weir. Falvey (2003) states that more research needs to be conducted on nappe interference, but until that is done a ratio of $L_{de}/B < 3$ should be maintained during the design phase.

A recent study by Crookston and Tullis (2013) appears to have addressed the issues associated with the Tullis, et al. (1995) design method. This article was not yet available at the time the physical model was being designed and constructed, however, t is worth noting that the issues discussed in this article would not have affected the design of the labyrinth used for this thesis as there were limited discrepancies found for a labyrinth with a side wall angle of 15°.

7.3.2. CFD Modelling and Validation

The reason models are built is to best represent what will be a prototype design, currently the most widely used way to do this is through physical modelling. CFD, however, has the scope to become cheaper, faster and possibly more accurate than physical modelling in time. This requires continual research into better ways to represent the behaviour of fluids and particularly how they interact. There is little doubt that computer power and the programs used to simulate real life scenarios, will continue to develop and become more and more capable. In the water engineering field there should be further emphasis placed on validation studies in order to assist the developers of these programs, specifically focussing on informing them of which circumstances they are accurate in and which they are not.

There will always be small errors of inaccuracy associated with CFD modelling, as there are with any scientific testing method, however, it is the unknown level of accuracy which limits the confidence that engineers are willing to place in the results produced through CFD. A capable knowledge of the risks associated with the reliance on a CFD model for design work could only lead to an increase in its usefulness in the field and in the amount of trust engineers are willing to place in results produced.

References

AIAA, 1998. *Guide for the Verification of Computatuinal Fluid Dynamics Simulations.* s.l.:AIAA G-077-1998.

ANSYS Inc., 2009. *ANSYS FLUENT 12.0 Theory Guide,* s.l.: Ansys Inc..

Chadwick, A., Morfett, J. & Borthwick, M., 2004. *Hydraulics in Civil and Environmental Engineering. Fourth Edition.* New York: Spon Press.

Crookston, B. M., 2010. *Labyrinth Weirs.* [Online]
Available at: http://digitalcommons.usu.edu/etd/802

Crookston, B. M. & Tullis, B. P., 2013. Hydraulic Design and Analysis of Labyrinth Weirs. *Journal of Irrigation and Drainage Engineering ASCE,* pp. 363-377.

Darvas, L. A., 1971. Performance and design of labyrinth weirs. *Journal of Hydraulic Engineering ASCE,* Issue 97(8), pp. 1246-1251.

Falvey, H. T., 2003. *Hydraulic Design of Labyrinth Weirs.* Virginia: ASCE Press.

Flowmetrix, 2012. [Online]
Available at: www.flowmetrix.co.za
[Accessed 15 08 2013].

Ghare, A. D., Mhaisalkar, V. A. & Porey, P. D., 2008. An Approach to Optimal Design of Trapezoidal Labyrinth Weirs. *World Applied Sciences Journal 3* , pp. 934-938.

Hay, N. & Taylor, G., 1970. Performance and Design of Labyrinth Weirs. *Journal of Hydraulic Engineering, ASCE,* 96(11), pp. 2337-2357.

Houston, K. L., 1982. *Hydraulic Model Study of Ute Dam Labyrinth Spillway,* Denver: Bureau of Reclamation Division of Research Hydraulics Branch.

Houston, K. L., 1983. *Hydraulic Model Study of Hyrum Dam Auxiliary Spillway,* Denver: Bureau of Reclamation Division of Research Hydraulics Branch.

Institute for Water and Environmental Engineering, 2012. *Investigation of Unsteady Flow Conditions at Dam Bottom Outlet Works Due to Air Entrainment During Gate Closure. Volume II: Computational Modelling,* Gezina: Water Research Commission.

Khode, B. V. & Tembhurkar, A. R., 2010. Evaluation and Analysis of Crest Coefficient for Labyrinth Weir. *World Applied Sciences Journal 11,* pp. 835-839.

Lux III, F. L. & Hinchcliff, D., 1985. *Design and Construction of Labyrinth Spillways.* Paris, France, International Commission on Large Dams, pp. 249-274.

NPARC Alliance, 2008. *CFD Verification and Validation Web Site,* s.l.: s.n.

Ouamane, A. & Lempérière, F., 2006. Design of a New Economic Shape of Weir.

Paxson, G. & Binder, D., 2009. *The Balancing Act: Considering Flooding Impacts in Design of Spillway Capacity Upgrades.* s.l., Association of State Dam Safety Officials.

Paxson, G., Campbell, D. & Monroe, J., 2011. *Evolving Design Approaches and Considerations For Labyrinth Spillways.* San Diego, U.S. Society on Dams, pp. 1645-1666.

Paxson, G. & Savage, B., 2006. *Labyrinth Spillways: Comparison of Two Popular U.S.A. Design Methods and Consideration of Non-Standard Approach Conditions and Geometries.* Brisbane, s.n., pp. 37-46.

Perez, R. A., 2008. *Uncertainty Analysis of Computational Fluid Dynamics Via Polynomial Chaos,* Blacksburg: s.n.

SANCOLD, 1991. *Safety Evaluation of Dams, Report No.4: Guidelines on Safety in Relation to Floods,* s.l.: South African National Committee on Large Dams (SANCOLD).

Savage, B., Frizell, K. & Crowder, J., 2004. *Brains versus Brawn: The Changing World of Hydraulic Model Studies.* [Online]
Available at: www.usbr.gov/pmts/hydraulics_/pubs/PAP/PAP-0933.pdf
[Accessed 22 05 2012].

Savage, B. M., Johnson, M. C. & Towler, B., 2009. *Hydrodynamic Forces on a Spillway: Can We Calculate Them?.* [Online]
Available at: http://www.flow3d.com/resources/technical-papers/water-and-environmental.html
[Accessed 29 05 2012].

Sharma, R. K. & Sharma, T. K., 1992. *Textbook of Irrigation Engineering Volume II: Dam Engineering (Including Water Power Engineering).* s.l.:Oxford and IBH Publishing Co. Pvt. Ltd..

Tullis, J. P., Amanian, N. & Waldron, D., 1995. Design of Labyrinth Spillways. *Journal of Hydraulic Engineering,* pp. 247-255.

U.S. Society on Dams, 2011. *21st Century Dam Design - Advances and Adaptations.* San Diego, California, U.S. Society on Dams.

U.S.B.R., 1987. *Design of Small Dams.* Third ed. Washington DC: U.S. Department of the Interior - Bureau of Reclamation.

Vermeyen, T., 1991. *Hydraulic Model Study of Ritschard Dam Spillways,* Denver: Bureau of Reclamation.

Versteeg, H. K. & Malalasekera, W., 1995. *An Introduction to Computational Fluid Dynamics.* Harlow: Longman Group Ltd.

WIKA, 2013. [Online]
Available at:
http://www.wika.co.za/publish/download_datasheets_PE_en_co.aspx?ActiveID=14267
[Accessed 15 08 2013].

Wormleaton, P. R. & Chau, C. T., 2000. Aeration Performance of Rectangular Planform Labyrinth Weirs. *Journal of Environmental Engineering*, pp. 456-465.

Appendix A: Labyrinth Weir Model Design Drawings

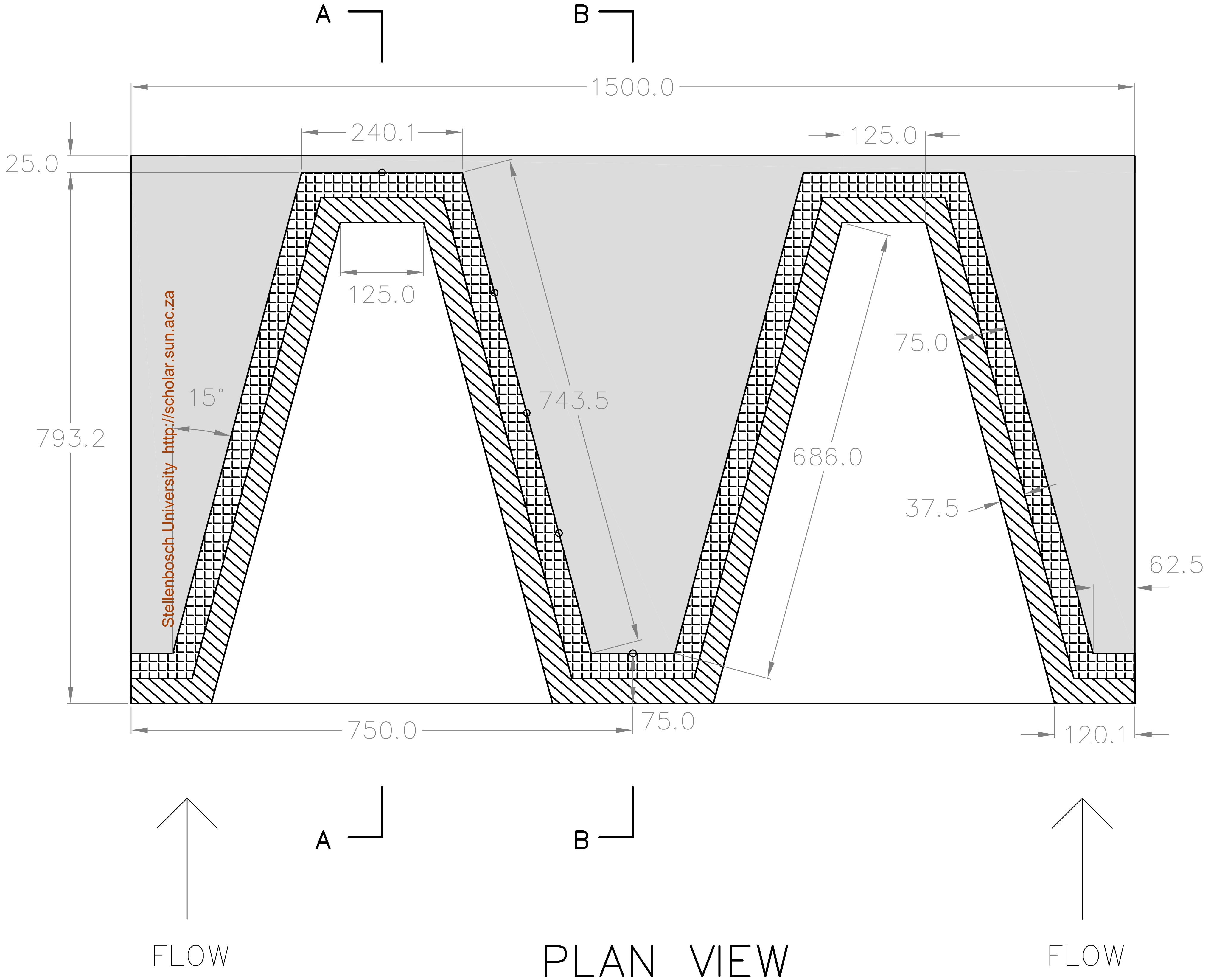

PLAN VIEW

LEGEND:

LABYRINTH WALLS ▨
STRUCTURAL BOUNDARIES —
WATER LEVEL —
BASE LEVEL PLATE ■
SLOPING DOWNSTREAM FLOOR ▭
PRESSURE SENSORS ○

NOTES:

ALL MEASUREMENTS IN MM.

THE DOWNSTREAM PORTION OF THE SPILLWAY FLOOR SLOPES AT ROUGHLY 1:20 WHILST THE UPSTREAM PORTION OF THE SPILLWAY FLOOR IS HORIZONTAL

MODEL SCALE 1:20.

PROJECT:
LABYRINTH SPILLWAY
TITLE:
MSc THESIS MODEL
DESIGN:
GUY ROBERTSON
DRAWING:
LABYRINTH PLAN VIEW
DRAWING NO.:
MODEL 001
DATE:
02-07-2012
SCALE:
0 50 100 250

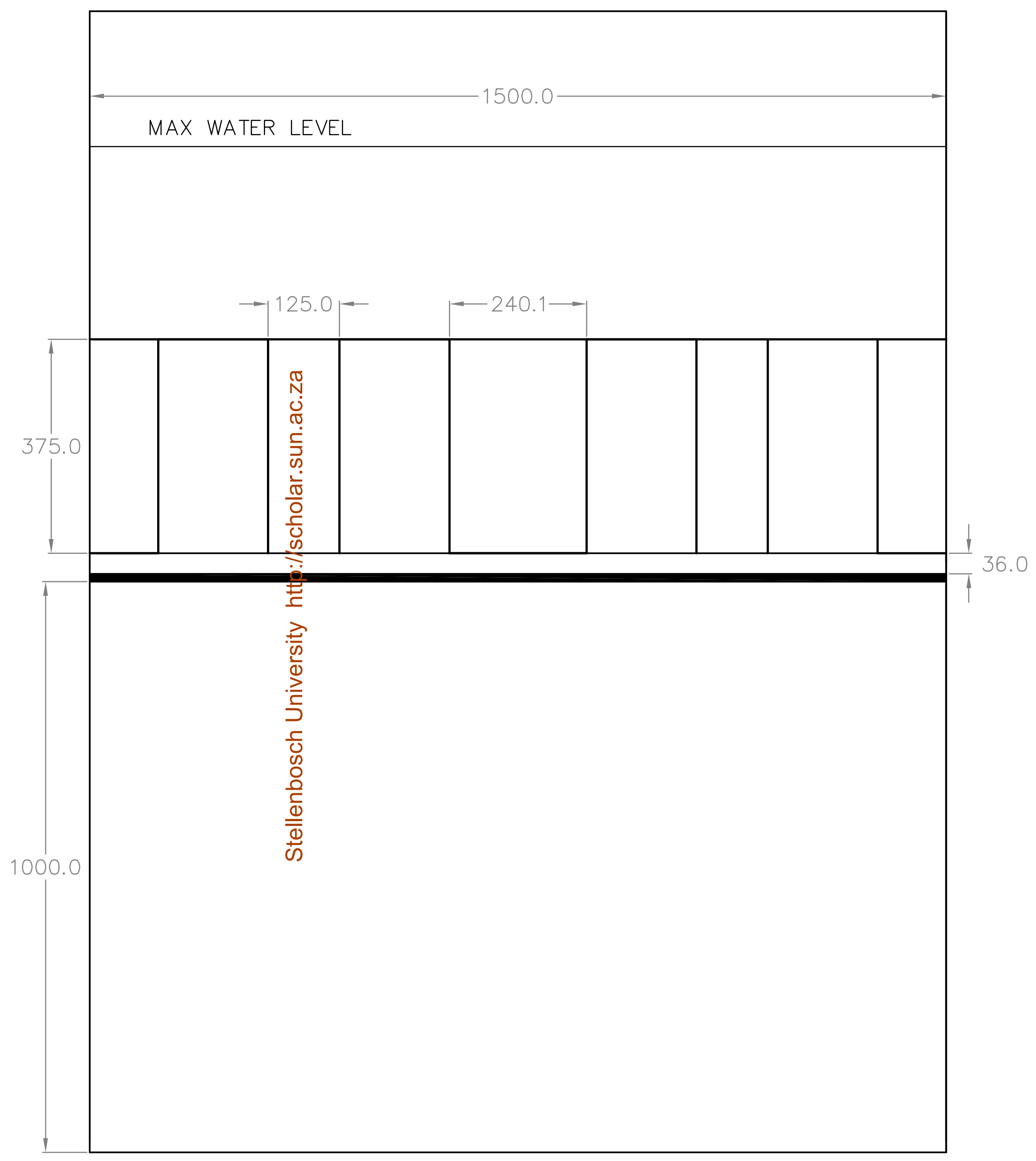

ELEVATION VIEW (FROM UPSTREAM)

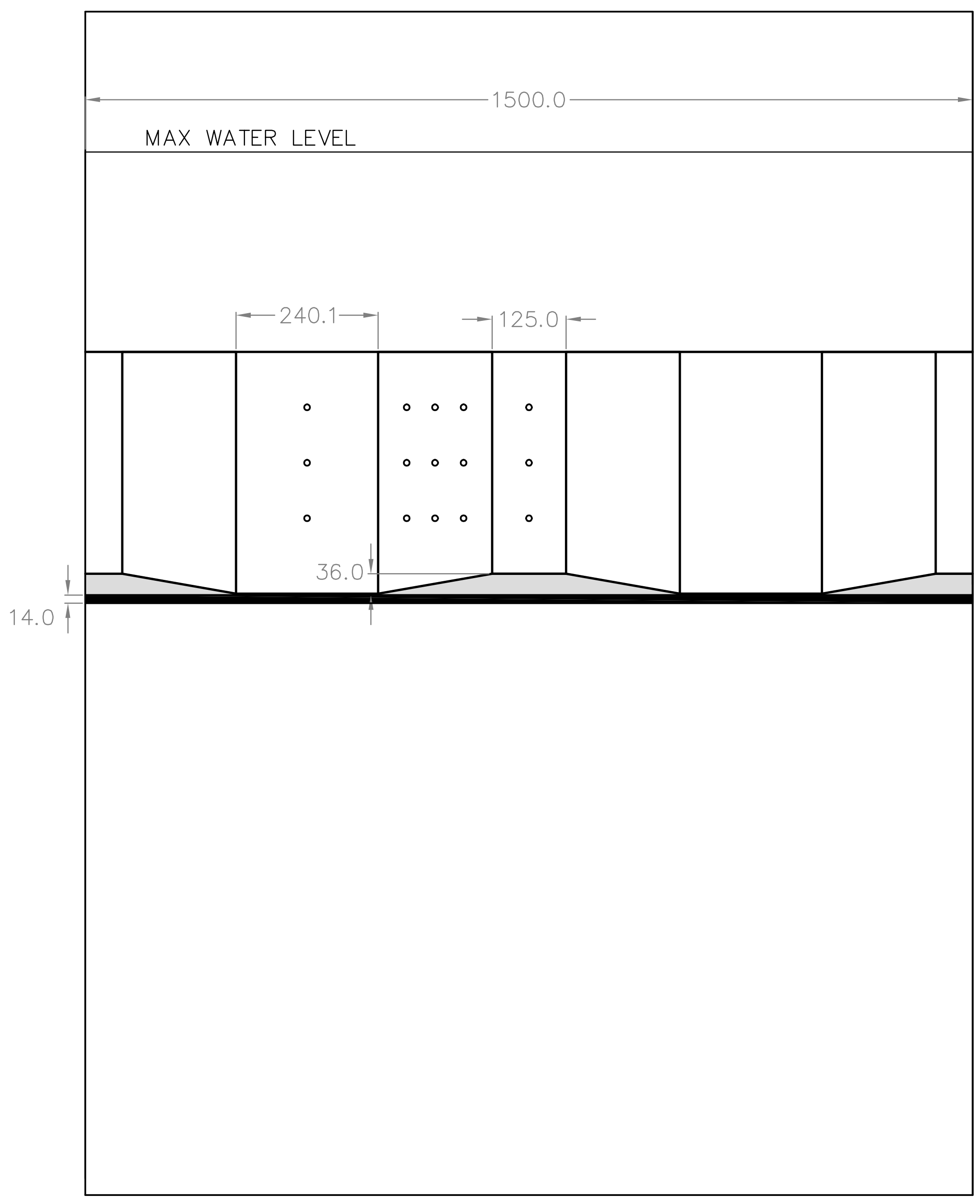

ELEVATION VIEW (FROM DOWNSTREAM)

LEGEND:

LABYRINTH WALLS	─
STRUCTURAL BOUNDARIES	─
WATER LEVEL	─
BASE LEVEL PLATE	━
SLOPING DOWNSTREAM FLOOR	▭
PRESSURE SENSORS	∘

NOTES:

ALL MEASUREMENTS IN MM.

THE DOWNSTREAM PORTION OF THE SPILLWAY FLOOR SLOPES AT 1:20 WHILST THE UPSTREAM PORTION OF THE SPILLWAY FLOOR IS HORIZONTAL

MODEL SCALE 1:20

PROJECT:
LABYRINTH SPILLWAY
TITLE:
MSc THESIS MODEL
DESIGN:
GUY ROBERTSON
DRAWING:
ELEVATION VIEWS
DRAWING NO.:
MODEL 002
DATE:
02–07–2012
SCALE:
0 100 250 500

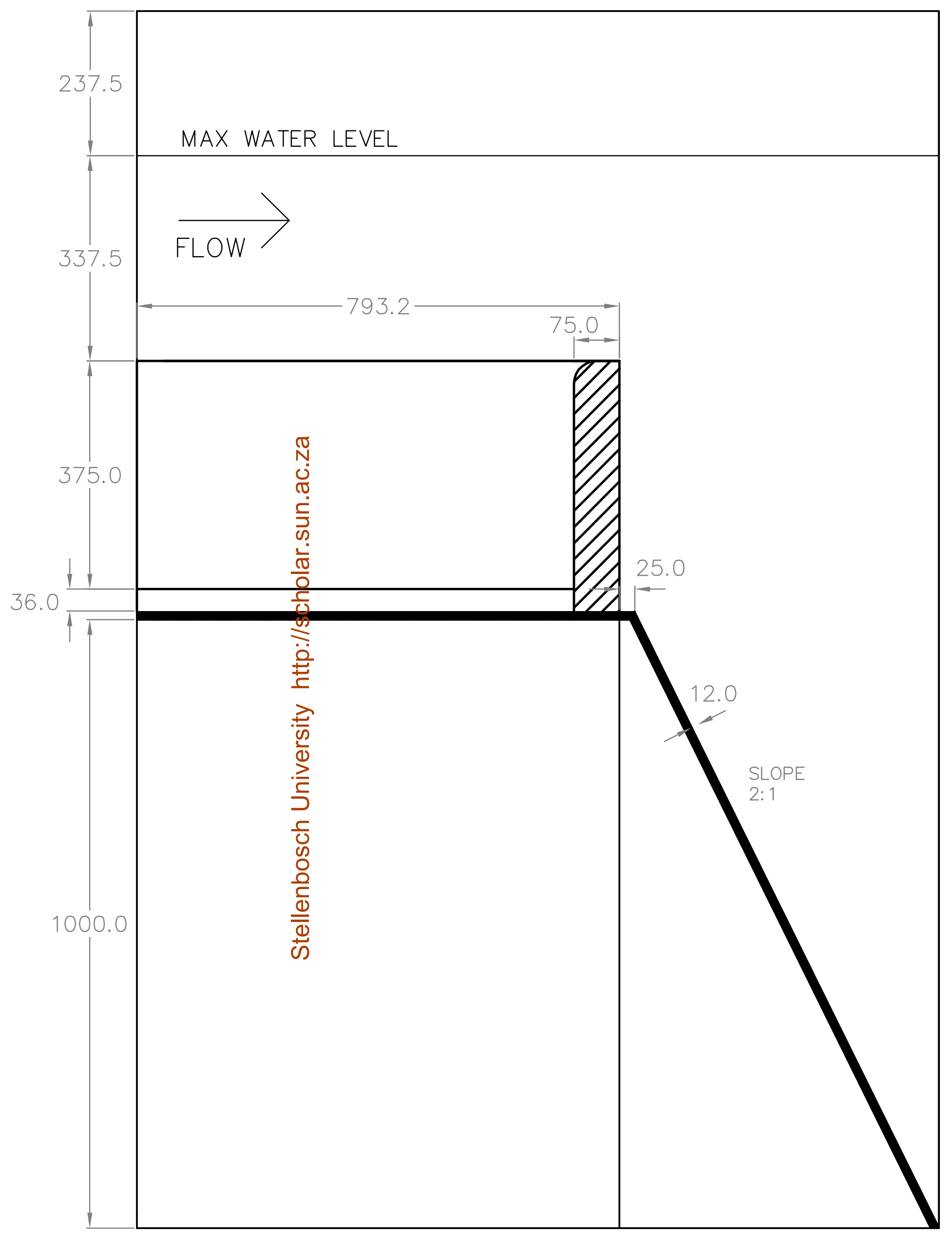

SECTION A – A (FLOW FROM LEFT)

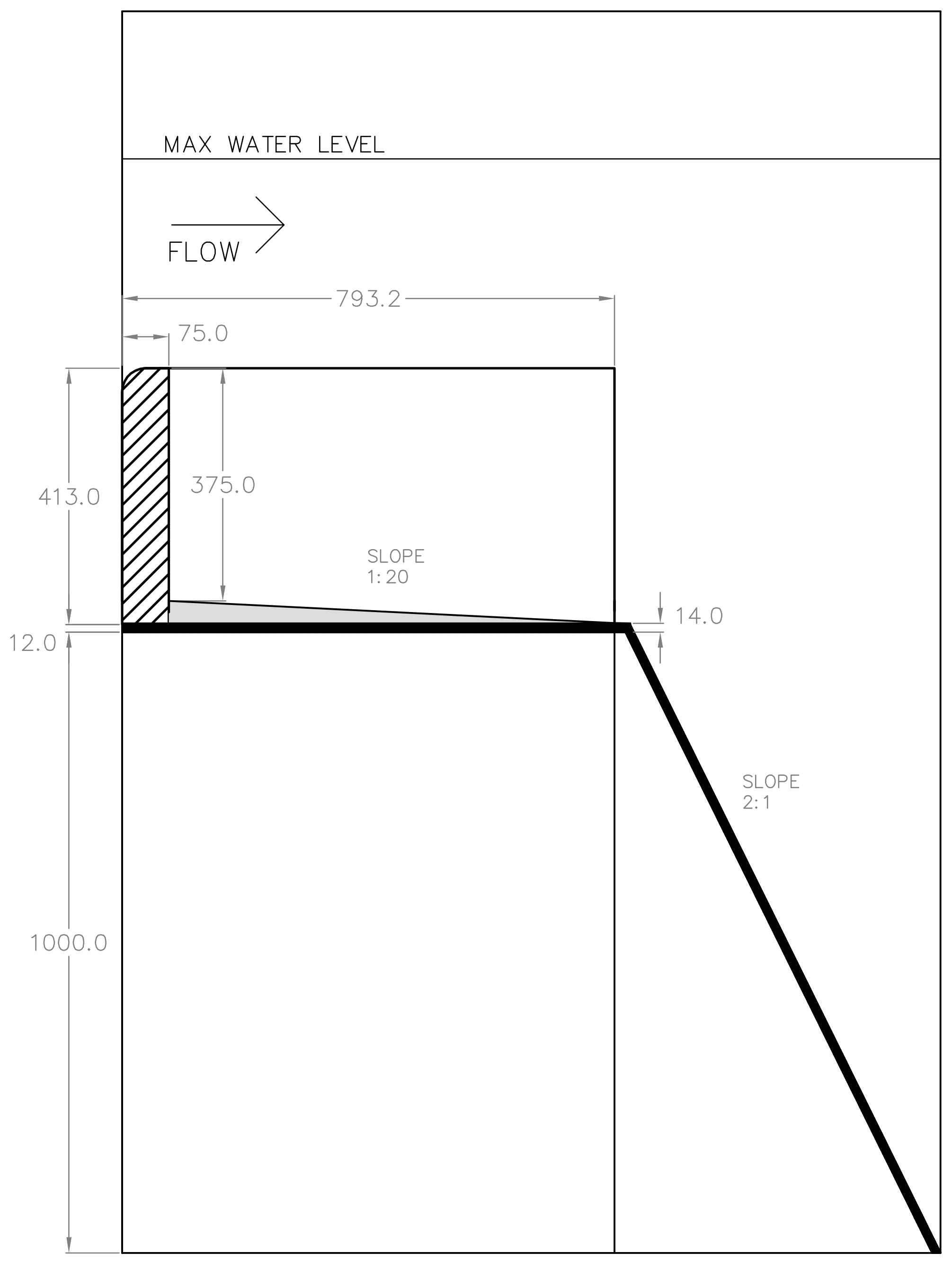

SECTION B – B (FLOW FROM LEFT)

LEGEND:

LABYRINTH WALLS ─
STRUCTURAL BOUNDARIES ─
WATER LEVEL ─
12MM BASE LEVEL PLATE ▬
SLOPING DOWNSTREAM FLOOR ▭

NOTES:

ALL MEASUREMENTS IN MM

THE DOWNSTREAM PORTION OF THE SPILLWAY FLOOR SLOPES AT 1:20 WHILST THE UPSTREAM PORTION OF THE SPILLWAY FLOOR IS HORIZONTAL

MODEL SCALE 1:20

PROJECT:
LABYRINTH SPILLWAY
TITLE:
MSc THESIS MODEL
DESIGN:
GUY ROBERTSON
DRAWING:
CROSS SECTIONS
DRAWING NO.:
MODEL 003
DATE:
02–07–2012
SCALE:
0 100 250 500

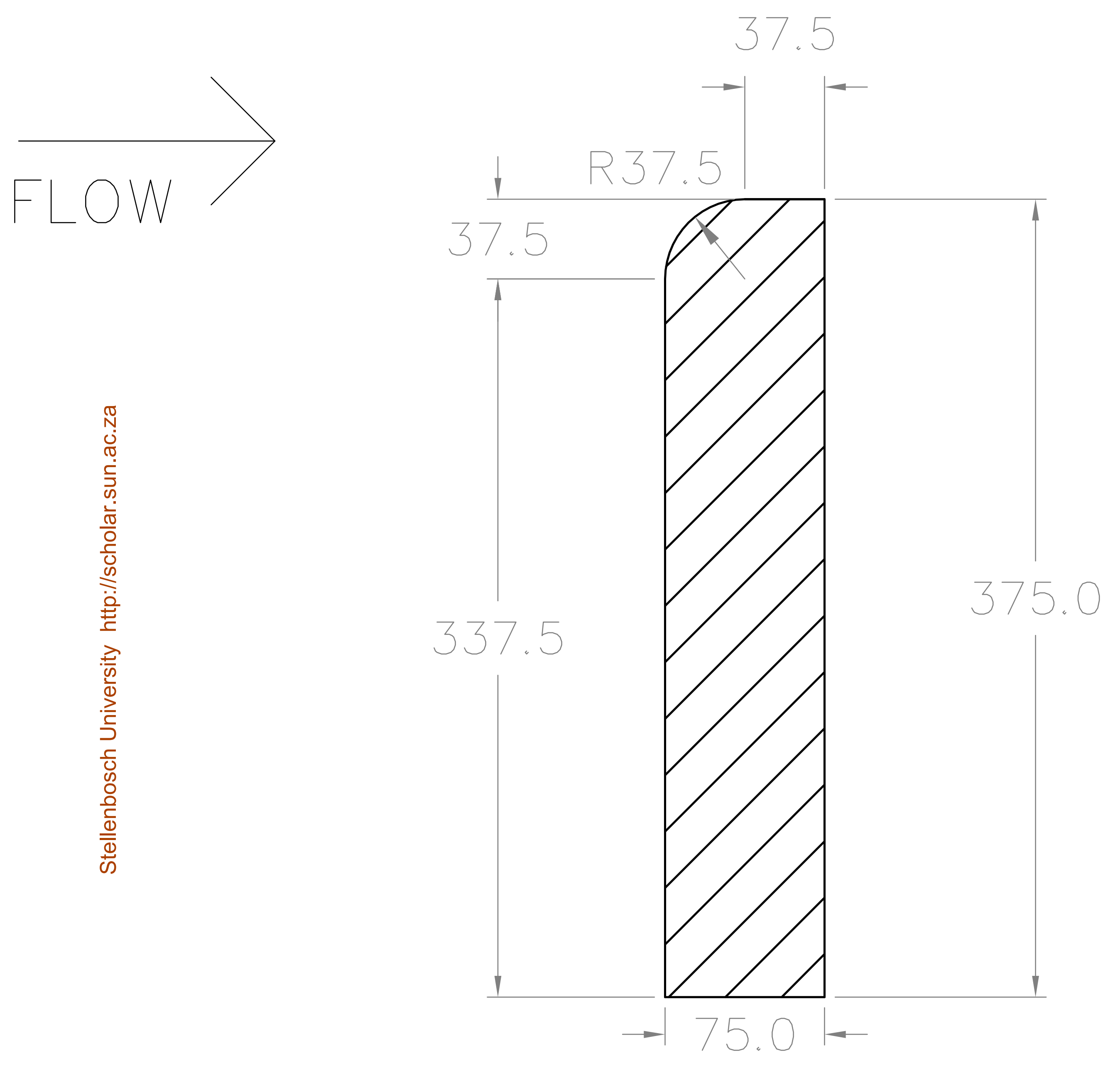

QUARTER–ROUND CREST

LEGEND:

LABYRINTH WALLS ———

AREAS:

TOP LABYRINTH WALLS	0.556 M^2
LABYRINTH WALLS FACES	3.060 M^2
BASE LEVEL	2.460 M^2

NOTES:

ALL MEASUREMENTS IN MM

IF THE RADIUS OF THE UPSTREAM CURVED (QUARTER–ROUND) CREST IS REQUIRED TO BE ROUNDED OFF IT SHOULD BE ROUNDED DOWN TO 37MM

MODEL SCALE 1:20

PROJECT:
LABYRINTH SPILLWAY
TITLE:
MSc THESIS MODEL
DESIGN:
GUY ROBERTSON
DRAWING:
CREST DETAIL
DRAWING NO.:
MODEL 004
DATE:
02–07–2012
SCALE:
0 25 50 100

Appendix B: Physical Modelling Results

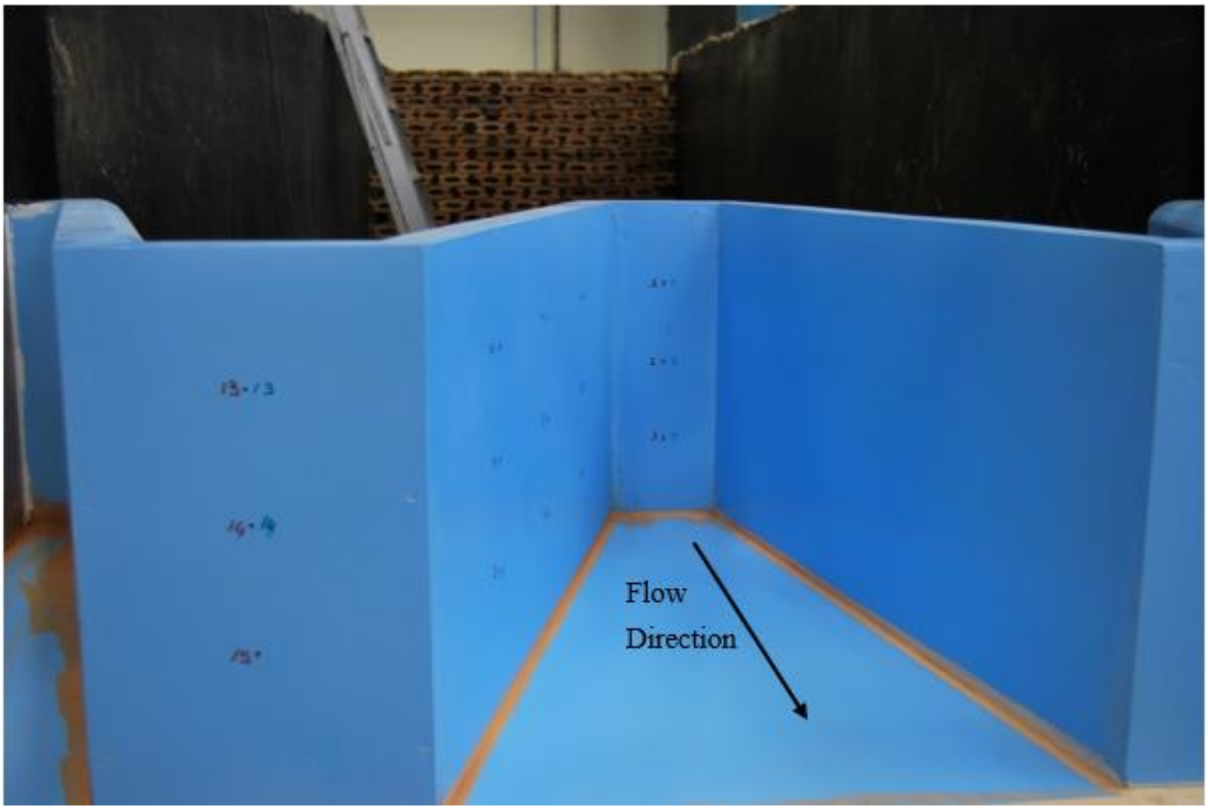

Figure B.1 Laboratory model showing pressure sensor positions and labels

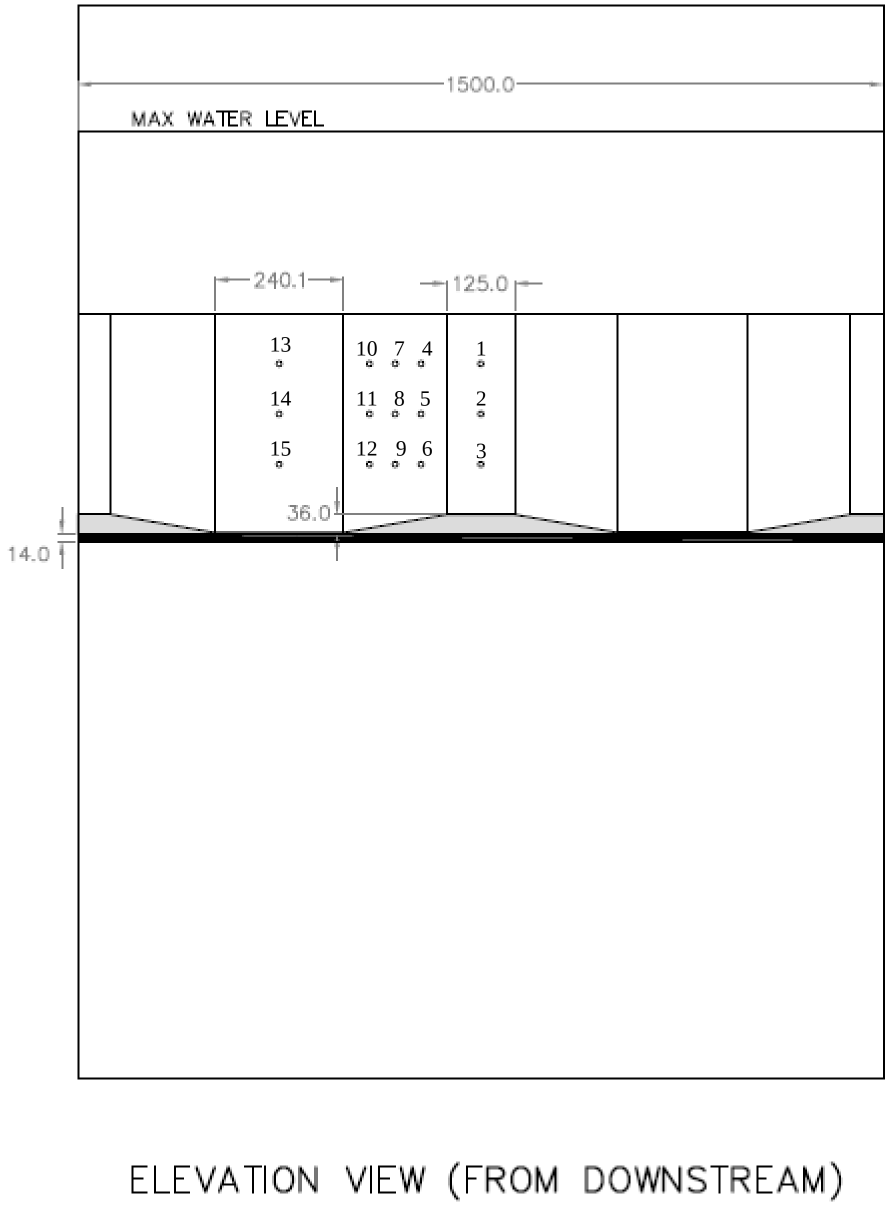

Figure B.2 Diagram showing the labyrinth model design from downstream, with labels for pressure sensors

Test 1: 215 m^3/s

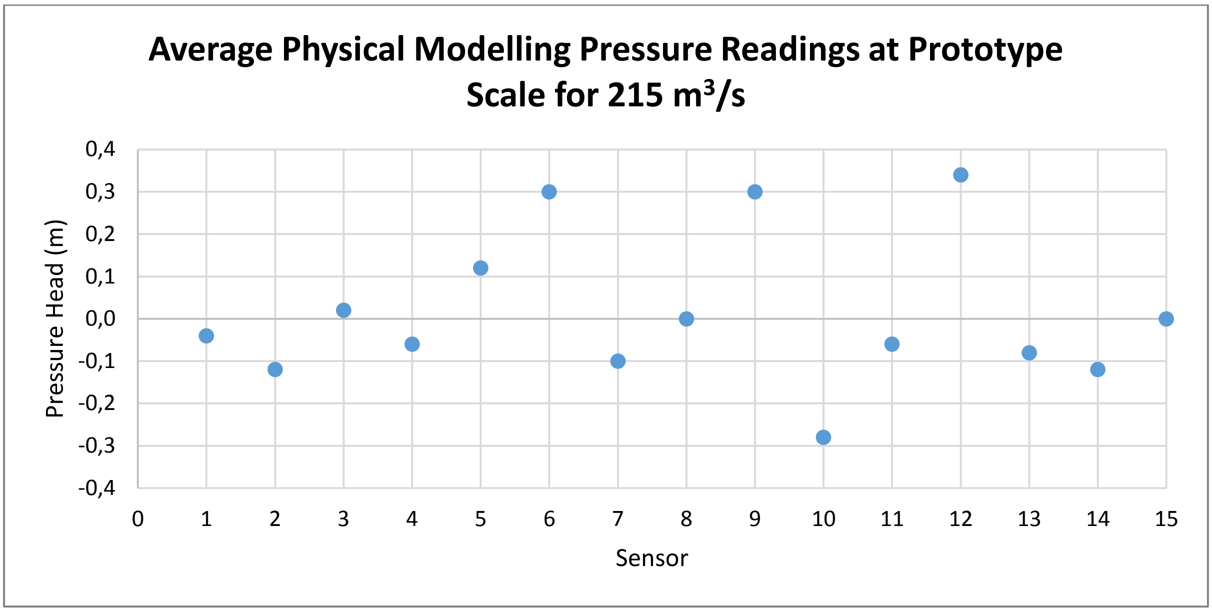

Figure B.3 Physical modelling average pressure readings for all sensors for a flow rate of 215 m^3/s at the prototype scale (60 l/s at a scale of 1:20)

Test 2: 361 m^3/s

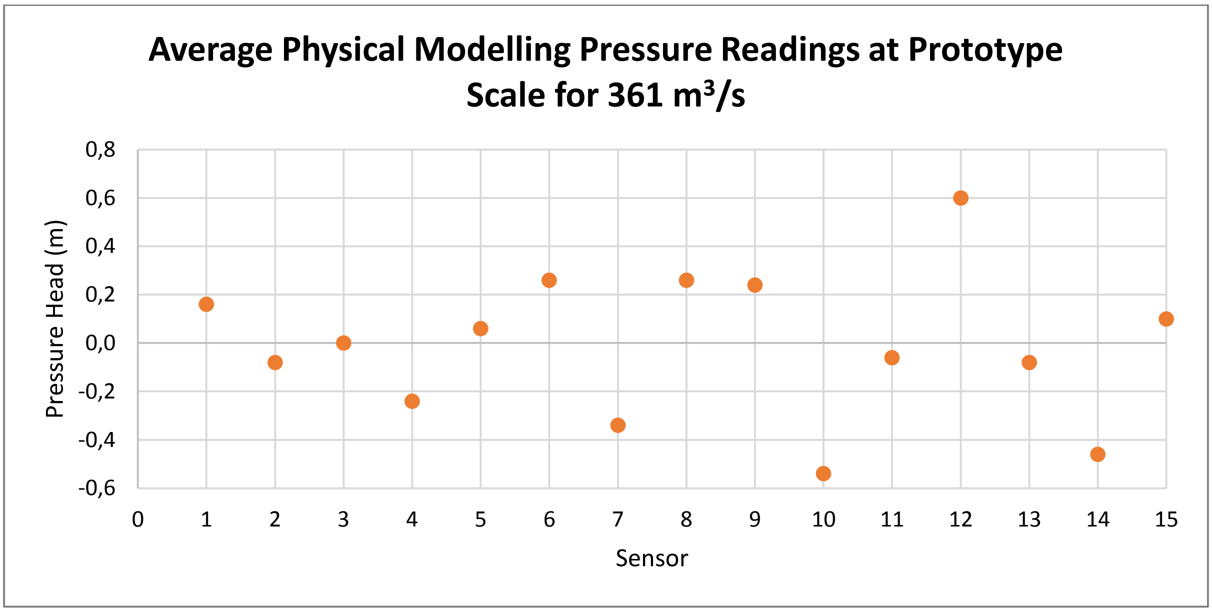

Figure B.4 Physical modelling average pressure readings for all sensors for a flow rate of 361 m^3/s at the prototype scale (101 l/s at a scale of 1:20)

Test 3: 544 m^3/s

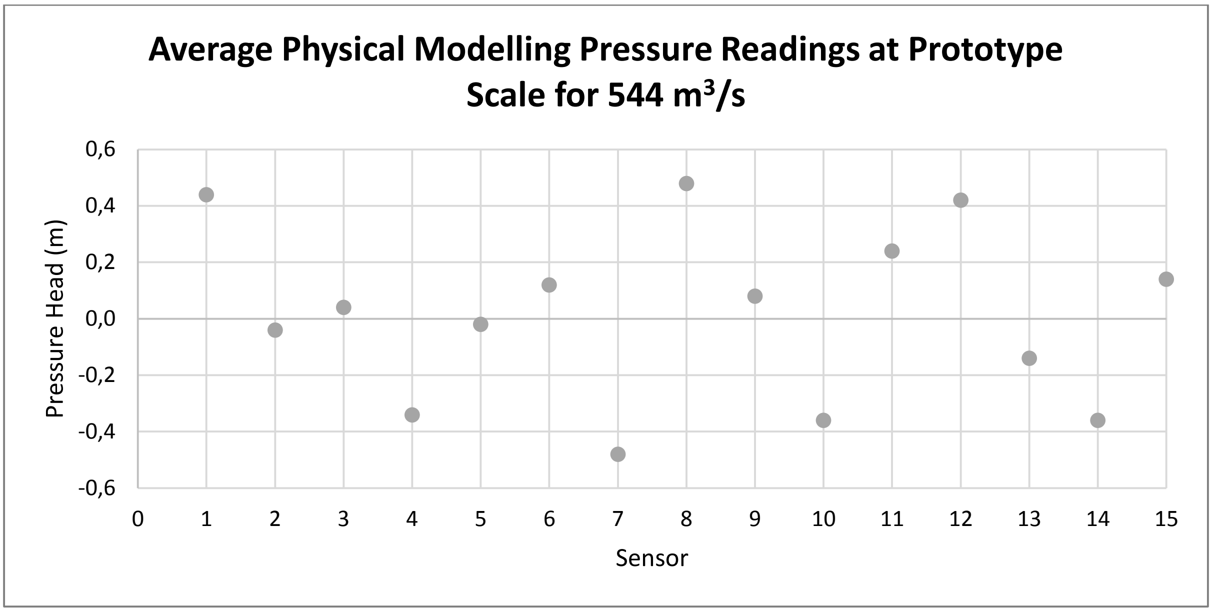

Figure B.5 Physical modelling average pressure readings for all sensors for a flow rate of 544 m^3/s at the prototype scale (152 l/s at a scale of 1:20)

Test 4: 712 m^3/s

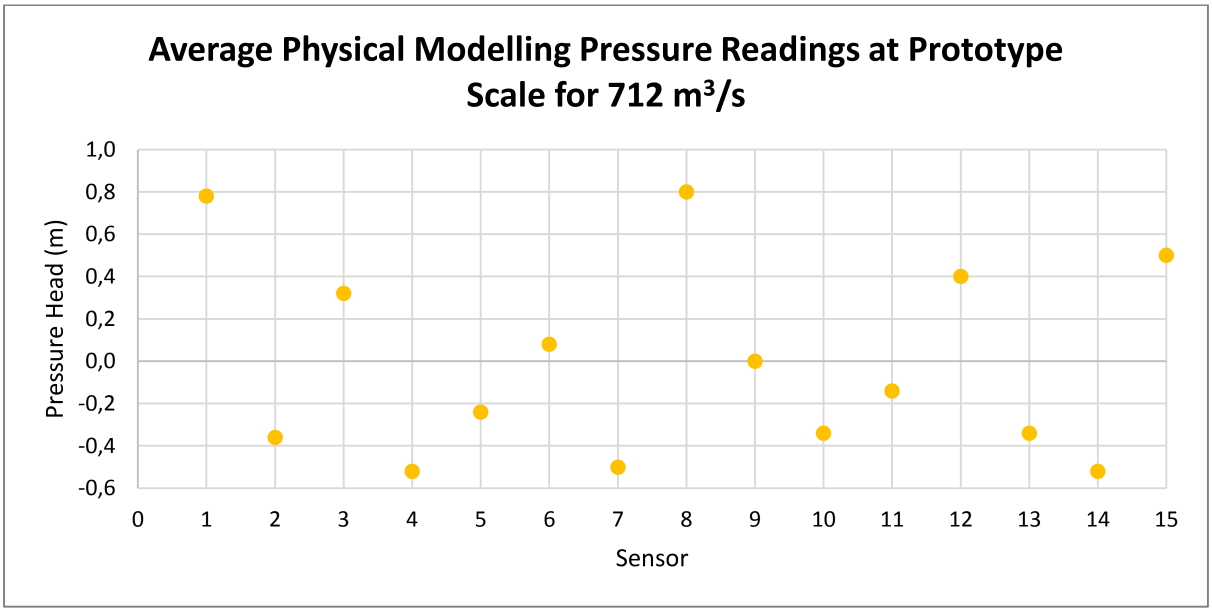

Figure B.6 Physical modelling average pressure readings for all sensors for a flow rate of 712 m^3/s at the prototype scale (199 l/s at a scale of 1:20)

Test 5: 898 m^3/s

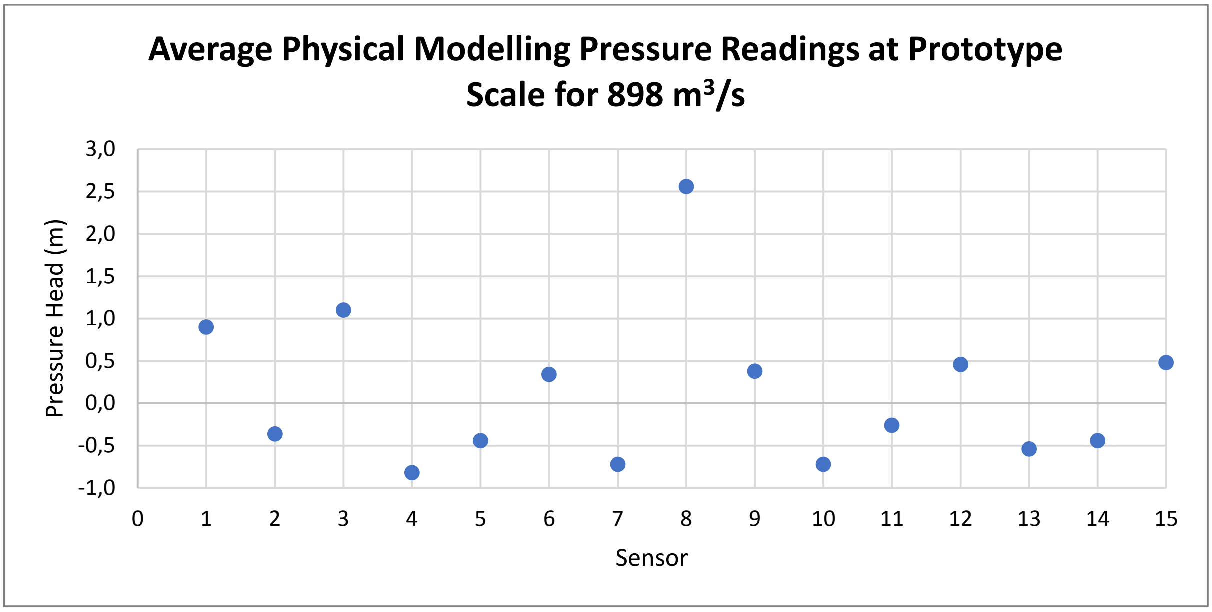

Figure B.7 Physical modelling average pressure readings for all sensors for a flow rate of 898 m^3/s *at the prototype scale (251 l/s at a scale of 1:20)*

Test 6: 1 063 m^3/s

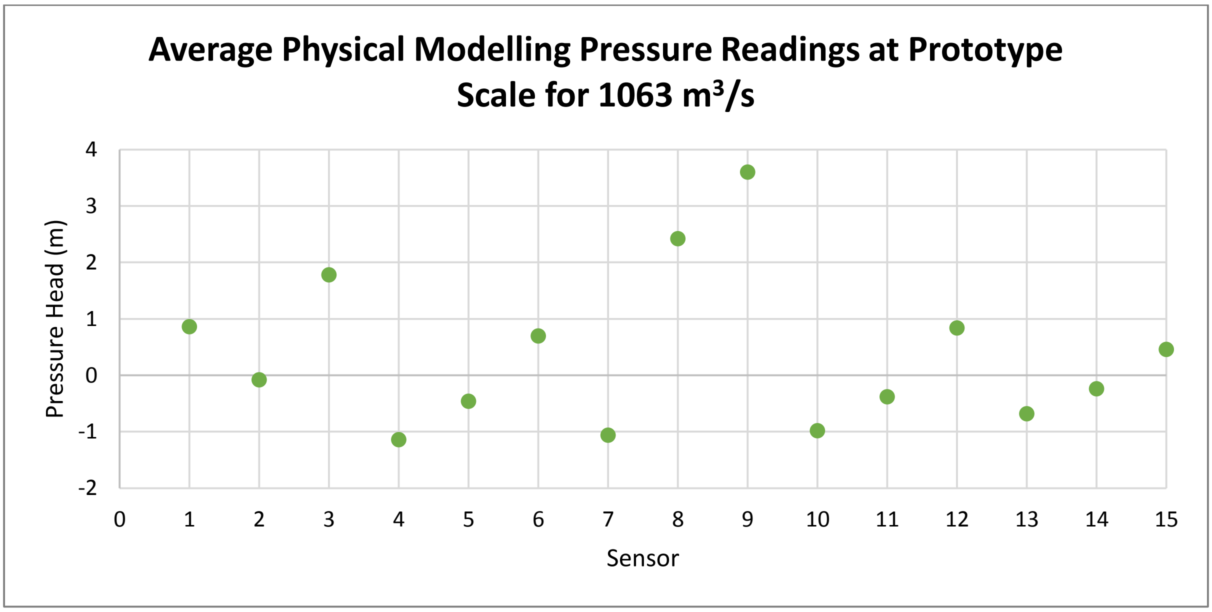

Figure B.8 Physical modelling average pressure readings for all sensors for a flow rate of 1 063 m^3/s *at the prototype scale (297 l/s at a scale of 1:20)*

Test 7: 1 249 m^3/s

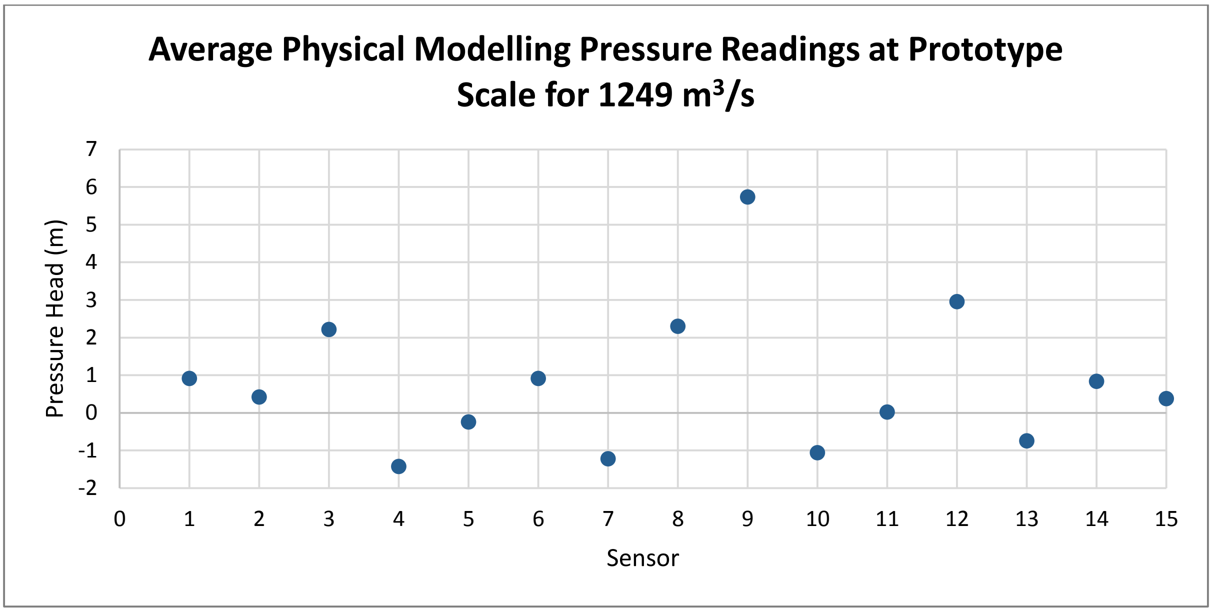

Figure B.9 Physical modelling average pressure readings for all sensors for a flow rate of 1 249 m^3/s at the prototype scale (349 l/s at a scale of 1:20)

Test 8: 1 424 m^3/s

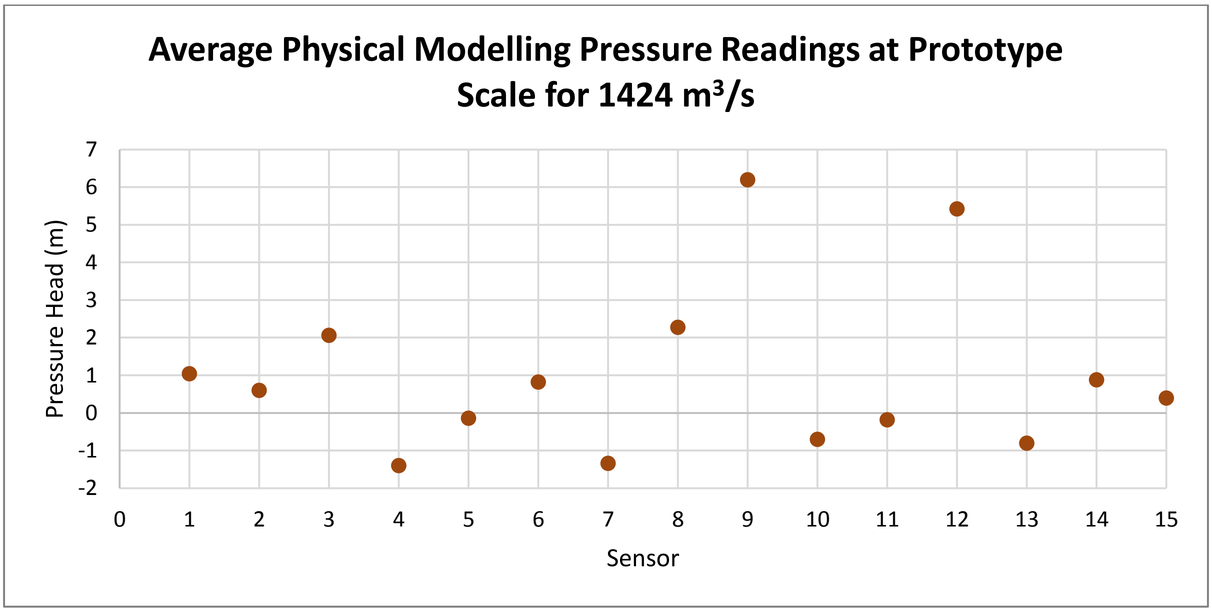

Figure B.10 Physical modelling average pressure readings for all sensors for a flow rate of 1 424 m^3/s at the prototype scale (398 l/s at a scale of 1:20)

Test 9: 1 606 m^3/s

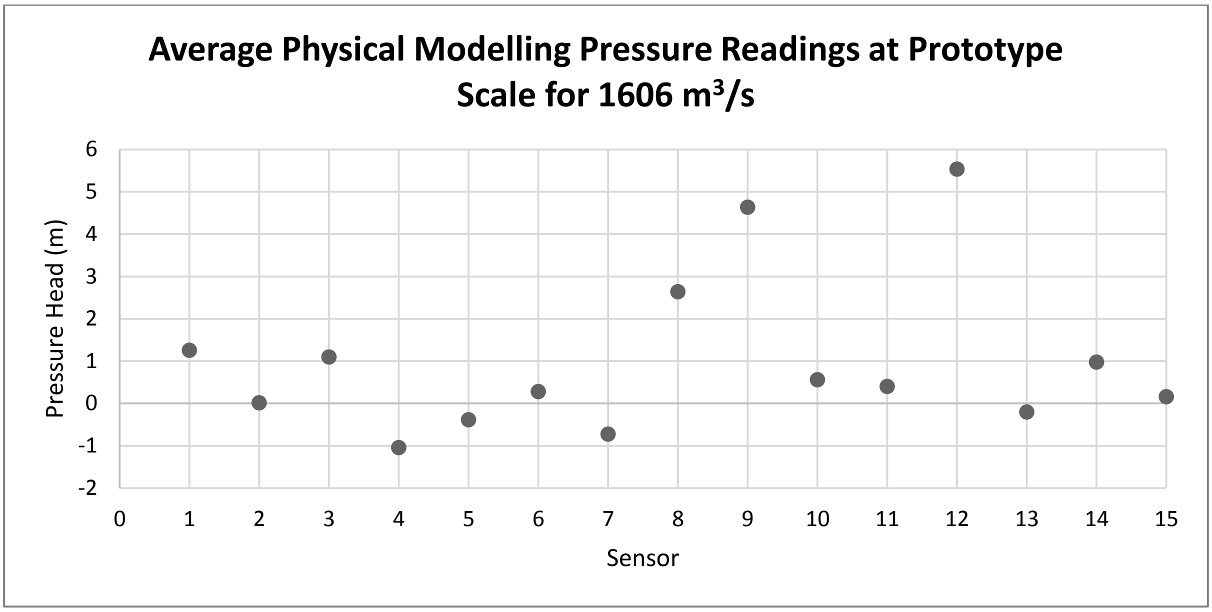

Figure B.11 Physical modelling average pressure readings for all sensors for a flow rate of 1 606 m^3/s at the prototype scale (449 l/s at a scale of 1:20)

Test 10: 1 789 m^3/s

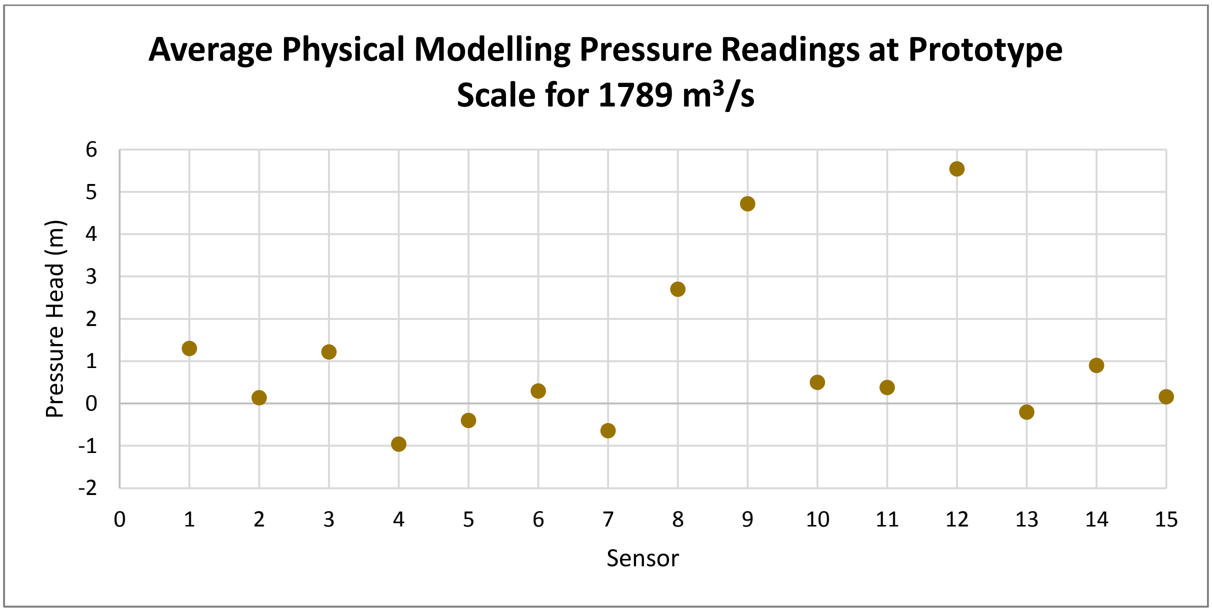

Figure B.12 Physical modelling average pressure readings for all sensors for a flow rate of 1 789 m^3/s at the prototype scale (500 l/s at a scale of 1:20)

Test 11: 1 968 m^3/s

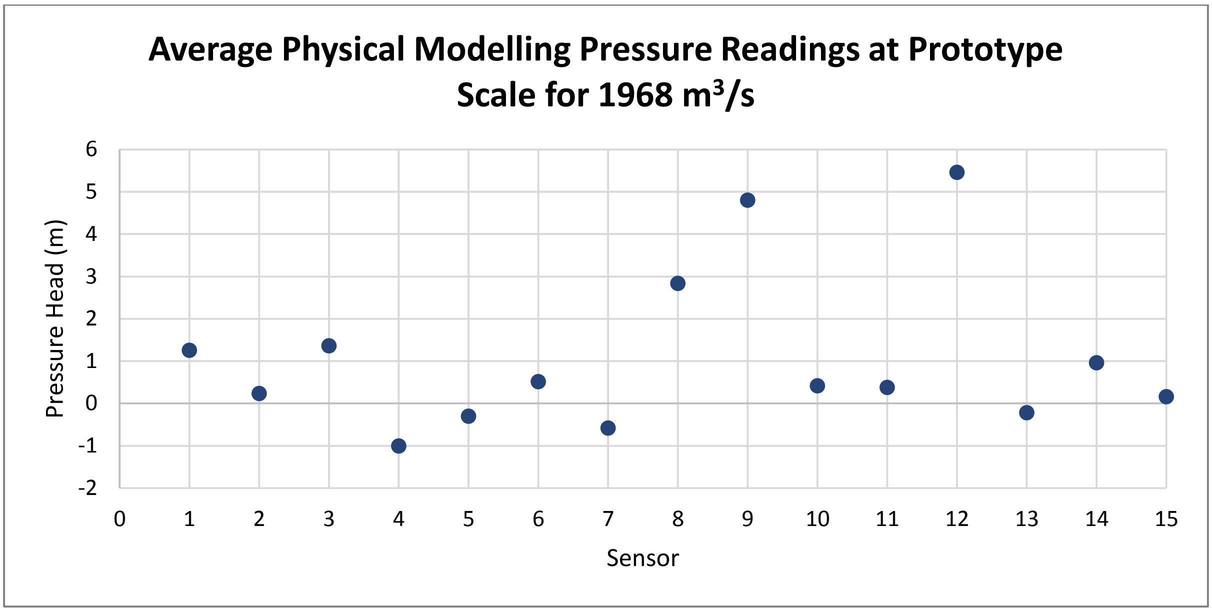

Figure B.13 Physical modelling average pressure readings for all sensors for a flow rate of 1 968 m^3/s *at the prototype scale (550 l/s at a scale of 1:20)*

Test 12: 2 136 m^3/s

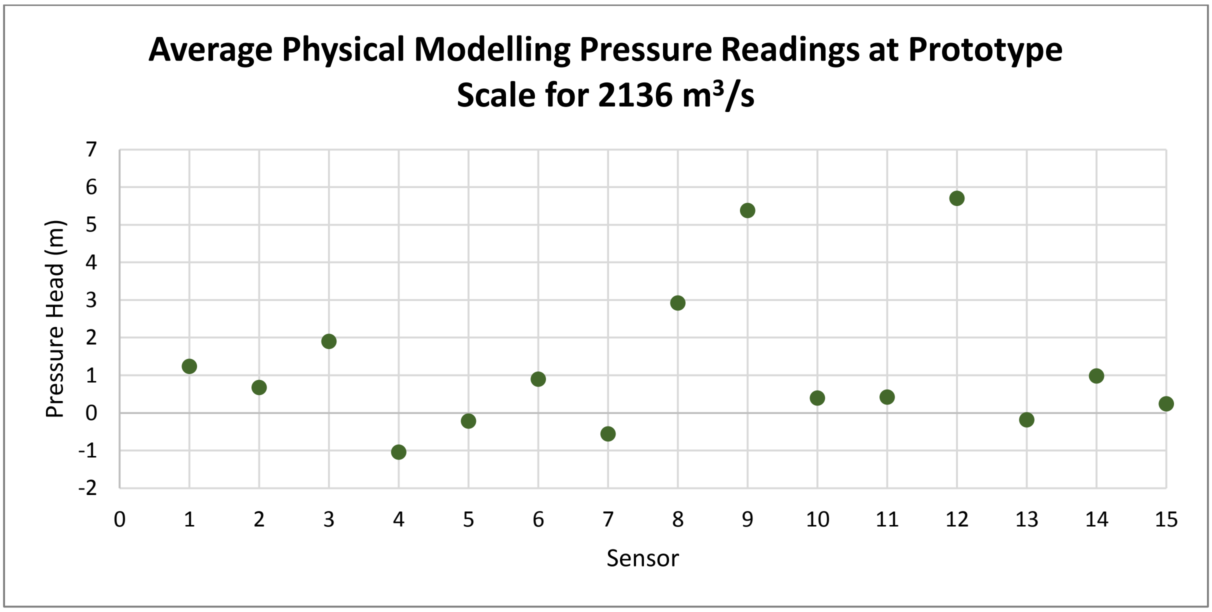

Figure B.14 Physical modelling average pressure readings for all sensors for a flow rate of 2 136 m^3/s *at the prototype scale (597 l/s at a scale of 1:20)*

Appendix C: Photographs of Physical Modelling

Figure C.1 Physical model viewed from downstream showing Perspex side walls and pressure sensor cables coming out from underneath the model

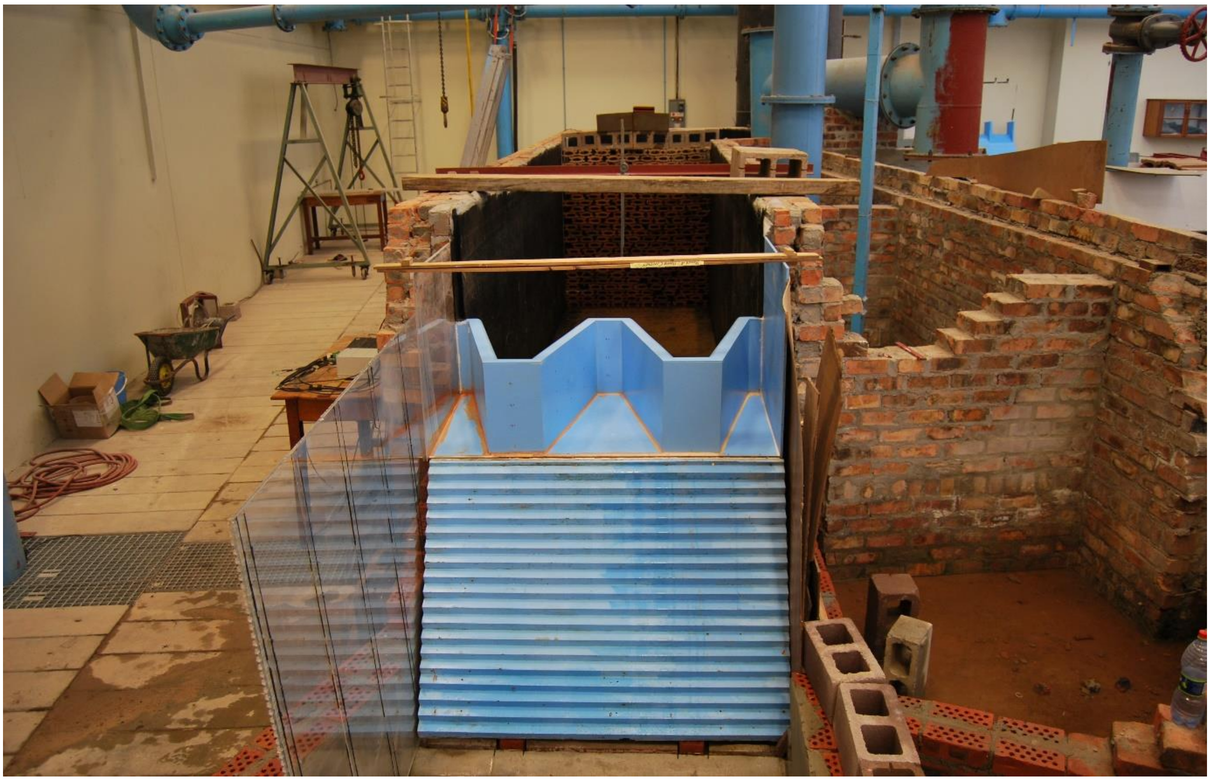

Figure C.2 Labyrinth weir model viewed from downstream showing weir crest, flume and baffle wall at upstream section of flume

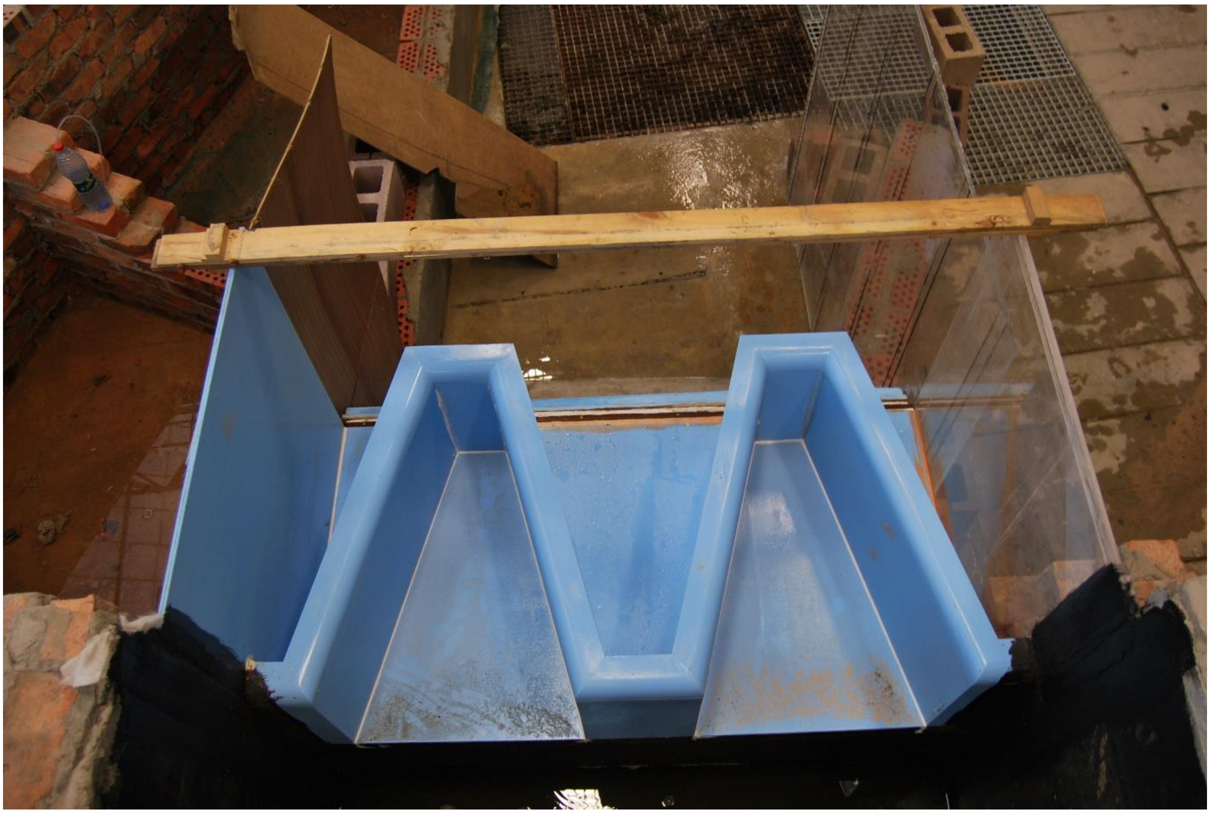

Figure C.3 Labyrinth weir crest viewed from above

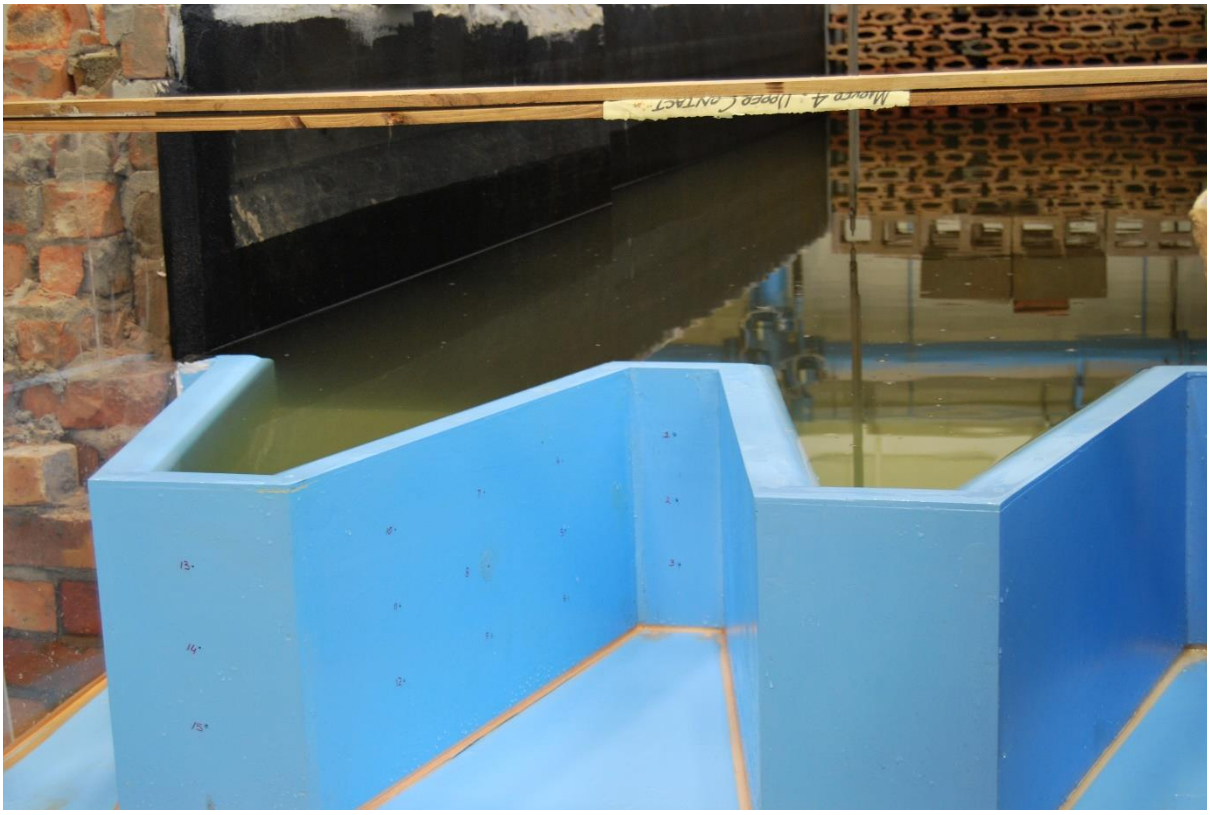

Figure C.4 Labyrinth weir crest viewed from downstream, showing water in the flume at the crest level and pressure sensor positions on the downstream crest face

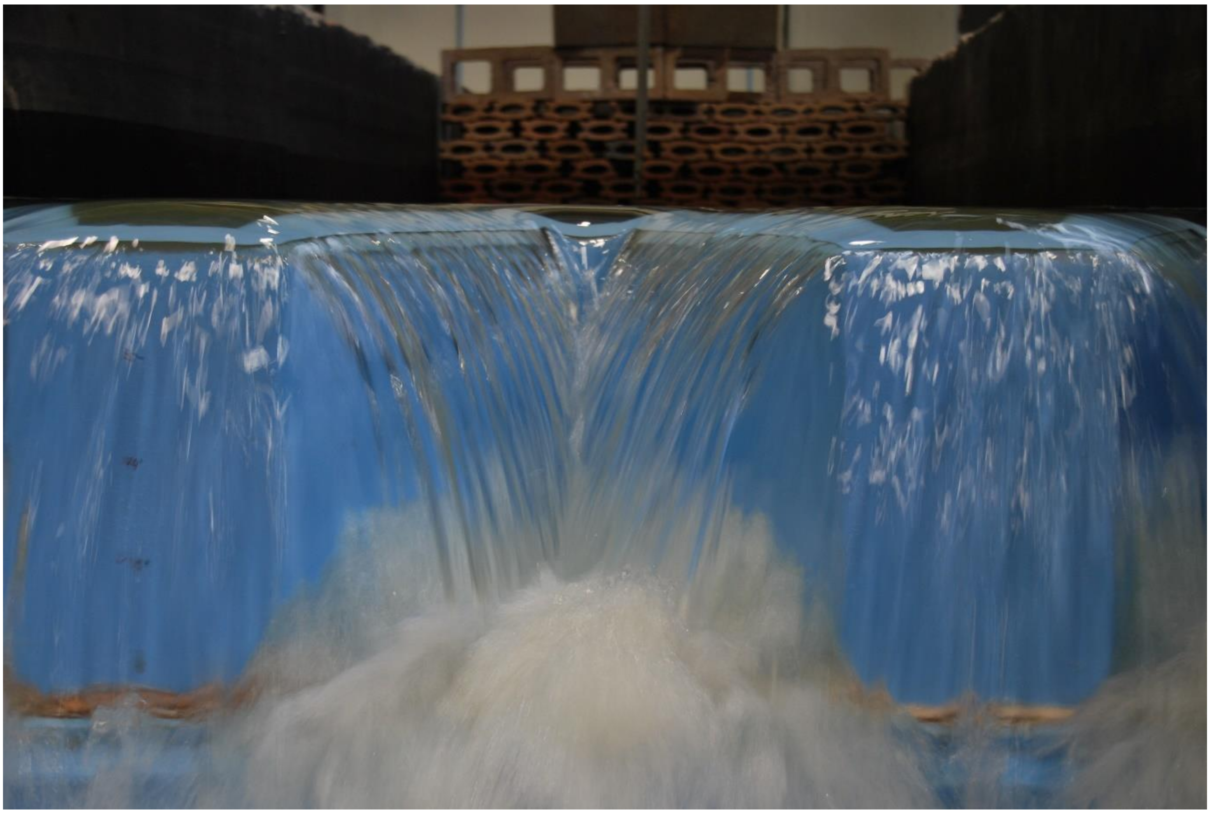

Figure C.5 Labyrinth weir under low flow conditions viewed from downstream indicating flow patterns, colliding nappes and aeration conditions

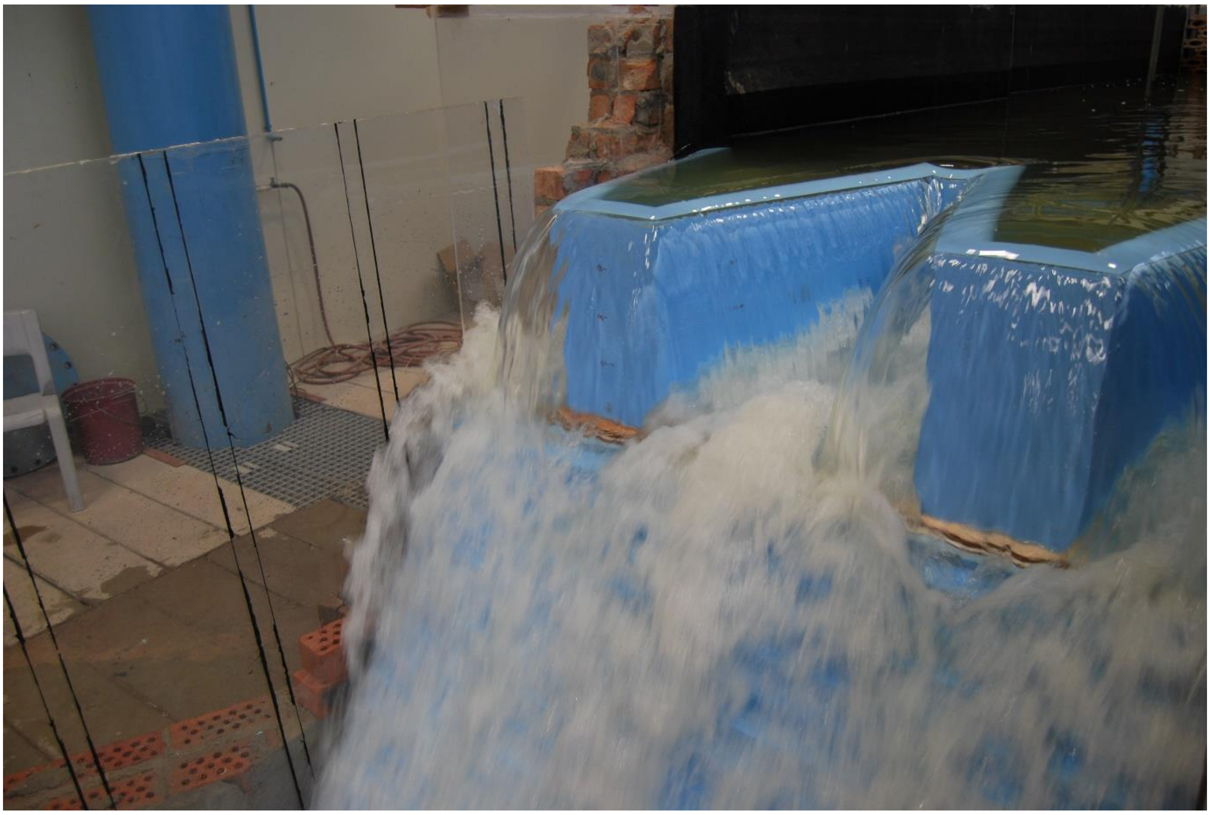

Figure C.6 Labyrinth weir viewed from downstream under low flow conditions, showing Perspex side walls and flow behaviour downstream of the weir

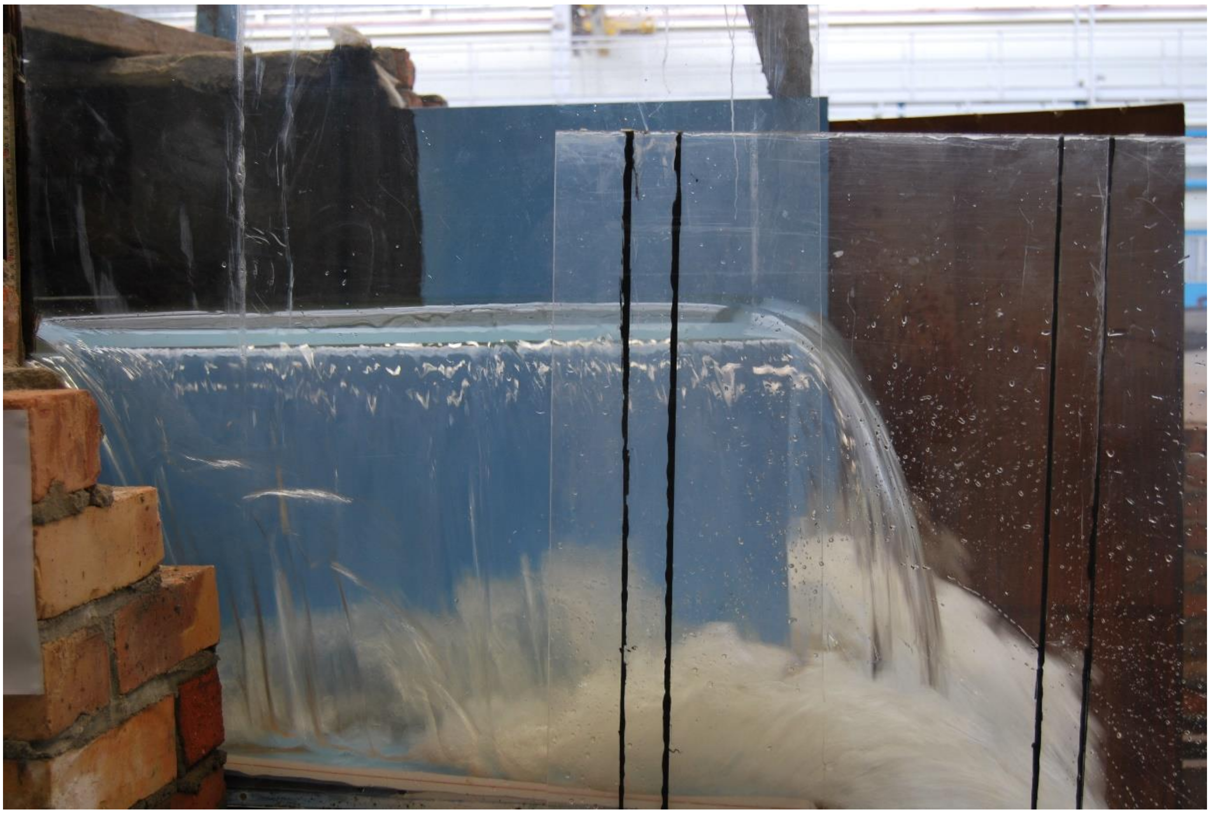

Figure C.7 Labyrinth weir side view under low flow conditions, showing aeration conditions, surcharge level and flow patterns

Figure C.8 Labyrinth weir viewed from downstream under medium flow conditions, showing turbulence, aeration and flow patterns

Figure C.9 Labyrinth weir model viewed from above under medium flow conditions, showing flow patterns and aration conditions

Figure C.10 Labyrinth weir viewed from the side under medium flow conditions, showing surcharge and aeration

Figure C.11 Labyrinth weir viewed from downstream nder high flow conditions, showing flow patterns and aeration conditions

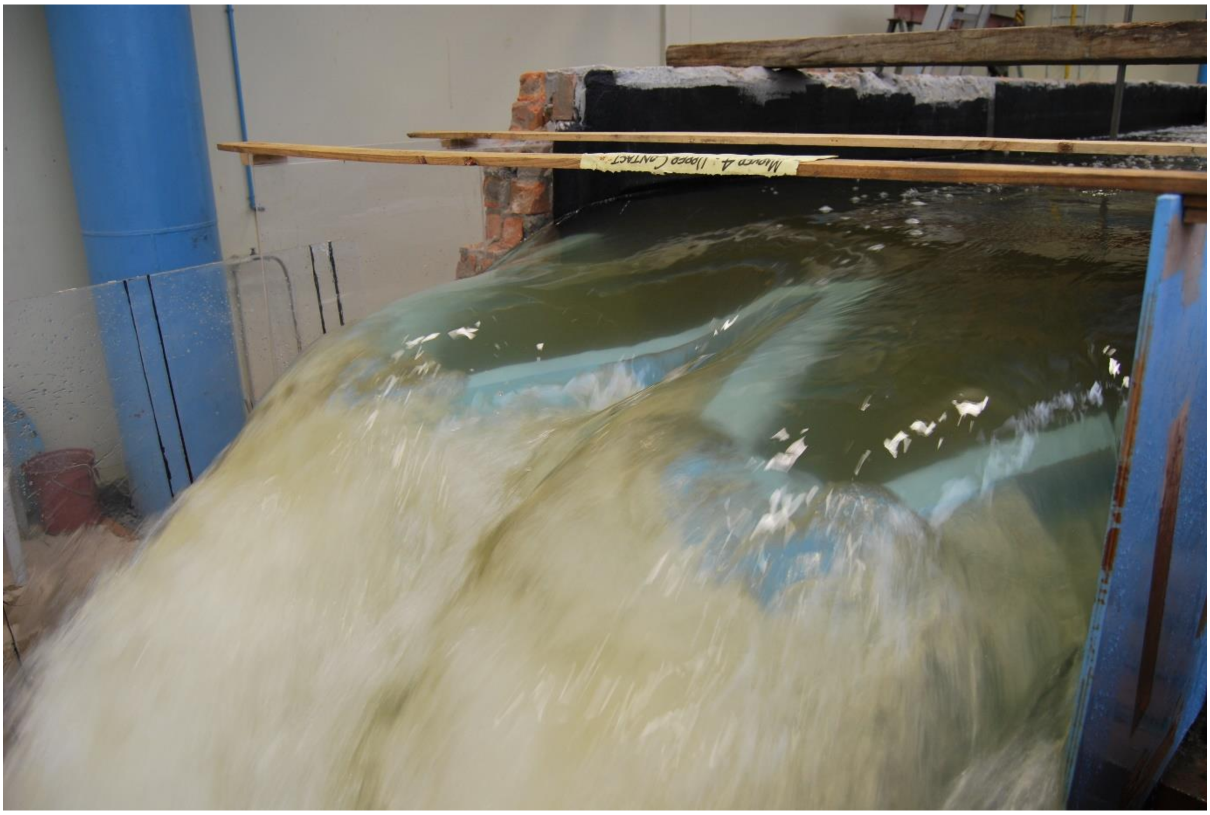

Figure C.12 Labyrinth weir viewed from downstream under high flow conditions, showing surcharge level, flow patterns and aeration conditions

Figure C.13 Labyrinth weir viewed from the side under high flow conditions, showing surcharge and aeration conditions

Figure C.14 Labyrinth weir viewed from downstream under high flow conditions, showing aeration conditions, turbulence and flow patterns

Appendix D: CFD Modelling Results

Test 1: 215 m^3/s

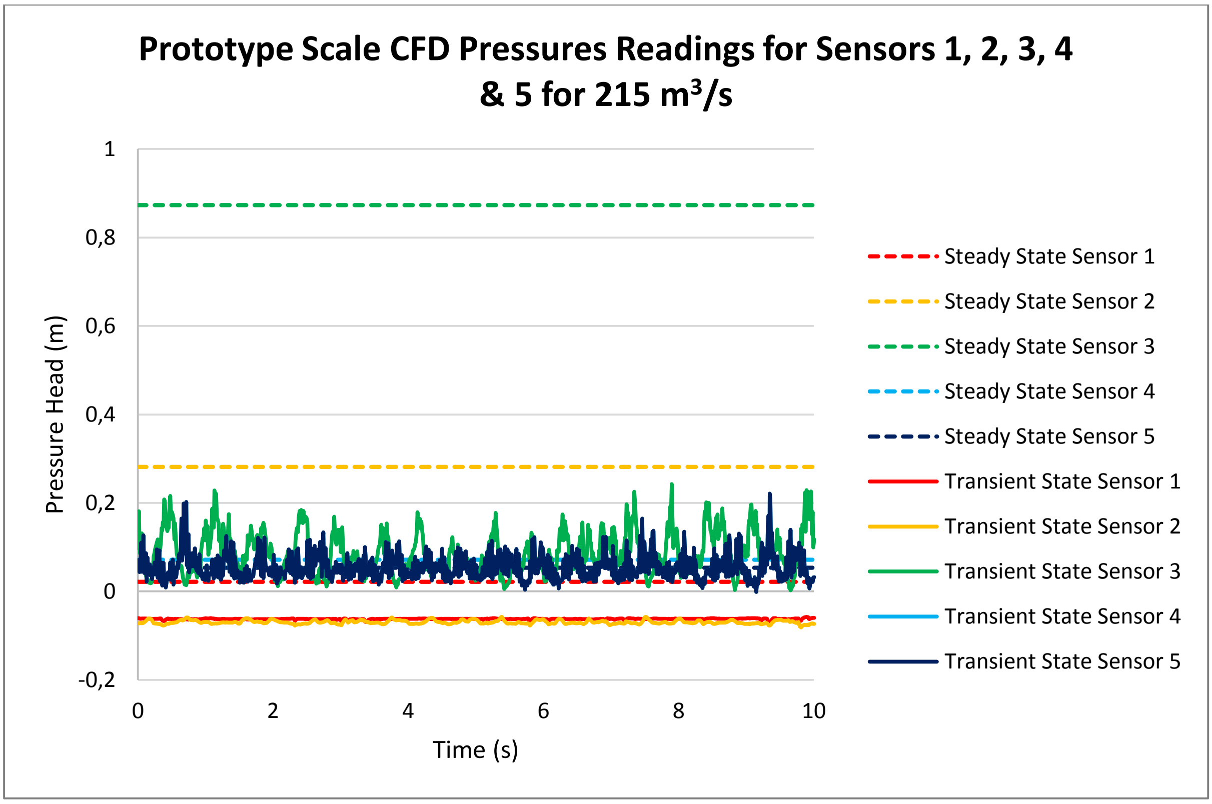

Figure D.1 Transient and steady state pressure readings for sensors 1-5 for a flow rate of 215 m^3/s at the prototype scale (60 l/s at a scale of 1:20)

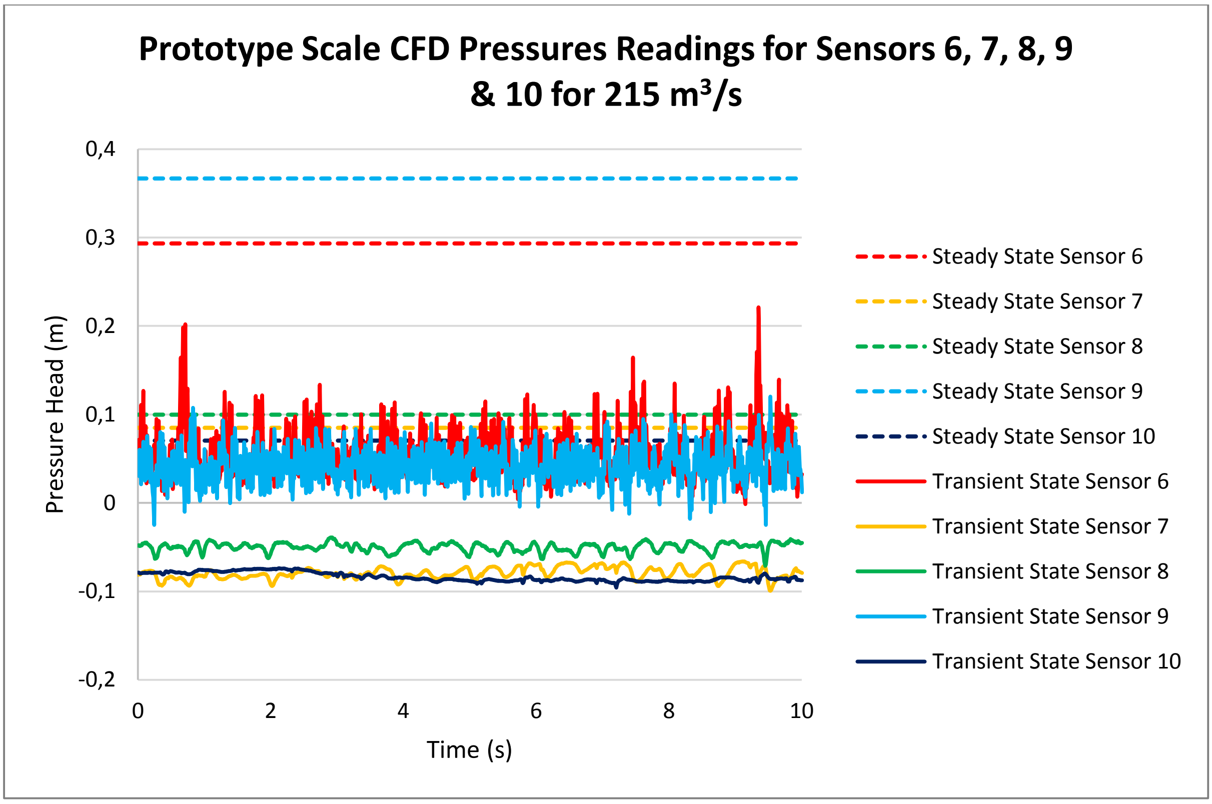

Figure D.2 Transient and steady state pressure readings for sensors 6-10 for a flow rate of 215 m^3/s at the prototype scale (60 l/s at a scale of 1:20)

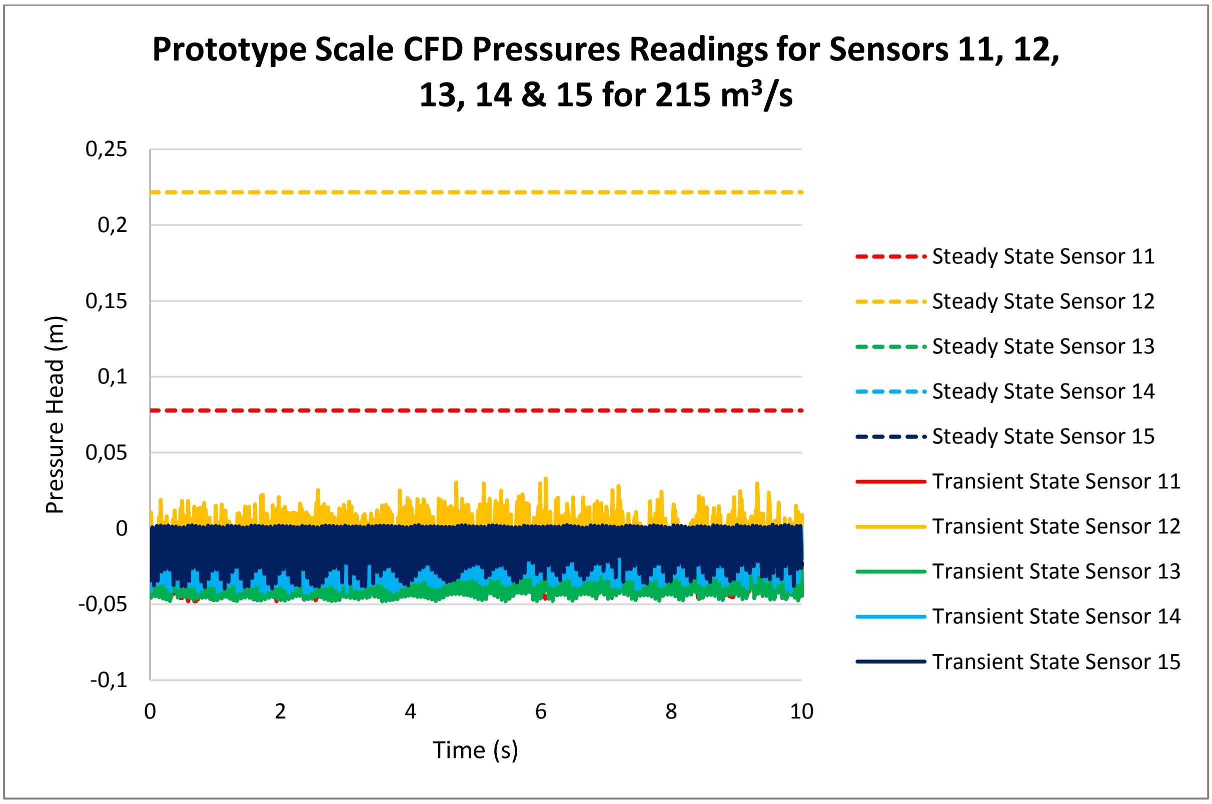

Figure D.3 Transient and steady state pressure readings for sensors 11-15 for a flow rate of 215 m^3/s at the prototype scale (60 l/s at a scale of 1:20)

Test 2: 361 m^3/s

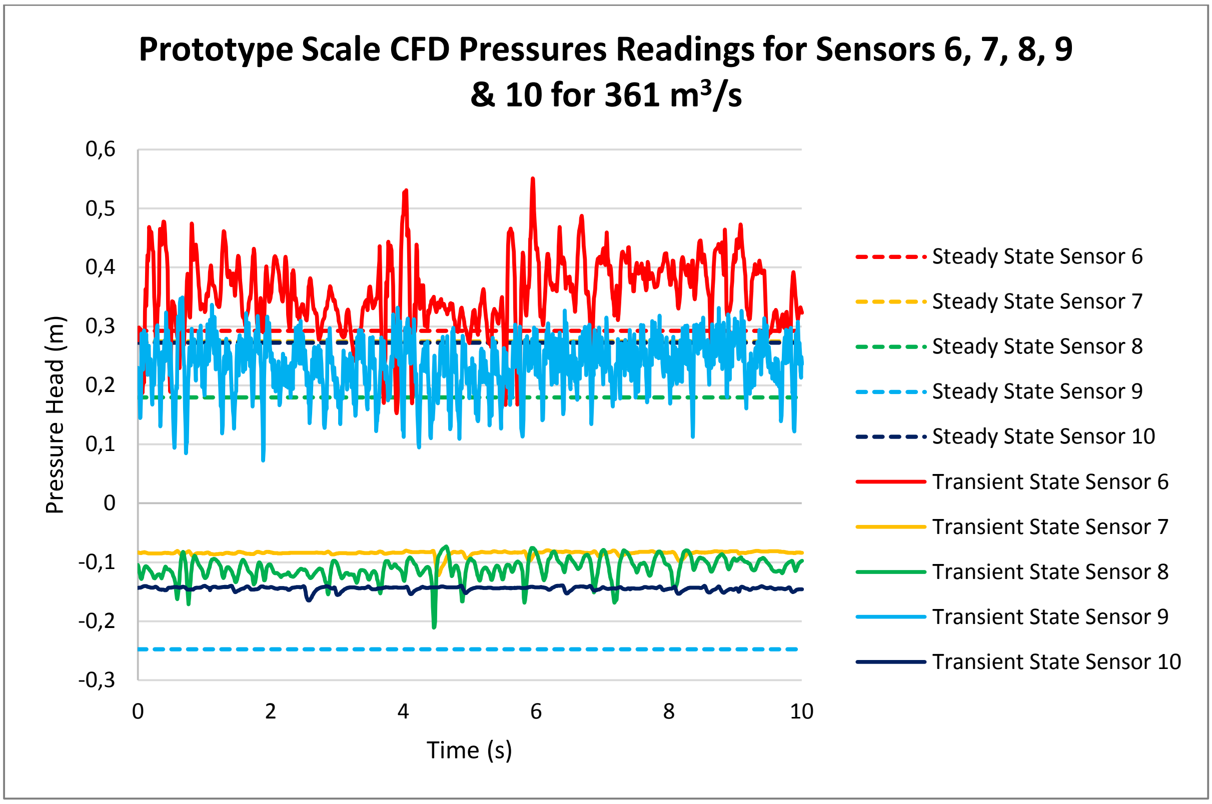

Figure D.4 Transient and steady state pressure readings for sensors 1-5 for a flow rate of 361 m^3/s at the prototype scale (101 l/s at a scale of 1:20)

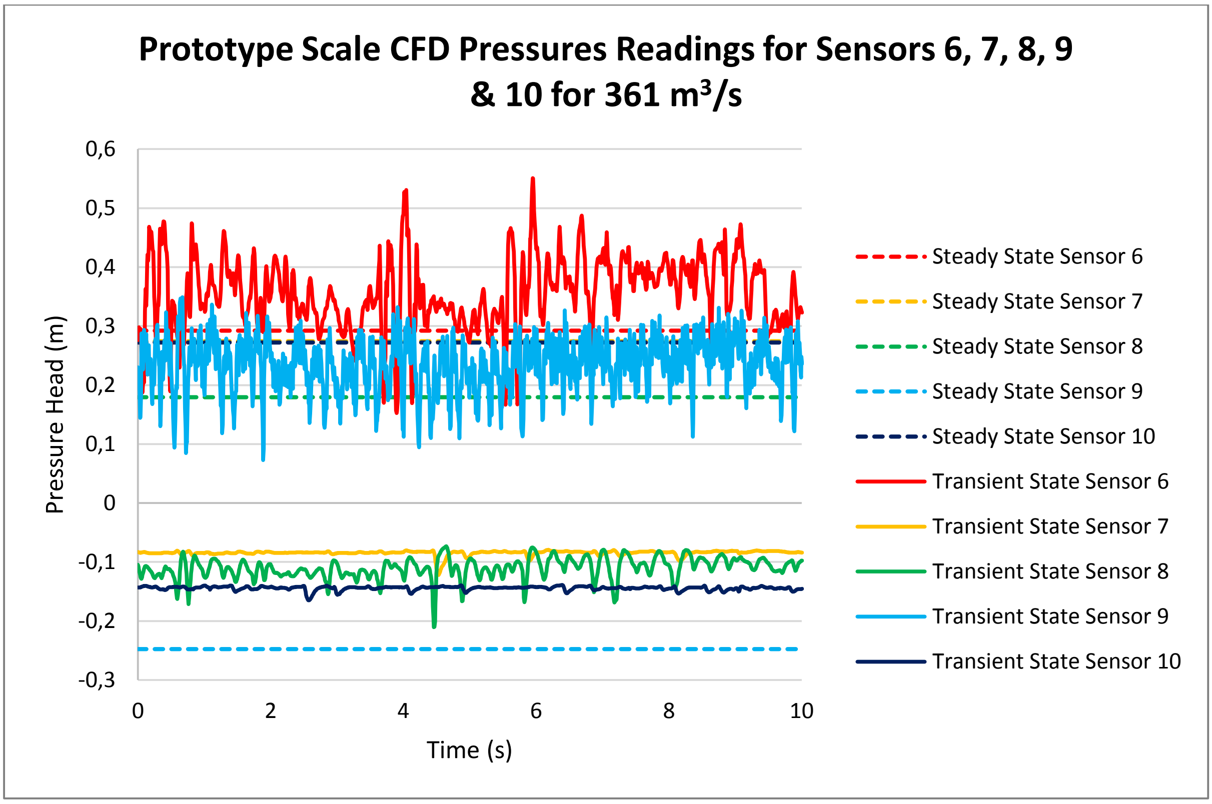

Figure D.5 Transient and steady state pressure readings for sensors 6-10 for a flow rate of 361 m^3/s at the prototype scale (101 l/s at a scale of 1:20)

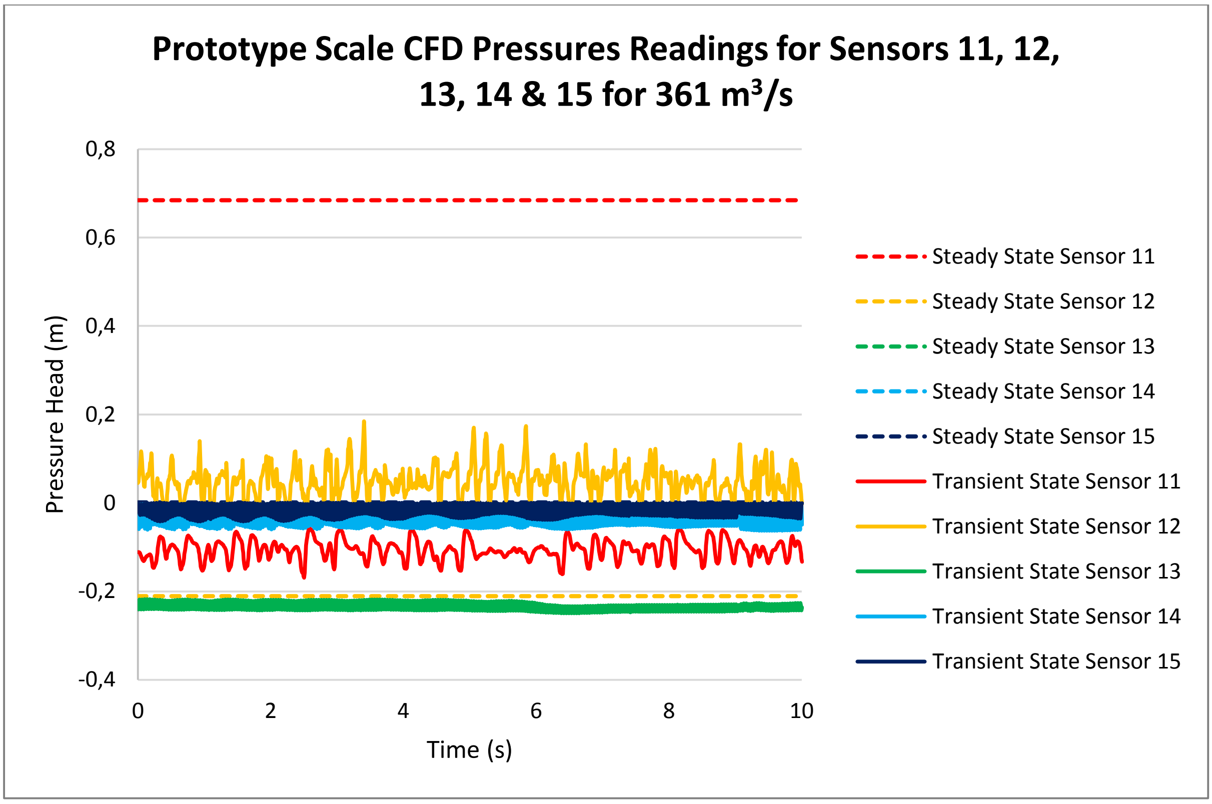

Figure D.6 Transient and steady state pressure readings for sensors 11-15 for a flow rate of 361 m^3/s at the prototype scale (101 l/s at a scale of 1:20)

Test 3: 544 m^3/s

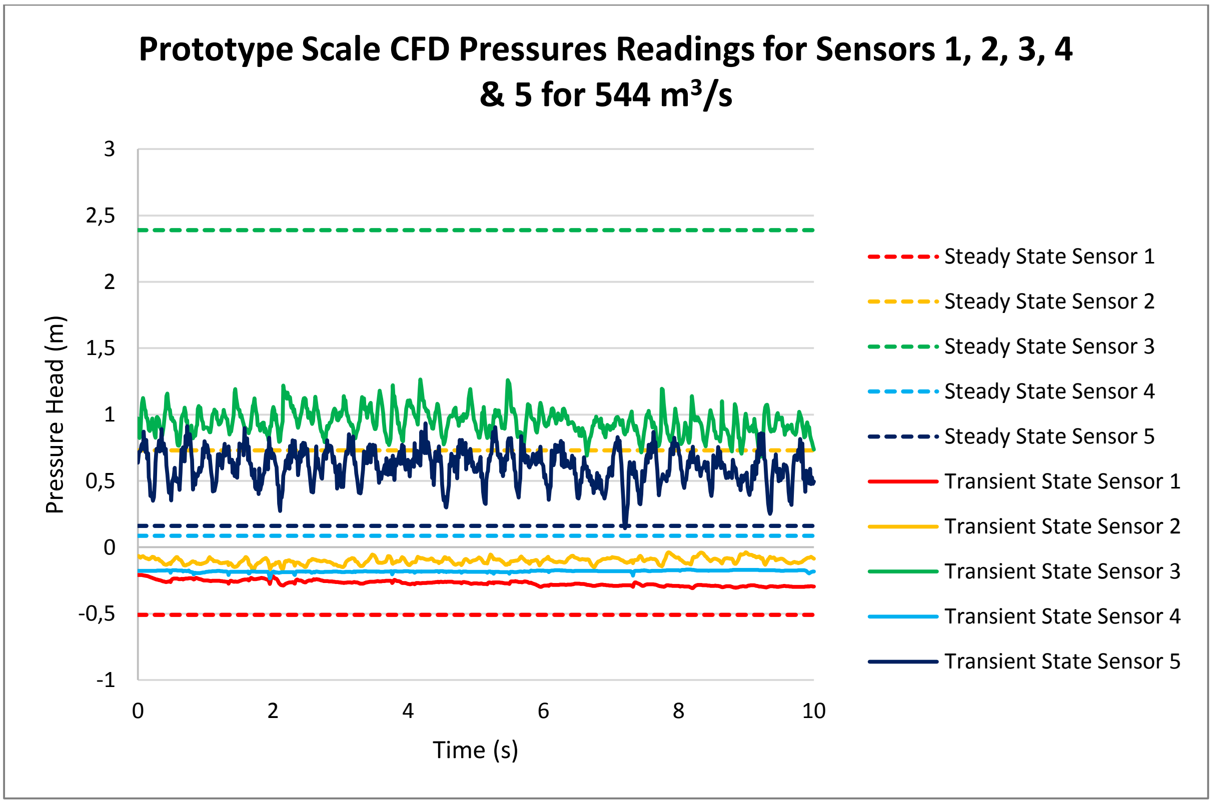

Figure D.7 Transient and steady state pressure readings for sensors 1-5 for a flow rate of 544 m^3/s at the prototype scale (152 l/s at a scale of 1:20)

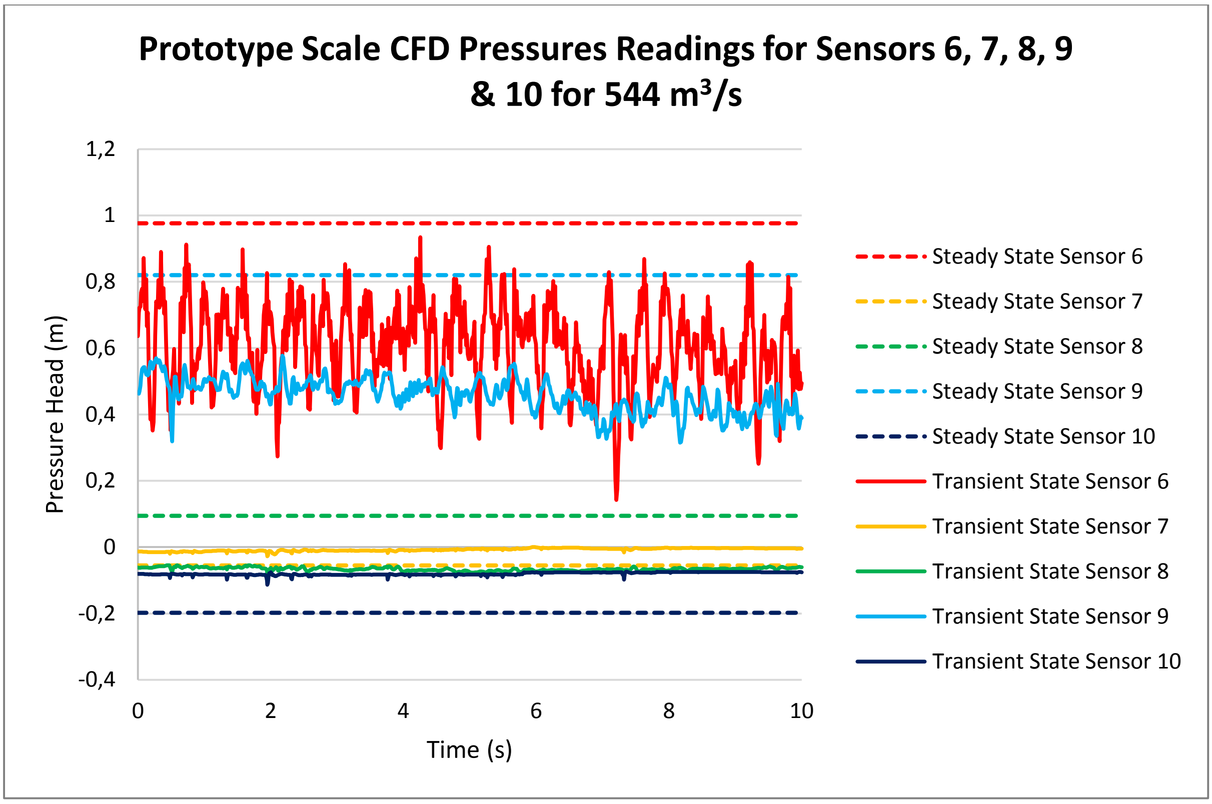

Figure D.8 Transient and steady state pressure readings for sensors 6-10 for a flow rate of 544 m^3/s at the prototype scale (152 l/s at a scale of 1:20)

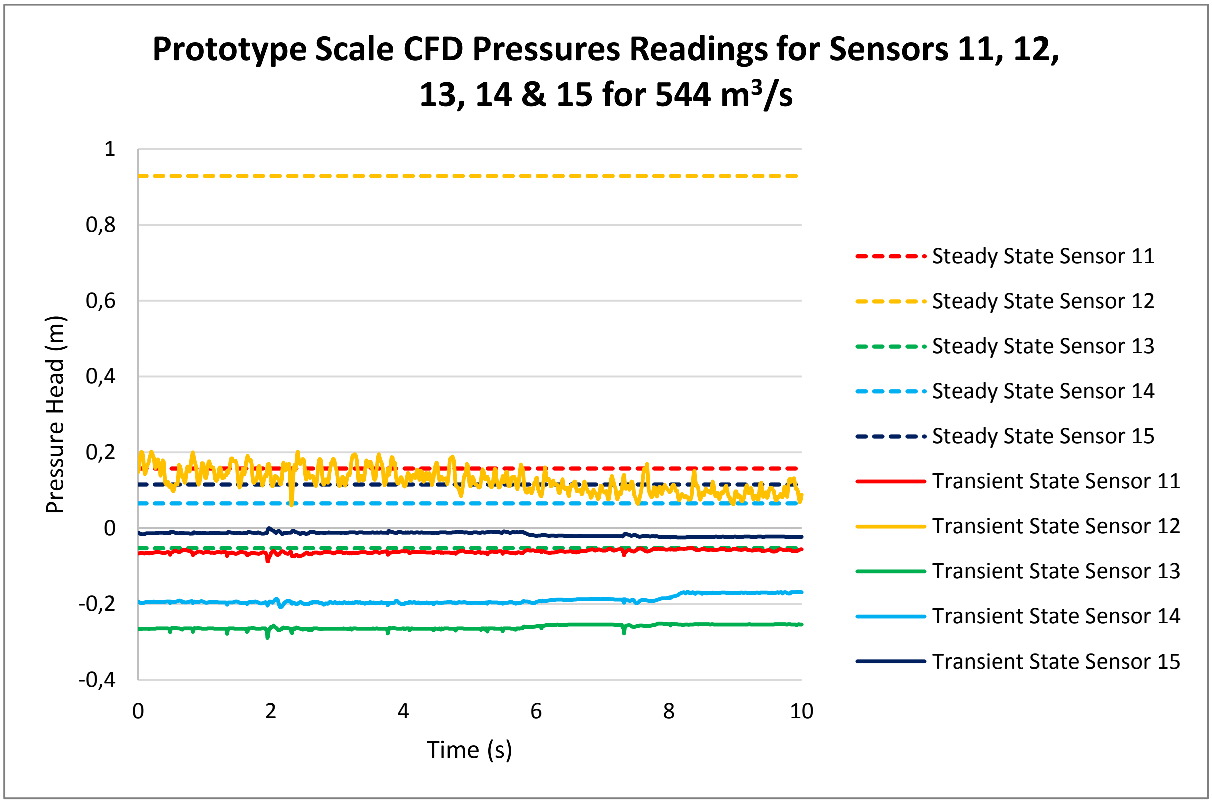

Figure D.9 Transient and steady state pressure readings for sensors 11-15 for a flow rate of 544 m^3/s at the prototype scale (152 l/s at a scale of 1:20)

Test 4: 712 m^3/s

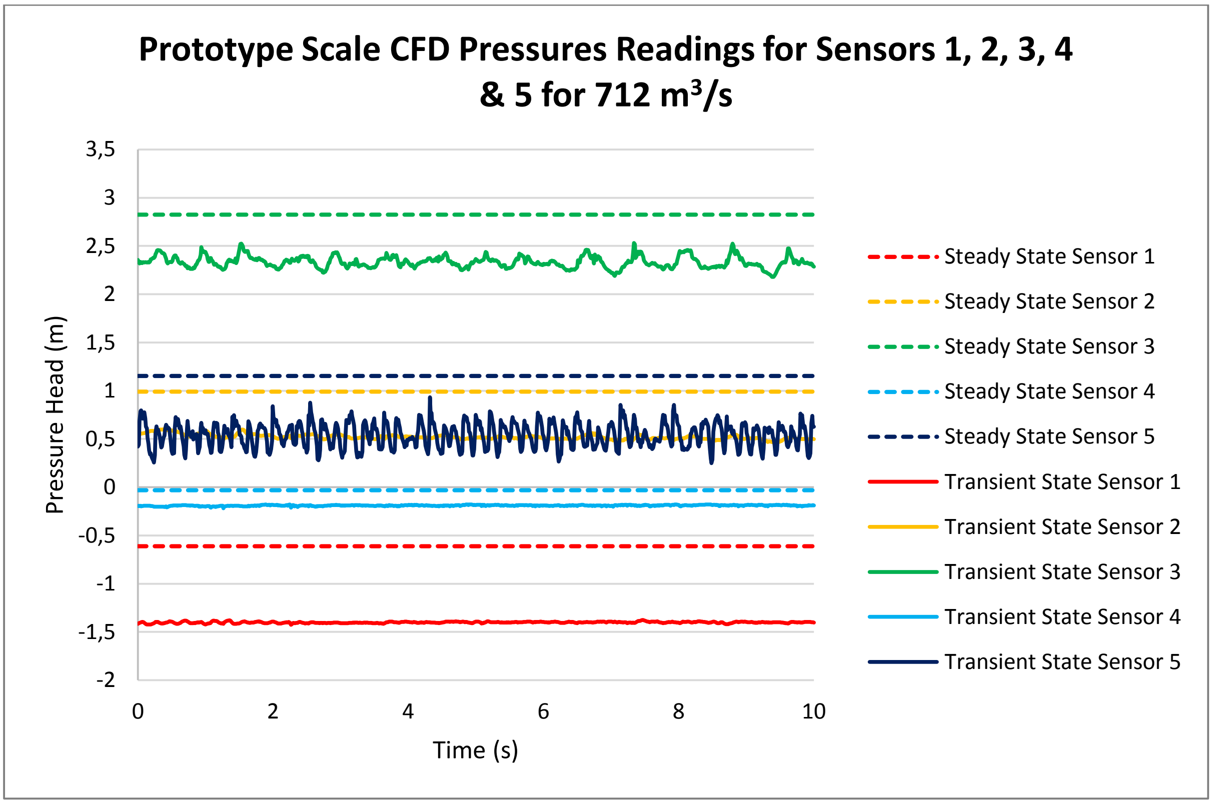

Figure D.10 Transient and steady state pressure readings for sensors 1-5 for a flow rate of 712 m^3/s at the prototype scale (199 l/s at a scale of 1:20)

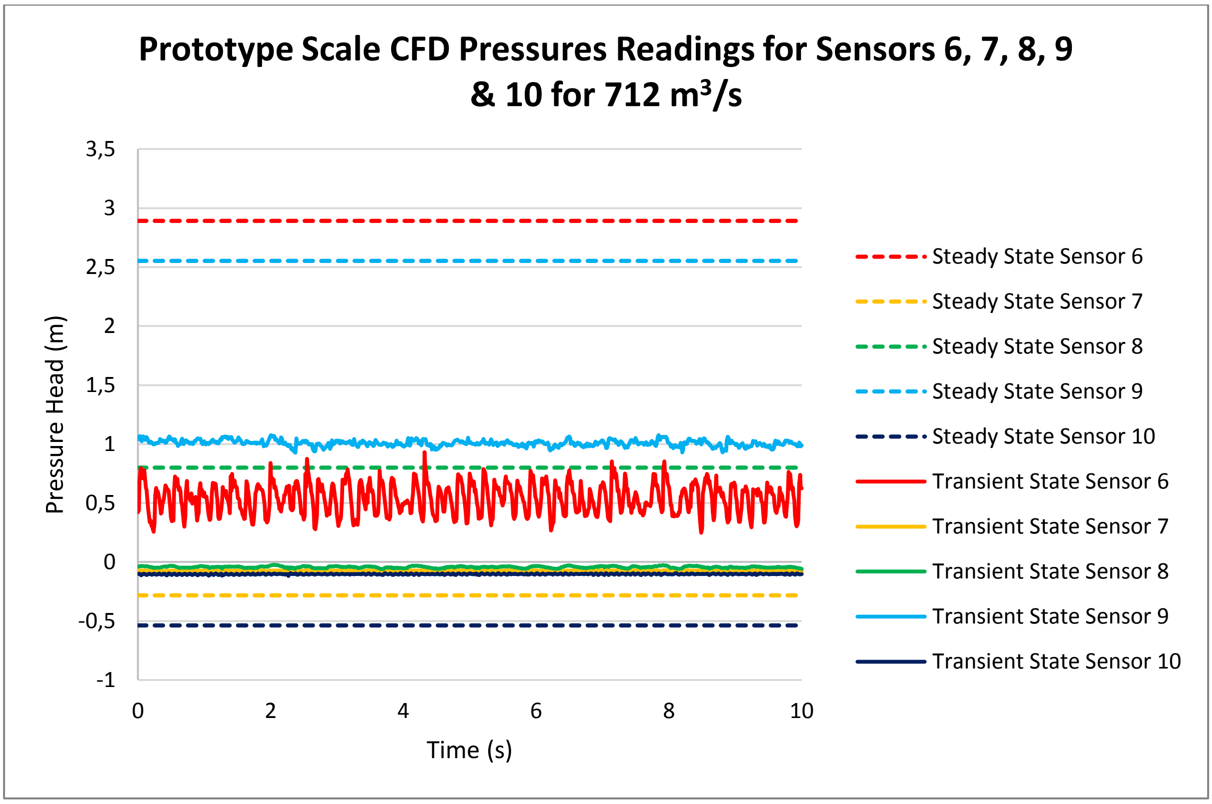

Figure D.11 Transient and steady state pressure readings for sensors 6-10 for a flow rate of 712 m^3/s at the prototype scale (199 l/s at a scale of 1:20)

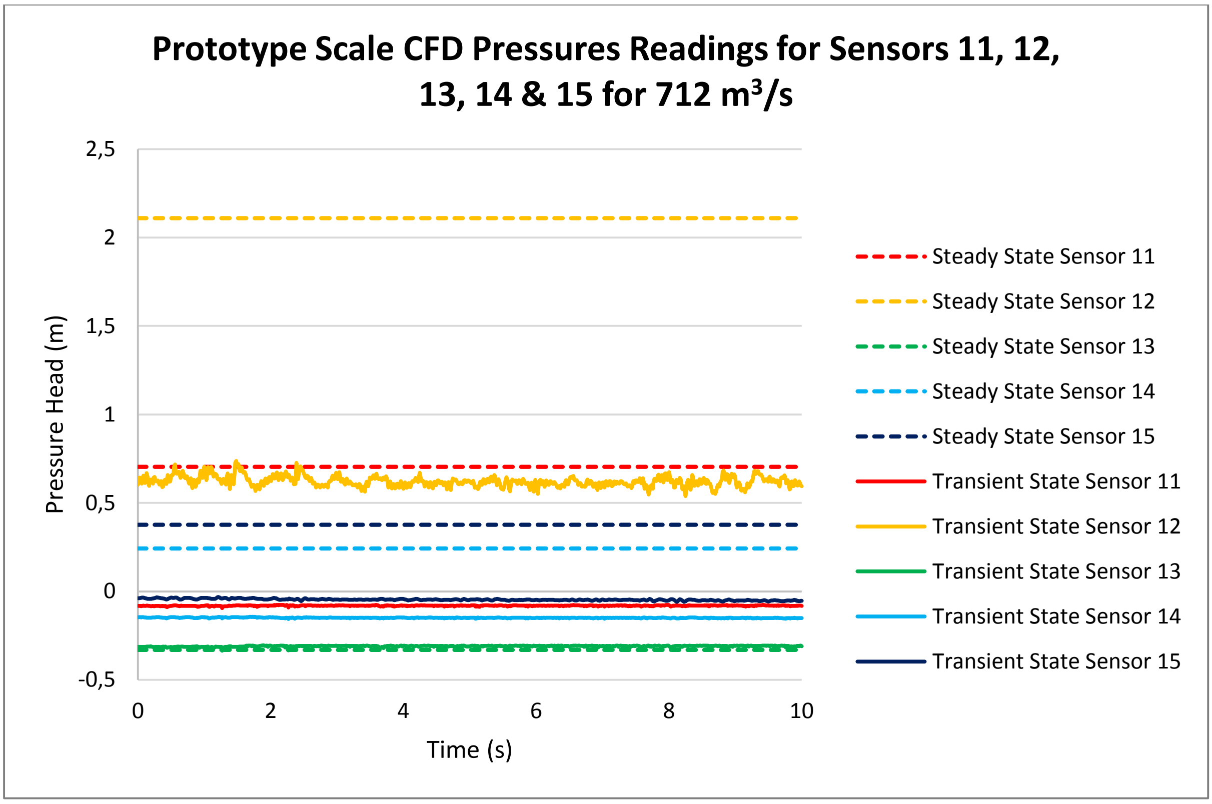

Figure D.12 Transient and steady state pressure readings for sensors 11-15 for a flow rate of 712 m^3/s at the prototype scale (199 l/s at a scale of 1:20)

Test 5: 898 m^3/s

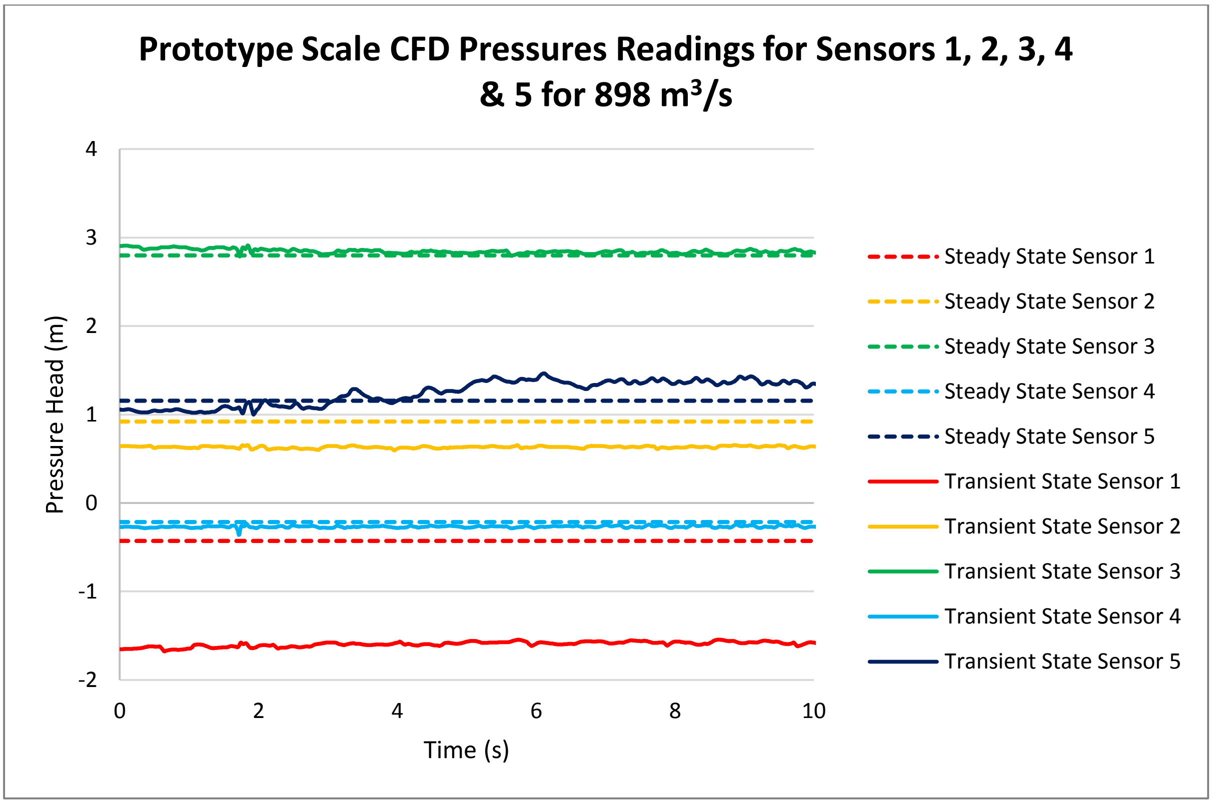

Figure D.13 Transient and steady state pressure readings for sensors 1-5 for a flow rate of 898 m^3/s at the prototype scale (251 l/s at a scale of 1:20)

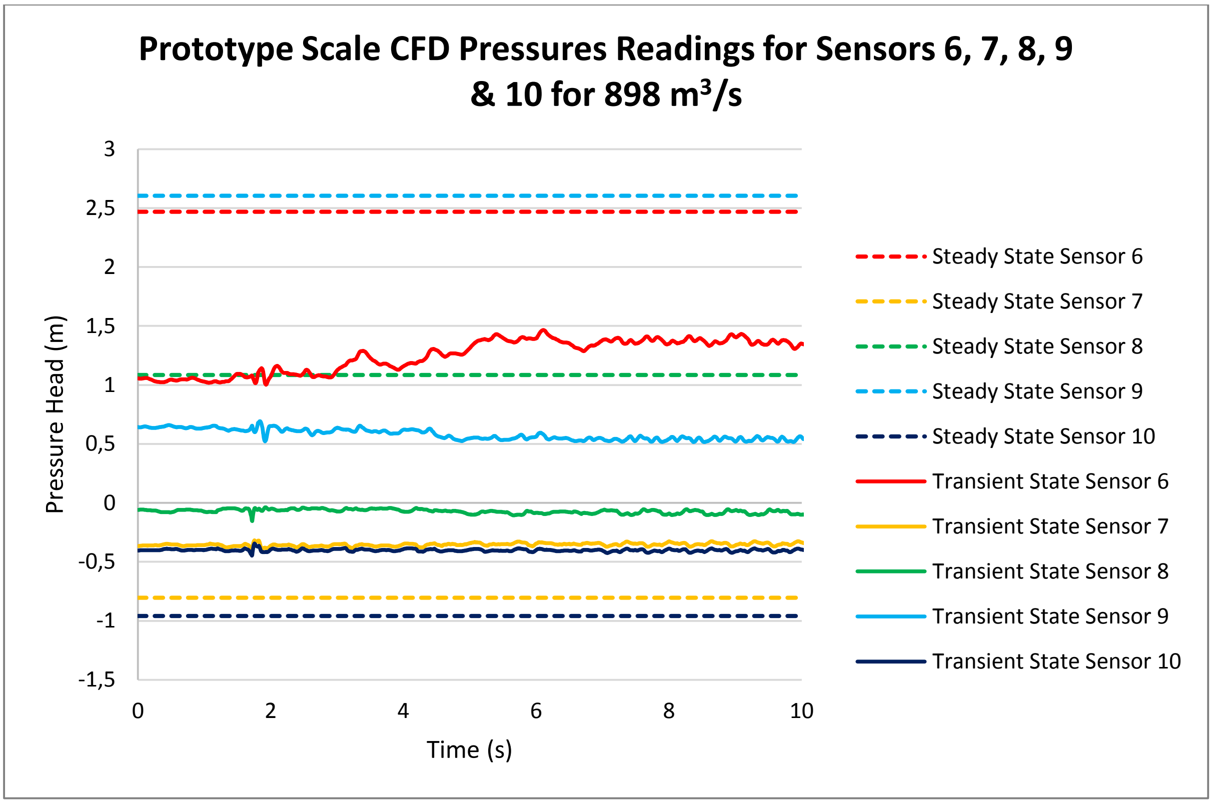

Figure D.14 Transient and steady state pressure readings for sensors 6-10 for a flow rate of 898 m^3/s at the prototype scale (251 l/s at a scale of 1:20)

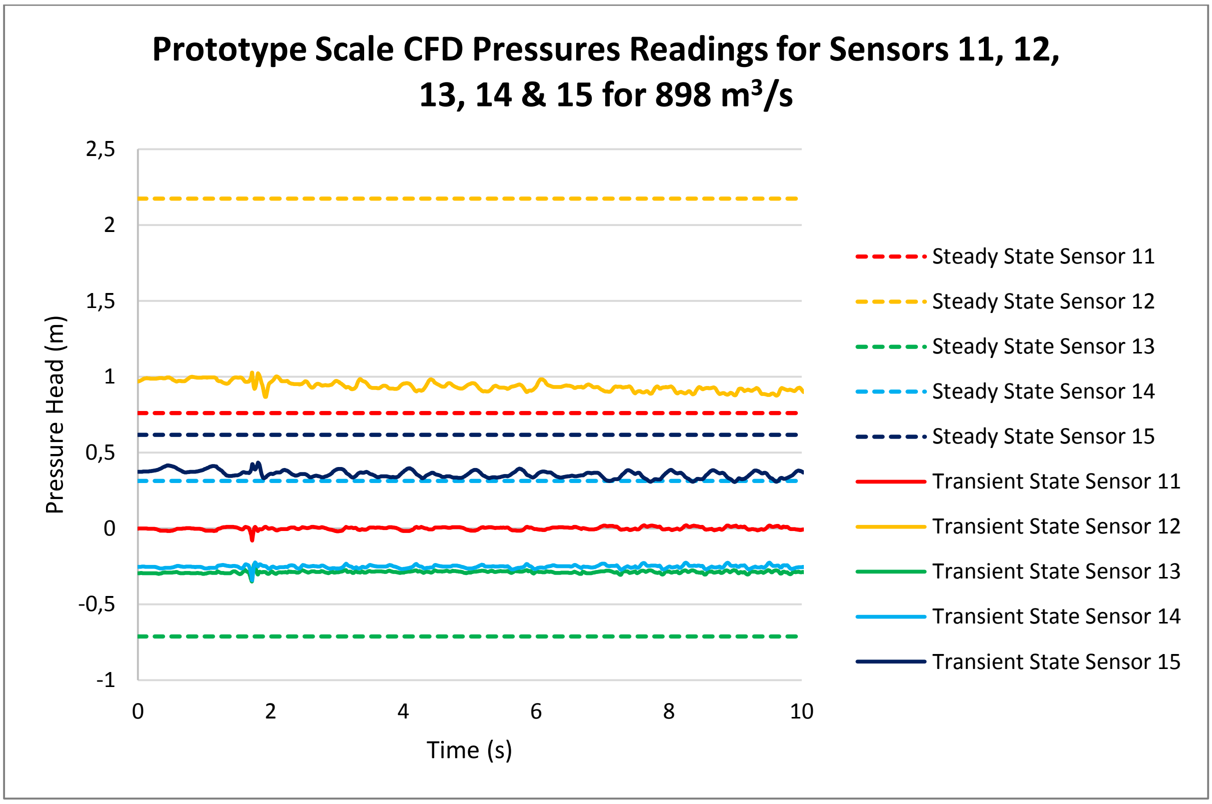

Figure D.15 Transient and steady state pressure readings for sensors 11-15 for a flow rate of 898 m^3/s at the prototype scale (251 l/s at a scale of 1:20)

Test 6: 1 063 m^3/s

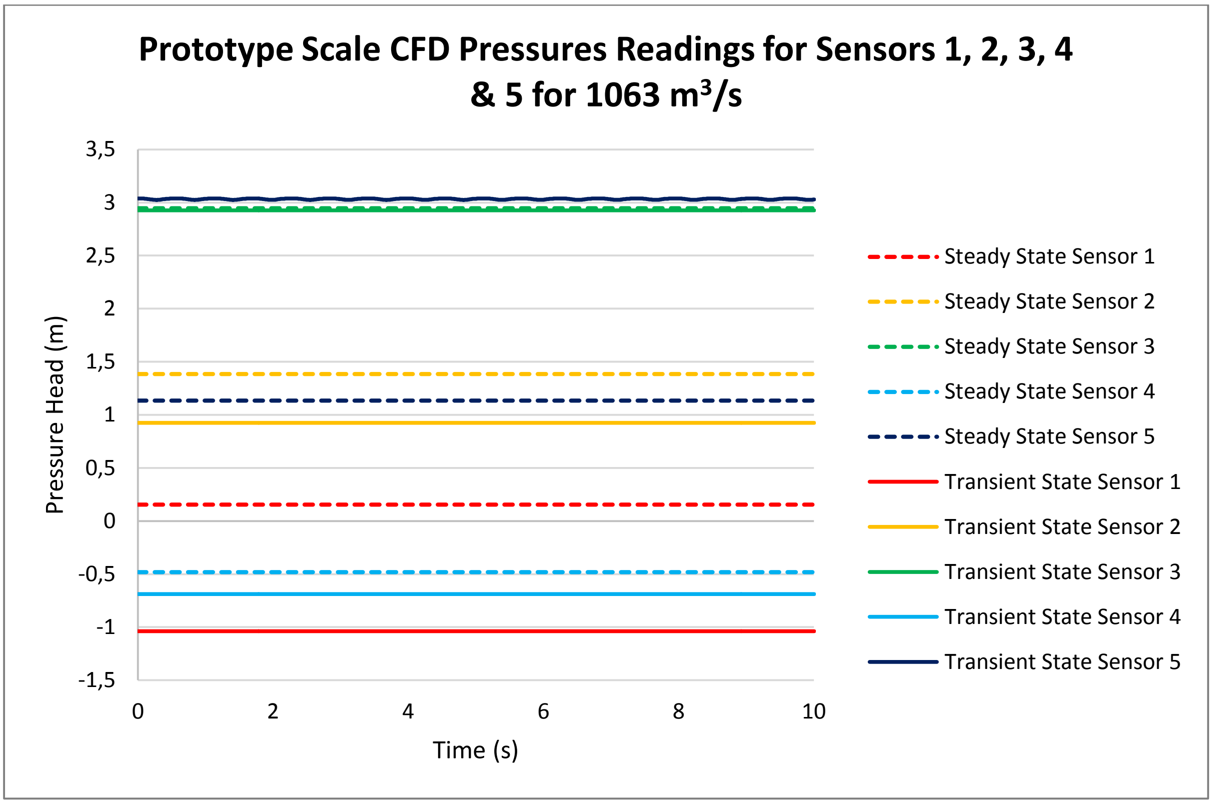

Figure D.16 Transient and steady state pressure readings for sensors 1-5 for a flow rate of 1 063 m^3/s at the prototype scale (297 l/s at a scale of 1:20)

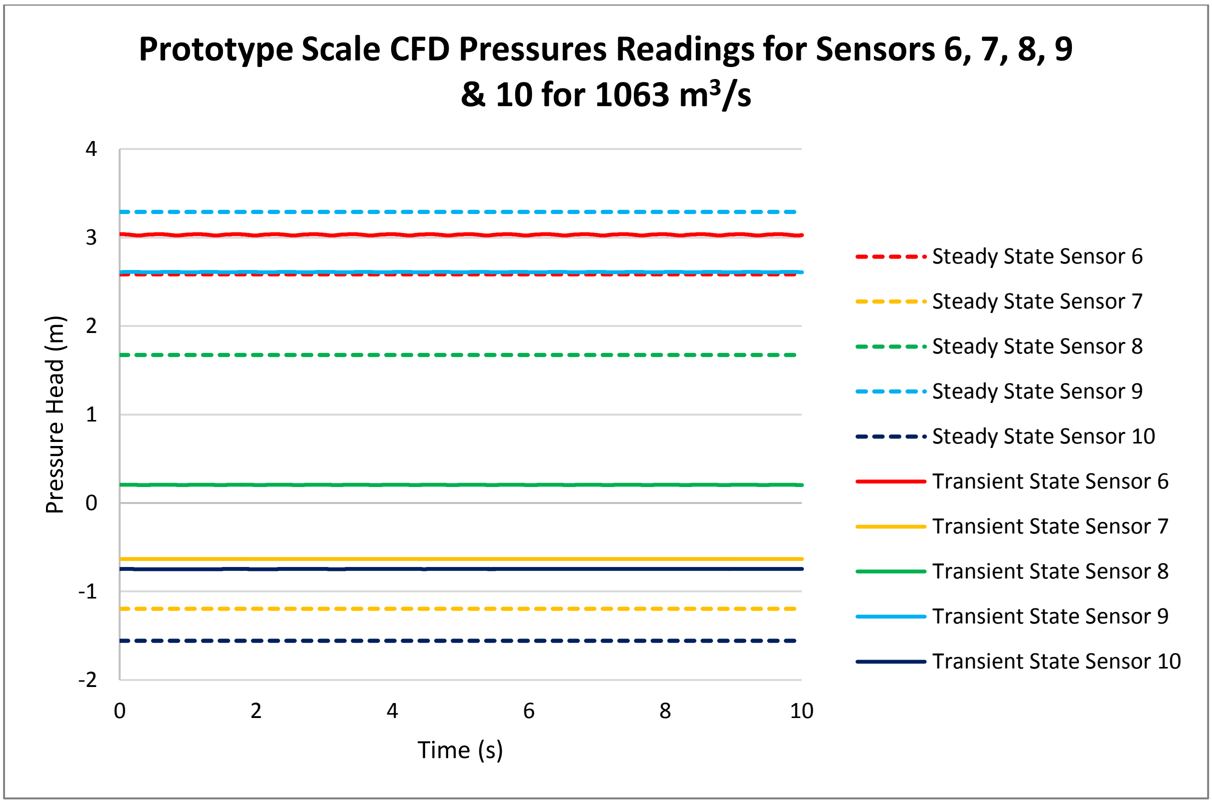

Figure D.17 Transient and steady state pressure readings for sensors 6-10 for a flow rate of 1 063 m^3/s at the prototype scale (297 l/s at a scale of 1:20)

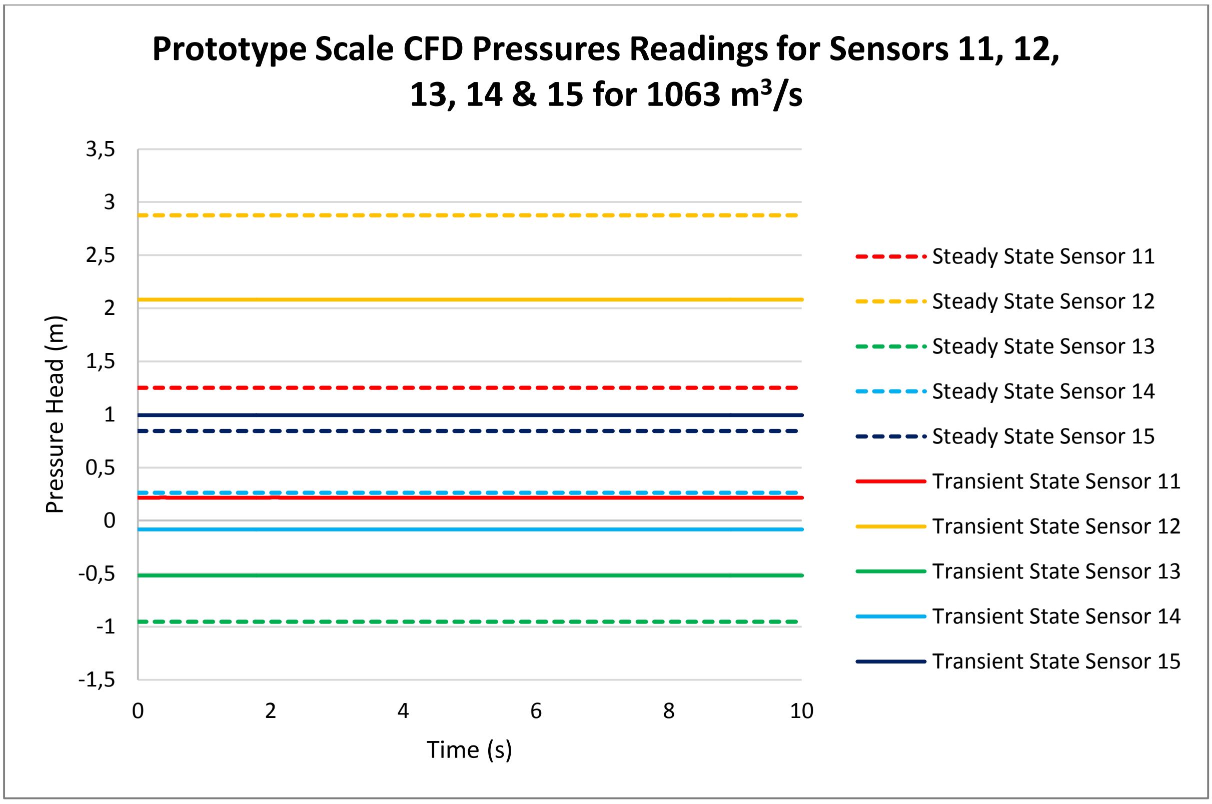

Figure D.18 Transient and steady state pressure readings for sensors 11-15 for a flow rate of 1 063 m^3/s at the prototype scale (297 l/s at a scale of 1:20)

Test 7: 1 249 m^3/s

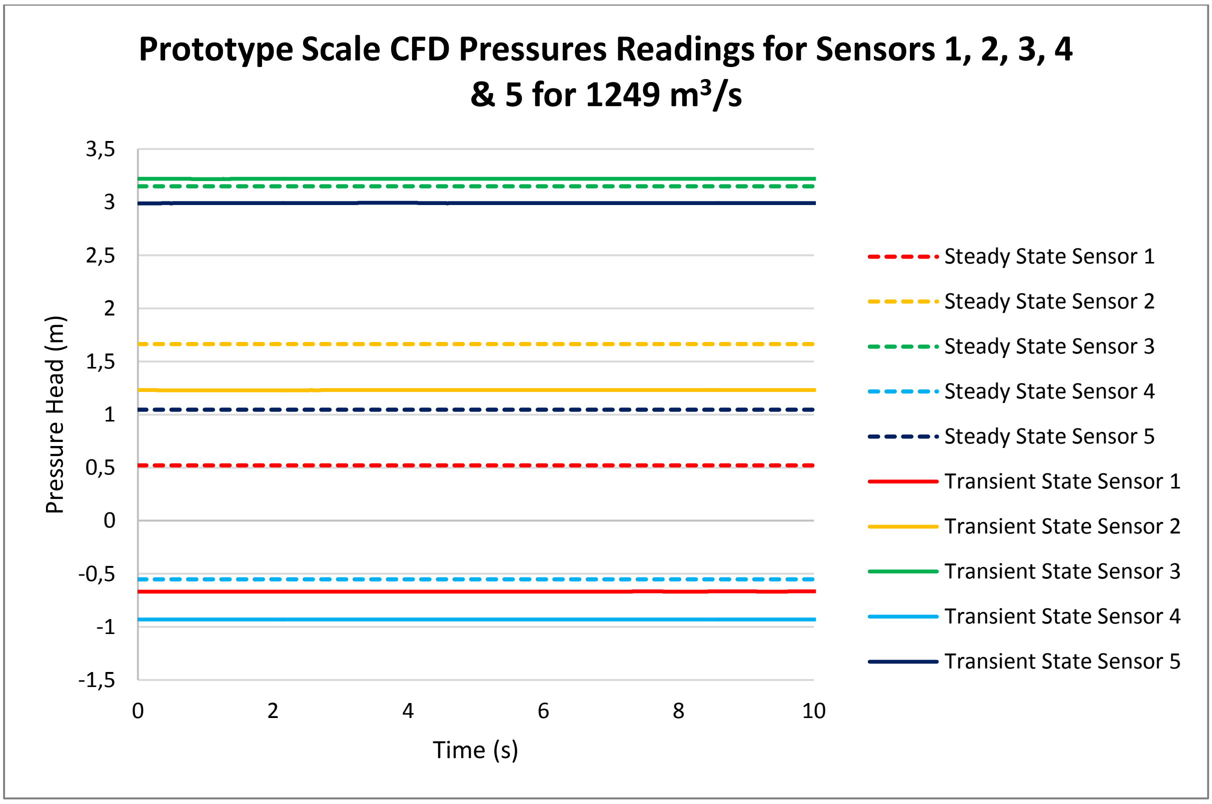

Figure D.19 Transient and steady state pressure readings for sensors 1-5 for a flow rate of 1 249 m^3/s at the prototype scale (349 l/s at a scale of 1:20)

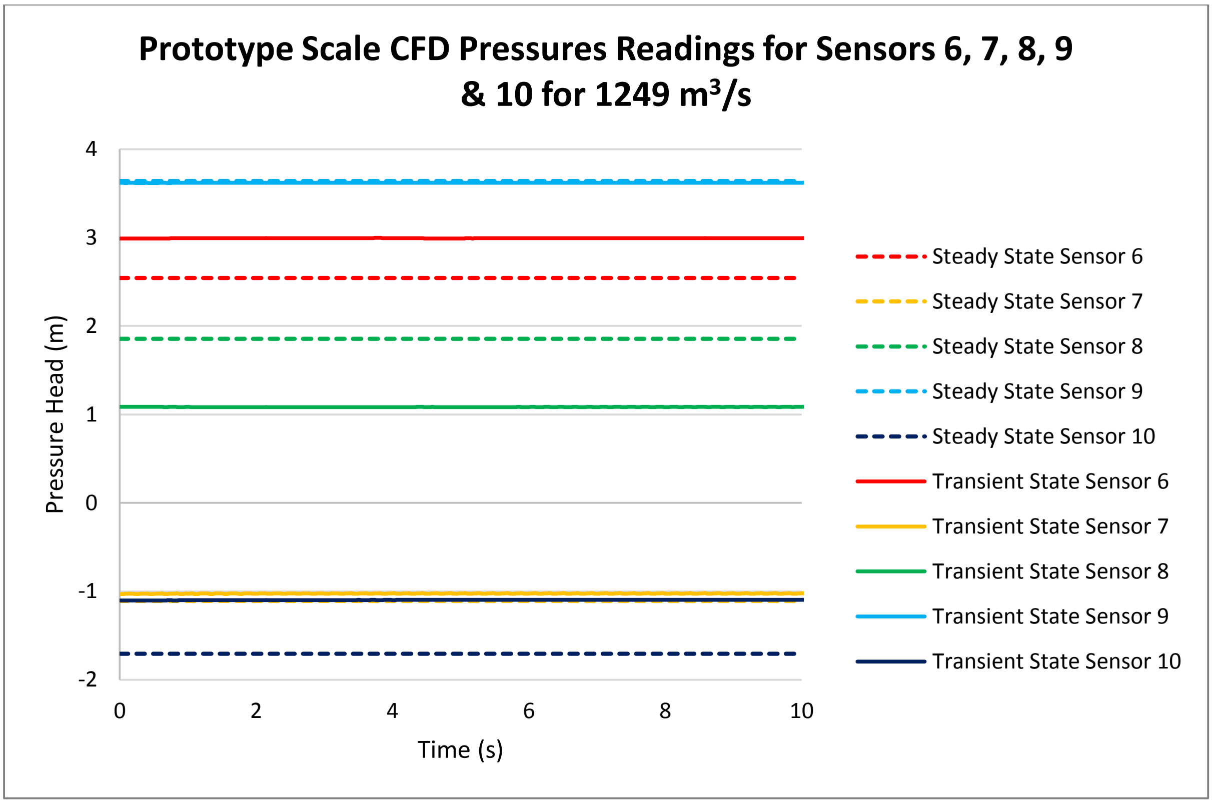

Figure D.20 Transient and steady state pressure readings for sensors 6-10 for a flow rate of 1 249 m^3/s at the prototype scale (349 l/s at a scale of 1:20)

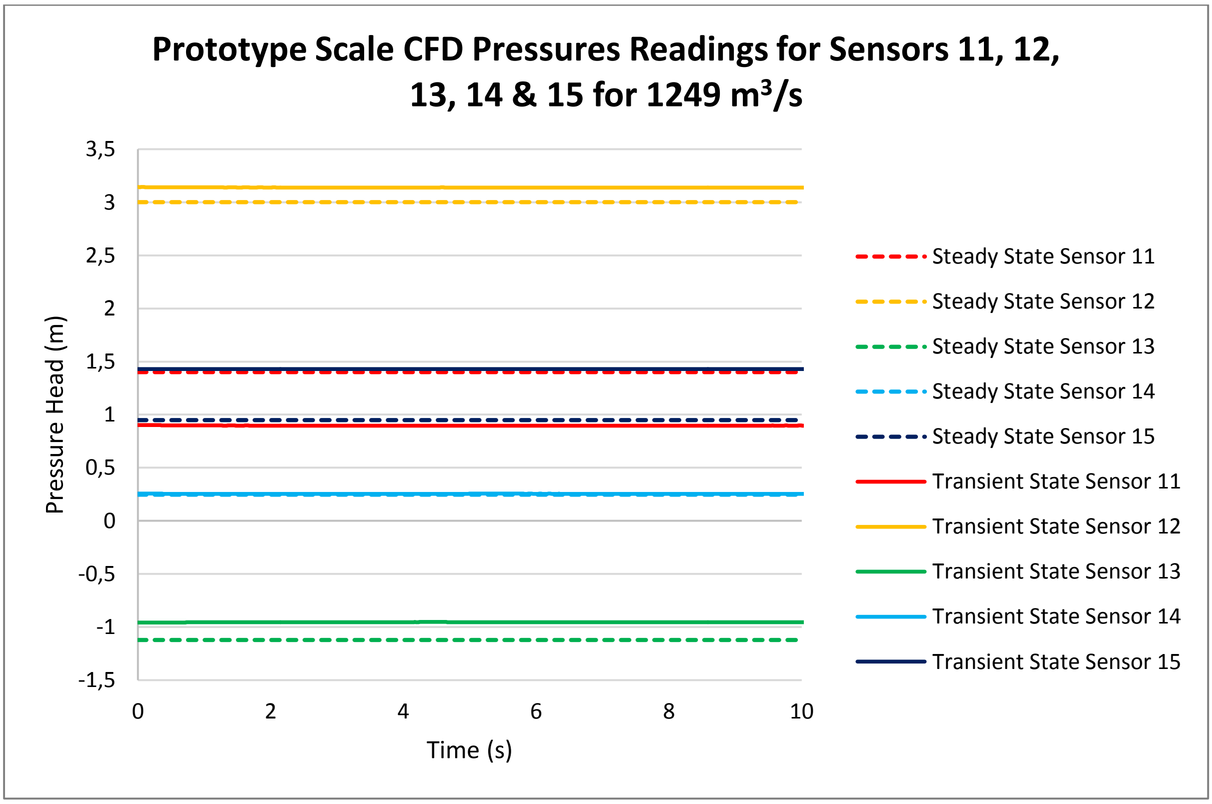

Figure D.21 Transient and steady state pressure readings for sensors 11-15 for a flow rate of 1 249 m^3/s at the prototype scale (349 l/s at a scale of 1:20)

Test 8: 1 424 m^3/s

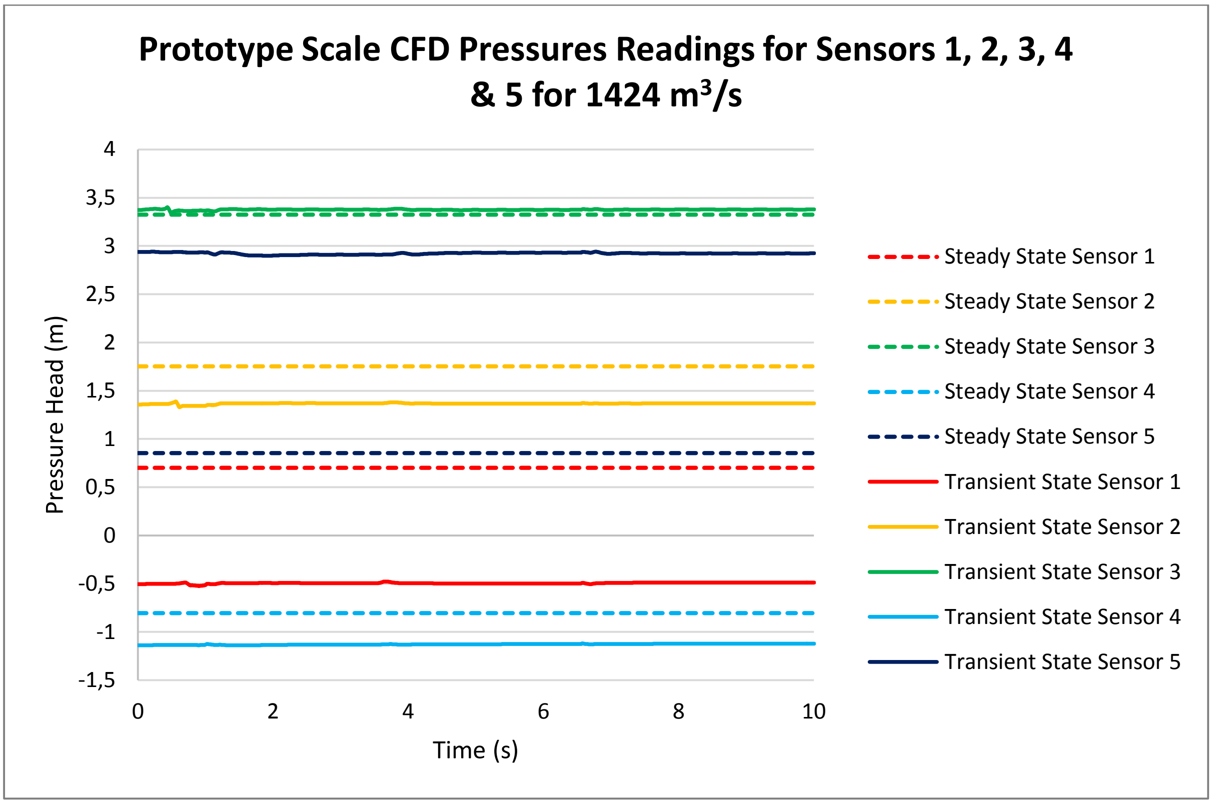

Figure D.22 Transient and steady state pressure readings for sensors 1-5 for a flow rate of 1 424 m^3/s at the prototype scale (398 l/s at a scale of 1:20)

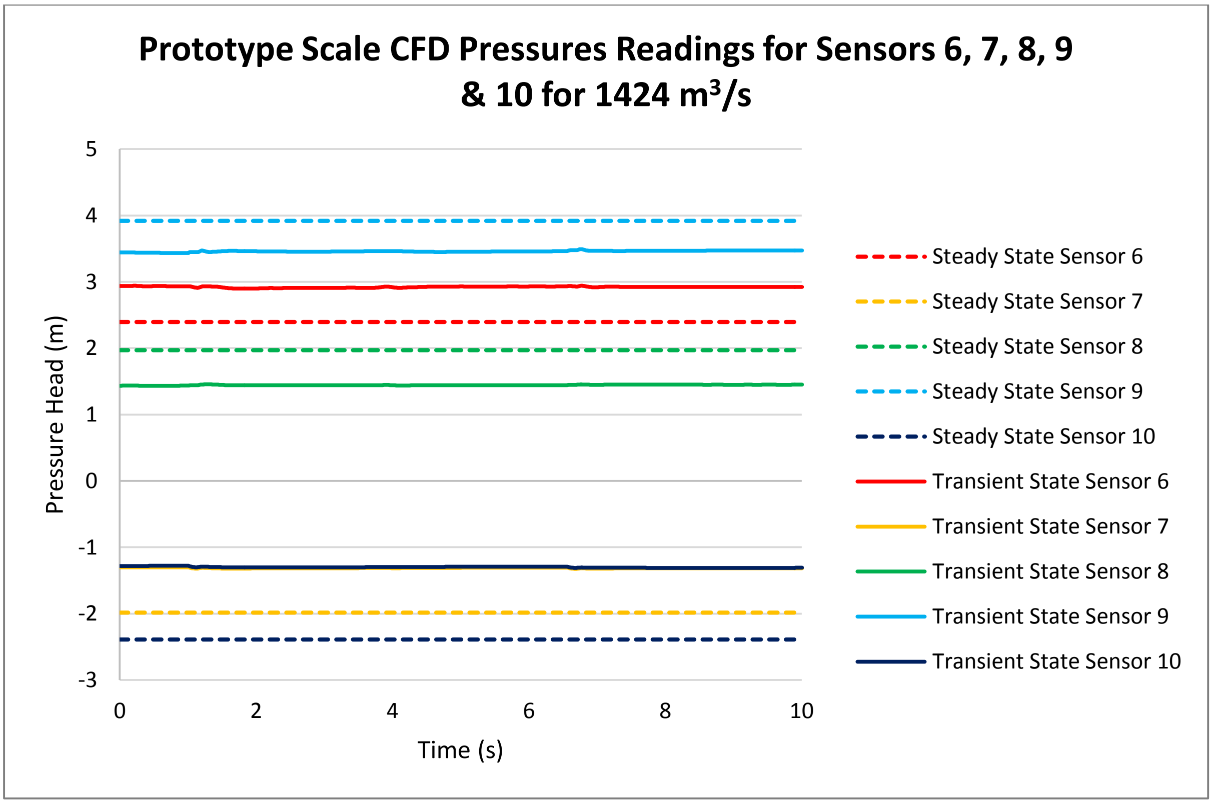

Figure D.23 Transient and steady state pressure readings for sensors 6-10 for a flow rate of 1 424 m^3/s at the prototype scale (398 l/s at a scale of 1:20)

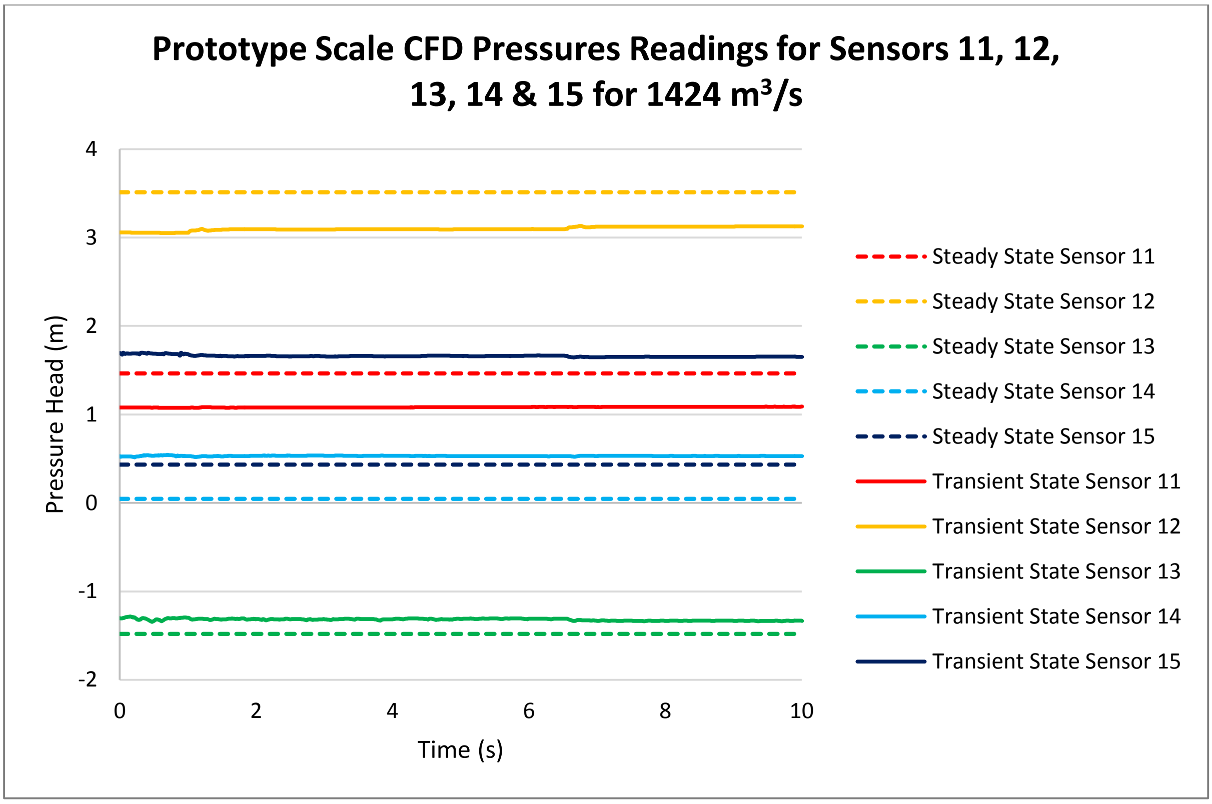

Figure D.24 Transient and steady state pressure readings for sensors 11-15 for a flow rate of 1 424 m^3/s at the prototype scale (398 l/s at a scale of 1:20)

Test 9: 1 606 m^3/s

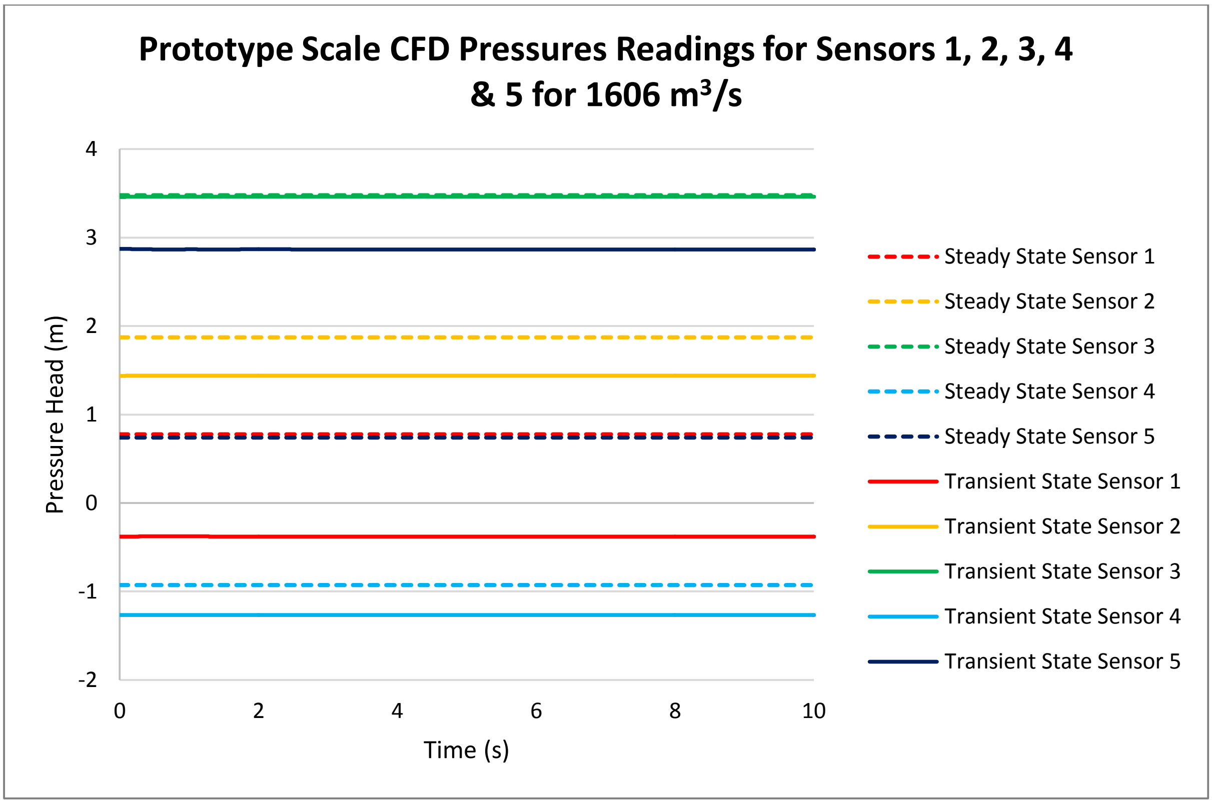

Figure D.25 Transient and steady state pressure readings for sensors 1-5 for a flow rate of 1 606 m^3/s at the prototype scale (449 l/s at a scale of 1:20)

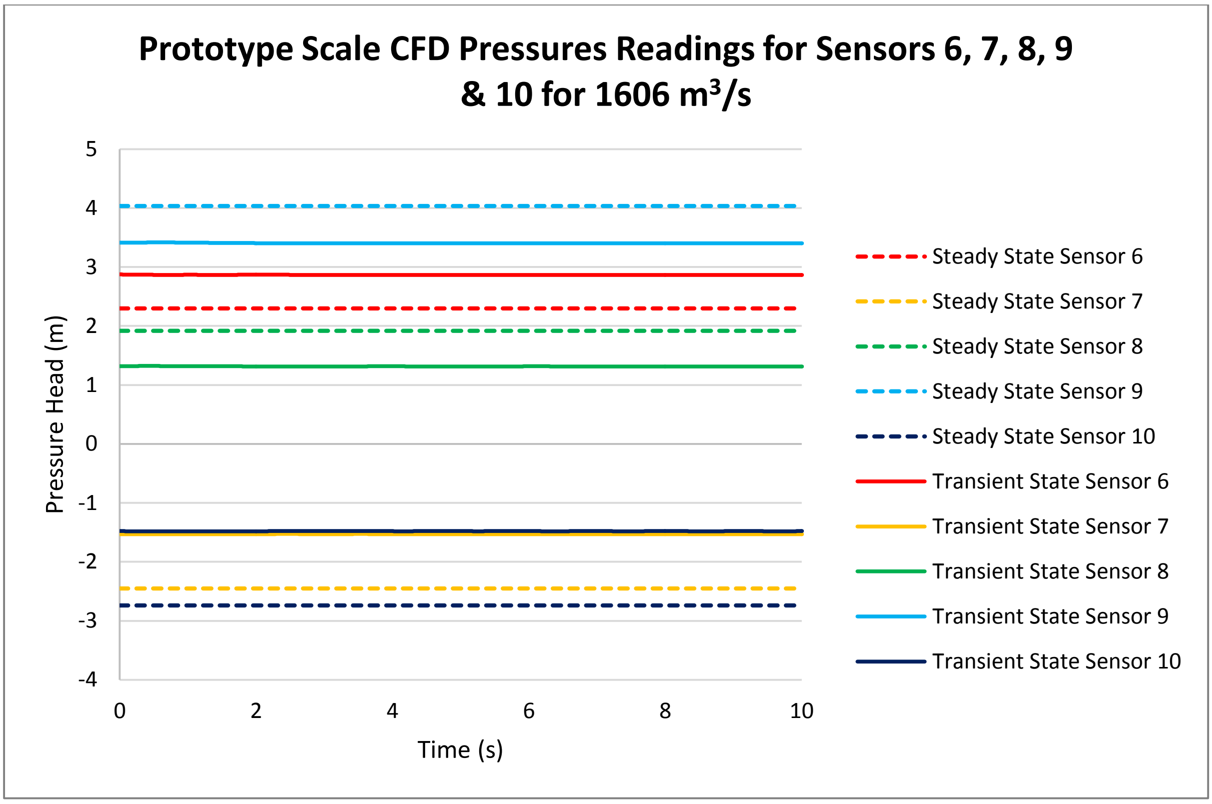

Figure D.26 Transient and steady state pressure readings for sensors 6-10 for a flow rate of 1 606 m^3/s at the prototype scale (449 l/s at a scale of 1:20)

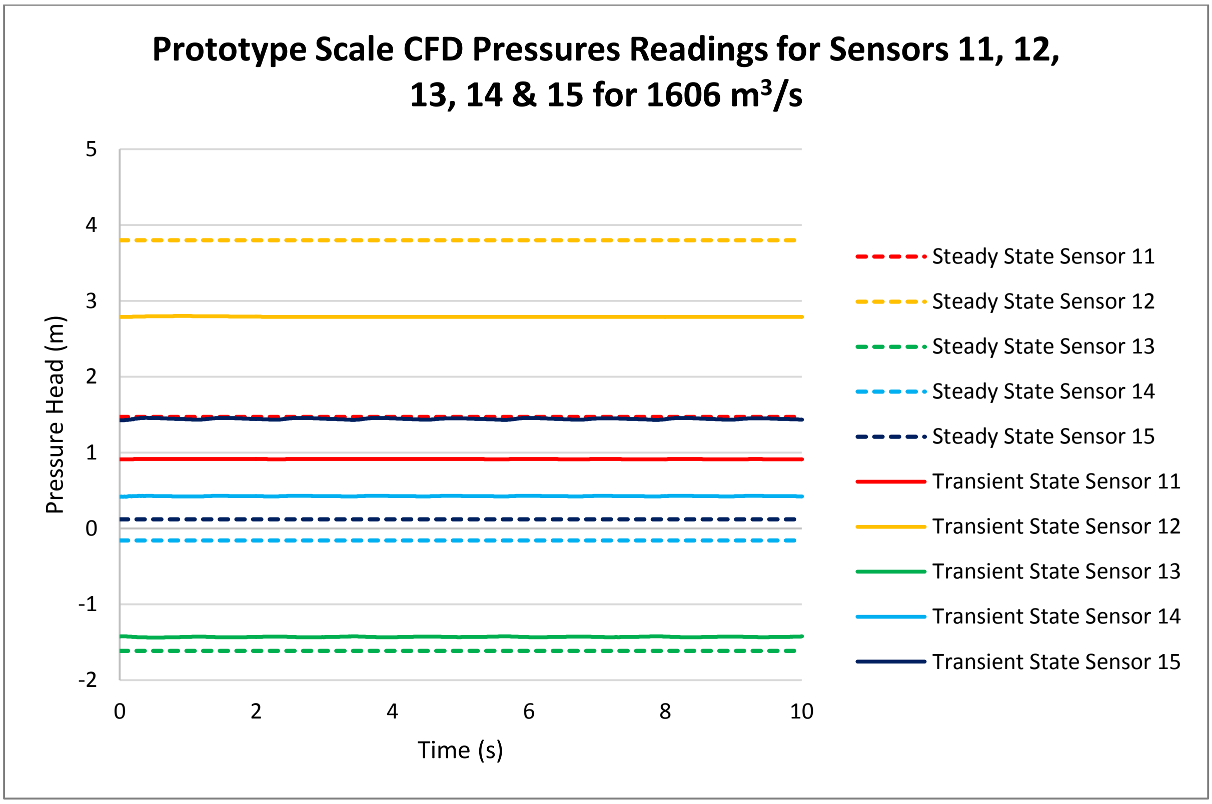

Figure D.27 Transient and steady state pressure readings for sensors 11-15 for a flow rate of 1 606 m^3/s at the prototype scale (449 l/s at a scale of 1:20)

Test 10: 1 789 m^3/s

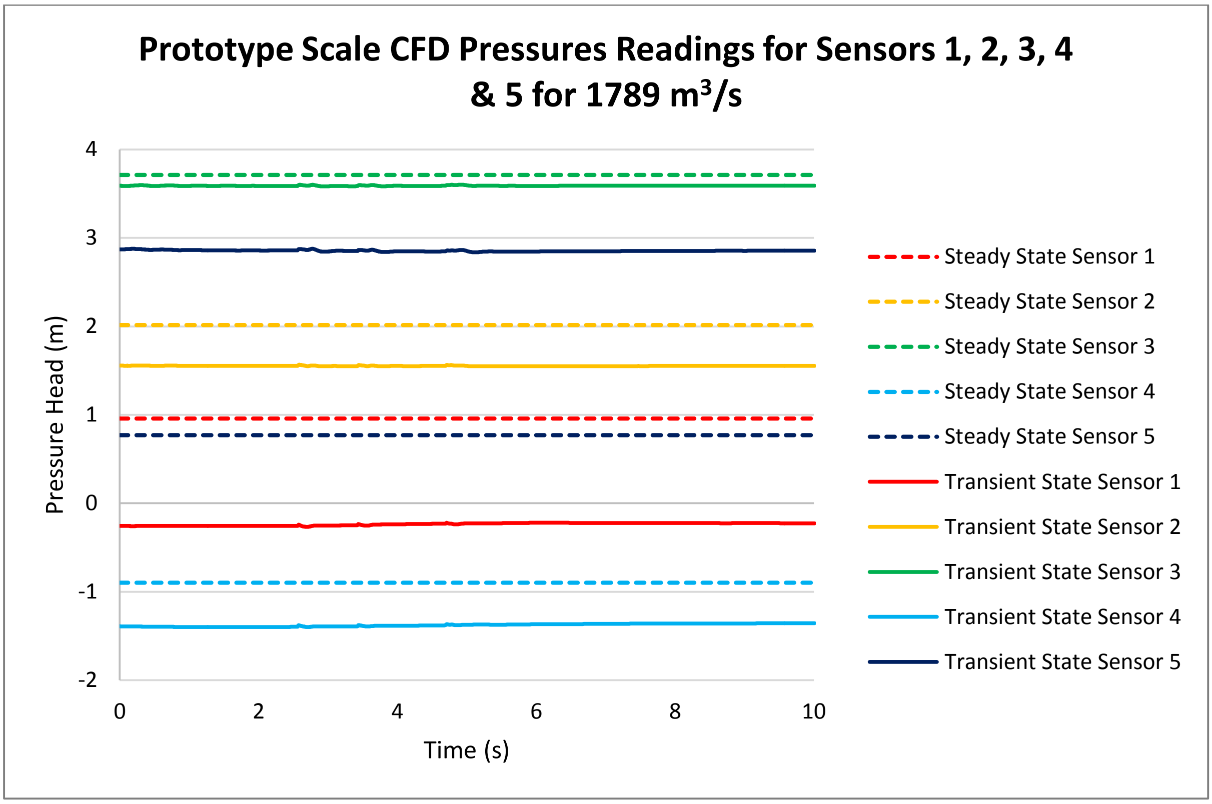

Figure D.28 Transient and steady state pressure readings for sensors 1-5 for a flow rate of 1 789 m^3/s at the prototype scale (500 l/s at a scale of 1:20)

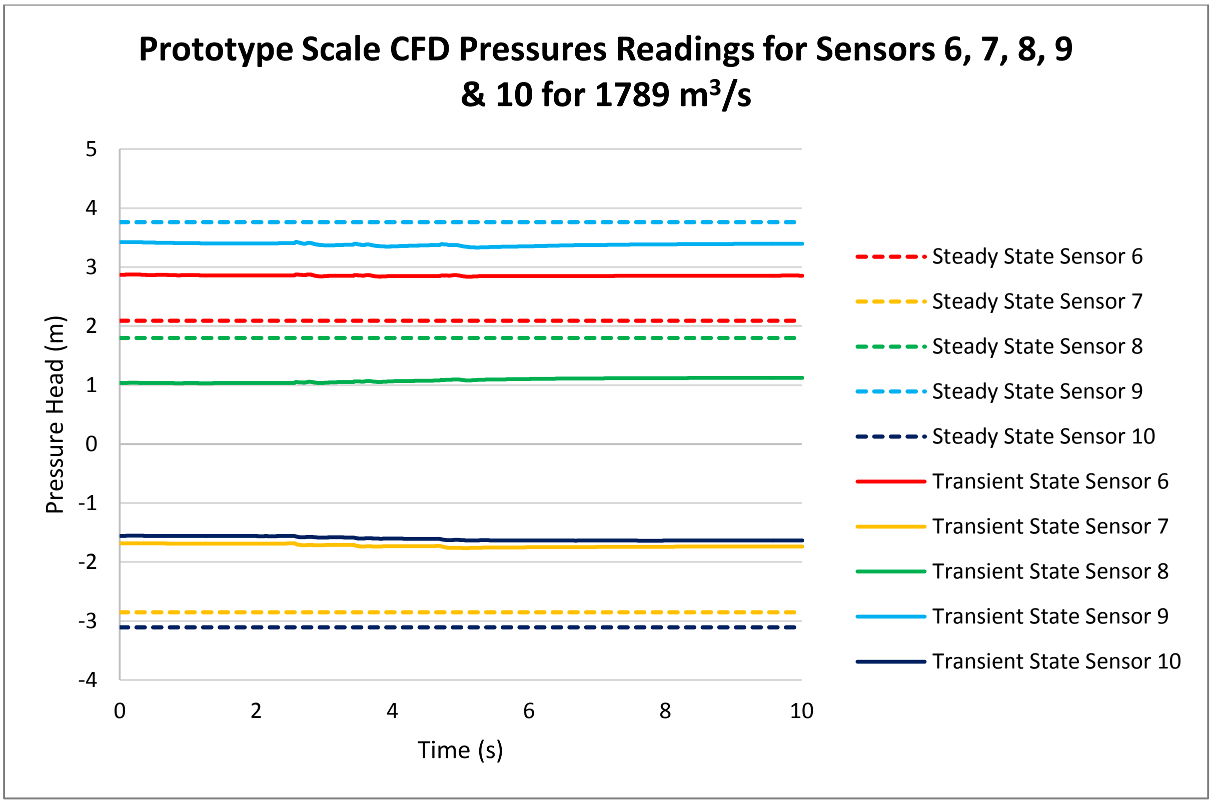

Figure D.29 Transient and steady state pressure readings for sensors 6-10 for a flow rate of 1 789 m^3/s at the prototype scale (500 l/s at a scale of 1:20)

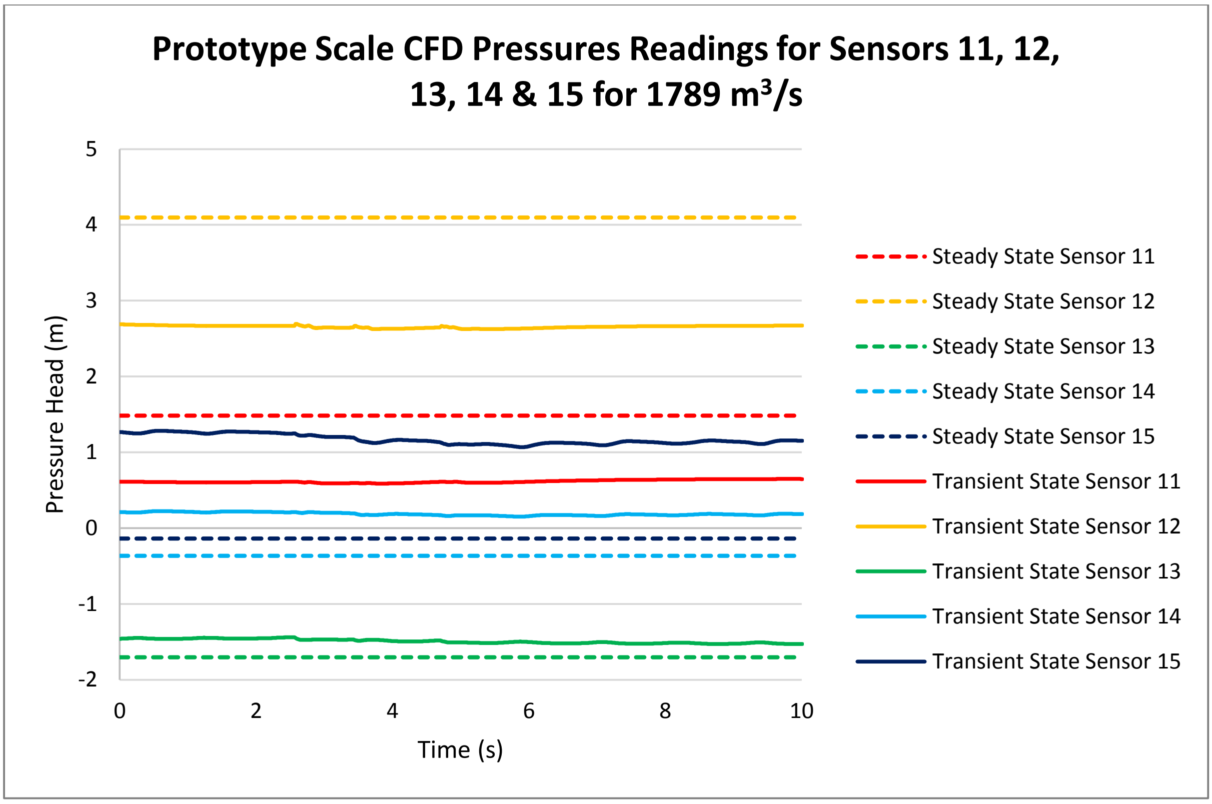

Figure D.30 Transient and steady state pressure readings for sensors 11-15 for a flow rate of 1 789 m^3/s at the prototype scale (500 l/s at a scale of 1:20)

Test 11: 1 968 m^3/s

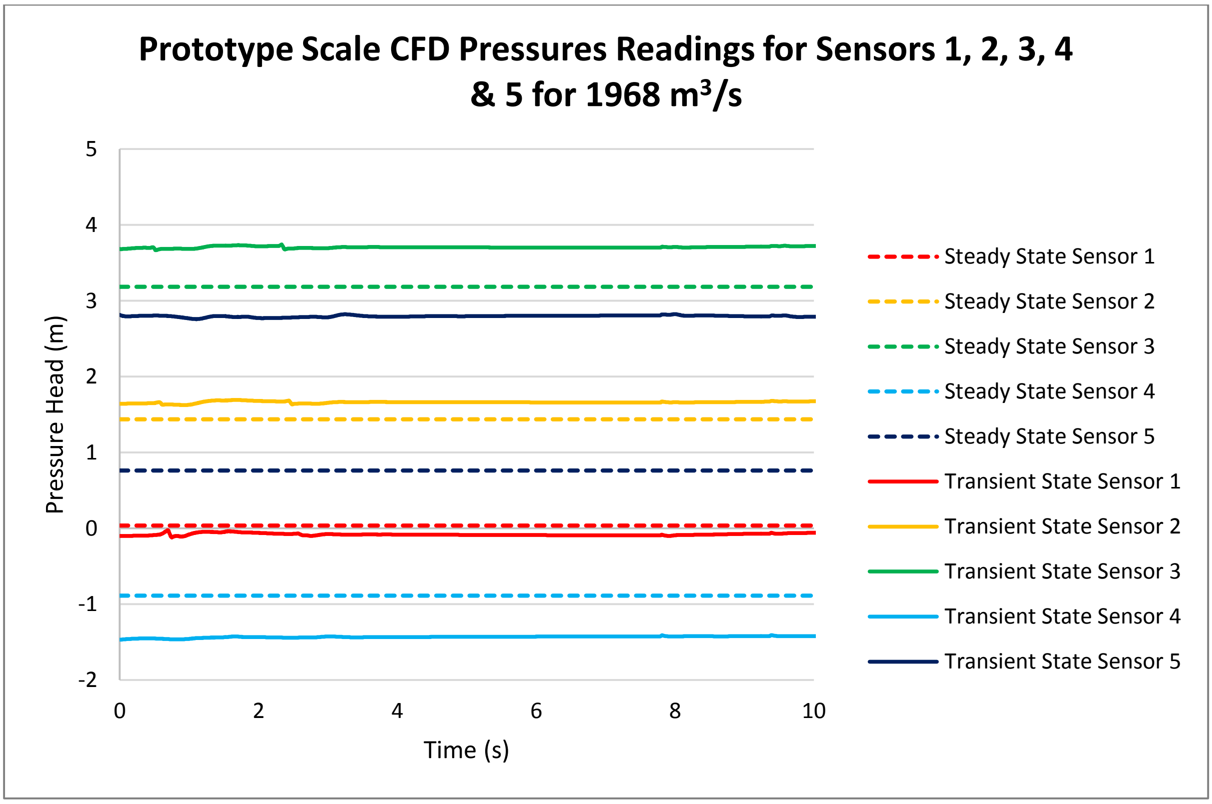

Figure D.31 Transient and steady state pressure readings for sensors 1-5 for a flow rate of 1 968 m^3/s at the prototype scale (550 l/s at a scale of 1:20)

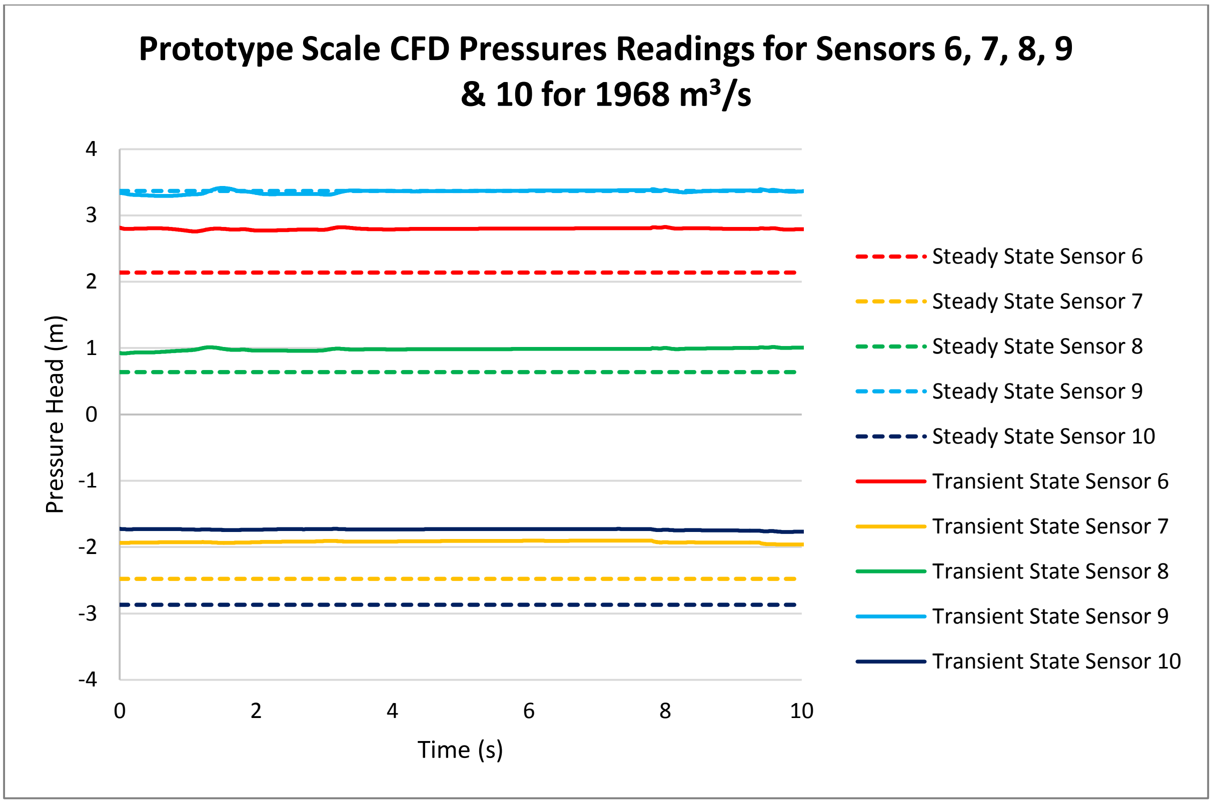

Figure D.32 Transient and steady state pressure readings for sensors 6-10 for a flow rate of 1 968 m^3/s at the prototype scale (550 l/s at a scale of 1:20)

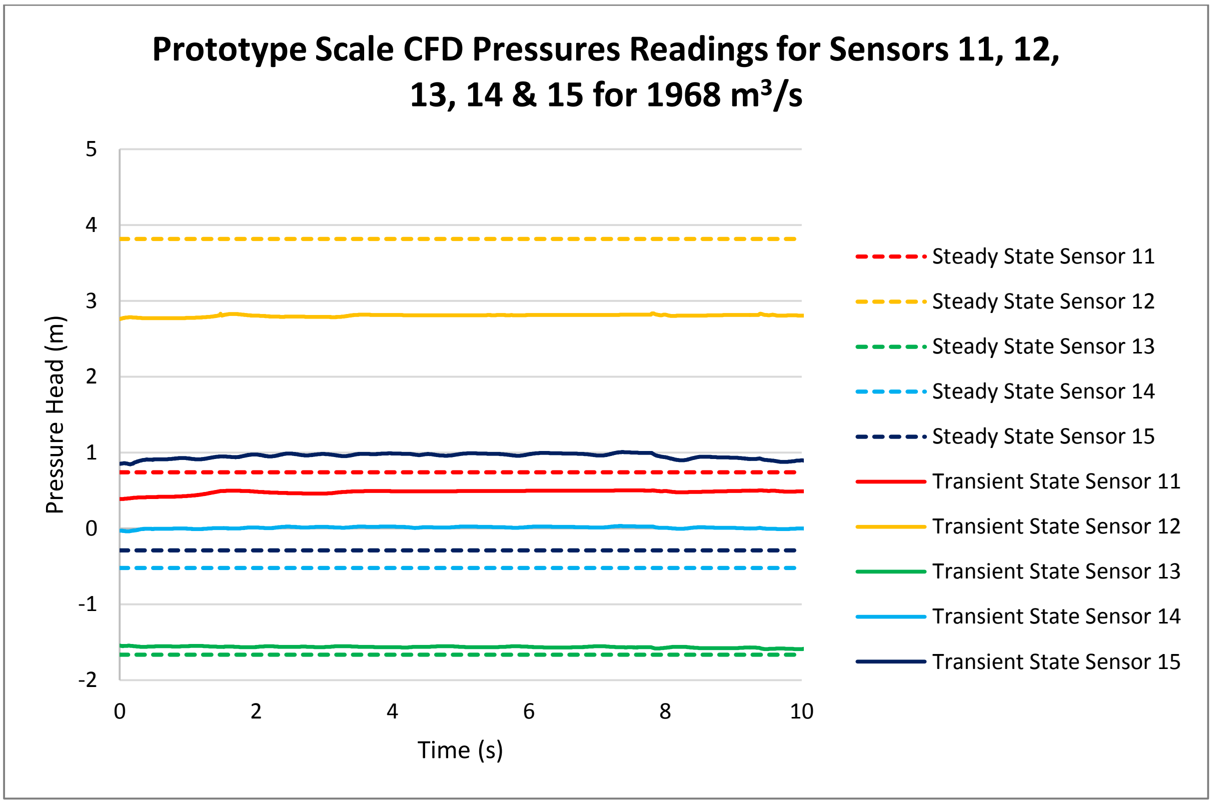

Figure D.33 Transient and steady state pressure readings for sensors 11-15 for a flow rate of 1 968 m^3/s at the prototype scale (550 l/s at a scale of 1:20)

Test 12: 2 136 m^3/s

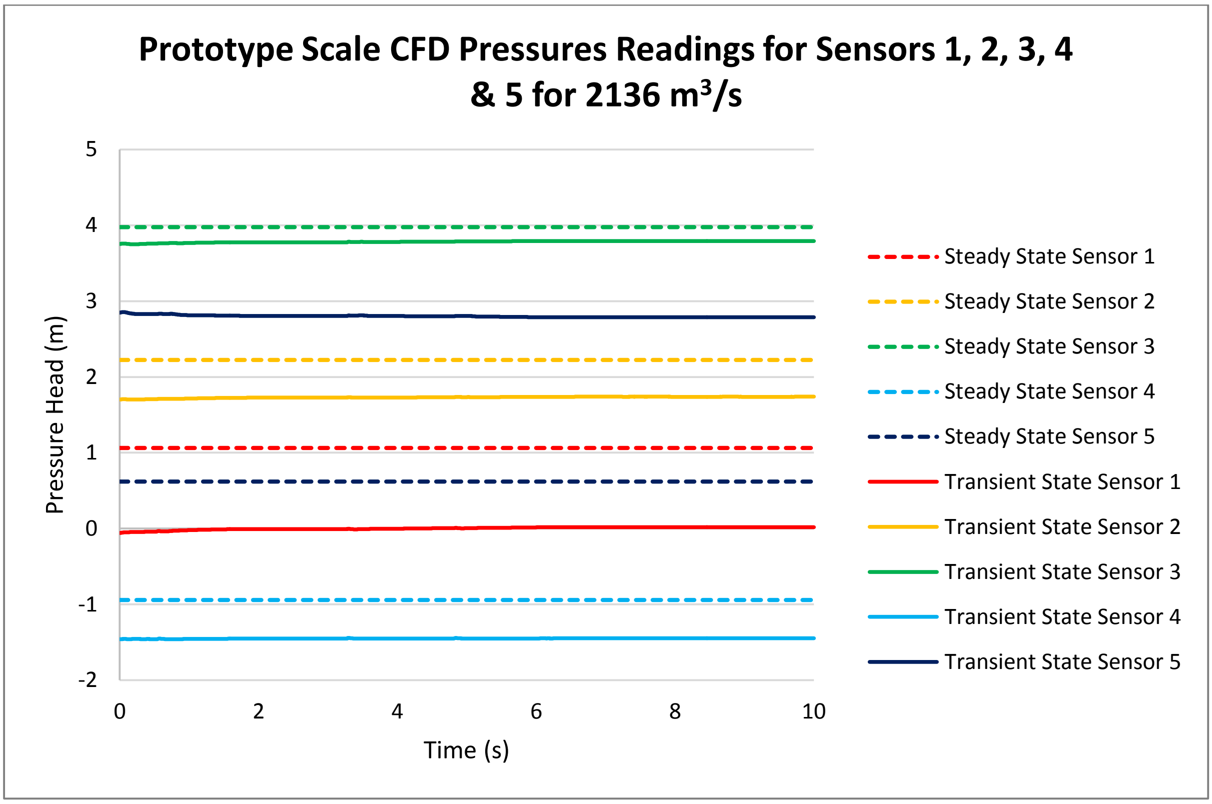

Figure D.34 Transient and steady state pressure readings for sensors 1-5 for a flow rate of 2 136 m^3/s at the prototype scale (597 l/s at a scale of 1:20)

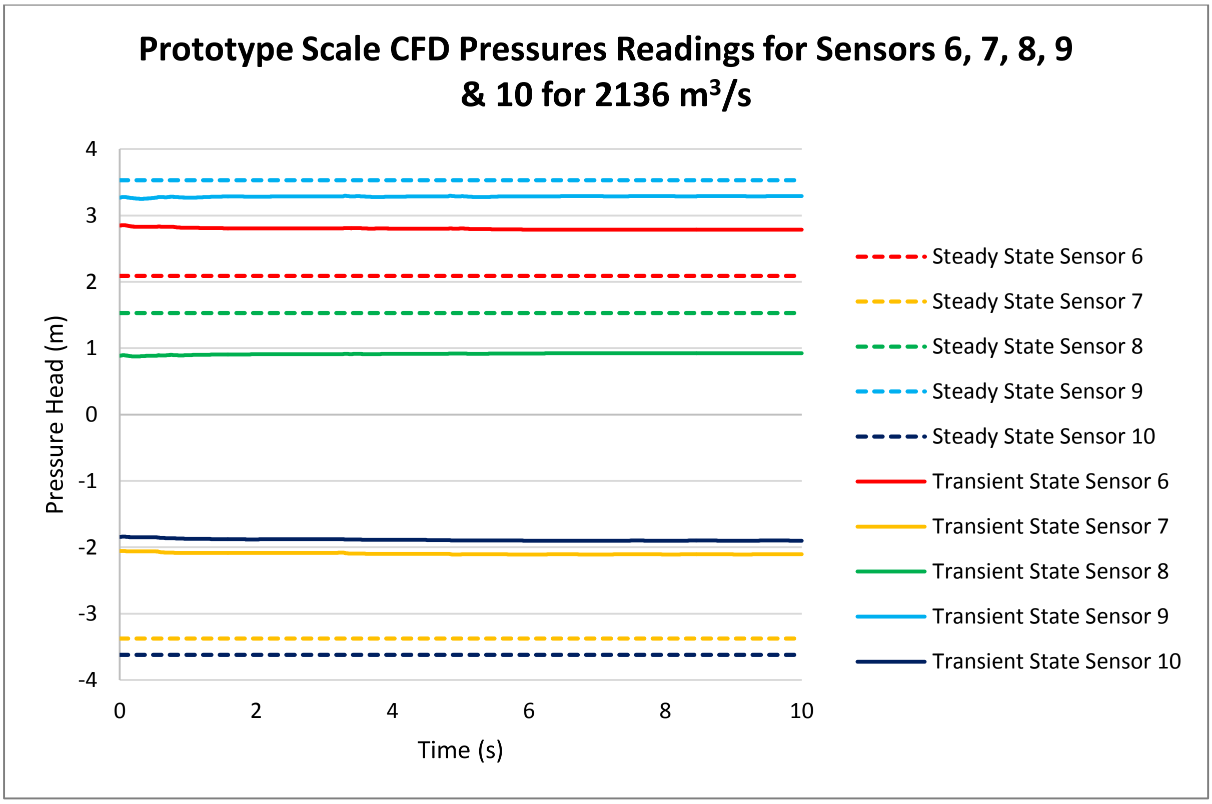

Figure D.35 Transient and steady state pressure readings for sensors 6-10 for a flow rate of 2 136 m^3/s at the prototype scale (597 l/s at a scale of 1:20)

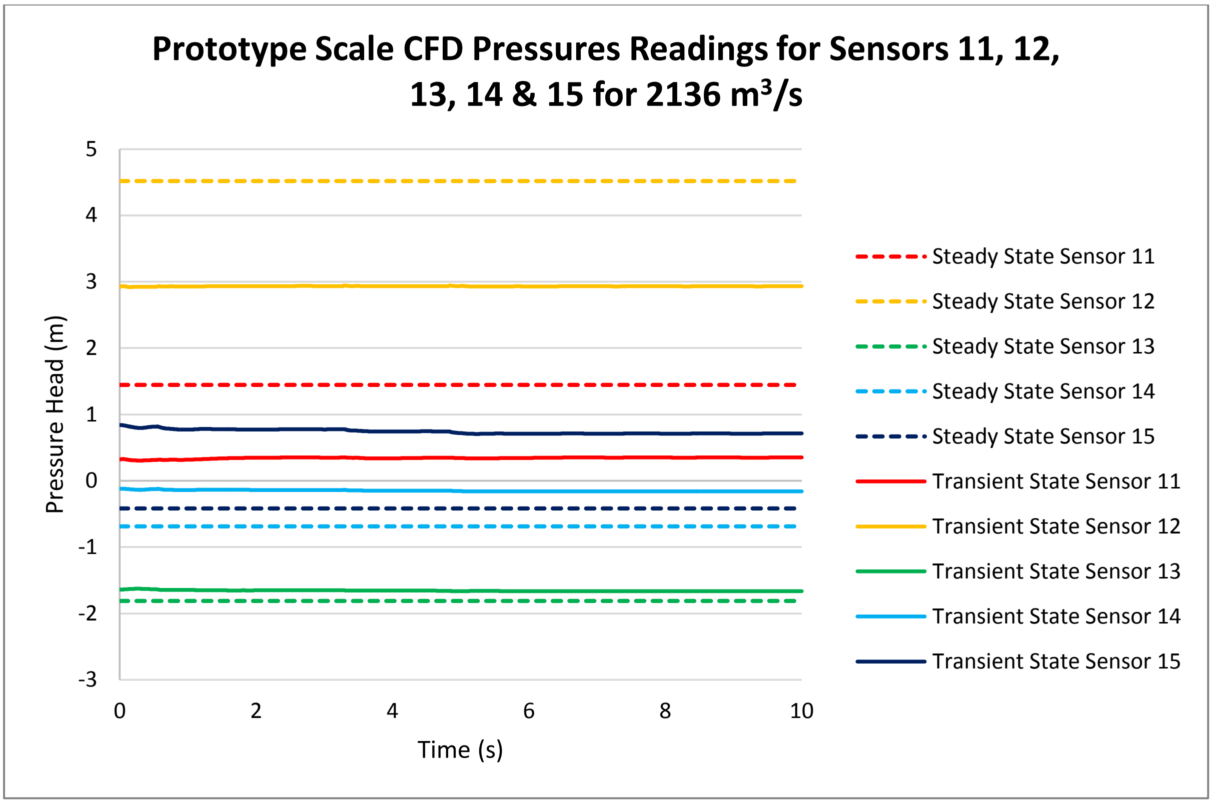

Figure D.36 Transient and steady state pressure readings for sensors 11-15 for a flow rate of 2 136 m^3/s at the prototype scale (597 l/s at a scale of 1:20)

Appendix E: Results Used for CFD Validation

Test 1: 215 m^3/s

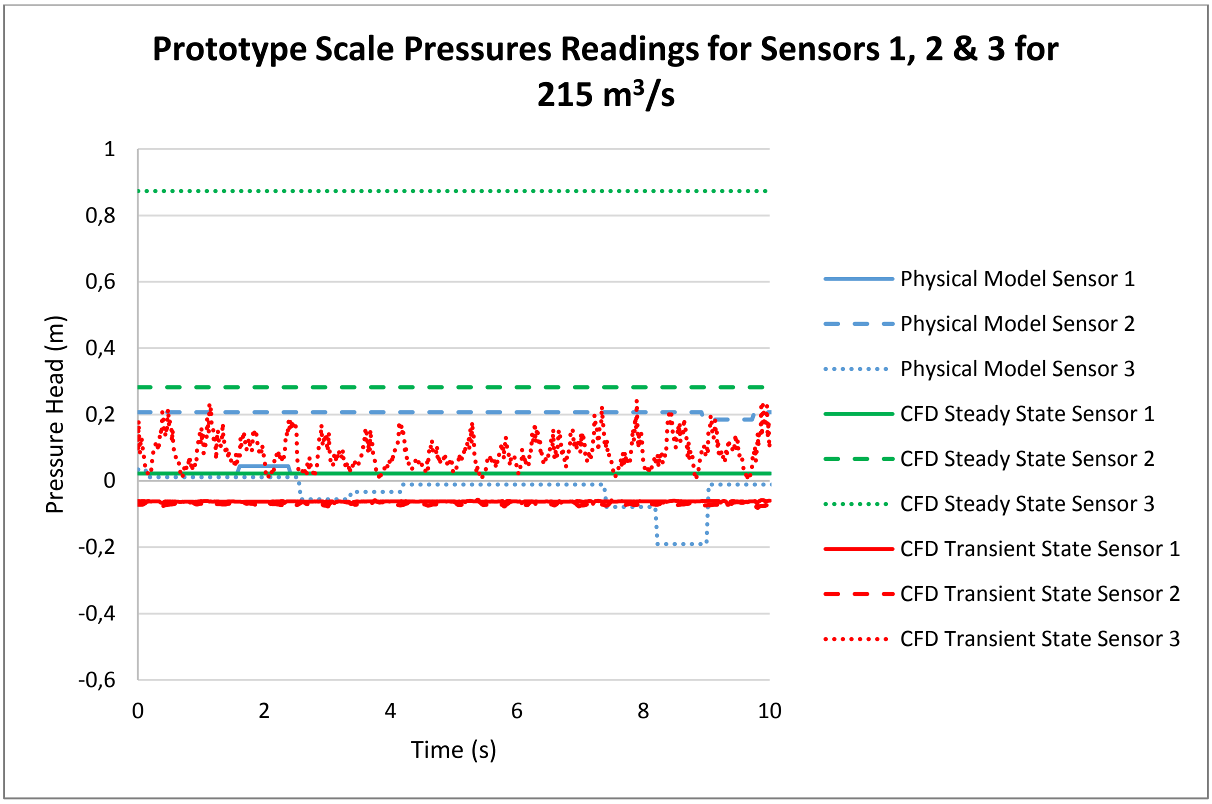

Figure E.1 Pressure readings for transient and steady state simulations and physical modelling for sensors 1-3 for a flow rate of 215 m^3/s at the prototype scale

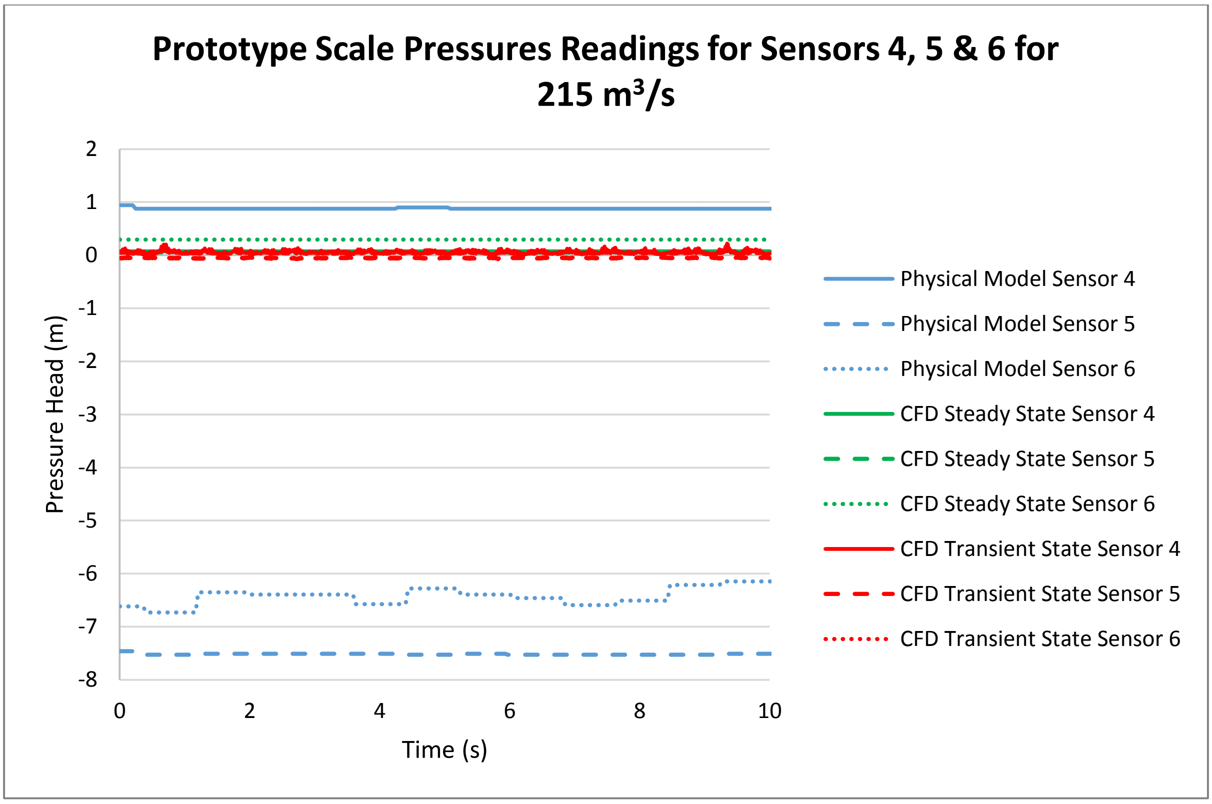

Figure E.2 Pressure readings for transient and steady state simulations and physical modelling for sensors 4-6 for a flow rate of 215 m^3/s at the prototype scale

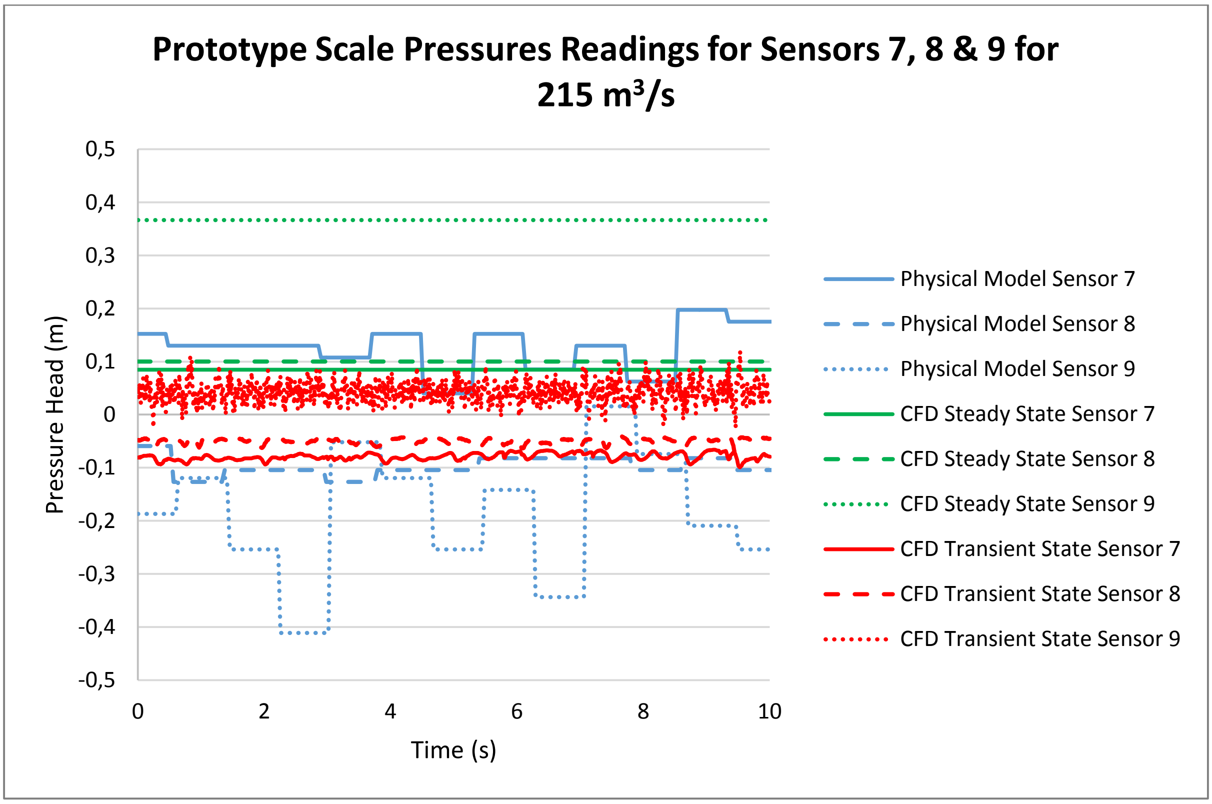

Figure E.3 Pressure readings for transient and steady state simulations and physical modelling for sensors 7-9 for a flow rate of 215 m^3/s at the prototype scale

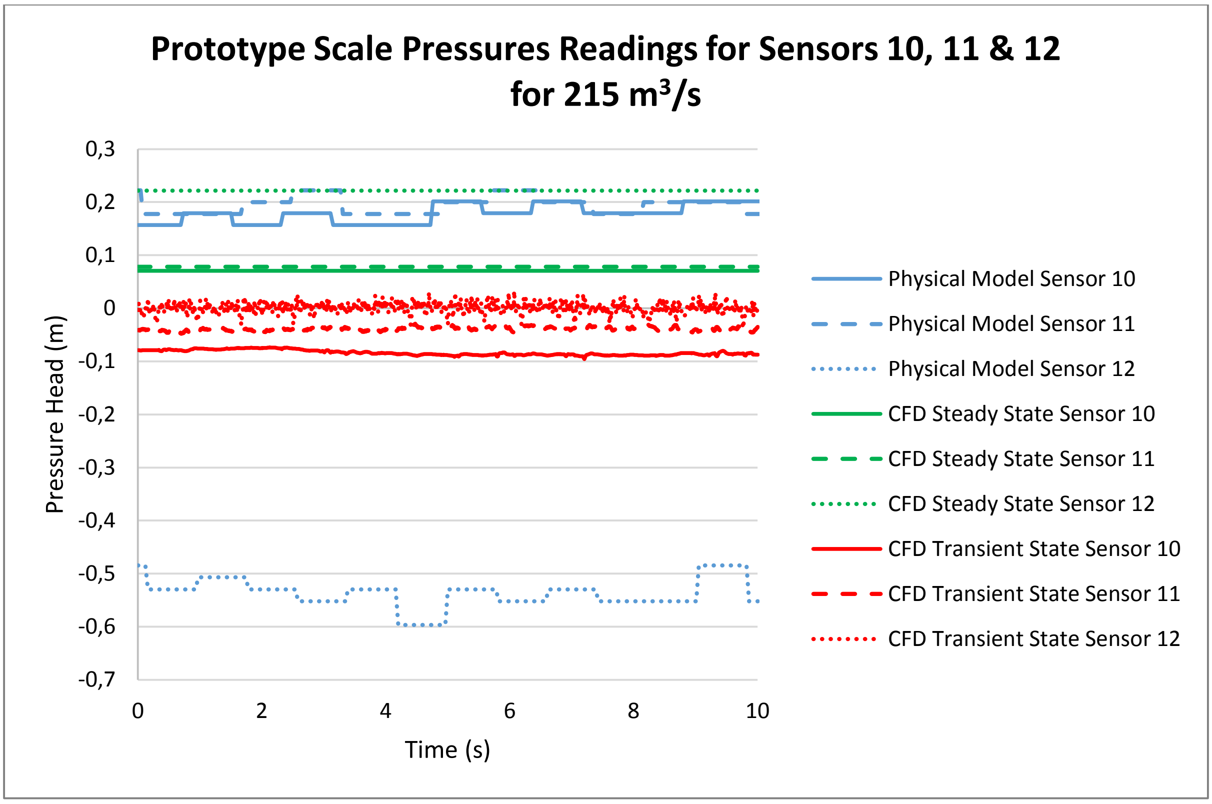

Figure E.4 Pressure readings for transient and steady state simulations and physical modelling for sensors 10-12 for a flow rate of 215 m^3/s at the prototype scale

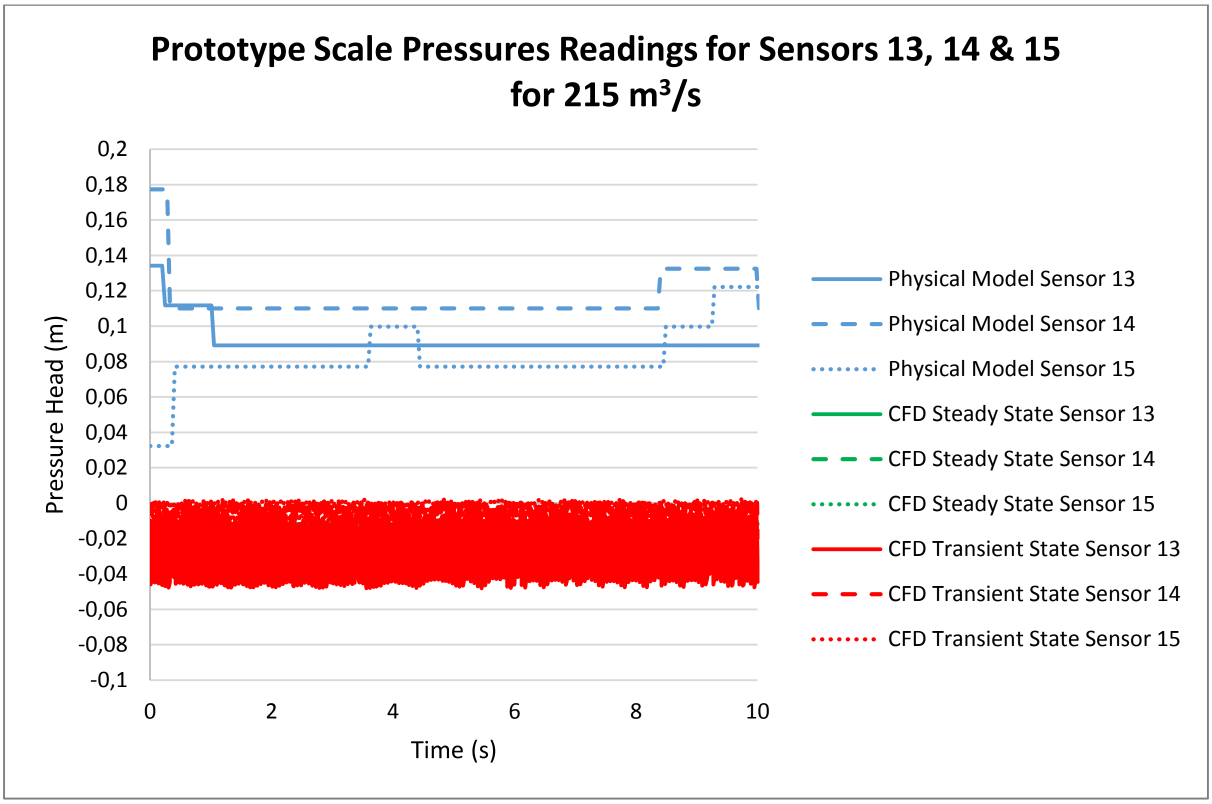

Figure E.5 Pressure readings for transient and steady state simulations and physical modelling for sensors 13-15 for a flow rate of 215 m^3/s at the prototype scale

Test 2: 361 m^3/s

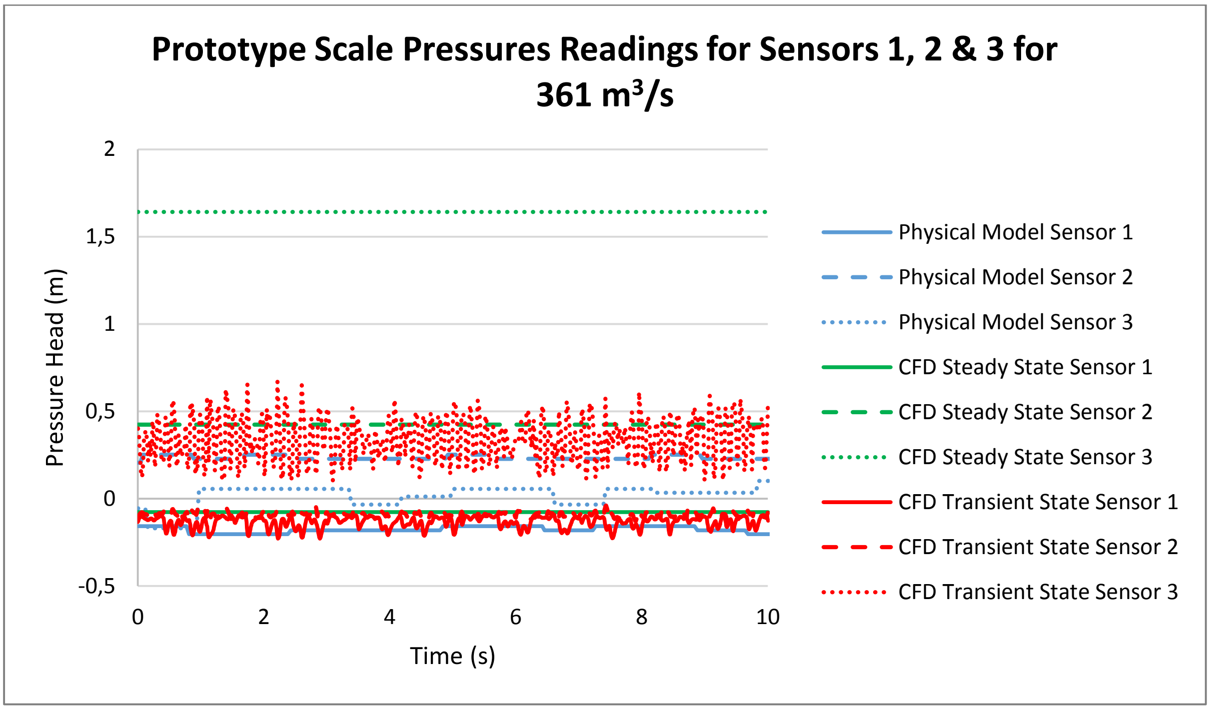

Figure E.6 Pressure readings for transient and steady state simulations and physical modelling for sensors 1-3 for a flow rate of 361 m^3/s at the prototype scale

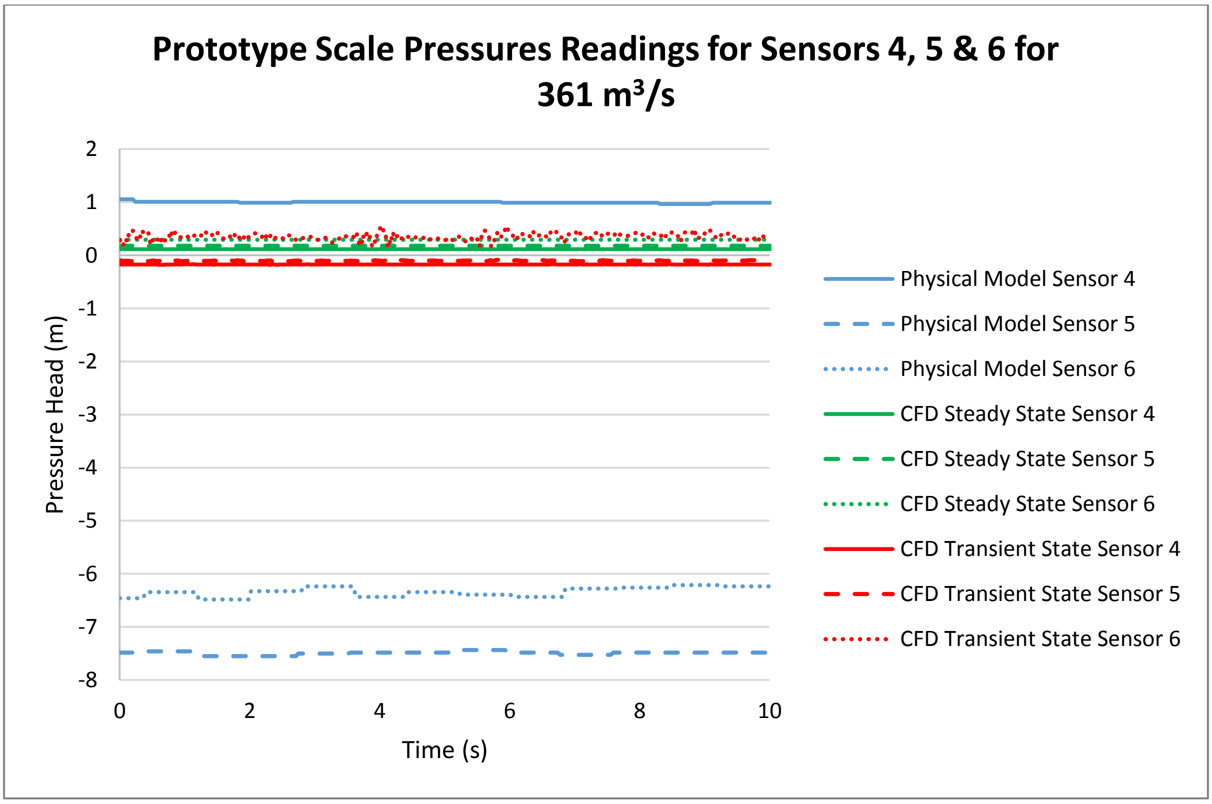

Figure E.7 Pressure readings for transient and steady state simulations and physical modelling for sensors 4-6 for a flow rate of 361 m^3/s at the prototype scale

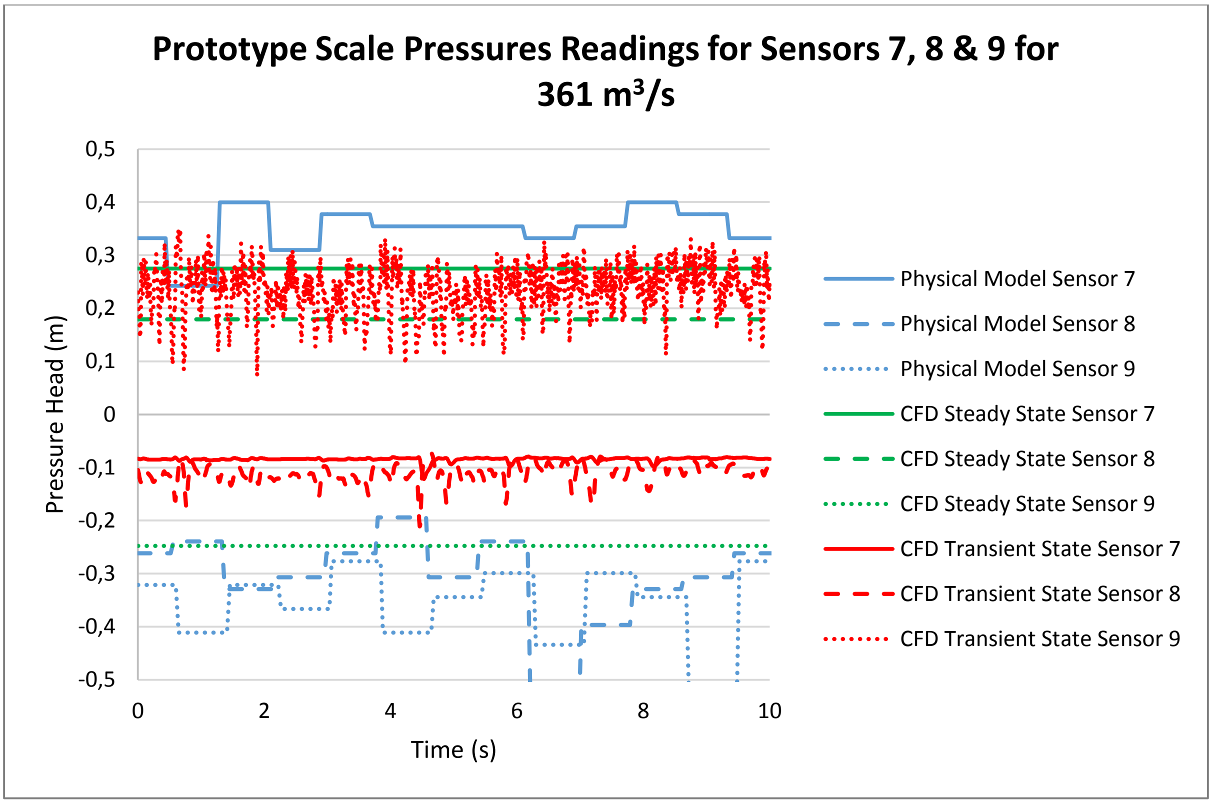

Figure E.8 Pressure readings for transient and steady state simulations and physical modelling for sensors 7-9 for a flow rate of 361 m^3/s at the prototype scale

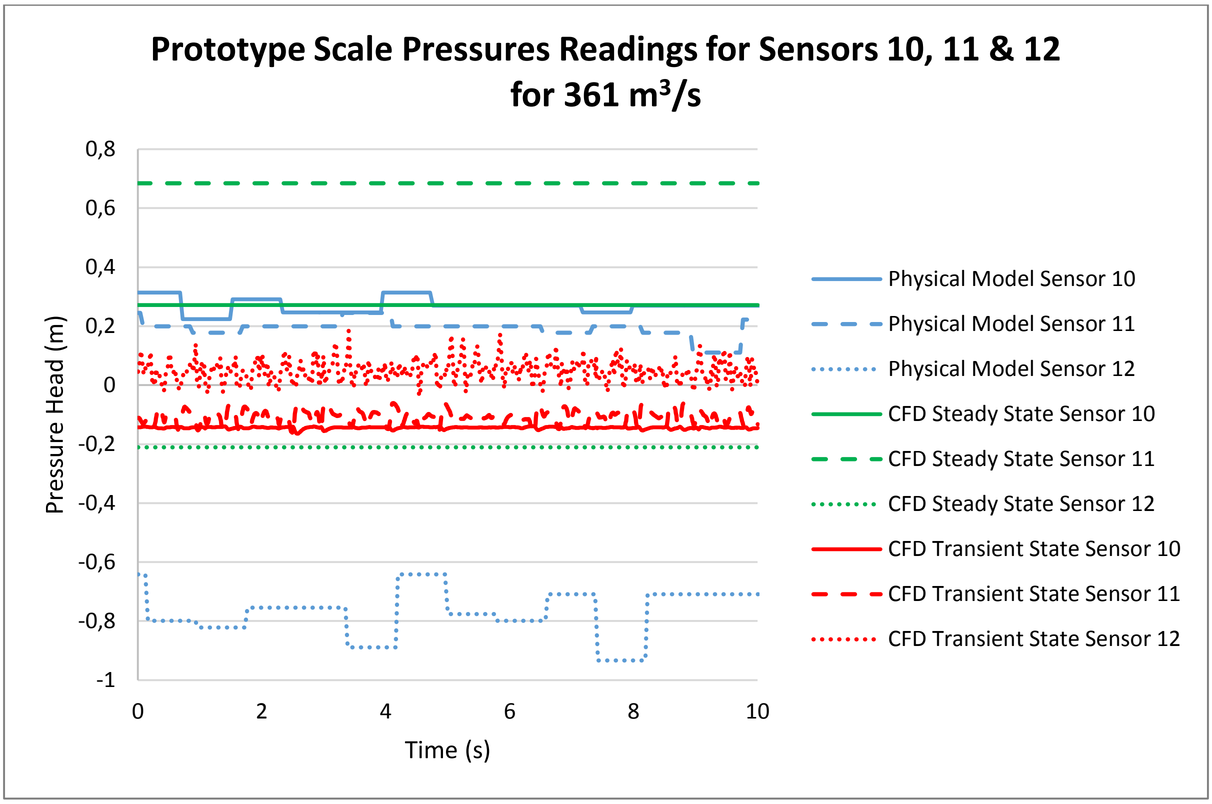

Figure E.9 Pressure readings for transient and steady state simulations and physical modelling for sensors 10-12 for a flow rate of 361 m^3/s at the prototype scale

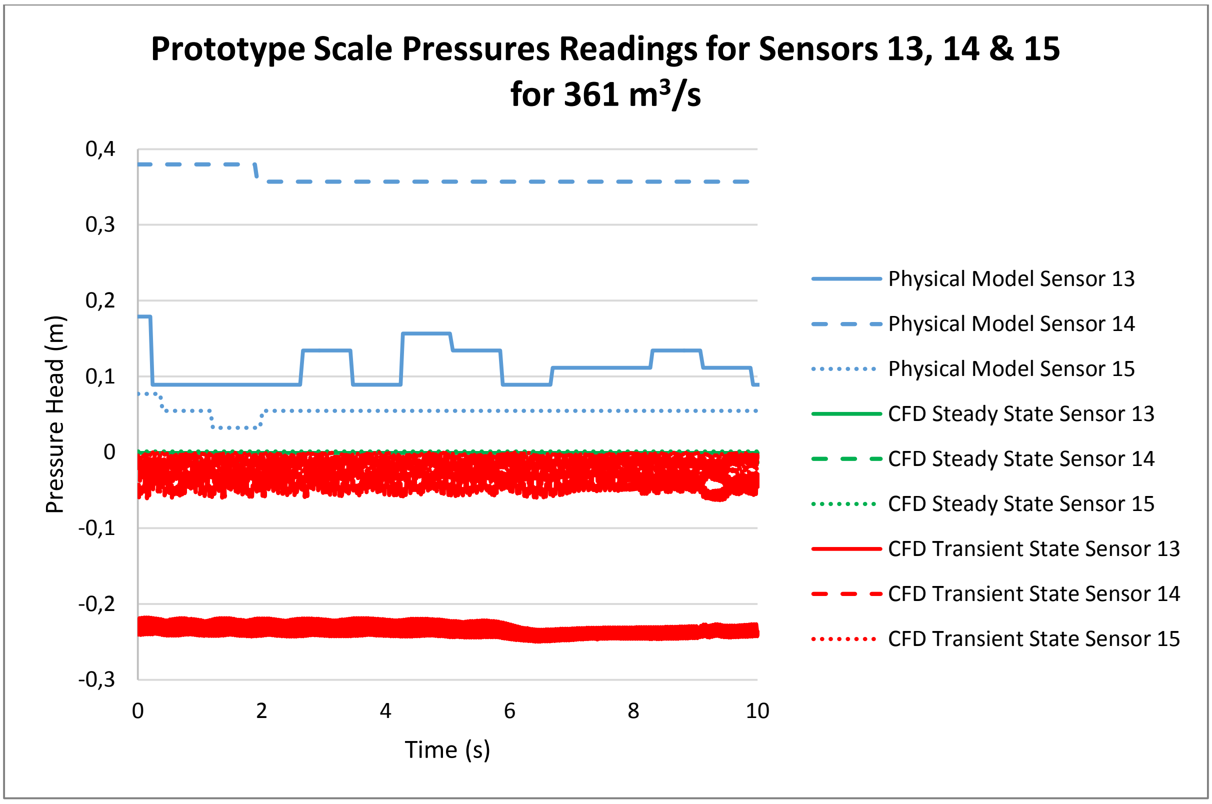

Figure E.10 Pressure readings for transient and steady state simulations and physical modelling for sensors 13-15 for a flow rate of 361 m^3*/s at the prototype scale*

Test 3: 544 m^3/s

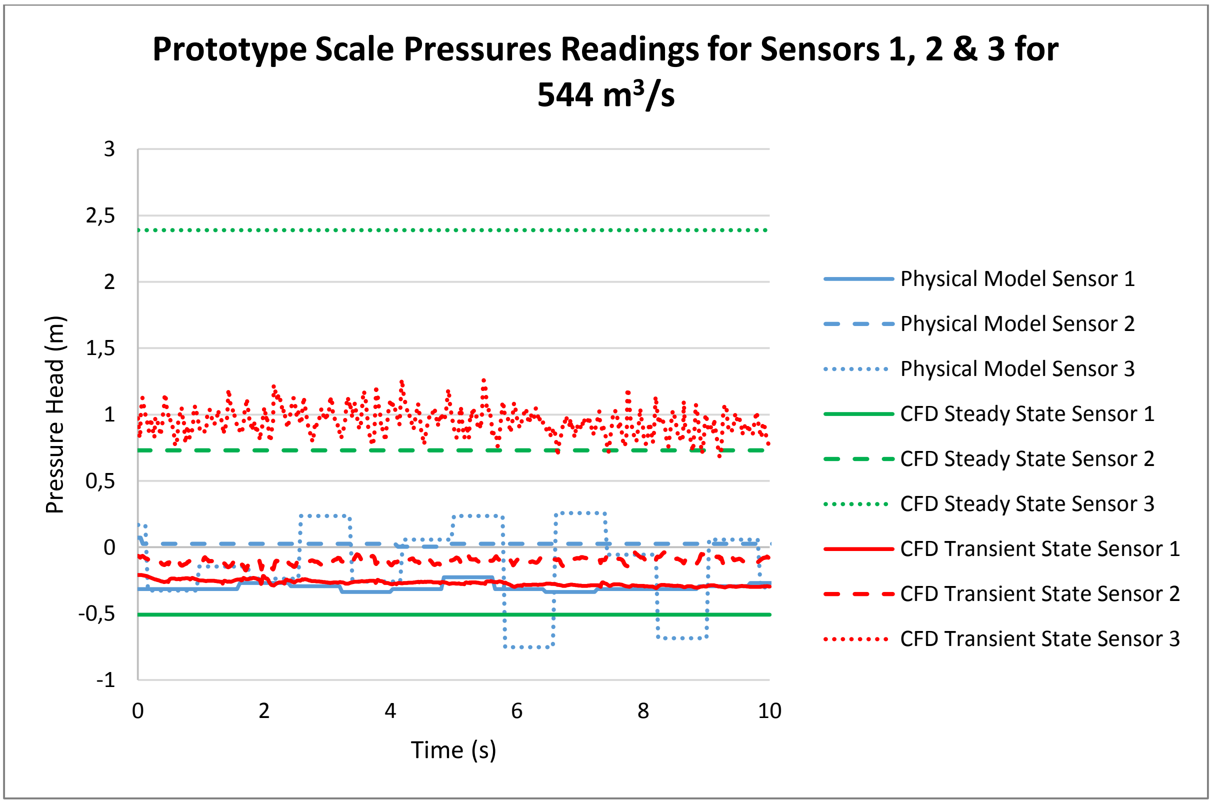

Figure E.11 Pressure readings for transient and steady state simulations and physical modelling for sensors 1-3 for a flow rate of 544 m^3*/s at the prototype scale*

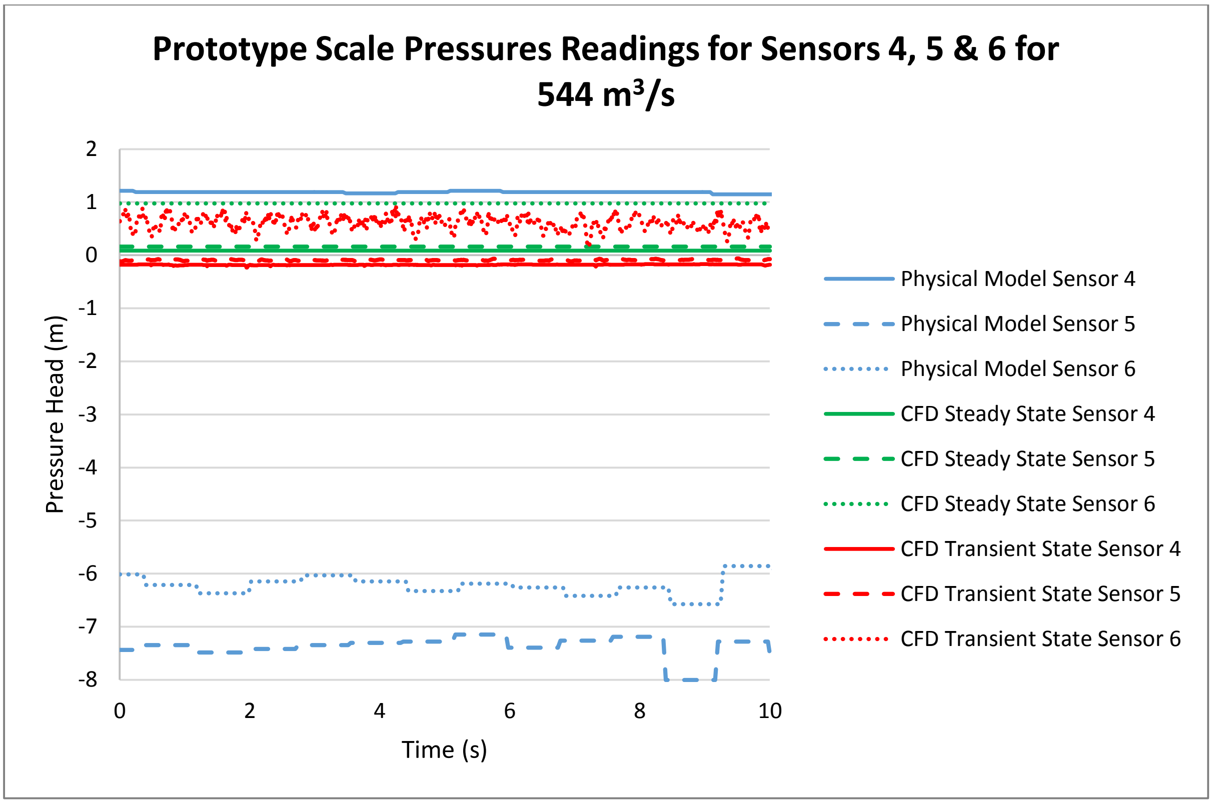

Figure E.12 Pressure readings for transient and steady state simulations and physical modelling for sensors 4-6 for a flow rate of 544 m^3*/s at the prototype scale*

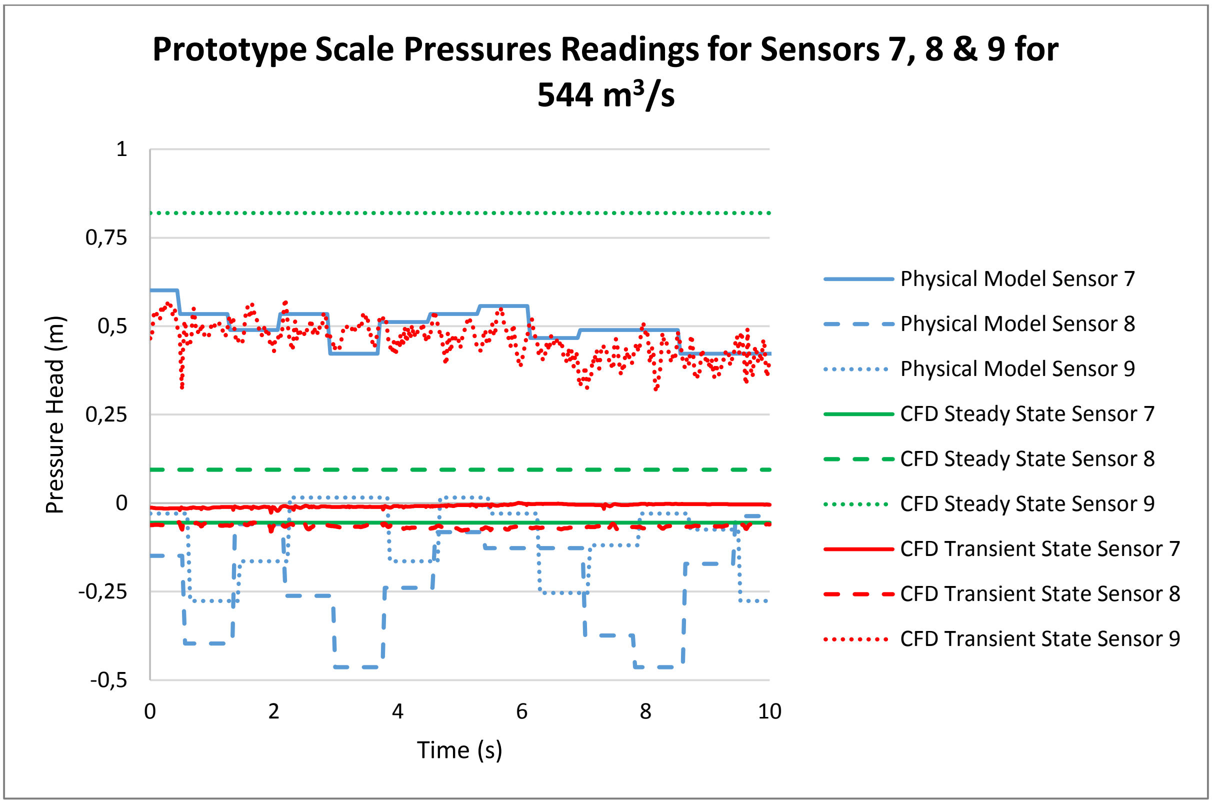

Figure E.13 Pressure readings for transient and steady state simulations and physical modelling for sensors 7-9 for a flow rate of 544 m^3*/s at the prototype scale*

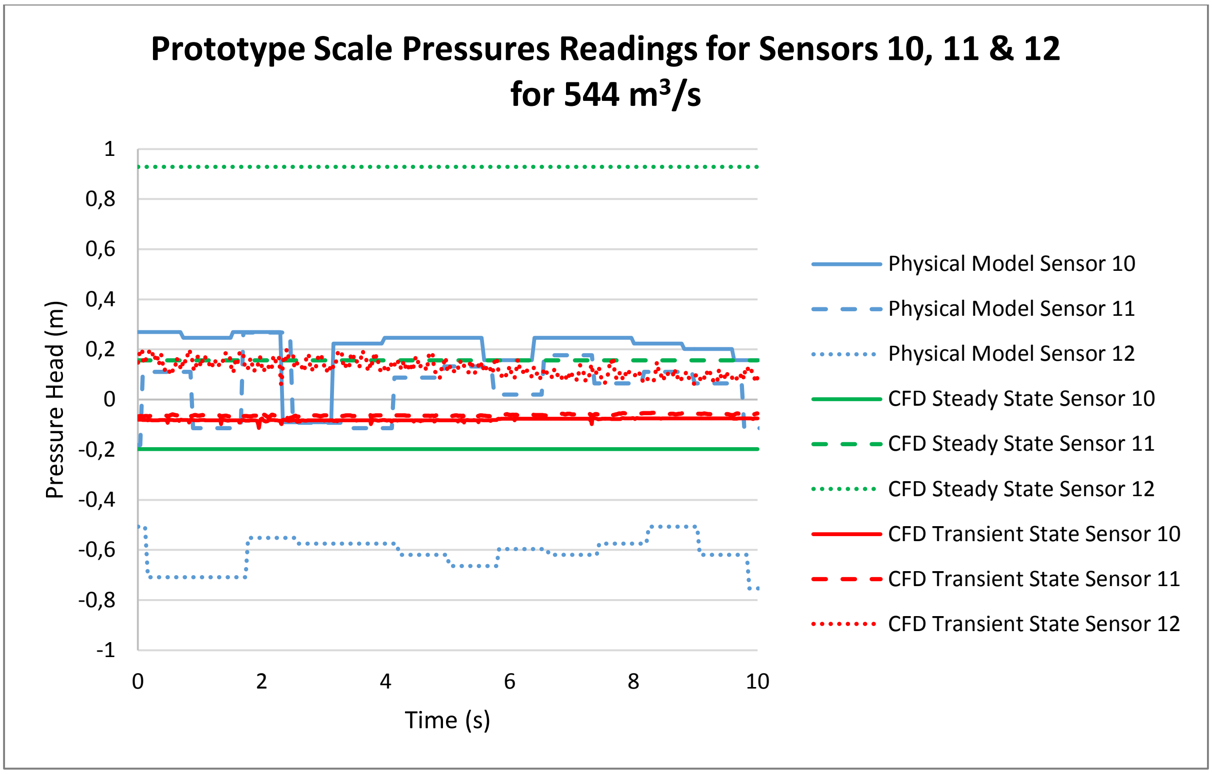

Figure E.14 Pressure readings for transient and steady state simulations and physical modelling for sensors 10-12 for a flow rate of 544 m^3/s at the prototype scale

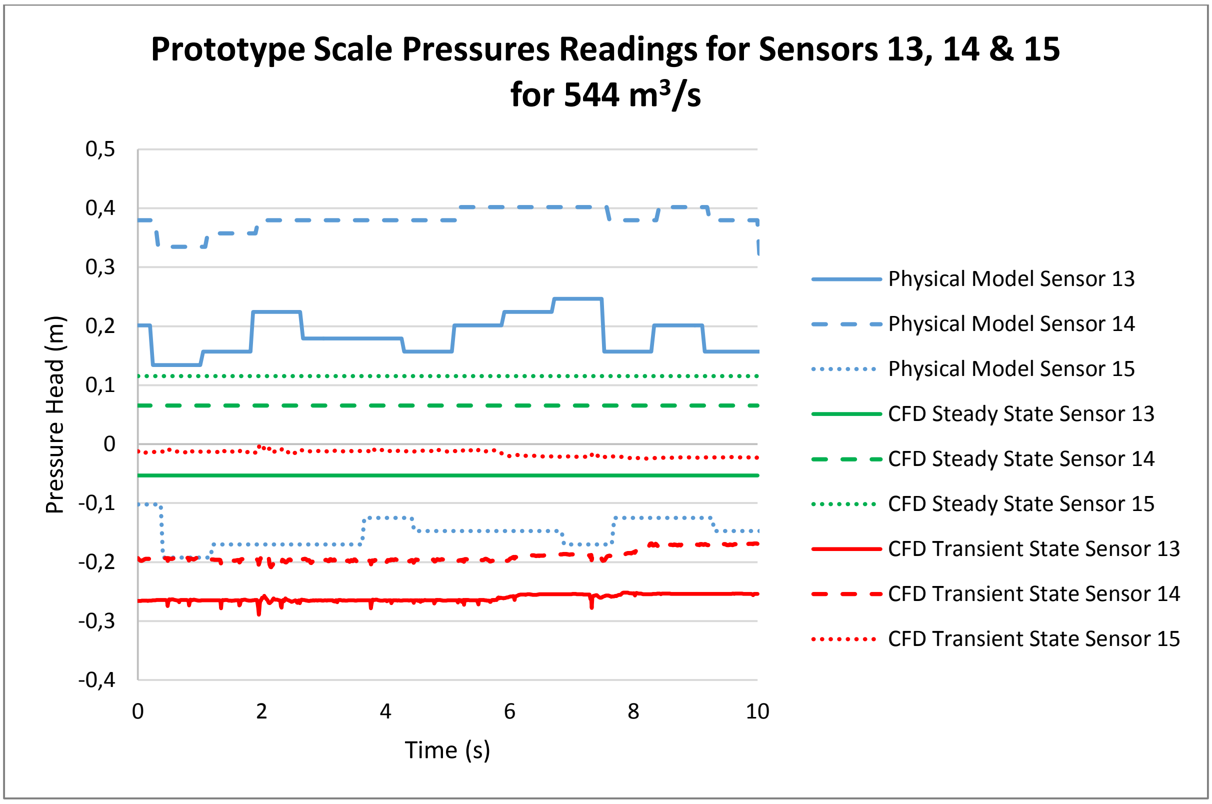

Figure E.15 Pressure readings for transient and steady state simulations and physical modelling for sensors 13-15 for a flow rate of 544 m^3/s at the prototype scale

Test 4: 712 m^3/s

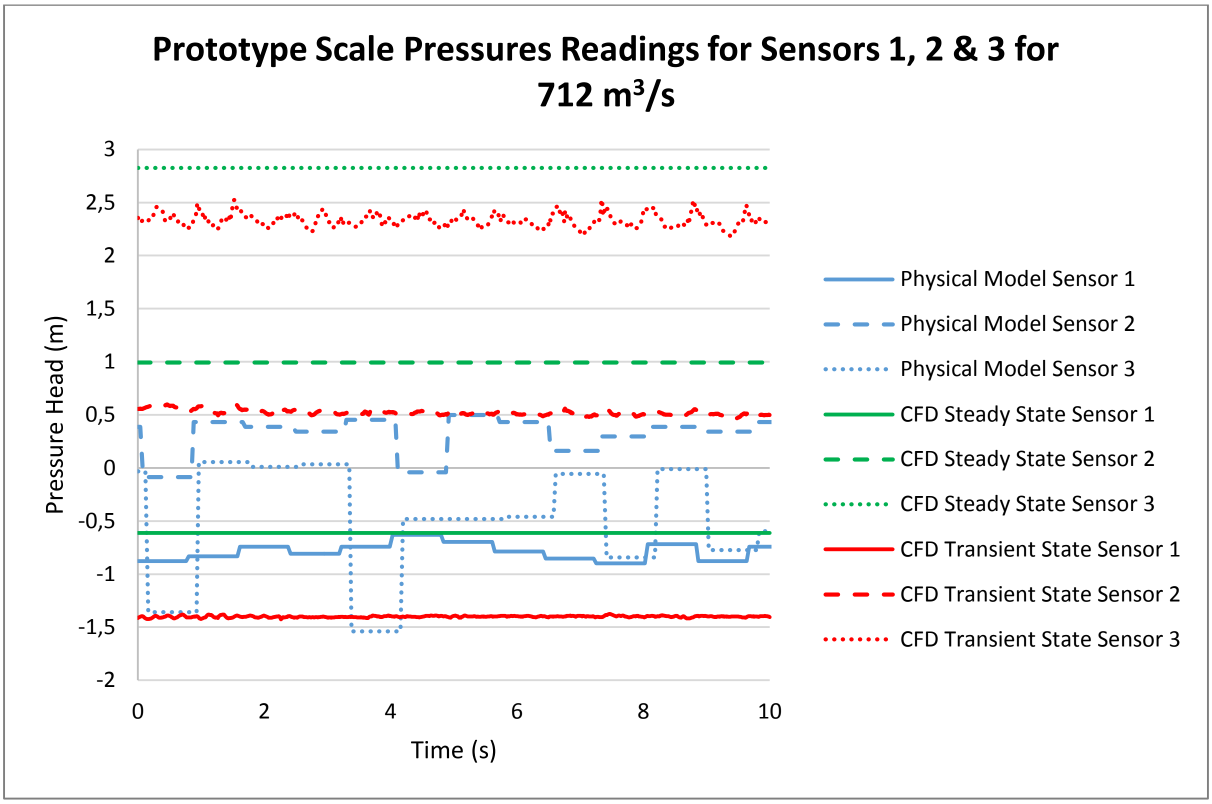

Figure E.16 Pressure readings for transient and steady state simulations and physical modelling for sensors 1-3 for a flow rate of 712 m^3/s at the prototype scale

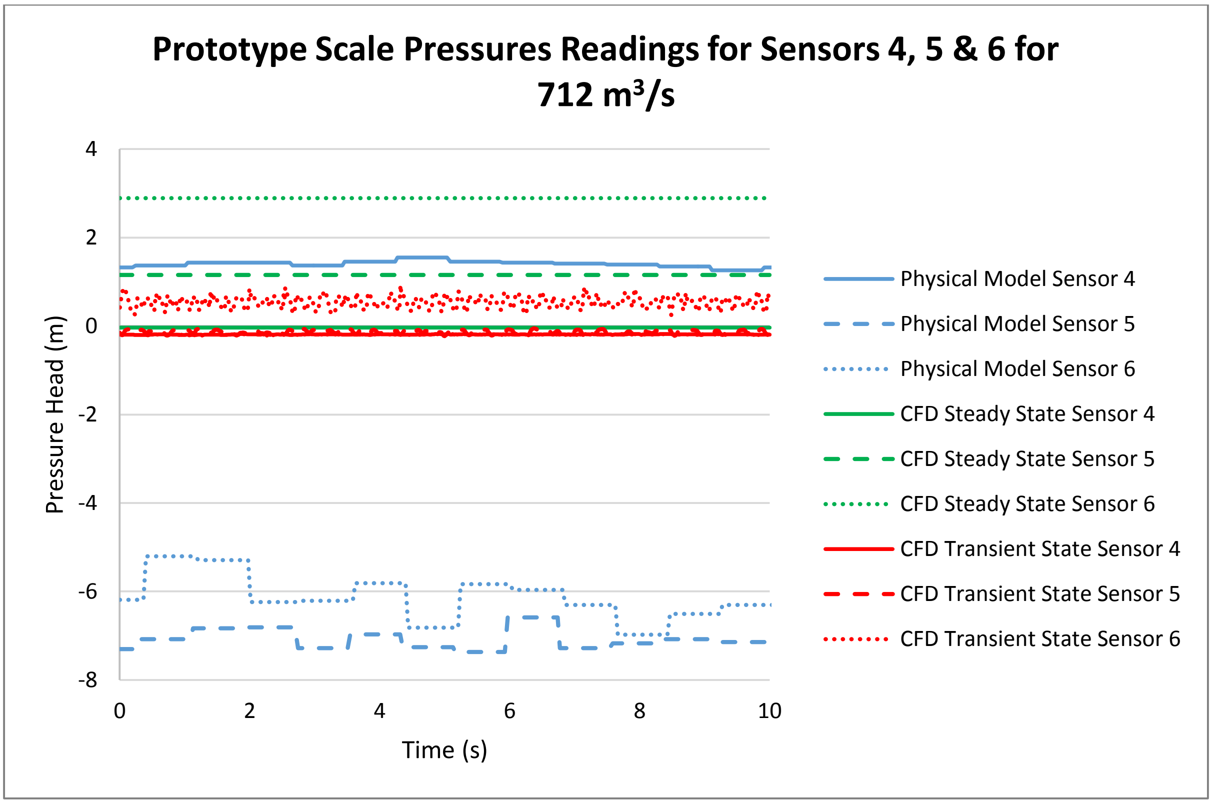

Figure E.17 Pressure readings for transient and steady state simulations and physical modelling for sensors 4-6 for a flow rate of 712 m^3/s at the prototype scale

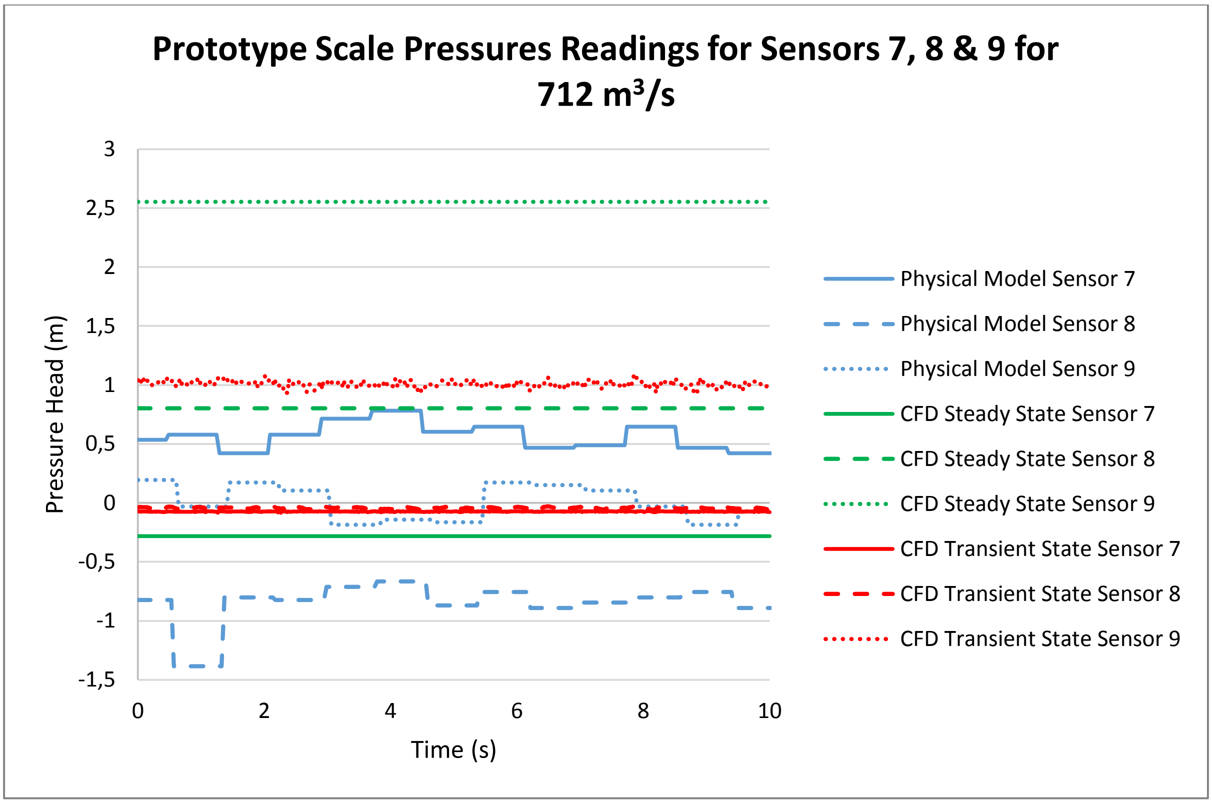

Figure E.18 Pressure readings for transient and steady state simulations and physical modelling for sensors 7-9 for a flow rate of 712 m^3/s at the prototype scale

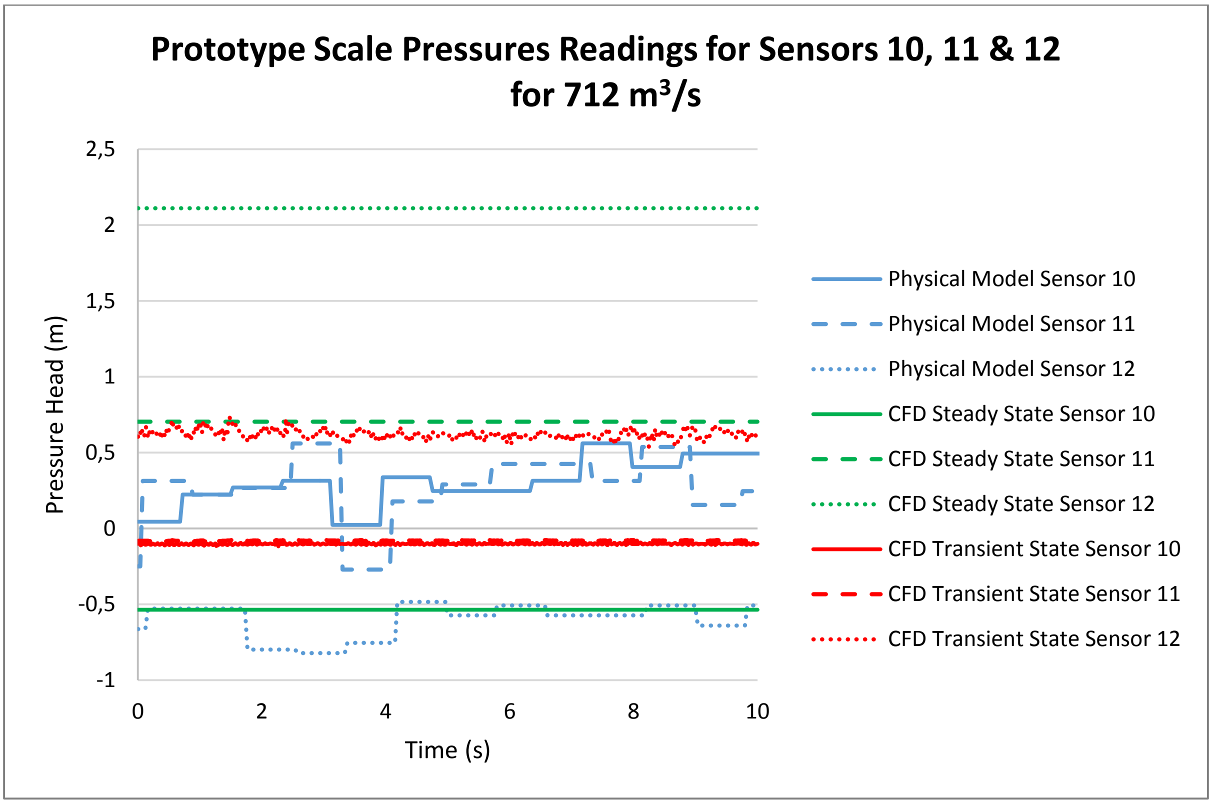

Figure E.19 Pressure readings for transient and steady state simulations and physical modelling for sensors 10-12 for a flow rate of 712 m^3/s at the prototype scale

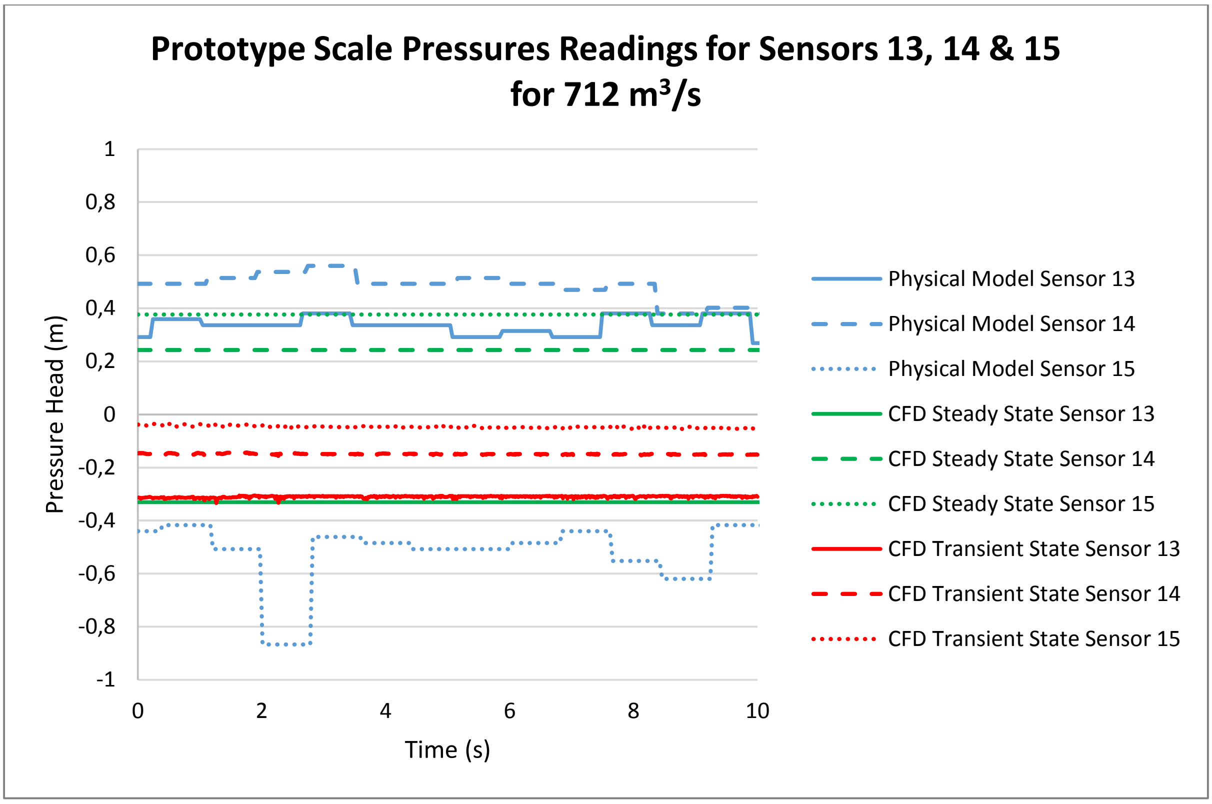

Figure E.20 Pressure readings for transient and steady state simulations and physical modelling for sensors 13-15 for a flow rate of 712 m^3/s at the prototype scale

Test 5: 898 m^3/s

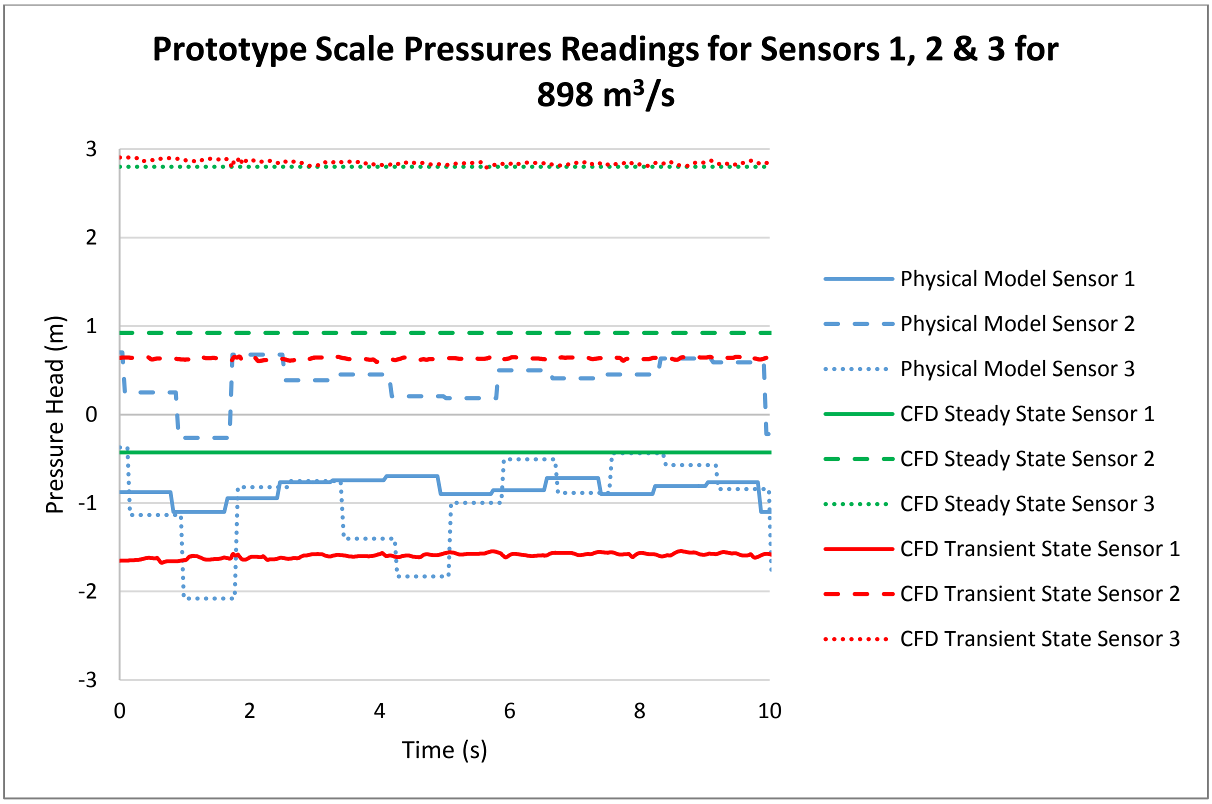

Figure E.21 Pressure readings for transient and steady state simulations and physical modelling for sensors 1-3 for a flow rate of 898 m^3/s at the prototype scale

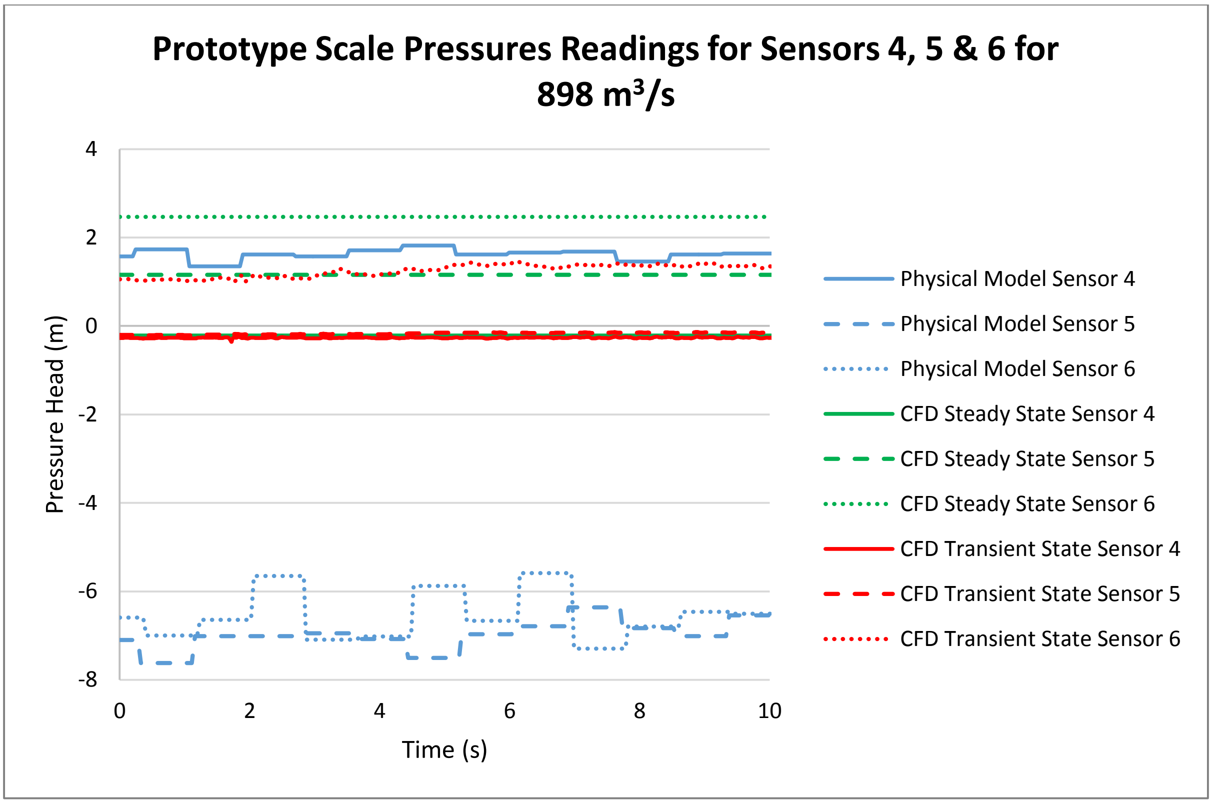

Figure E.22 Pressure readings for transient and steady state simulations and physical modelling for sensors 4-6 for a flow rate of 898 m^3/s at the prototype scale

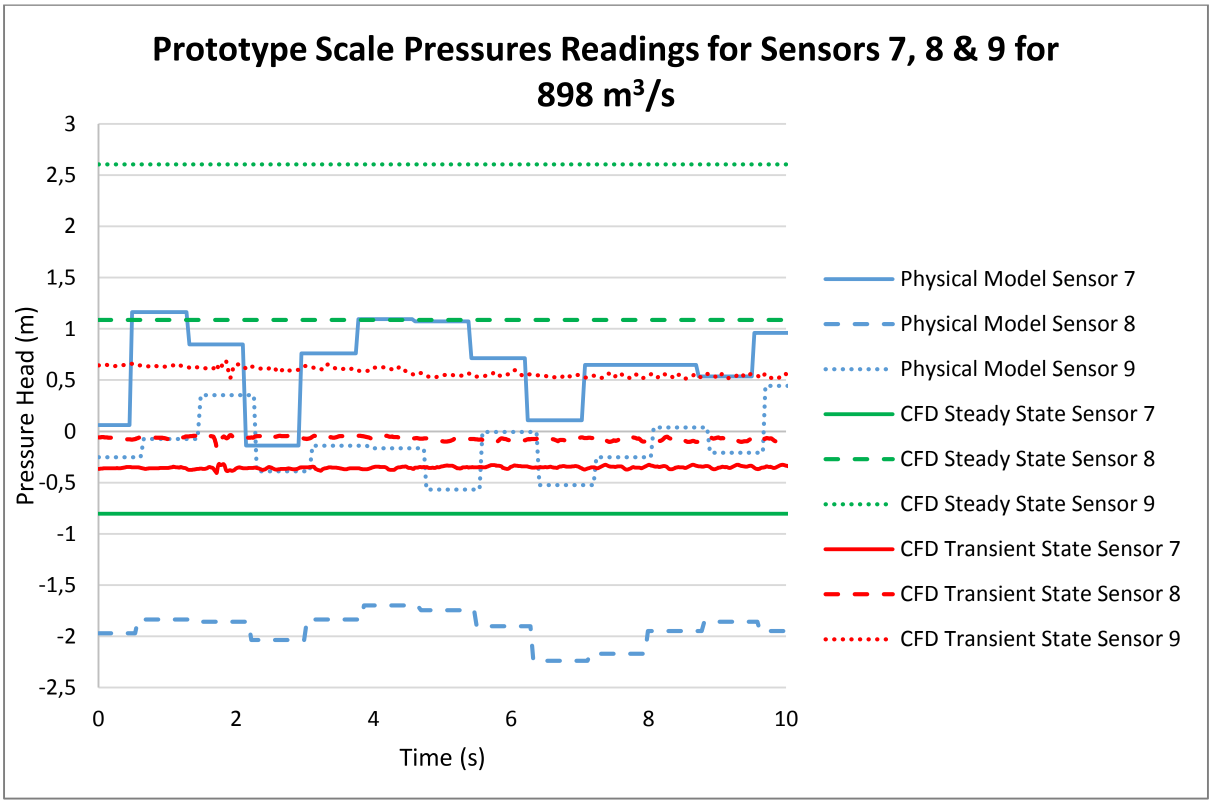

Figure E.23 Pressure readings for transient and steady state simulations and physical modelling for sensors 7-9 for a flow rate of 898 m^3/s at the prototype scale

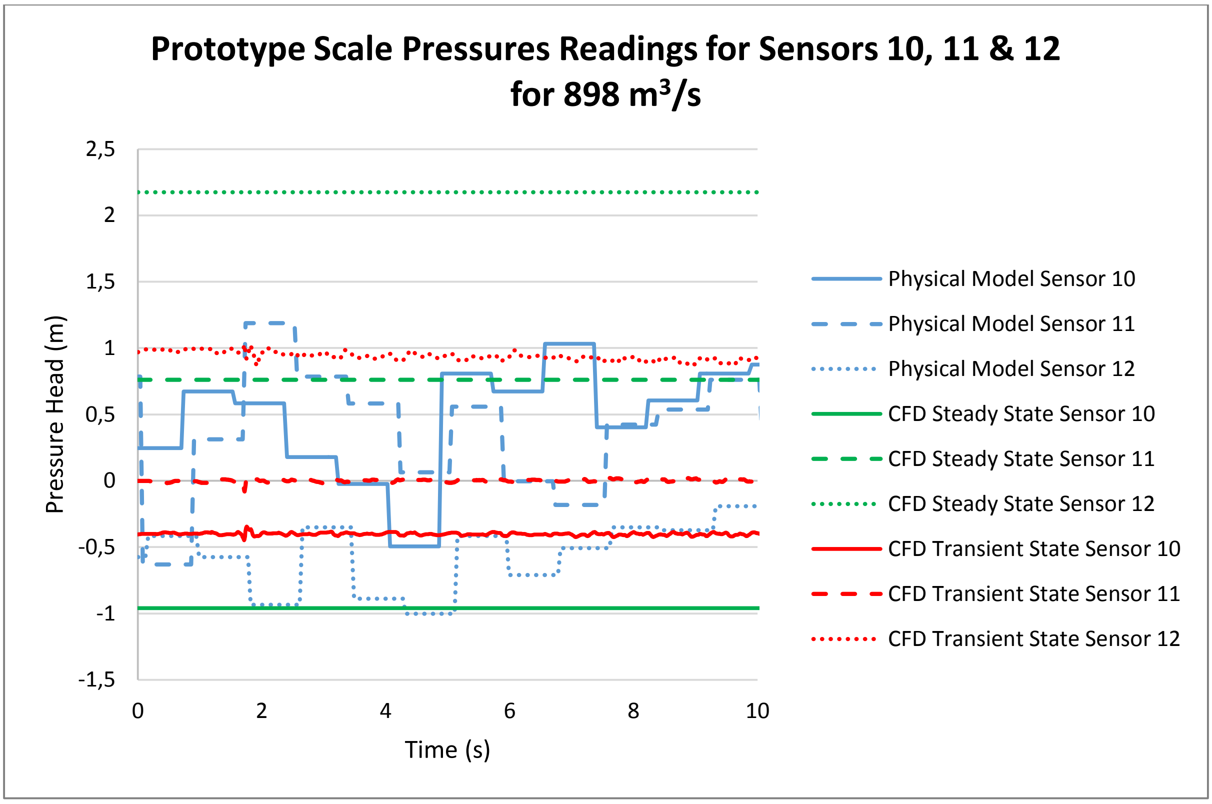

Figure E.24 Pressure readings for transient and steady state simulations and physical modelling for sensors 10-12 for a flow rate of 898 m^3/s at the prototype scale

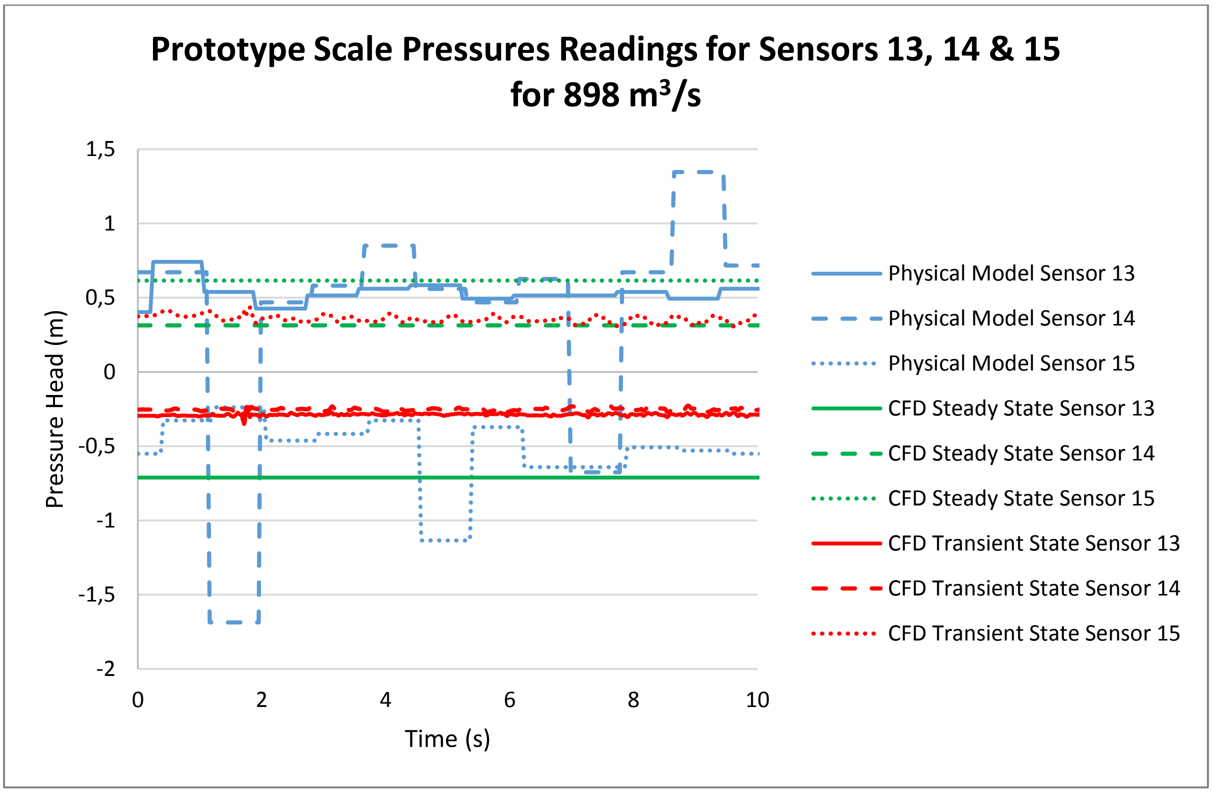

Figure E.25 Pressure readings for transient and steady state simulations and physical modelling for sensors 13-15 for a flow rate of 898 m^3/s at the prototype scale

Test 6: 1 063 m^3/s

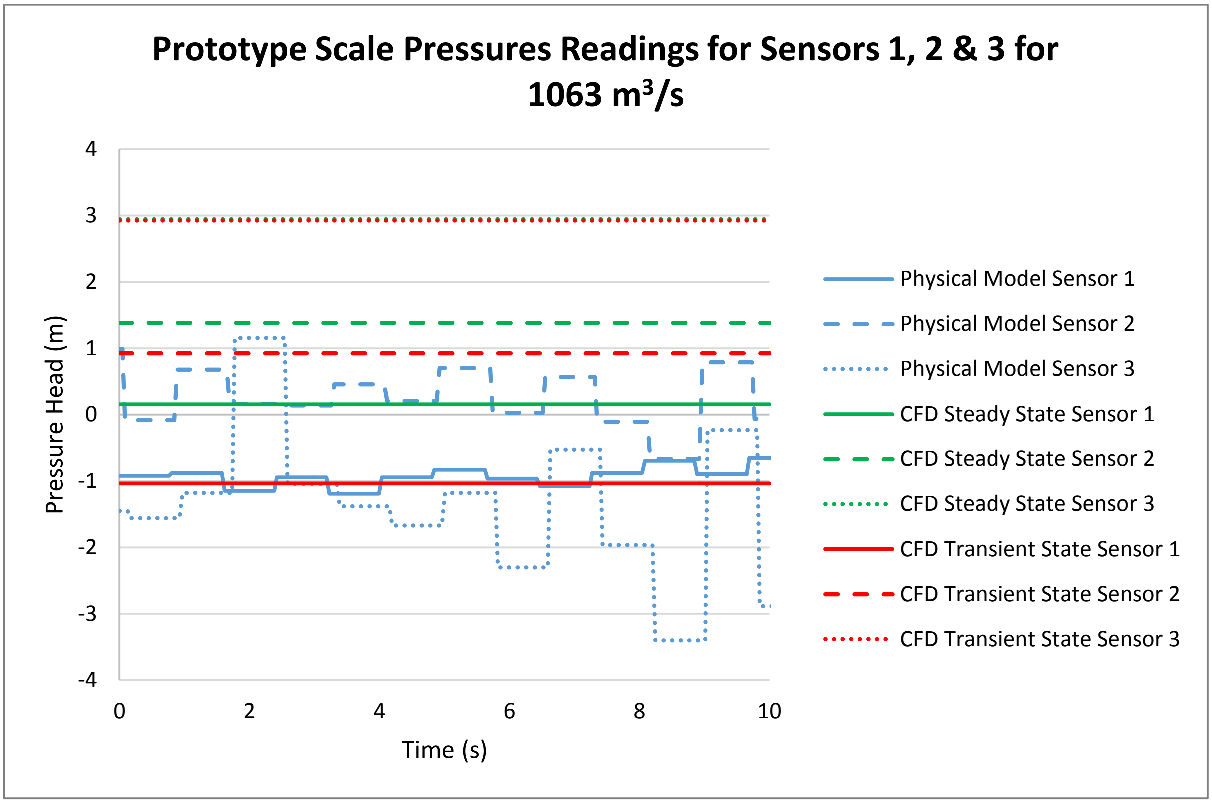

Figure E.26 Pressure readings for transient and steady state simulations and physical modelling for sensors 1-3 for a flow rate of 1 063 m^3/s at the prototype scale

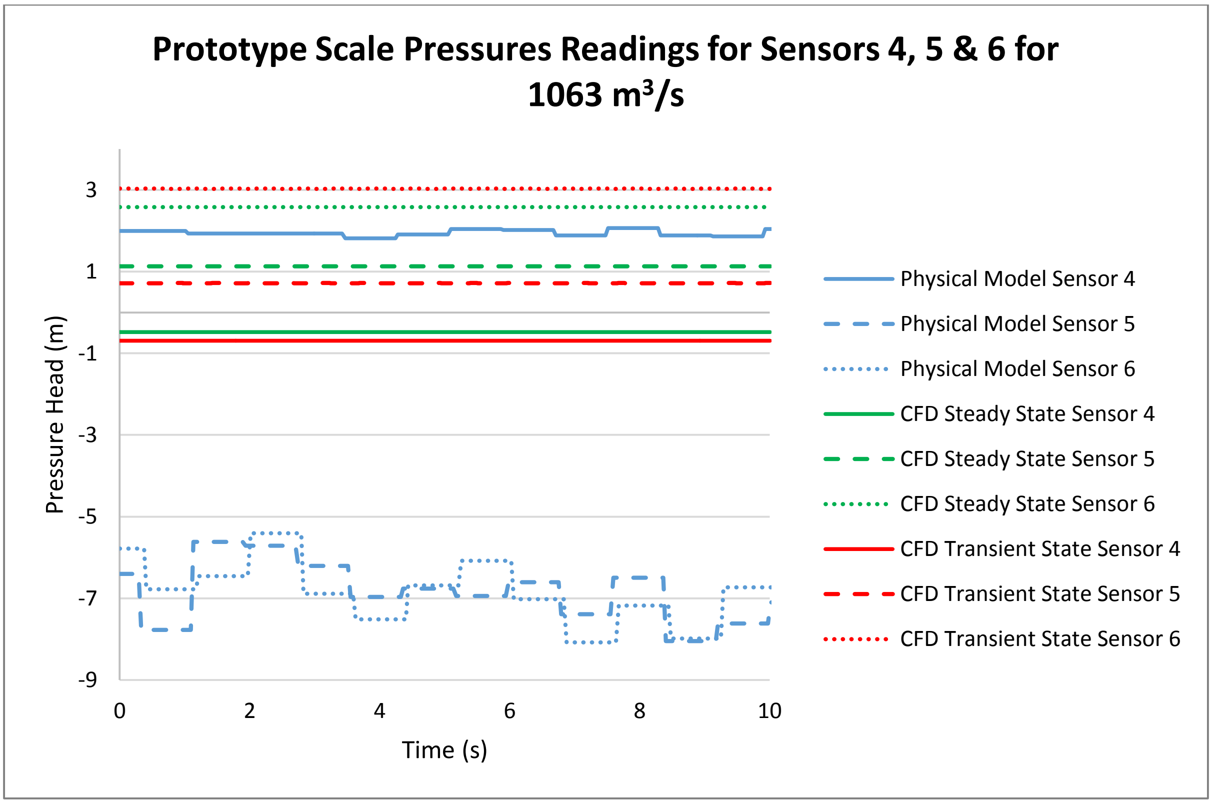

Figure E.27 Pressure readings for transient and steady state simulations and physical modelling for sensors 4-6 for a flow rate of 1 063 m^3/s at the prototype scale

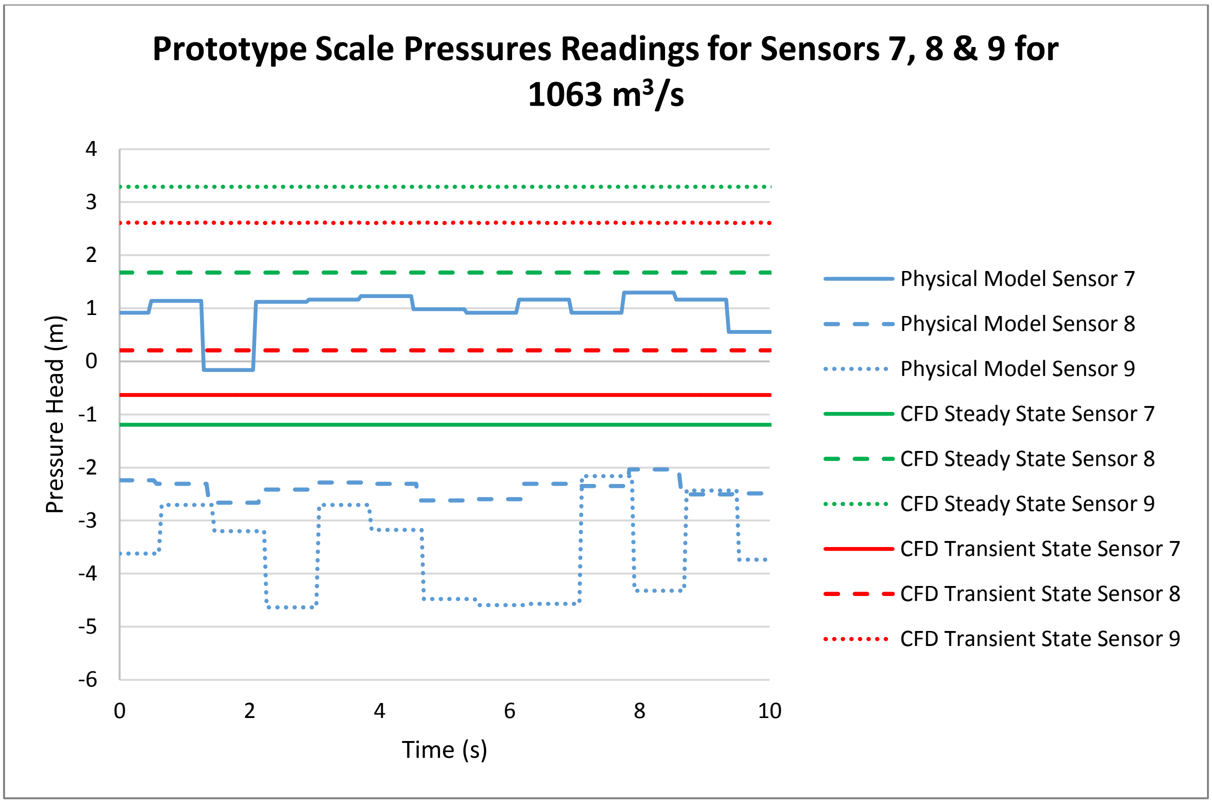

Figure E.28 Pressure readings for transient and steady state simulations and physical modelling for sensors 7-9 for a flow rate of 1 063 m^3/s at the prototype scale

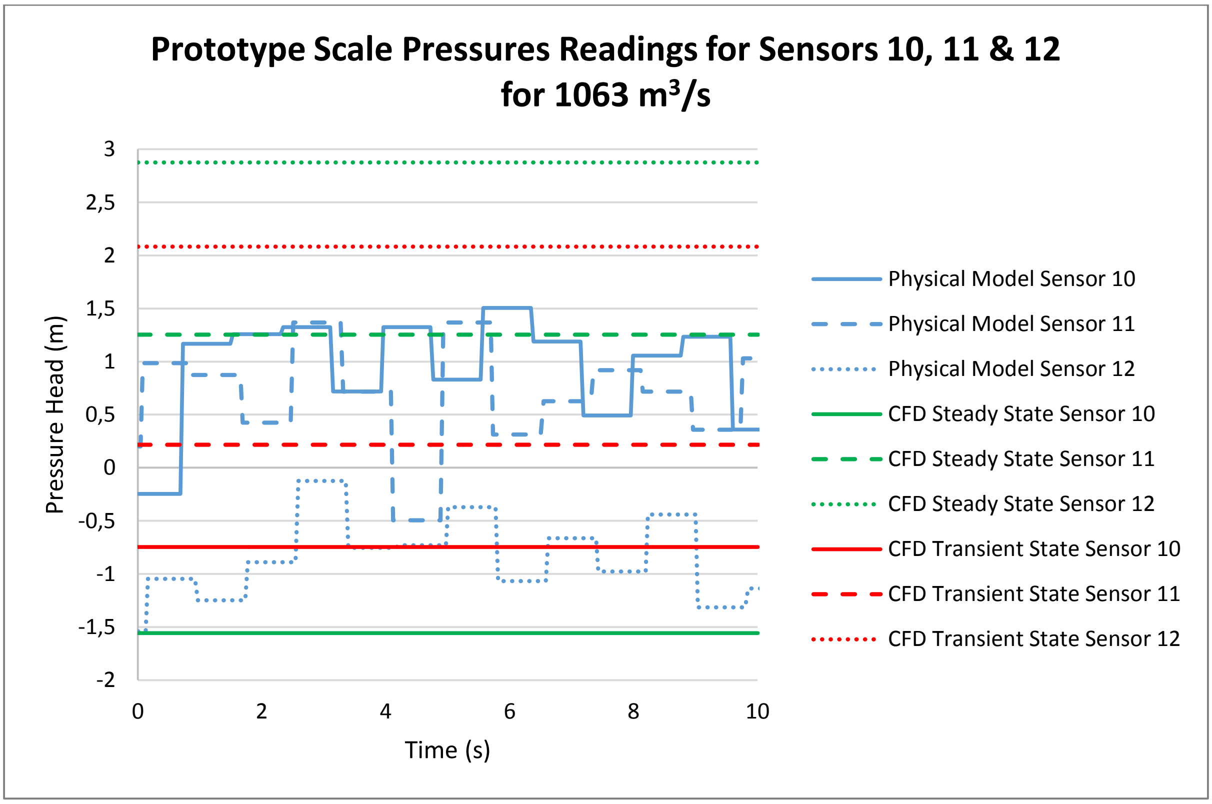

Figure E.29 Pressure readings for transient and steady state simulations and physical modelling for sensors 10-12 for a flow rate of 1 063 m^3/s at the prototype scale

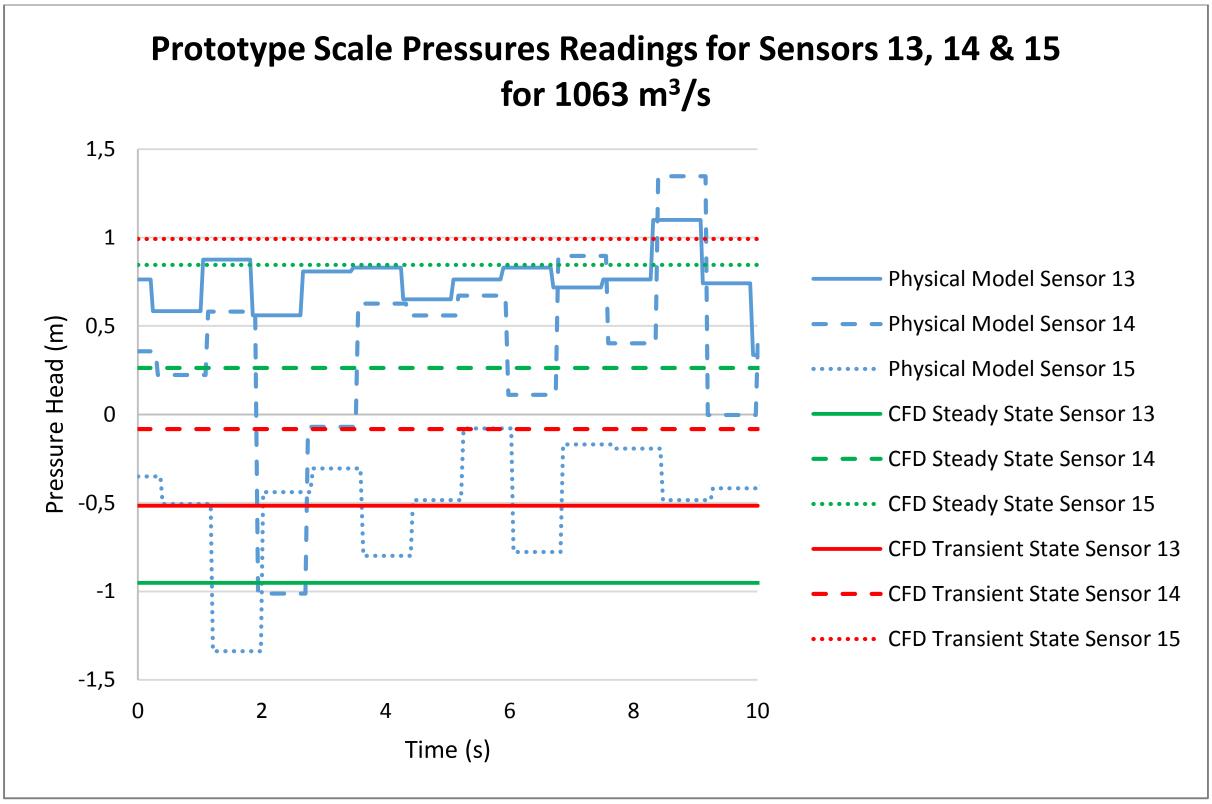

Figure E.30 Pressure readings for transient and steady state simulations and physical modelling for sensors 13-15 for a flow rate of 1 063 m^3/s at the prototype scale

Test 7: 1 249 m^3/s

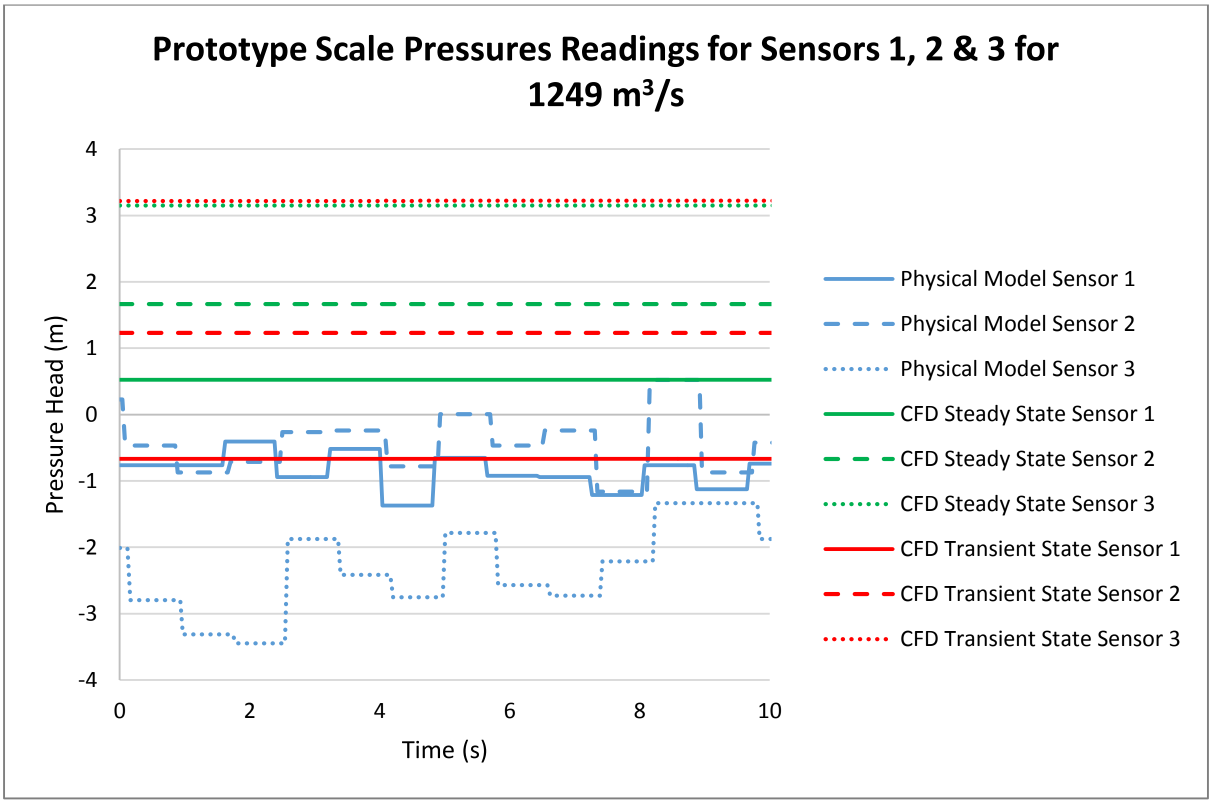

Figure E.31 Pressure readings for transient and steady state simulations and physical modelling for sensors 1-3 for a flow rate of 1 249 m^3/s at the prototype scale

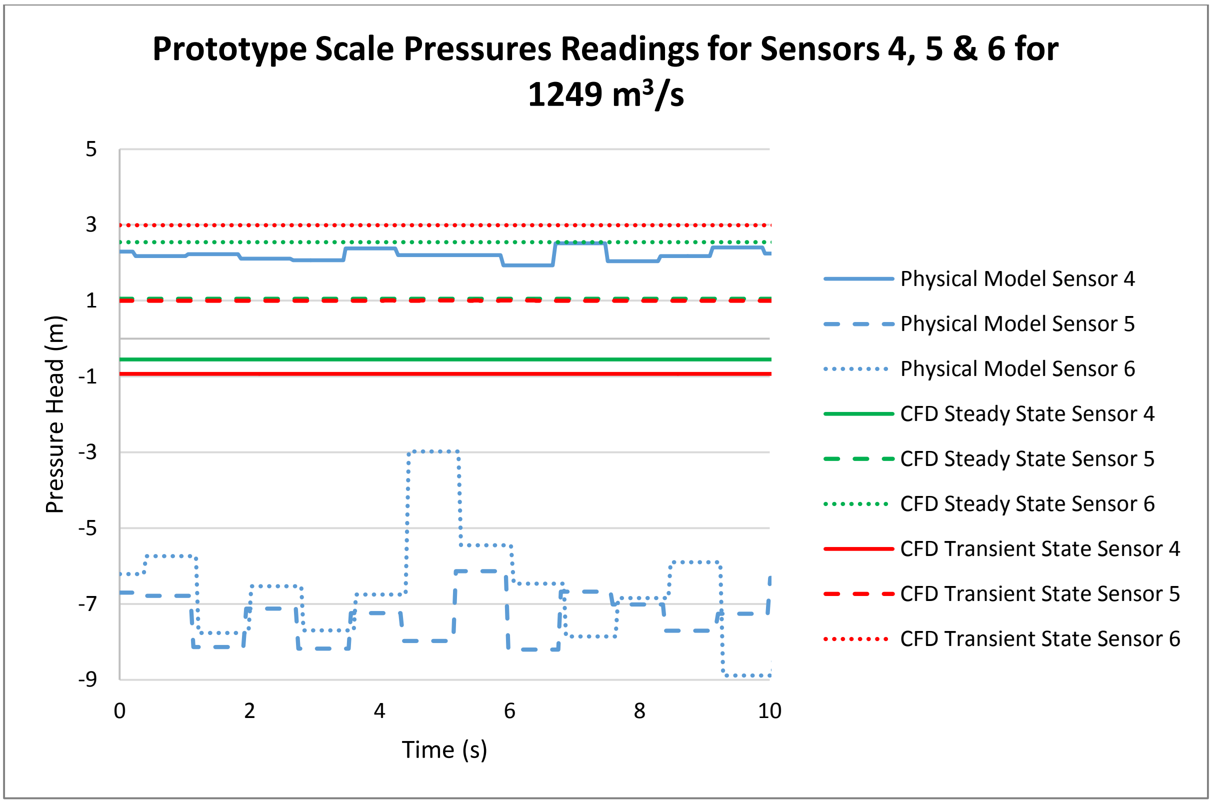

Figure E.32 Pressure readings for transient and steady state simulations and physical modelling for sensors 4-6 for a flow rate of 1 249 m^3/s at the prototype scale

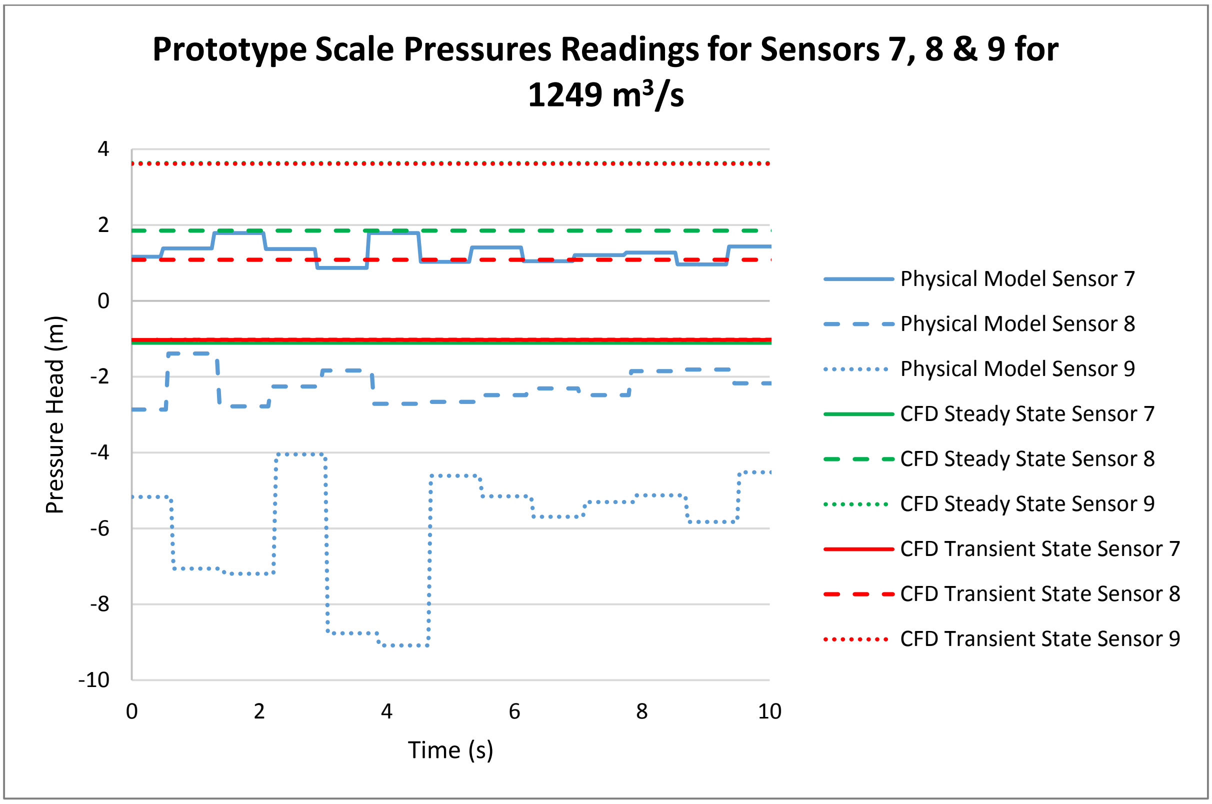

Figure E.33 Pressure readings for transient and steady state simulations and physical modelling for sensors 7-9 for a flow rate of 1 249 m^3/s at the prototype scale

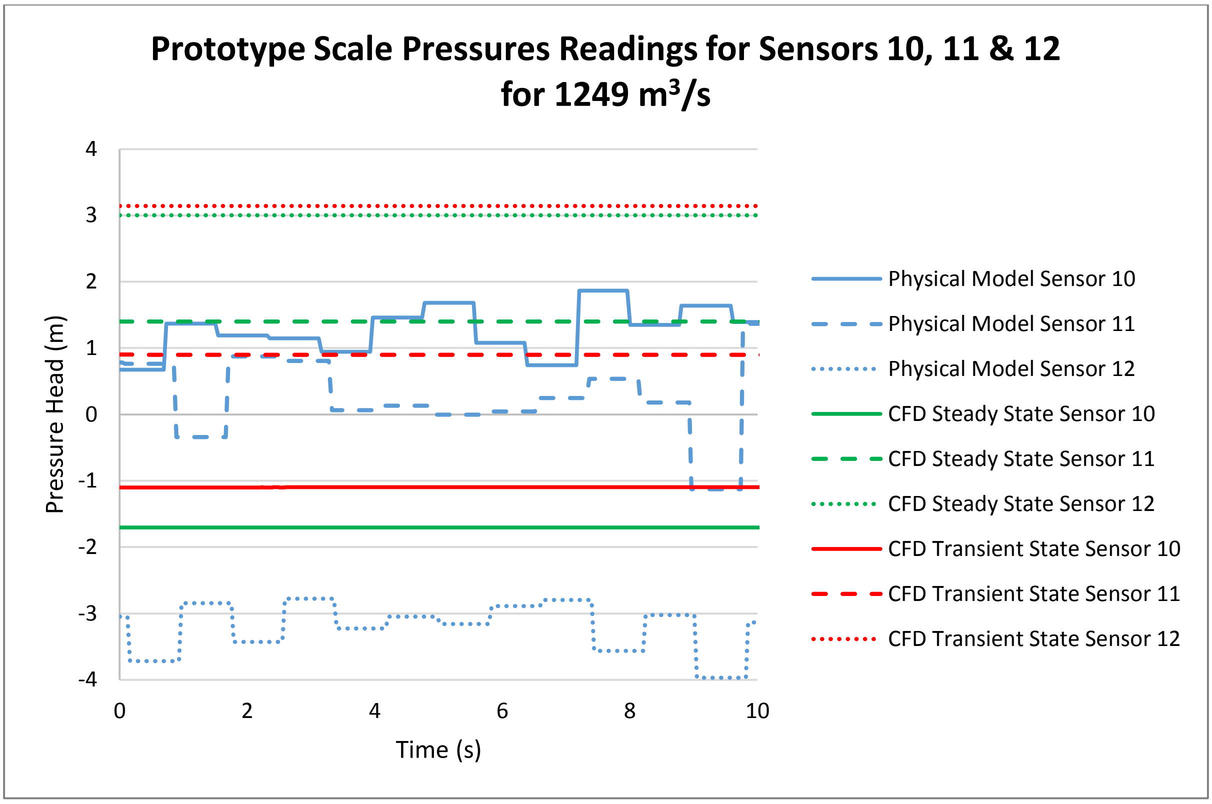

Figure E.34 Pressure readings for transient and steady state simulations and physical modelling for sensors 10-12 for a flow rate of 1 249 m^3/s at the prototype scale

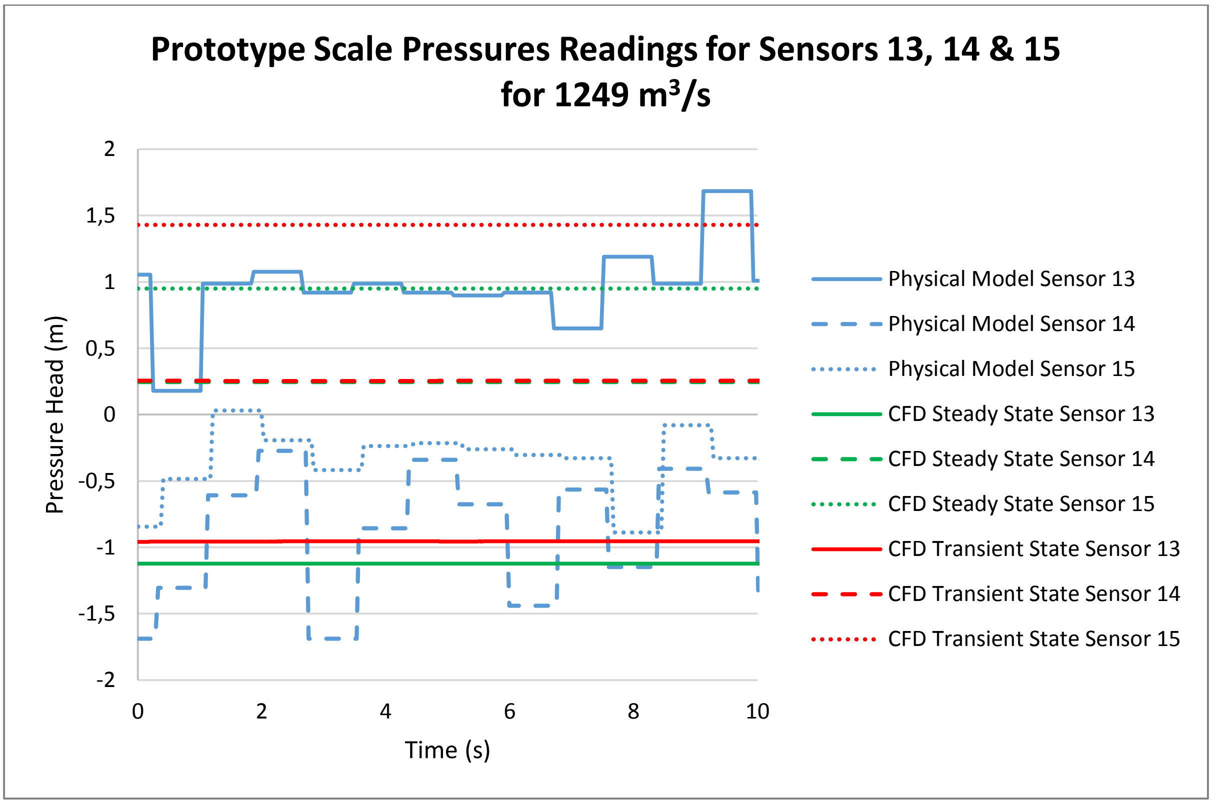

Figure E.35 Pressure readings for transient and steady state simulations and physical modelling for sensors 13-15 for a flow rate of 1 249 m^3/s at the prototype scale

Test 8: 1 424 m^3/s

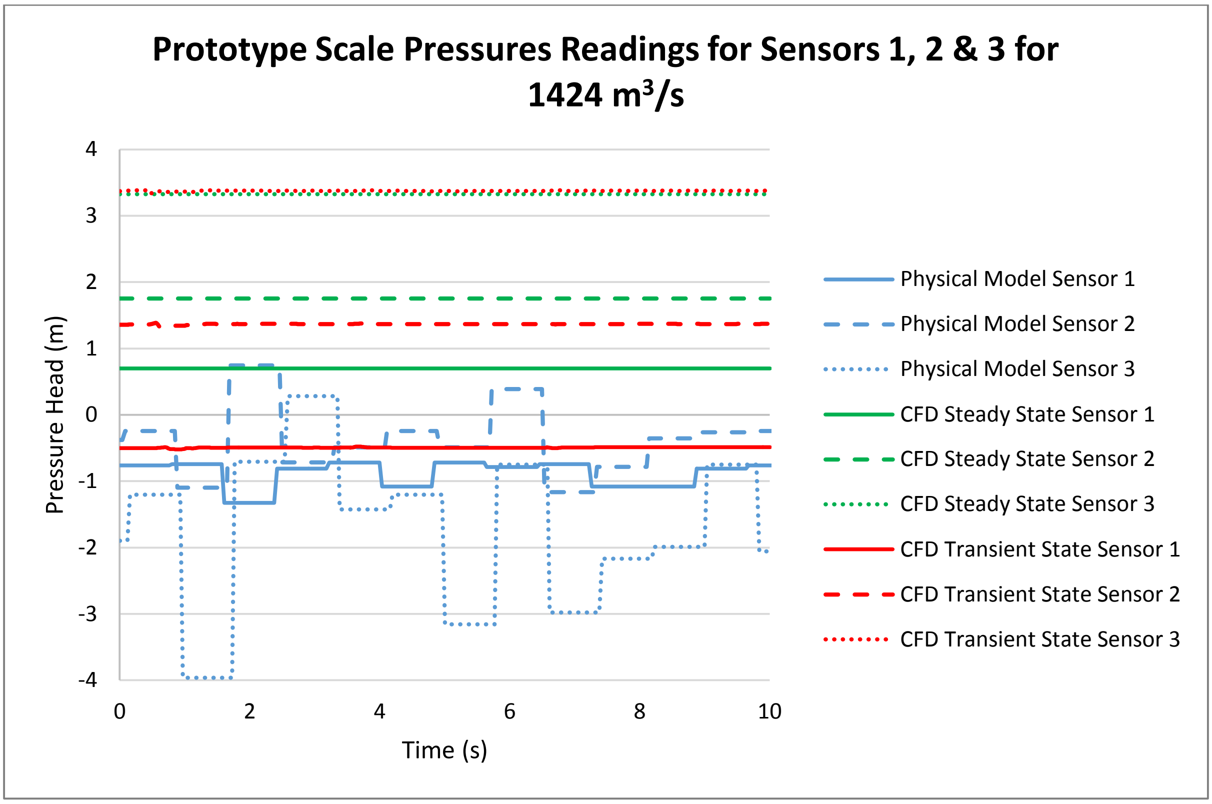

Figure E.36 Pressure readings for transient and steady state simulations and physical modelling for sensors 1-3 for a flow rate of 1 424 m^3/s at the prototype scale

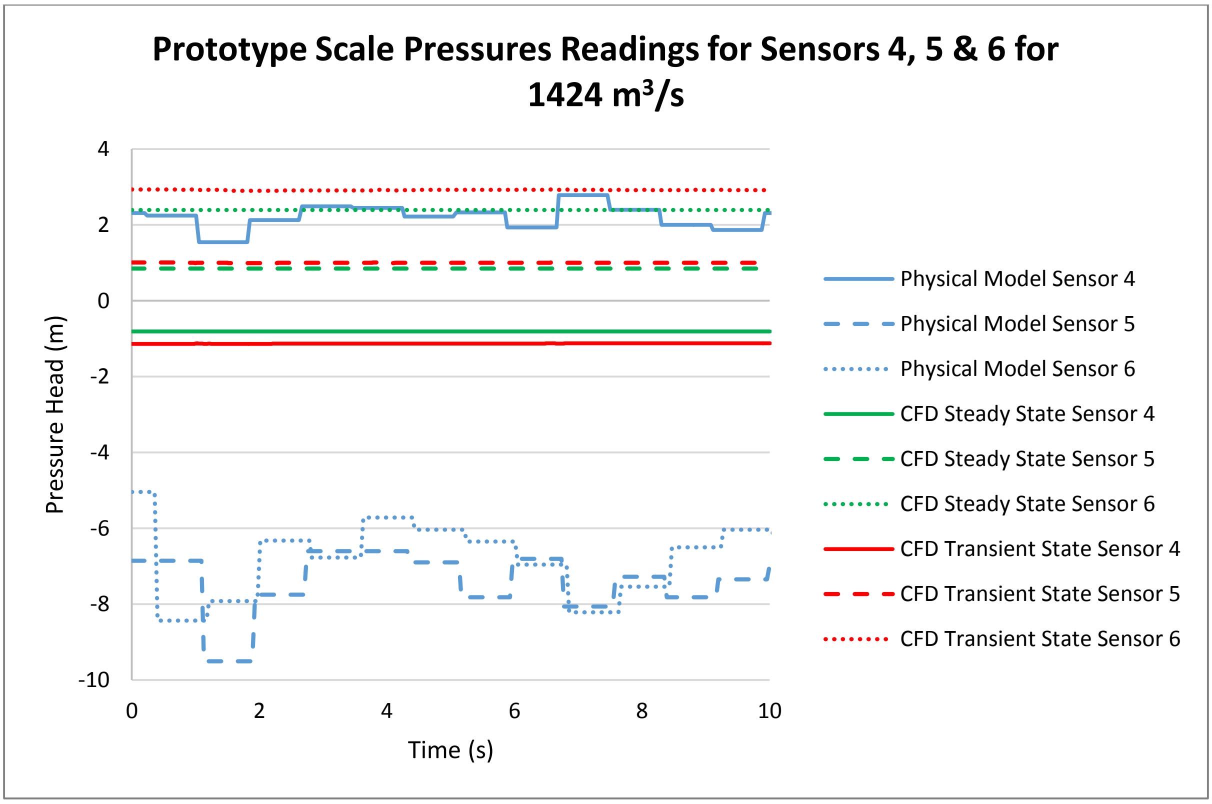

Figure E.37 Pressure readings for transient and steady state simulations and physical modelling for sensors 4-6 for a flow rate of 1 424 m^3/s at the prototype scale

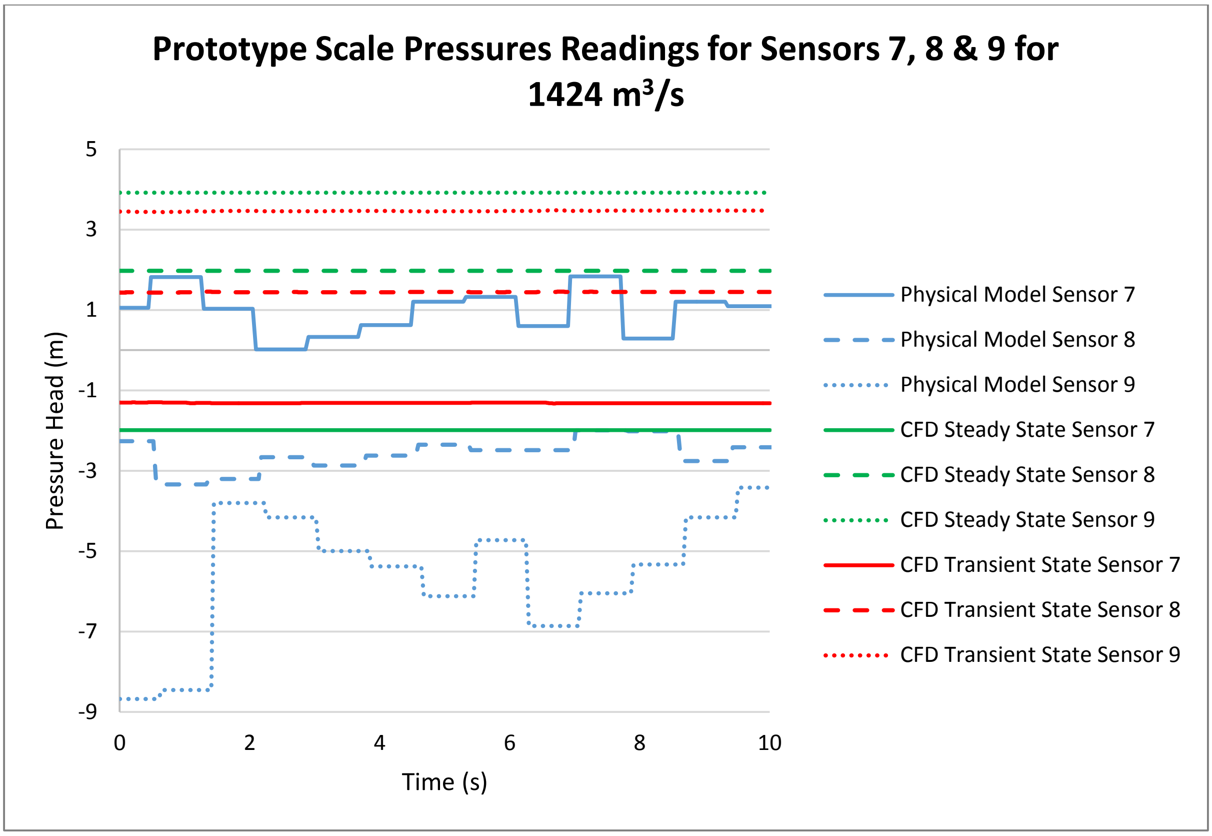

Figure E.38 Pressure readings for transient and steady state simulations and physical modelling for sensors 7-9 for a flow rate of 1 424 m^3/s at the prototype scale

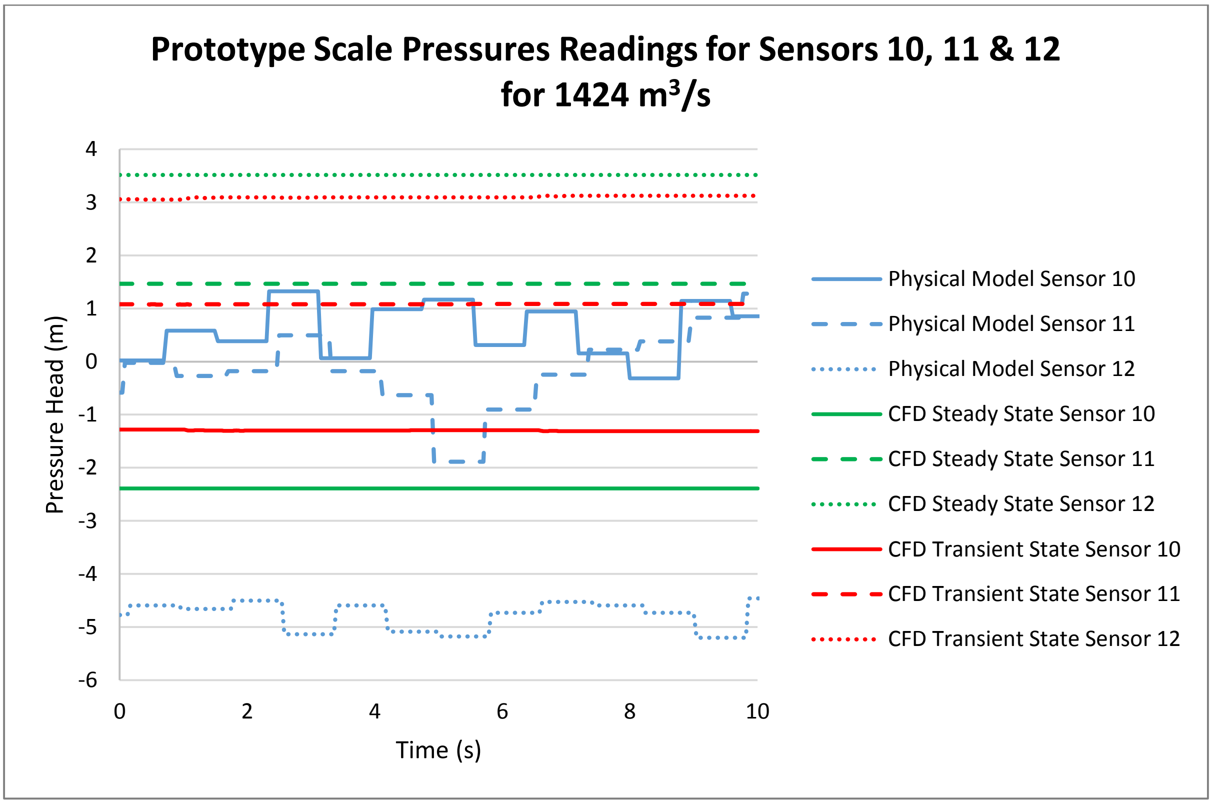

Figure E.39 Pressure readings for transient and steady state simulations and physical modelling for sensors 10-12 for a flow rate of 1 424 m^3/s at the prototype scale

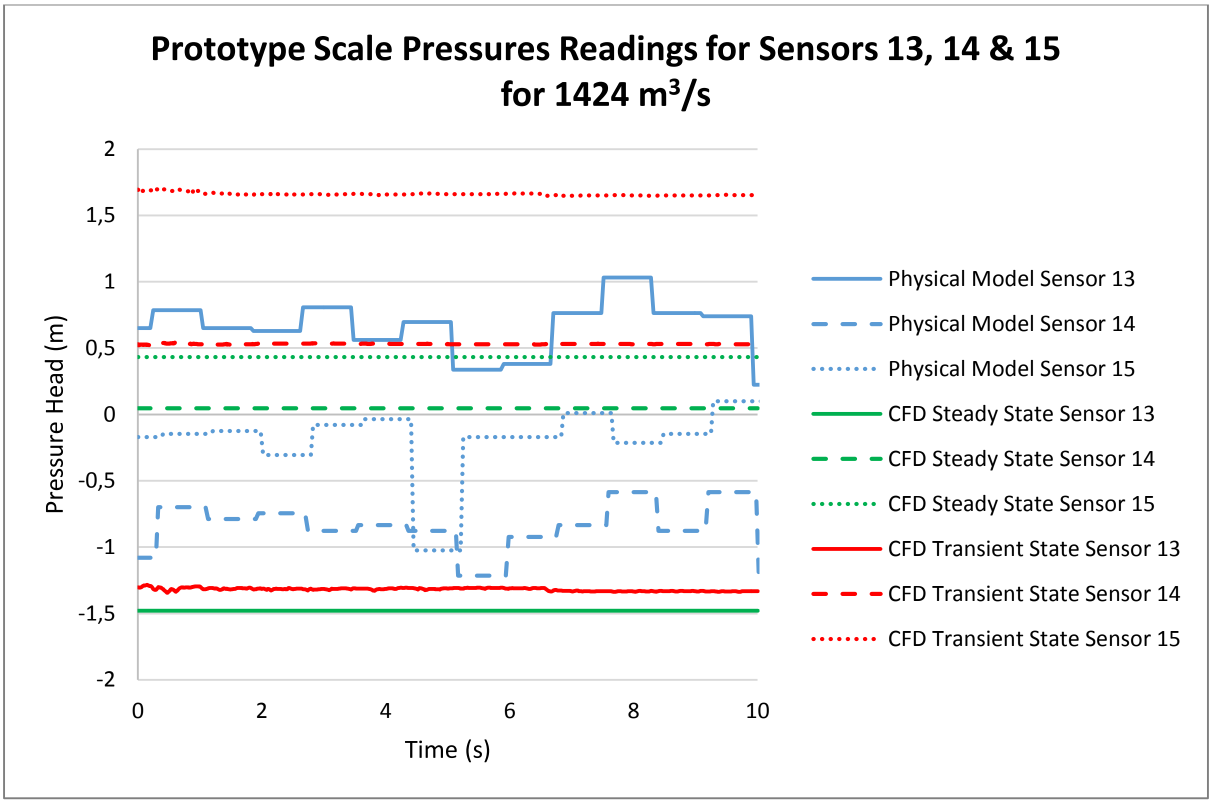

Figure E.40 Pressure readings for transient and steady state simulations and physical modelling for sensors 13-15 for a flow rate of 1 424 m^3/s at the prototype scale

Test 9: 1 606 m^3/s

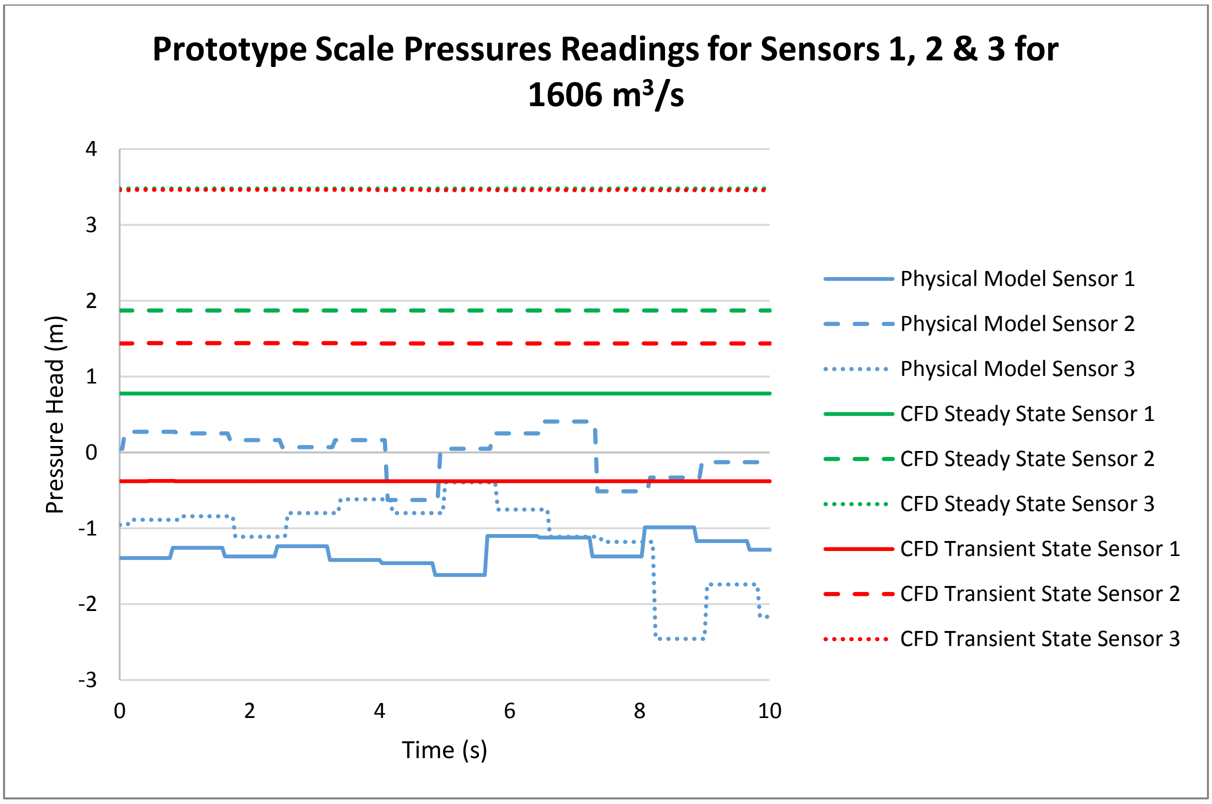

Figure E.41 Pressure readings for transient and steady state simulations and physical modelling for sensors 1-3 for a flow rate of 1 606 m^3/s at the prototype scale

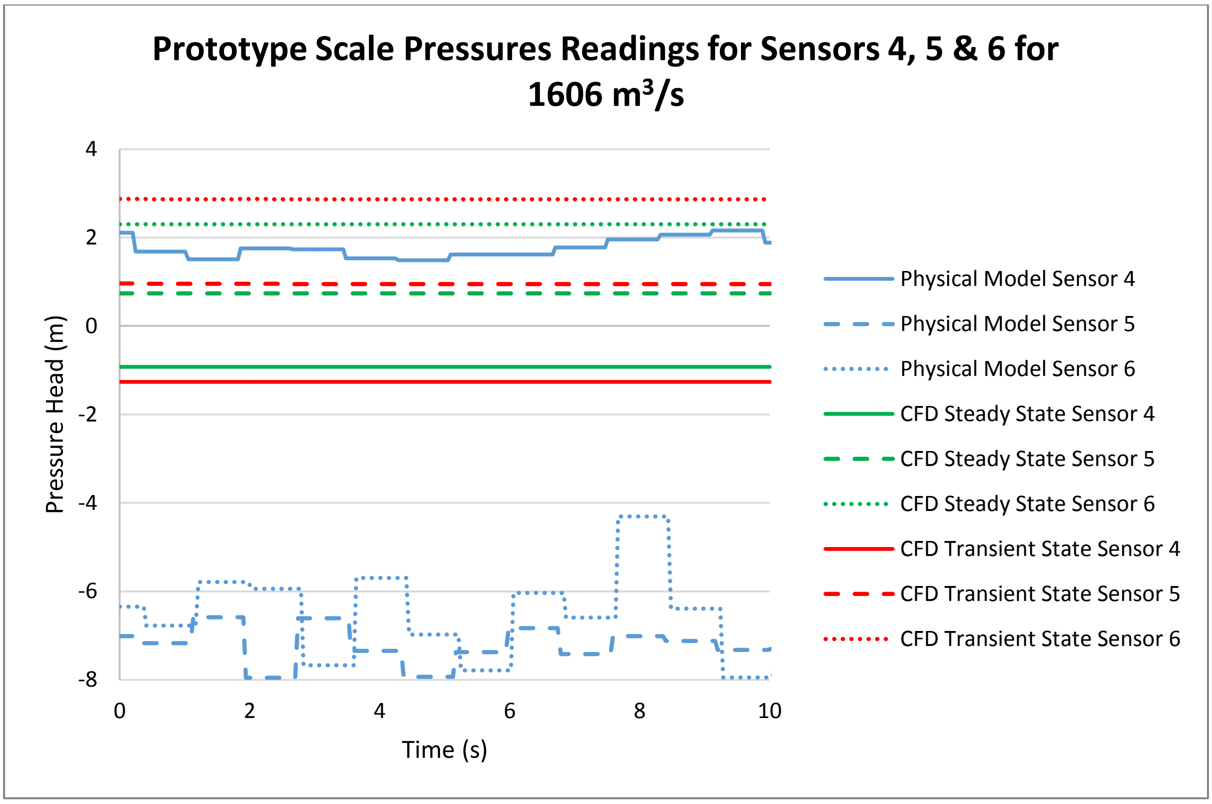

Figure E.42 Pressure readings for transient and steady state simulations and physical modelling for sensors 4-6 for a flow rate of 1 606 m^3/s at the prototype scale

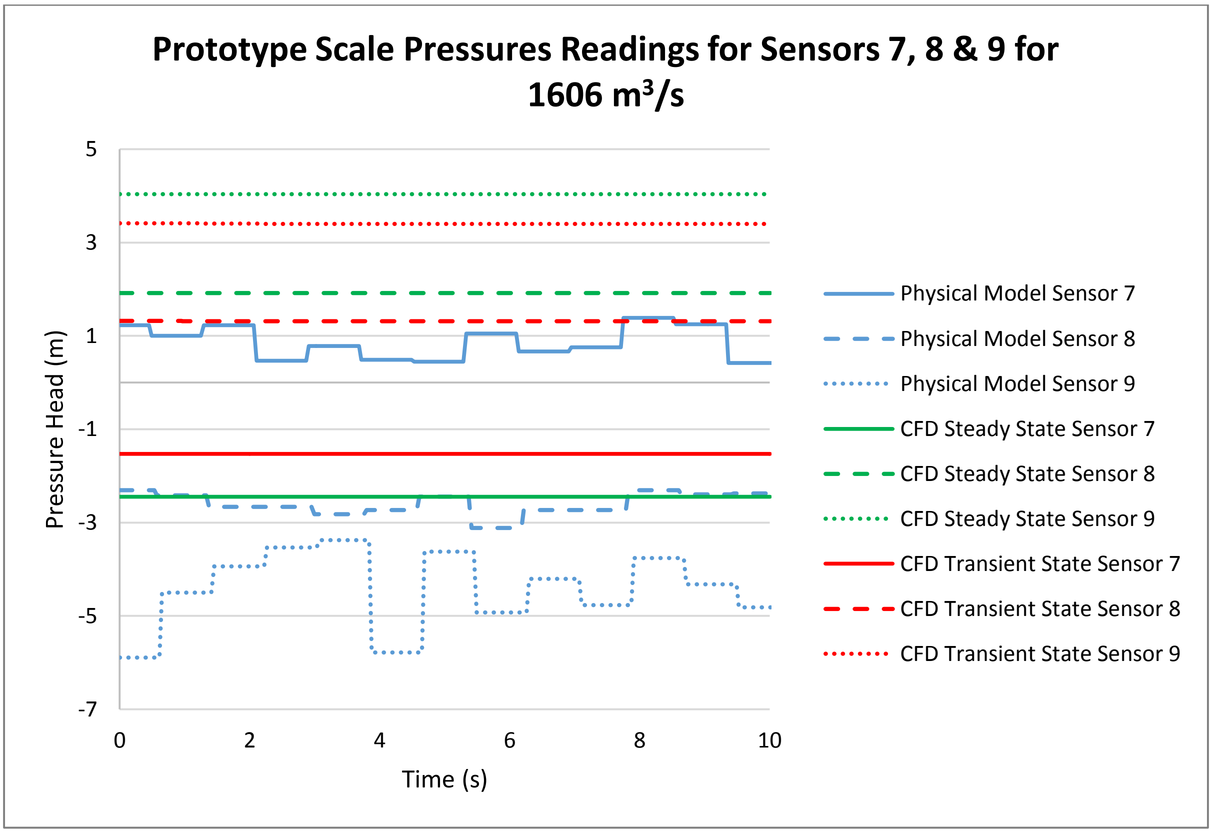

Figure E.43 Pressure readings for transient and steady state simulations and physical modelling for sensors 7-9 for a flow rate of 1 606 m^3/s at the prototype scale

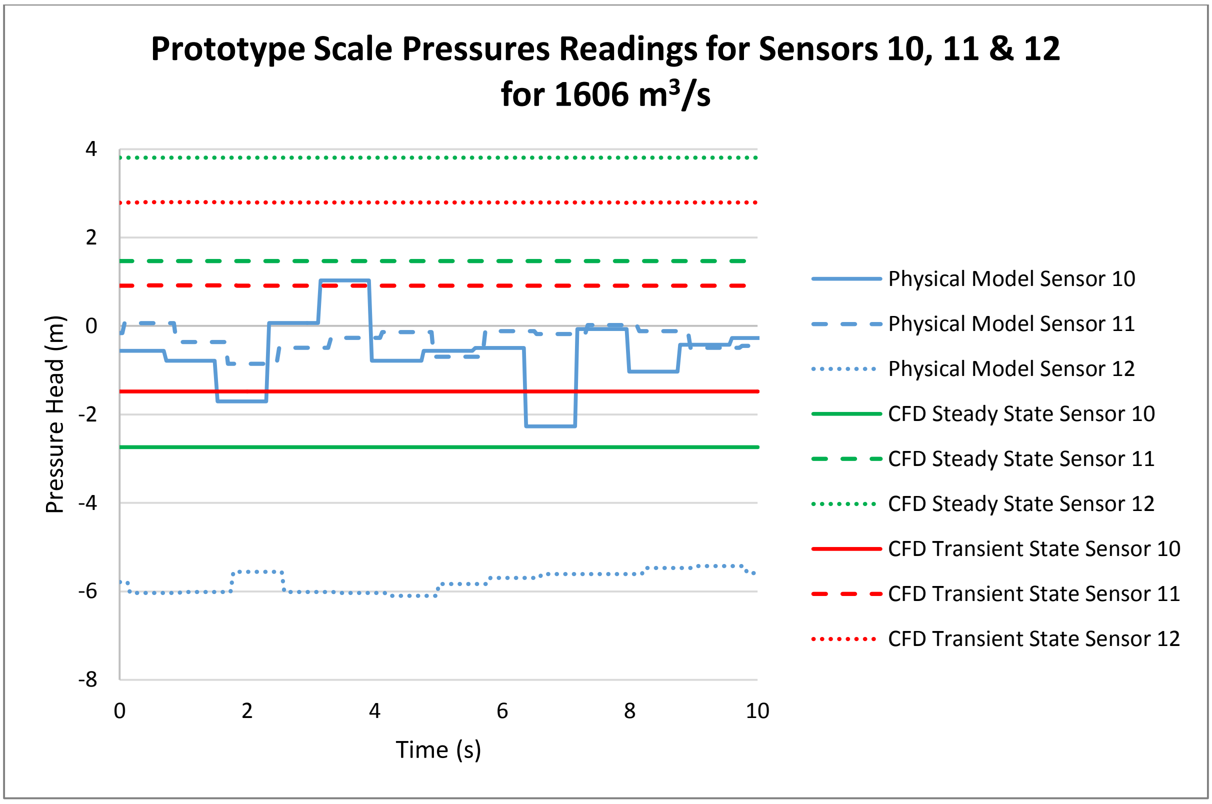

Figure E.44 Pressure readings for transient and steady state simulations and physical modelling for sensors 10-12 for a flow rate of 1 606 m^3/s at the prototype scale

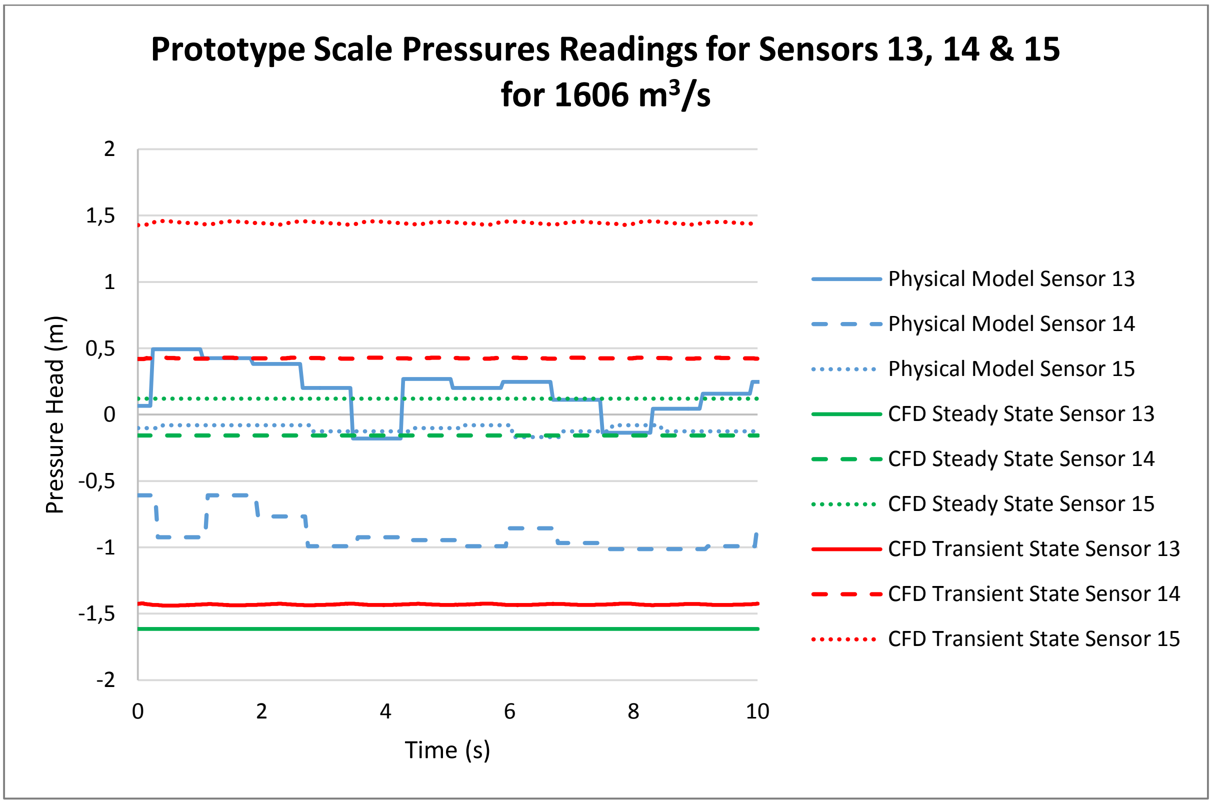

Figure E.45 Pressure readings for transient and steady state simulations and physical modelling for sensors 13-15 for a flow rate of 1 606 m^3/s at the prototype scale

Test 10: 1 789 m^3/s

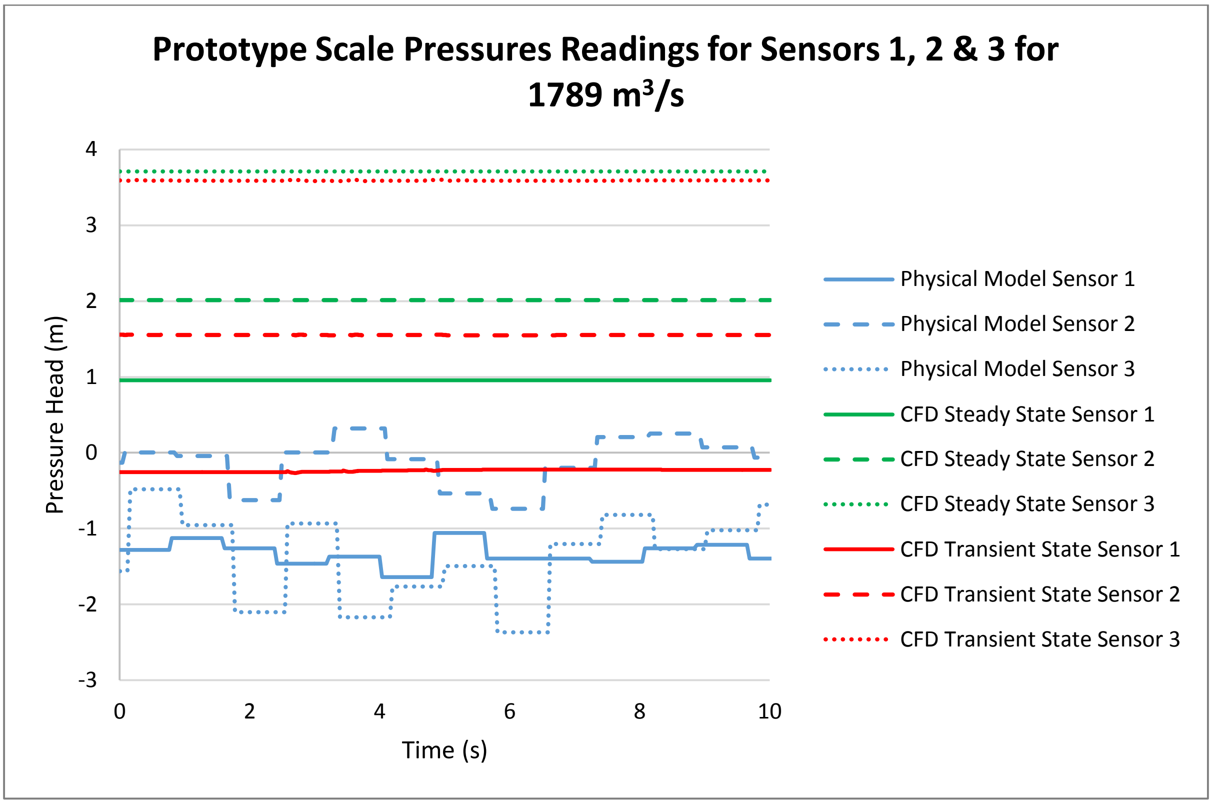

Figure E.46 Pressure readings for transient and steady state simulations and physical modelling for sensors 1-3 for a flow rate of 1 789 m^3/s at the prototype scale

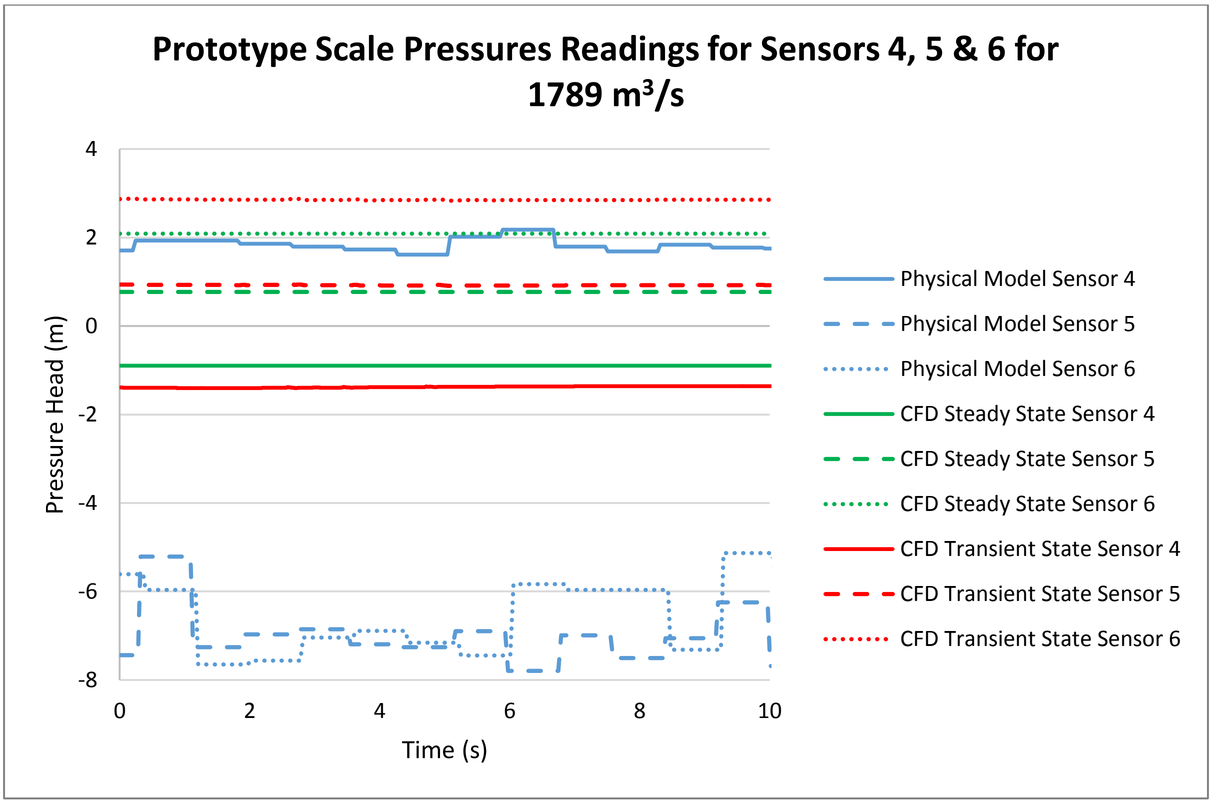

Figure E.47 Pressure readings for transient and steady state simulations and physical modelling for sensors 4-6 for a flow rate of 1 789 m^3/s at the prototype scale

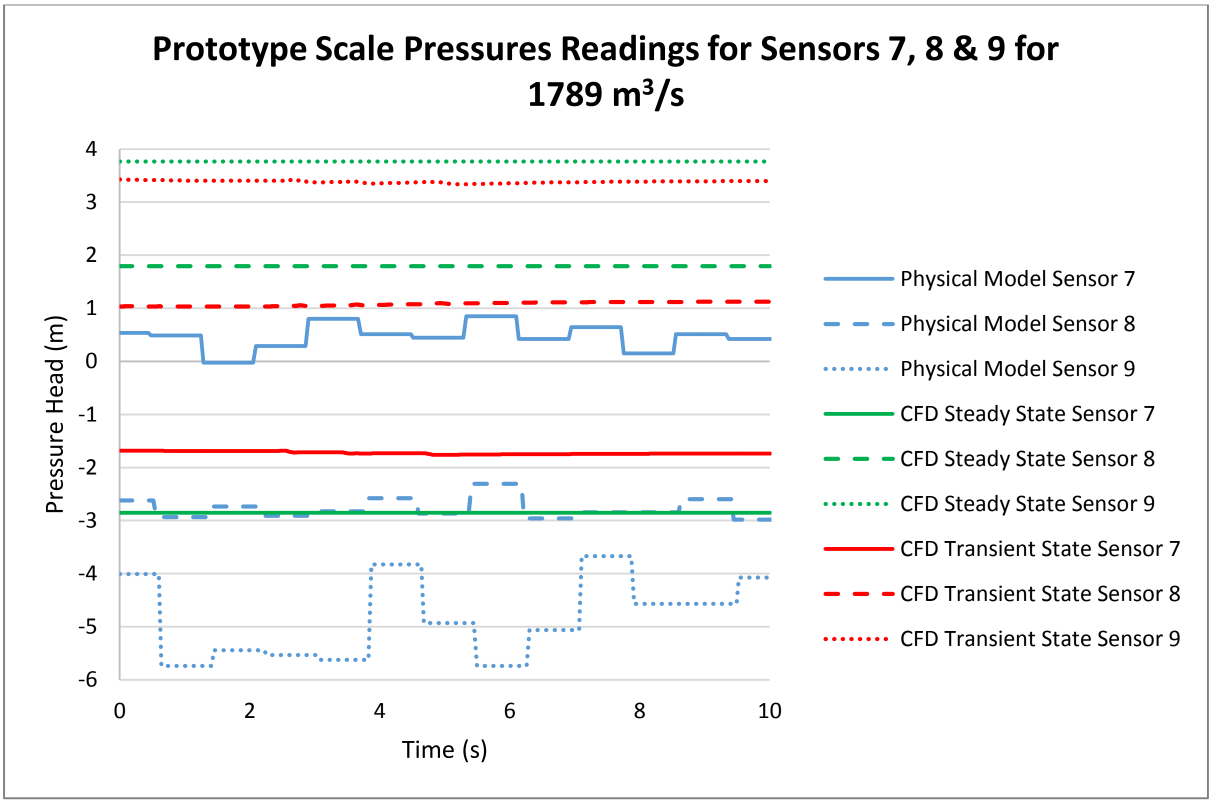

Figure E.48 Pressure readings for transient and steady state simulations and physical modelling for sensors 7-9 for a flow rate of 1 789 m^3/s at the prototype scale

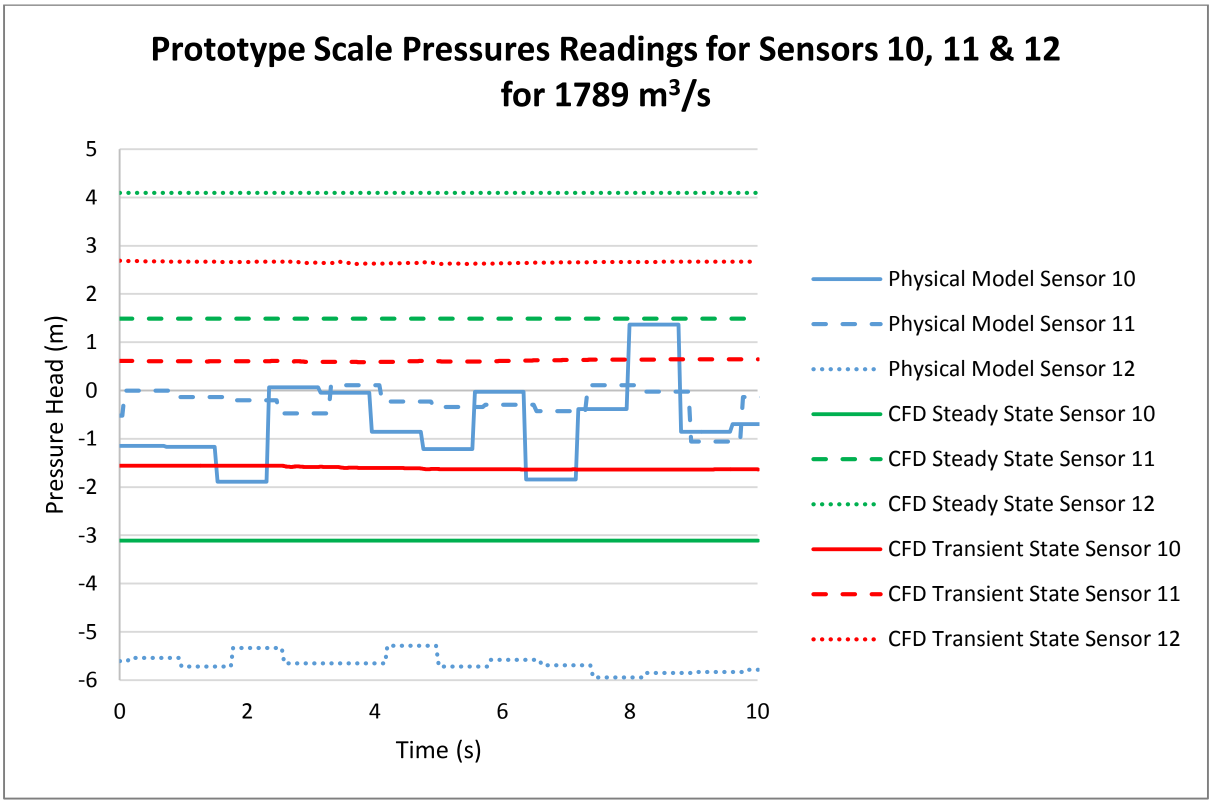

Figure E.49 Pressure readings for transient and steady state simulations and physical modelling for sensors 10-12 for a flow rate of 1 789 m^3/s at the prototype scale

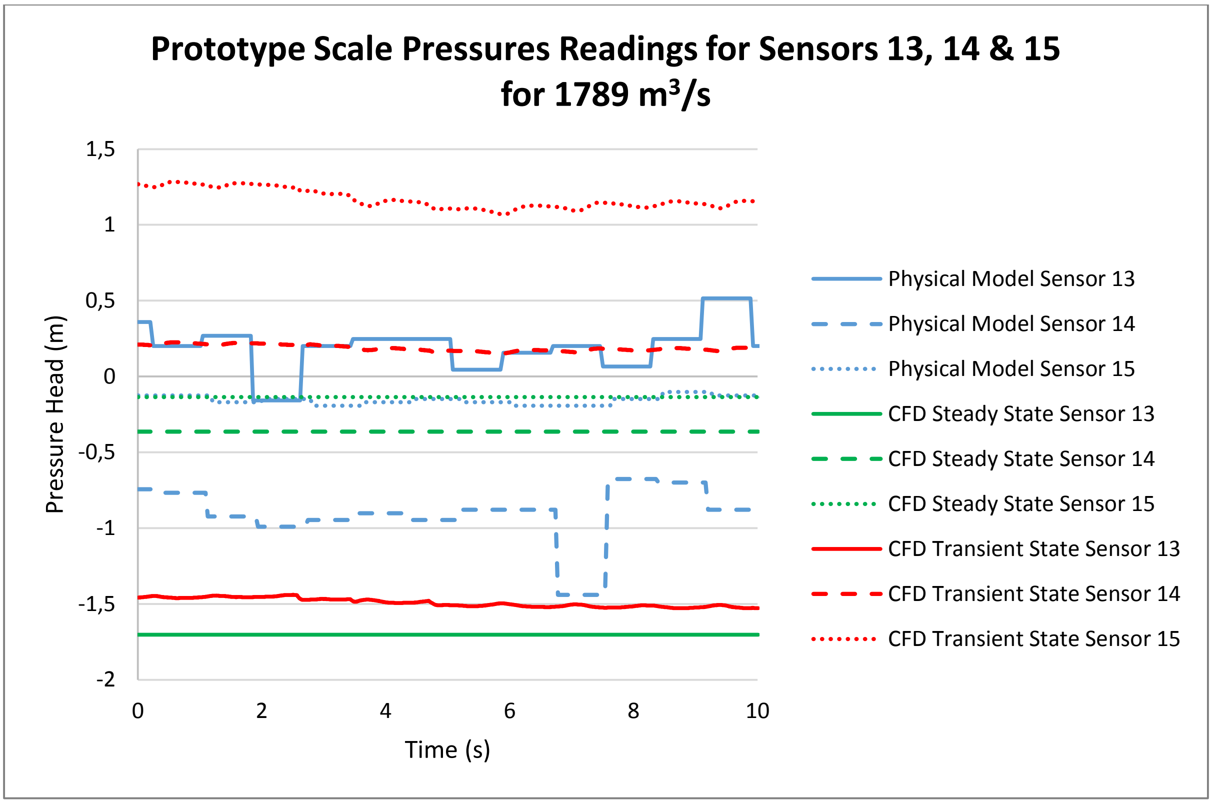

Figure E.50 Pressure readings for transient and steady state simulations and physical modelling for sensors 13-15 for a flow rate of 1 789 m^3/s at the prototype scale

Test 11: 1 968 m^3/s

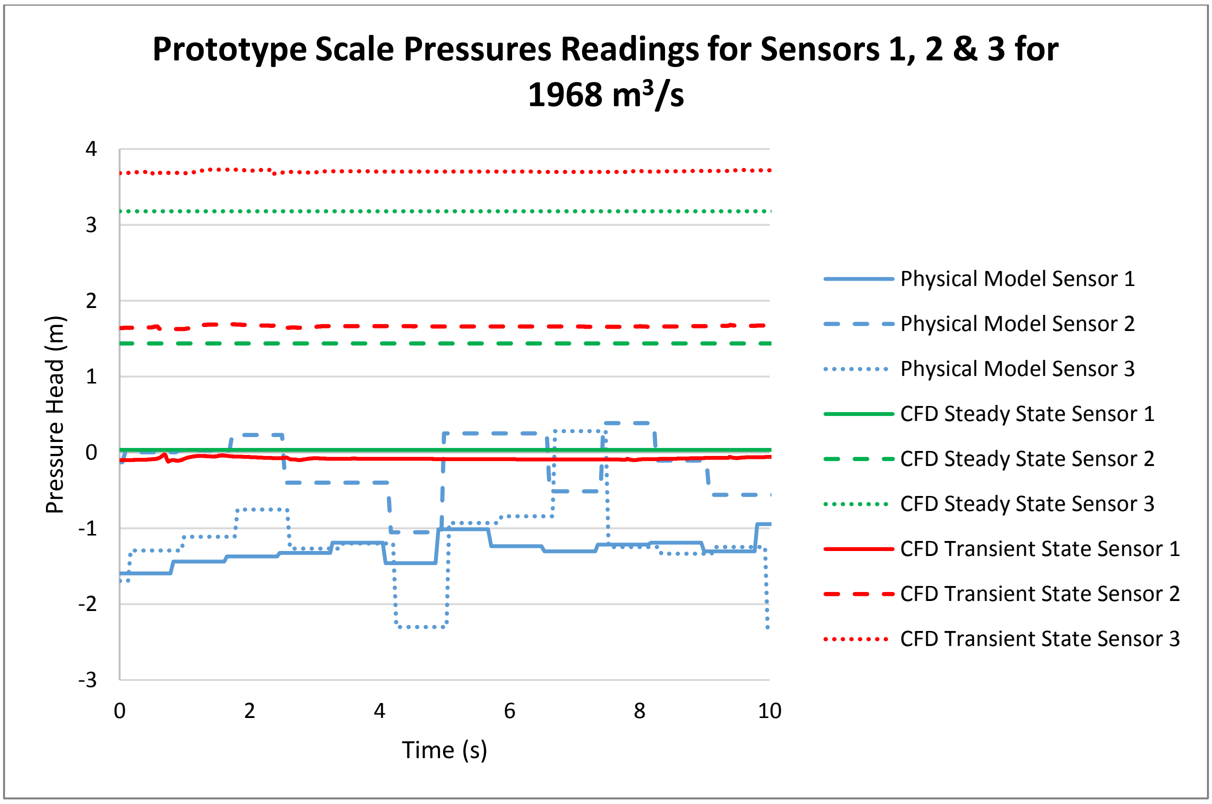

Figure E.51 Pressure readings for transient and steady state simulations and physical modelling for sensors 1-3 for a flow rate of 1 968 m^3/s at the prototype scale

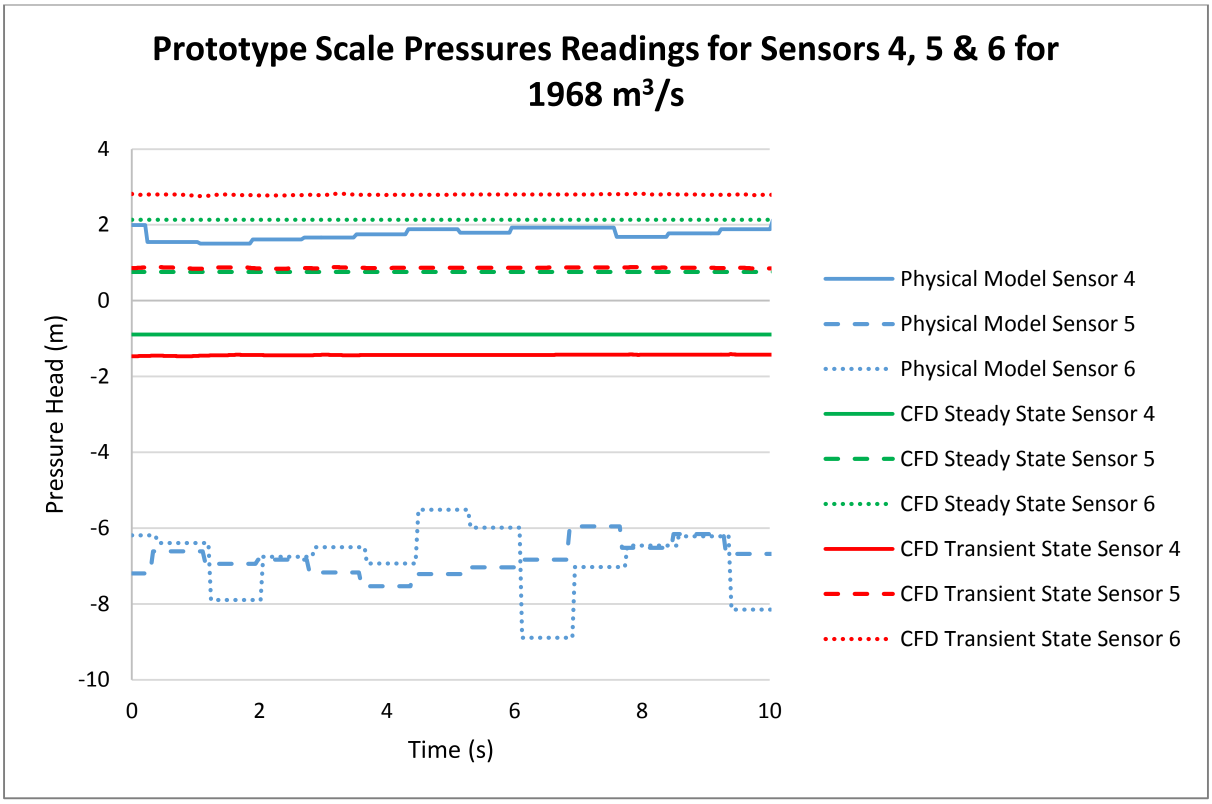

Figure E.52 Pressure readings for transient and steady state simulations and physical modelling for sensors 4-6 for a flow rate of 1 968 m^3/s at the prototype scale

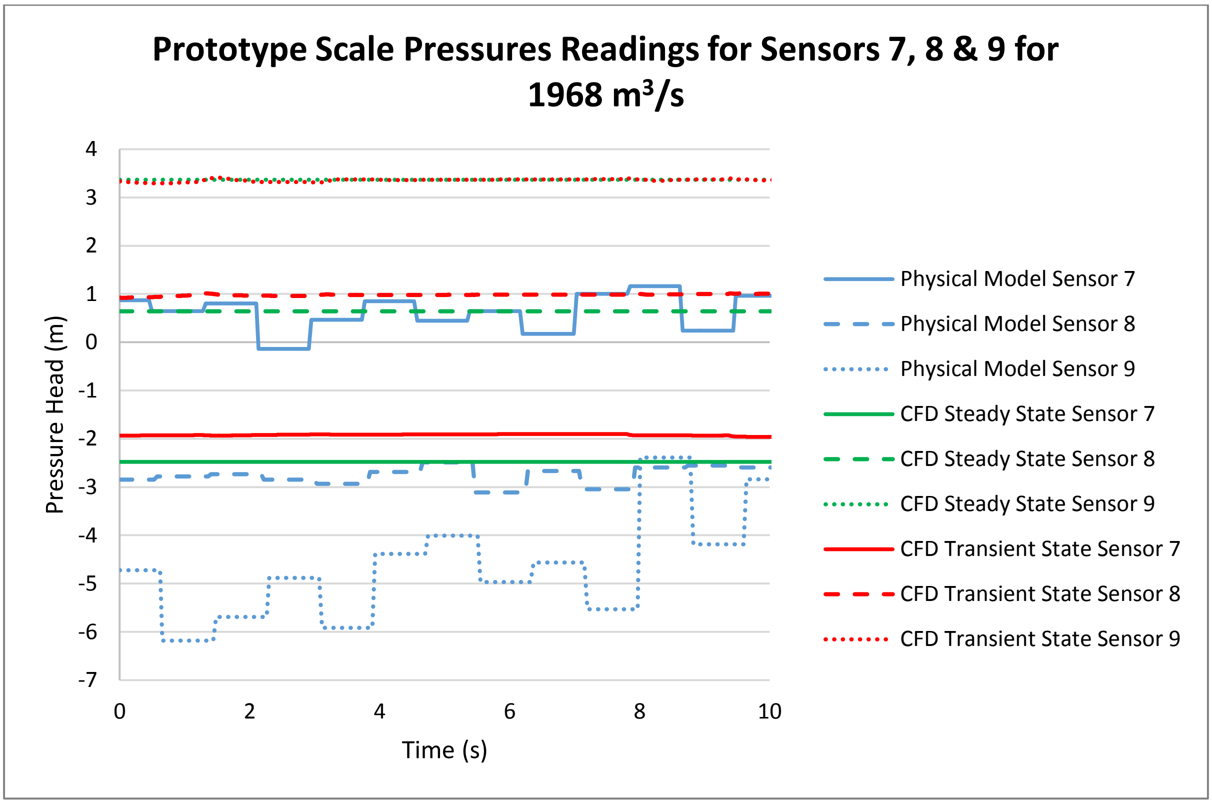

Figure E.53 Pressure readings for transient and steady state simulations and physical modelling for sensors 7-9 for a flow rate of 1 968 m^3/s at the prototype scale

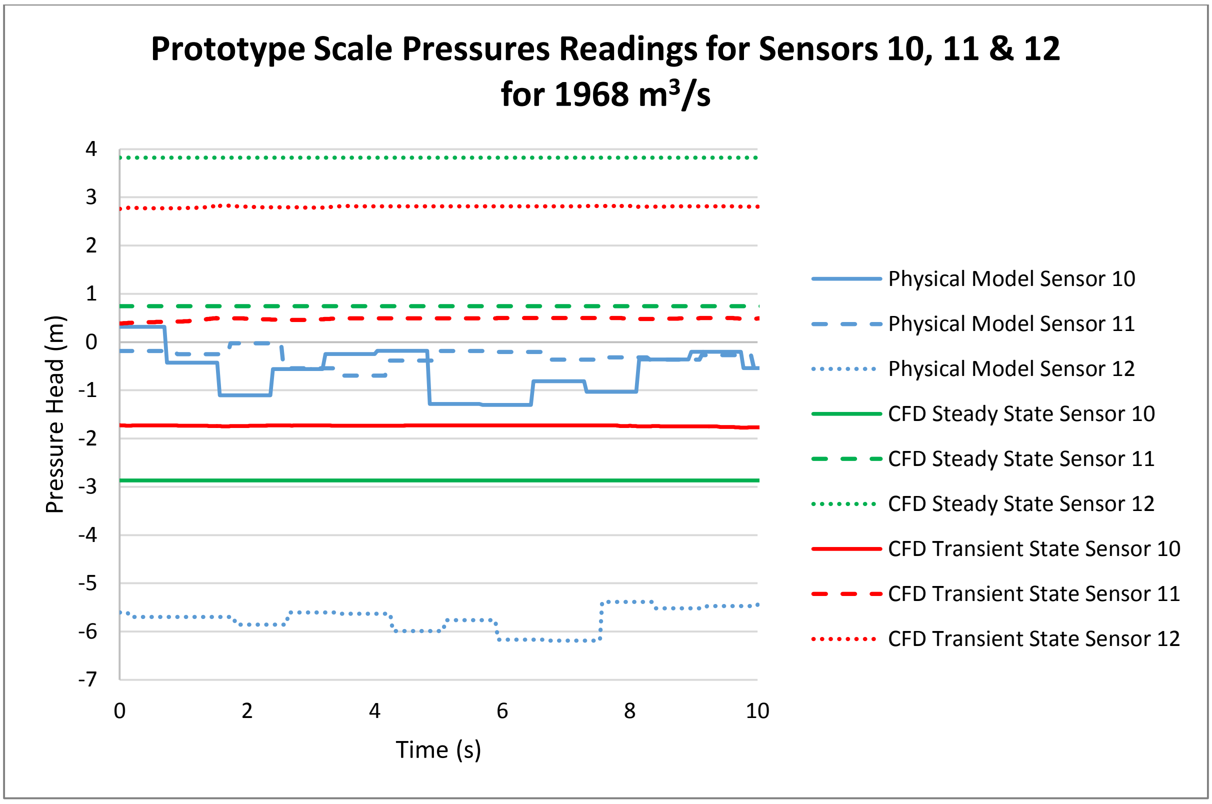

Figure E.54 Pressure readings for transient and steady state simulations and physical modelling for sensors 10-12 for a flow rate of 1 968 m^3/s at the prototype scale

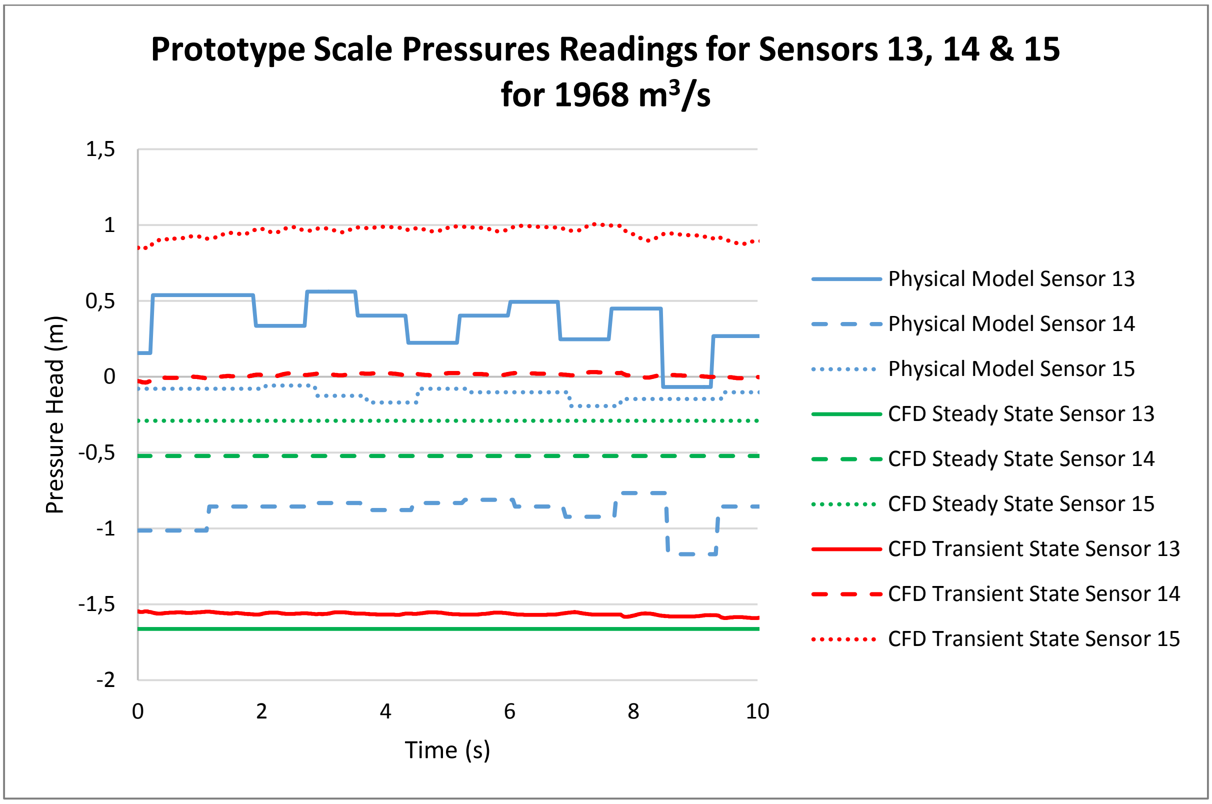

Figure E.55 Pressure readings for transient and steady state simulations and physical modelling for sensors 13-15 for a flow rate of 1 968 m^3/s at the prototype scale

Test 12: 2 136 m^3/s

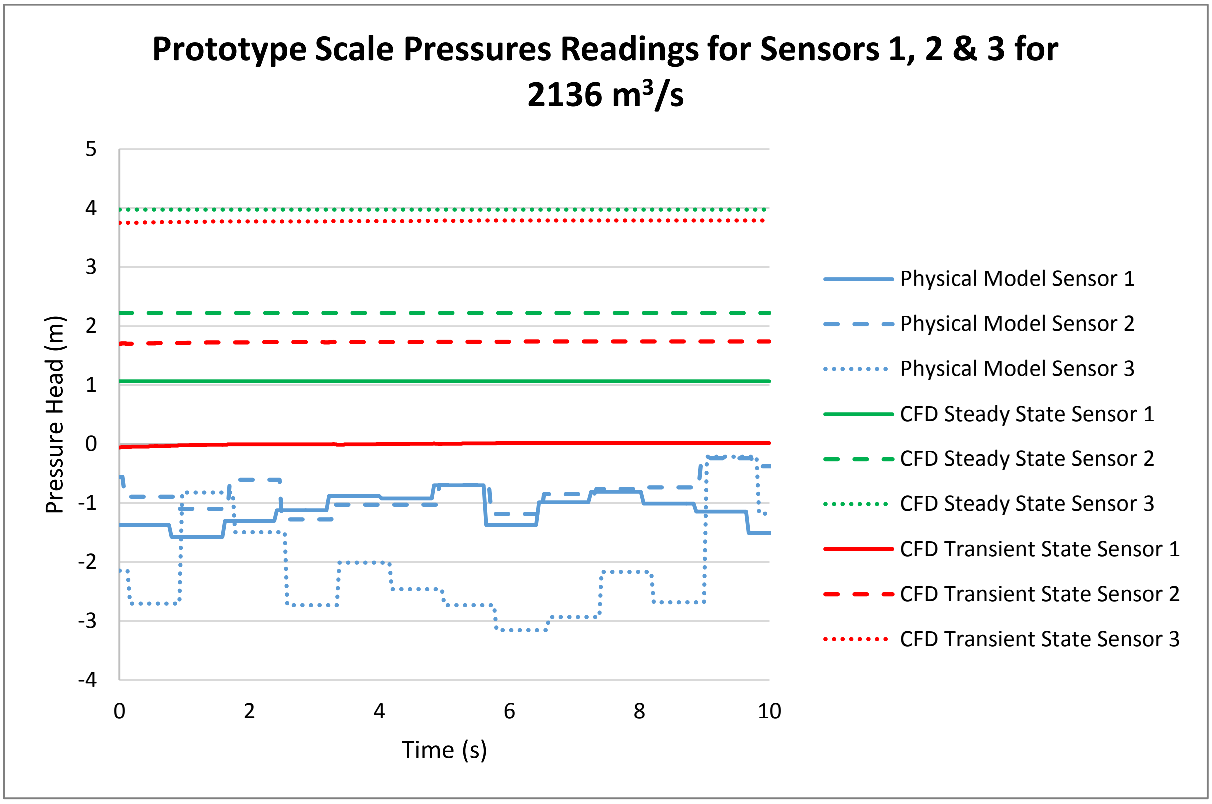

Figure E.56 Pressure readings for transient and steady state simulations and physical modelling for sensors 1-3 for a flow rate of 2 136 m^3/s at the prototype scale

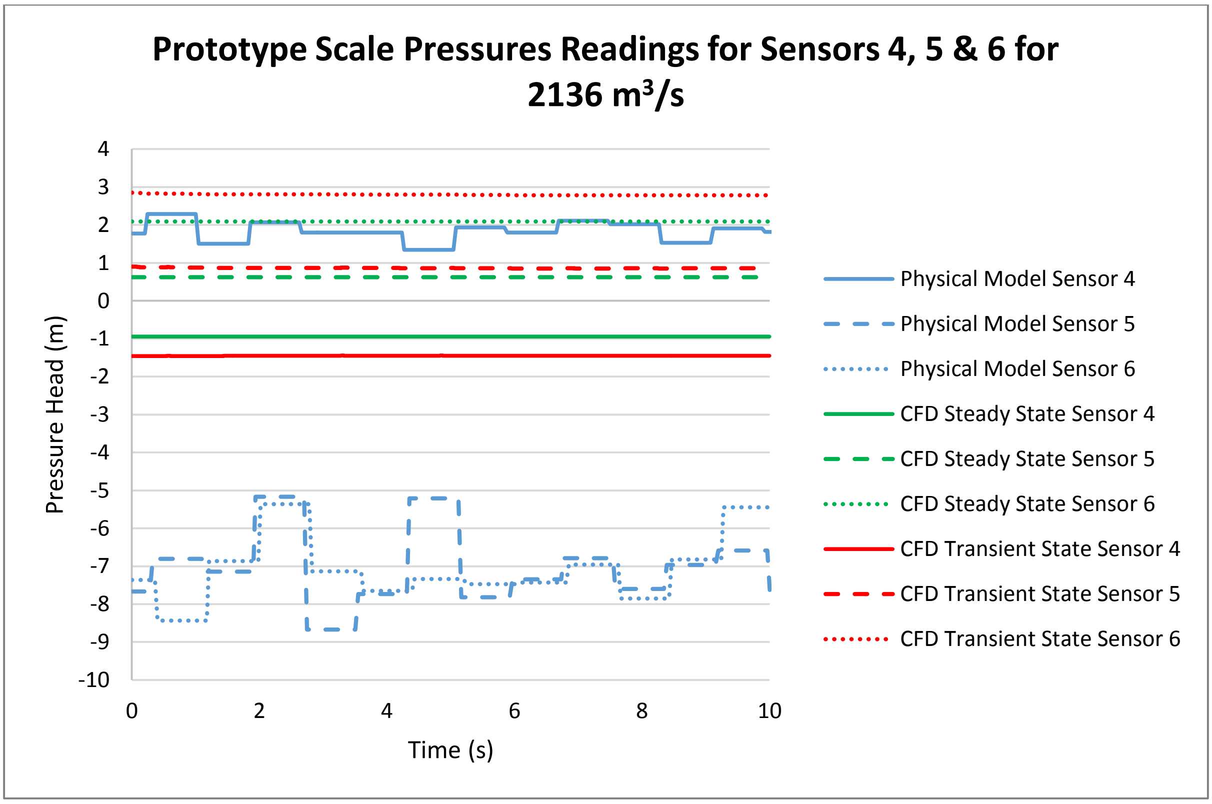

Figure E.57 Pressure readings for transient and steady state simulations and physical modelling for sensors 4-6 for a flow rate of 2 136 m^3/s at the prototype scale

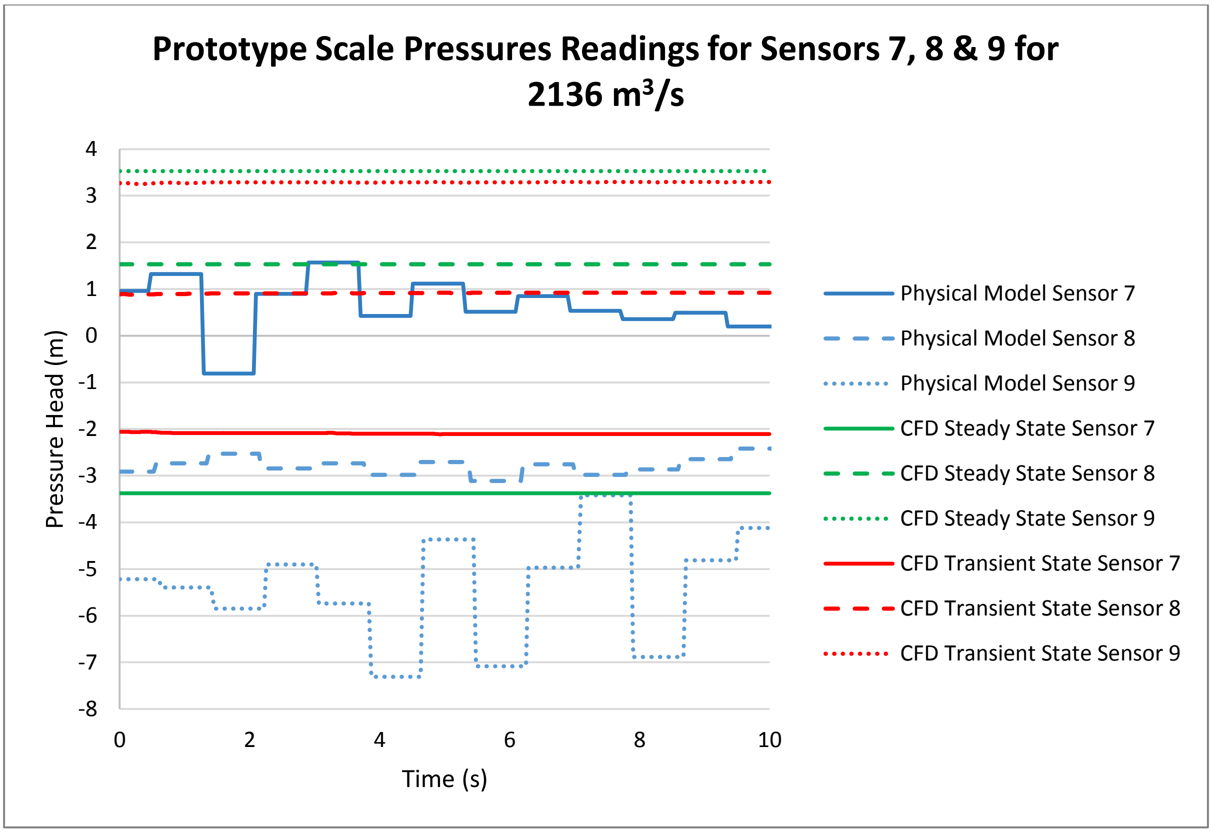

Figure E.58 Pressure readings for transient and steady state simulations and physical modelling for sensors 7-9 for a flow rate of 2 136 m^3/s at the prototype scale

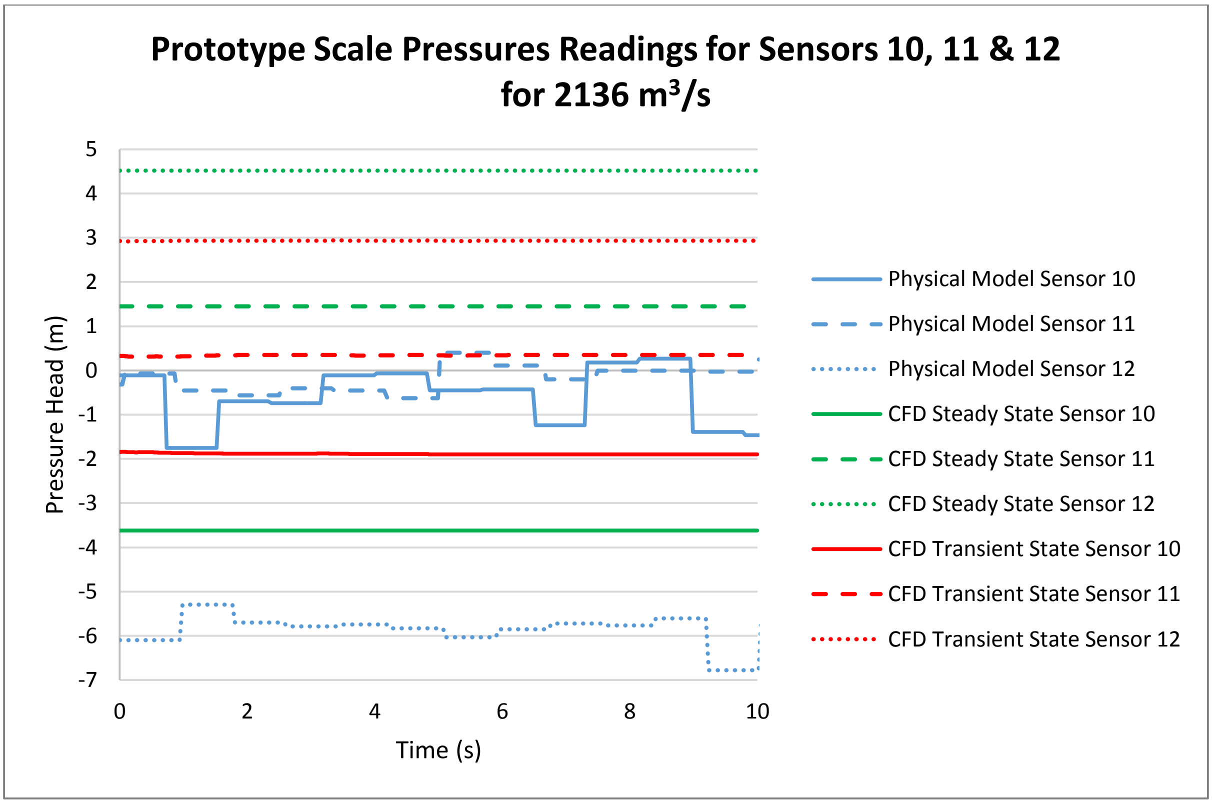

Figure E.59 Pressure readings for transient and steady state simulations and physical modelling for sensors 10-12 for a flow rate of 2 136 m^3/s at the prototype scale

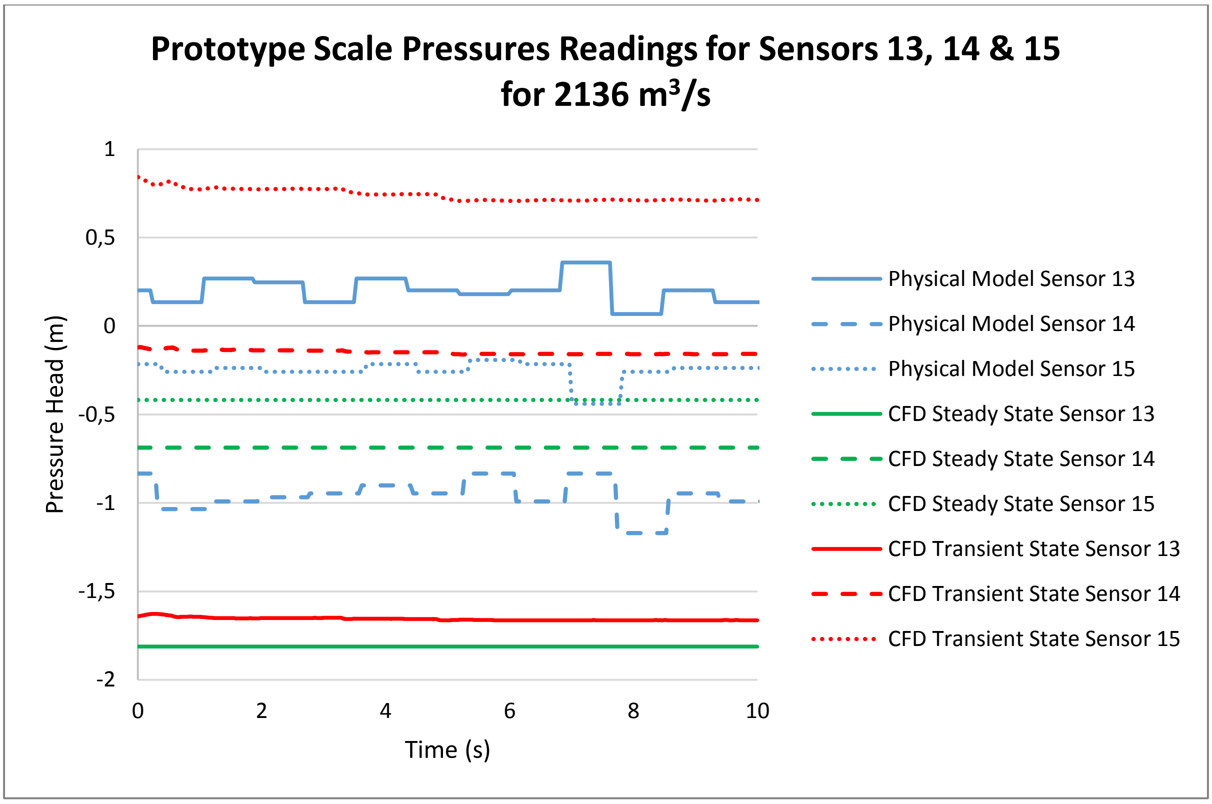

Figure E.60 Pressure readings for transient and steady state simulations and physical modelling for sensors 13-15 for a flow rate of 2 136 m^3/s at the prototype scale